

# VERÖFFENTLICHUNGEN

des Fachgebietes Bodenmechanik und Grundbau  
der Technischen Universität Kaiserslautern

---

**Herausgeber: Prof. Dr.-Ing. C. Vrettos**

---

Heft 18

EXPERIMENTAL AND NUMERICAL INVESTIGATIONS ON  
WHEEL-SOIL INTERACTIONS IN CALIBRATED NEAR-SURFACE  
SOIL MODEL

von

**Salomi Papamichael**

---

KAISERSLAUTERN 2019



Vom Fachbereich Bauingenieurwesen  
der Technischen Universität Kaiserslautern

zur  
Verleihung des akademischen Grades  
DOKTOR-INGENIEUR (Dr.-Ing.)  
genehmigte

**DISSERTATION**

D 386

Tag der Einreichung: 29. Juli 2019

Tag der mündlichen Prüfung: 12. November 2019

Dekan: Prof. Dr. rer. nat. Oliver Kornadt

Berichterstatter: Prof. Dr.-Ing. habil. Christos Vrettos  
Priv.-Doz. Dr.-Ing. Andreas Becker  
Prof. Dr.-Ing. Frank Rackwitz

Autorin dieses Heftes ist

**Salomi Papamichael**

Wissenschaftliche Mitarbeiterin am Fachgebiet Bodenmechanik und  
Grundbau der Technischen Universität Kaiserslautern





# Editor's Foreword

The experimental and numerical investigation of terramechanical problems is a new research field in soil mechanics. It concerns the interaction of tired wheels or tools with the ground. Such problems are characterized by large deformations. The insight gained so far derives primarily from experimental investigations, on the basis of which simplified interaction models have been established. The numerical simulation is performed either by the DEM or by explicit FEM algorithms. A particular challenge is imposed by the low pressure level prevailing in the vicinity of the terrain surface in contrast to high pressures encountered in classical geotechnical engineering problems. The present thesis deals with the experimental investigation and numerical simulation of a compliant wheel/tire in interaction with unsaturated soil. While in most of the works in the literature these two aspects are treated separately, an integral consideration is made here.

An essential parameter is the in-situ density. Empirical methods are critically reviewed and applied in a field test on Mount Etna. The tests in the laboratory comprise compressional and shear tests on various materials, as well as large direct shear tests on a flat tire section to assess soil-tire interface parameters. Stationary tests on a compliant wheel resting on a soil layer are carried out to identify the effects of moisture content on the vertical soil-wheel interaction. Results of the experiments are then used to parametrize an elasto-plastic soil model that is subsequently used in numerical simulations of a moving wheel by means of an explicit FEM code. The results are used to assess the effects of the initial driving parameters on the response characteristics.

The present dissertation provides a significant contribution to experimental and numerical terramechanics, and can be used as a starting point to more elaborate models involving various terrain types, advanced constitutive laws for the soil and different operation modes.

Christos Vrettos



# Preface

This dissertation work was carried out at the Technical University Kaiserslautern and was supported partly by "Stiftung zur Förderung begabter Studierender und des wissenschaftlichen Nachwuchses, Rheinland-Pfalz, Deutschland" and partly by a scholarship from the division of Soil Mechanics and Foundation Engineering of the Technical University Kaiserslautern. The field investigations were carried out in the frame of the Helmholtz Alliance "Robotic Exploration of Extreme Environments – ROBEX" project.

At this point I would like to express my deepest appreciation to my supervisor Prof. Christos Vrettos for supporting me during this incomparable journey and for supervising my scientific work.

I would also like to thank my co-supervisor Dr. Andreas Becker for his helpful advice and Prof. Frank Rackwitz for reviewing my dissertation.

Appreciation is due to Mr. Ronald Günther and his team, especially to Belend Atroshi, for carrying out part of the experiments and supporting me in the laboratory as needed.

Last but not least, I would like to thank my friends and family who supported me in my long journey towards a doctoral degree.

Salomi Papamichael



# Table of Contents

	Page
<b>Foreword.....</b>	<b>i</b>
<b>Preface .....</b>	<b>iii</b>
<b>Table of Contents .....</b>	<b>v</b>
<b>List of Symbols .....</b>	<b>ix</b>
Latin Symbols.....	ix
Greek Symbols .....	x
Abbreviations .....	x
<b>Abstract.....</b>	<b>xiii</b>
<b>1 Introduction .....</b>	<b>1</b>
<b>2 State of the Art.....</b>	<b>4</b>
2.1 Properties of near-surface soils .....	4
2.1.1 Terrestrial soils .....	4
2.1.2 Extraterrestrial soils.....	14
2.2 Basic terramechanical models .....	17
2.2.1 General.....	17
2.2.2 Pressure vs sinkage models .....	18
2.2.3 Shear stress vs displacements models .....	21
2.3 FEM models in terramechanical applications .....	23

<b>3 In situ relative density: Reevaluation of DPH relationships and comparisons to CPT .....</b>	<b>30</b>
3.1 Introduction.....	30
3.2 Relative density in sands .....	31
3.3 Discussion.....	35
<b>4 Field investigation on the planetary analogue site Mount Etna .....</b>	<b>36</b>
4.1 Introduction.....	36
4.2 Experimental set up and site characterization .....	36
4.3 Shear strength testing in the laboratory .....	41
4.4 In situ penetration and density tests.....	42
4.5 Conclusions.....	45
<b>5 Small scale shallow penetration tests.....</b>	<b>46</b>
5.1 Introduction.....	46
5.2 Soil classification.....	46
5.3 Triaxial and oedometer tests.....	48
5.4 Penetration tests in containers of different sizes .....	53
5.4.1 Laboratory tests .....	53
5.4.2 Correlations for relative density .....	56
5.4.3 Correlations for the shear strength parameters.....	59
5.4.4 Boundary effects.....	61
5.5 Discussion.....	63
<b>6 Stationary tests on non-pneumatic wheel .....</b>	<b>64</b>

6.1	Introduction.....	64
6.2	Soil material tested .....	66
6.3	Non pneumatic wheel .....	67
6.4	Direct shear tests.....	68
6.4.1	Shear tests for wheel-soil interface properties .....	68
6.4.2	Shear tests of soil.....	72
6.5	Experimental procedure for the wheel tests .....	75
6.6	Results.....	76
6.7	Discussion.....	85
<b>7</b>	<b>FEM simulations.....</b>	<b>86</b>
7.1	Introduction and model set up .....	86
7.2	Wheel material model.....	91
7.3	Soil model.....	92
7.4	Calibration procedure for wheel-soil interaction.....	97
7.4.1	Steel rigid base .....	97
7.4.2	Compliant base .....	98
7.5	Results from the rolling simulation .....	104
7.5.1	Free rolling of various materials .....	104
7.5.2	Sensitivity to vertical force and to angular velocity.....	115
7.5.3	Braking, free rolling, driving.....	119
7.6	Discussion.....	124

<b>8 Summary and Outlook.....</b>	<b>128</b>
<b>Literature.....</b>	<b>132</b>
<b>Appendices.....</b>	<b>142</b>
A Results of oedometer tests .....	142
B Results from direct shear tests .....	147
C Further results from the wheel's tests.....	150



# List of Symbols

## Latin Symbols

Herein, the most significant symbols are presented in order to enable a smooth readability of the dissertation. All symbols used are defined in the text.

ALLVD	Viscous dissipated energy
$c$	Cohesion of the MC failure criterion
$c_{\text{int}}$	Cohesion of interface between soil-tool
$c_{\text{int},r}$	Residual cohesion of interface between soil-tool
$c_r$	Residual cohesion of soil
CAREA	Contact area
$C_N$	Stress Normalization factor
$d_n$	Particle diameter
$d_{50}$	Mean grain diameter
$d_{1,2}$	Cohesion of the Drucker Prager Model shown in eq.(52)
$e$	Void ratio
$E$	Young's modulus
$E_s$	Constrained modulus
$g_i$	Shear relaxation or shear traction relaxation modulus ratio $\bar{g}_i^P$ in eq.(44)
$\bar{g}_i^P$	Material constant in eq.(44)
$g_R(t)$	Dimensionless relaxation modulus eq.(44)
$G$	The flow potential as defined in eq.(53)
$I_D$	Relative Density
$I_F$	$(e_{\text{max}} - e_{\text{min}})/e_{\text{min}}$
$K$	Flow stress ratio in Drucker Prager constitutive model
$n_{\text{max},\text{min}}$	Maximum and minimum porosity respectively
$N_{nL,nH}$	Measured number of blows per $n$ cm penetration with for DPL or DPH

$N'_{nL,nH}$	Measured number of blows per $n$ cm penetration below groundwater for DPL and DPH
$N_{10,1N}$	Normalized value of $N_{10}$ to 1 atm
$q_c$	Tip resistance of Cone Penetration Test
$q_{c1N}$	Normalized cone resistance to 1 atm
$q_d$	Tip resistance of Dynamic Penetration test
$RF_n$	Reaction force in the $n$ direction in FEM model
$RM_n$	Reaction moment in the $n$ direction in FEM model
$S_{nn}$	Stress in the n-n direction in FEM model
$u_n$	Displacement in the n direction in the FEM model
$U$	The strain energy per unit of reference volume in eq.(38)
$v_n$	Velocity in the n-axis of the FEM model

## Greek Symbols

$\beta$	Angle of the Drucker-Prager model
$\nu$	Poisson's ratio
$\sigma_{yield}$	Yield stress in the Drucker Prager hardening model
$\varphi$	Friction angle
$\varphi_{int}$	Soil/tool friction angle
$\varphi_{int,r}$	Soil/tool residual friction angle
$\varphi_r$	Residual friction angle
$\psi$	Dilation angle

## Abbreviations

$C_F$	Correction Factor
CPT	Cone Penetration Test
CPTu	Cone Penetration Test with pore water measurements
DP	Dynamic Probing

DPH, DPL, DPM,DPSH	Dynamic Probing Heavy, Light, Medium, Super Heavy
EVM	Etna volcanic material
FC	Fines content
FEM	Finite Element Method
JSC-1	Johnson Space Center lunar simulant
JSC-1A	Clone of the JSC-1 simulant
JSC Mars-1A	Johnson Space Center Mars simulant
MMS	Mojave Mars Simulant
MSS-D	Mars Soil Simulant - finer
NPT	Non pneumatic tire
Panda <sup>®</sup>	Lightweight Dynamic Penetrometer
SBTn	Soil Behavior Type normalized
Tweel <sup>®</sup>	Michelin Tweel
WF34 sand	Mars simulant from quartz sand on Earth



# Abstract

The research area of terramechanics is relatively new and there are still many gaps that need to be filled to ensure a common effort towards improving and advancing related technologies. The most important requirement is the establishment of standards that will be followed worldwide for the development and optimization of terramechanical applications.

The main focus of the research lies in the interpretation and application of results and correlations of soil properties from in situ testing and subsequent use in terramechanical applications. The empirical correlations and current procedures were mainly developed for medium to large depths, and therefore they were re-evaluated and adjusted herein to reflect the current state of knowledge for the assessment of near-surface soil.

For testing technologies, a field investigation to a moon analogue site was carried out. Focus was placed in the assessment of the near surface soil properties. Samples were collected for subsequent analysis in laboratory conditions. Further laboratory experiments in extraterrestrial soil simulants and other terrestrial soils were conducted and correlations with relative density and shear strength parameters were attempted. The correlations from the small scale laboratory experiments, and the new re-evaluated correlation for relative density from the previous chapter, were checked with the data from the field investigation and resulted in promising results.

Additionally, single tire-soil tests were carried out, which enable the investigation of the localized soil response in order to advance current wheel designs and subsequently the vehicle's mobility. Furthermore, numerical simulations were done to aid the investigation of the tire-soil interaction.

Summing up, current relationships for estimating relative density of near surface soil were re-evaluated, and subsequently correlated to shear strength parameters that are the main input to model soil in numerical analyses. Single tire-soil tests were carried out and were used as a reference to calibrate the interaction of the tire and the soil and subsequently were utilized to model rolling scenarios which enable the assessment of soil trafficability and vehicle's mobility.



# 1 Introduction

Terramechanics is a new research area that lacks yet a single standard to guide the research related to terramechanical terrestrial off-road applications and extraterrestrial missions. Soil and terrain datasets are required for real time evaluations of terrain trafficability and vehicle mobility. Focus should be placed on the near-surface soil. Understanding the soil types and the effects of water content on terrain trafficability is essential for optimizing vehicle mobility.

In situ testing is used worldwide for estimation of soil properties which consist part of the main input for soil models in terramechanical applications. Static and dynamic tests are utilized on site investigations. The results from the tests could be used directly to vehicle mobility models or after cross-correlating with other parameters. Shear strength parameters, which are the main parameters of numerical soil models, can't be measured directly on a site and therefore empirical correlations are needed. A dominant correlated parameter to in situ testing is the relative density. Empirical techniques and correlations of these tests are mostly related to medium and large depths and therefore careful consideration is required for assessment of the near-surface soil.

Planetary analogues sites are essential for testing technologies and equipment for future exploration missions. Gathered data from these kind of field investigations, may be limited due to time constraints, equipment limitations, personnel etc. Samples from field investigations are usually limited in number and therefore soil simulants are used in order to conduct more tests in controlled laboratory conditions. Combination of field investigations and laboratory experiments can provide the necessary information and correlations for successful planning of future operations in Space and regions with difficult ground conditions.

Since the 1960s simplified empirical soil-tire models were proposed. Nowadays finite element model and advance numerical techniques are used to capture the complex interaction between vehicle and terrain. Most of the soil numerical models are not calibrated with measured soil parameters. Instead soil models from the literature are used, and therefore the numerical results are not calibrated to real case scenarios of the specific wheel-soil interaction. Simplifications in the numerical analysis and in the soil models

can lead to a blind validation of a model. A promising method for calibrating wheel-soil interaction, is the inexpensive single tire-soil experiments.

One major objective of this research is to reevaluate current relationships for estimating relative density of near surface soil from in-situ testing, and subsequently correlating to shear strength parameters in order to accurately model the soil in numerical analyses. Second major objective is to provide soil properties of specific soils and showcase how laboratory tests can provide the required parameters for subsequent use in a numerical soil model. Third major objective is to utilize a cost effective approach of carrying out single tire-soil experiments in controlled laboratory conditions for subsequent numerical simulations for evaluation and optimization of a current wheel design. In this type of tests, the soil response can be separated from the complex vehicle dynamics and the wheel design can be optimized for an enhanced vehicle mobility by calibrating the experiments with FEM models.

Chapter 2 summarizes the current state of art regarding investigation on terrestrial and extraterrestrial soils, basic terramechanical models and finite element methods in terramechanics.

Chapter 3 presents a reevaluation of DPH relationships and comparisons with current methodologies used for CPT. A stress normalization procedure is suggested for DPH, similar to the one followed by the CPT based procedures.

Chapter 4 presents a field investigation to an analogue site to demonstrate a possible way to transfer current methodologies and procedures to extraterrestrial investigations and regions with difficult ground conditions.

Chapter 5 focuses on laboratory small scale penetration tests on primarily soil simulants including, triaxial tests, oedometer tests, and penetration tests in containers of different sizes.

Chapter 6 describes wheel tests conducted with a special non-pneumatic wheel for calibrating wheel's and soil's behavior under loading.

Chapter 7 presents numerical simulations of the wheel tests. The calibrated wheel model is used to model rolling on the calibrated soil models and other complementary soil, for various rolling scenarios.



Chapter 8 summarizes the research work done and discusses possible future research possibilities based on the work done in this thesis.

## **2 State of the Art**

### **2.1 Properties of near-surface soils**

#### **2.1.1 Terrestrial soils**

The use of in-situ testing to measure soil properties for subsequent use in design methods is very common in standard site investigations. Empirical correlations based on theories have been developed through the years to relate soil parameters such as soil stratigraphy, density, friction angle, undrained shear strength, stress history, Young's and shear modulus, compressibility and liquefaction resistance to the values obtained from in situ testing. The soil properties correlate quite well with in-situ testing values. Naturally there are some limitations that have to be considered while testing. In this thesis two different types of in-situ testing were considered: dynamic and static penetration tests. Soil properties can be deduced from the obtained parameters of penetration tests.

##### **2.1.1.1 Cone penetration test CPT**

The Cone Penetration Test CPT is the most common test employed nowadays for site investigations providing a continuous profile of the subsoil conditions. Both electrical and mechanical CPT's are used. The set-up of the electrical CPT is specified by DIN EN ISO 22476-1 (replacement for DIN 4094-1); the mechanical CPT is regulated in DIN EN ISO 22476-12. DIN EN ISO 22476-1 contains an equation for determining the corrected tip resistance  $q_t$ , taking into account the measured excess pore water pressure. Relationships to determine the relative density are given in DIN 4020 for the soil groups SE, SW and GW. According to DIN 18196 SE corresponds to poorly graded sand, SW/GW to well graded sand and gravel, SI to intermediate graded sand, GE to poorly graded gravel and GI to intermediate graded gravel. Conversion factors between the two CPT device types are not specified in that ISO standard.

### ***-Soil Classification from CPT***

The stratigraphic profile can be interpreted from CPT using different empirical diagrams. In design practice, the most commonly used classification procedure is based on the normalized soil behavior type SBTn chart by Robertson (1990, 2010). A first screening can be accomplished solely by using the soil index  $I_c$  which has been proposed by Robertson and Wride (1998) to capture the soil type. Sand mixtures – silty sand to sandy silt exhibit values of  $I_c = 2.05-2.60$ , clean sands to silty sands have  $I_c = 1.31-2.05$  and gravelly sand to dense sand values of  $I_c$  less than 1.31. The  $I_c$  is defined as follow:

$$I_c = \left[ (3.47 - \log Q_m)^2 + (\log F_r + 1.22)^2 \right]^{0.5} \quad (1)$$

$$F_r = \frac{f_s}{q_t - \sigma_{v0}} \times 100\% \quad (2)$$

$$Q_m = \left( \frac{q_t - \sigma_{v0}}{p_a} \right) \left( \frac{p_a}{\sigma'_{v0}} \right)^n \quad (3)$$

$$n = 0.381I_c + 0.05 \left( \frac{\sigma'_{v0}}{p_a} \right) - 0.15 \leq 1.0 \quad (4)$$

where  $q_t$  is the the corrected tip resistance accounting for pore water effects,  $F_r$  is the normalized friction ratio,  $Q_m$  is the normalized cone resistance,  $I_c$  is the soil behaviour index,  $n$  is the stress normalization exponent,  $\sigma_{v0}$  is the in-situ initial vertical stress,  $\sigma'_{v0}$  is the in-situ initial vertical effective stress and  $p_a$  is the atmospheric pressure.

The in-situ stresses can either be calculated assuming appropriate values of the soil unit weight or estimated directly using the following equation (Robertson & Cabal, 2015):

$$\frac{\gamma}{\gamma_w} = \left[ 0.27 \log R_f + 0.36 \log \left( \frac{q_t}{p_a} \right) + 1.236 \right] \frac{G_s}{2.65} \quad (5)$$

where  $\gamma$  is the unit weight of soil,  $\gamma_w$  is the unit weight of water,  $G_s$  is the specific gravity of the soil material.

Another classification is the one suggested by Eslami & Fellenius (2004) that requires merely the values of the measured sleeve friction  $f_s$  and the effective cone resistance  $q_E$ .

### ***-Application example of the soil stratigraphy method***

The method was considered utilizing CPT field data from the Mediterranean Region and laboratory tests on retrieved samples (Papamichael & Vrettos, 2018). The region comprises onshore and offshore sands, silts, clays and organic soils thus providing a seldom opportunity to evaluate the applicability of CPT as a site investigation tool. Adjacent to each borehole, one CPTu test was performed. Near each onshore borehole an additional CPT was carried out to supplement the data. Due to equipment limitations, the maximum depths investigated by the CPTu were up to 30 m both onshore and offshore. Cone end resistance  $q_c$ , sleeve friction  $f_s$ , and pore water pressure  $u_2$  measured behind the cone were recorded during the tests. Effects of pore water pressure on the measured values were negligible, and further analysis was carried out with the uncorrected raw values  $q_c$  and  $f_s$ , i.e. assuming that the corrected cone resistance value  $q_t$  equals  $q_c$ . The tests that were conducted on retrieved samples from the boreholes for all soils included i) grain size distribution with mean grain diameter  $d_{50}$ , uniformity coefficient  $C_U$  and fines content percentage  $FC \%$ , and ii) Atterberg limits and organic content for the cohesive soils. Soil classification was made according to the Unified Soil Classification System USCS. The data were the basis for the definition of the stratigraphy in the tunnel design, and are used herein for the assessment of the available CPT-based soil classification charts.

In the following, soil classification derived from laboratory testing is compared to the predictions by CPT charts. Only the results for cohesionless soils are presented here. Figure 1 show the CPT data plotted on the SBTn chart. Silty gravels are falsely plotted in the zone 3 in all charts. Silty sand is plotted quite well on the corresponding zones, although a few data sets are plotted in zones 3, 4 and 7 instead. It can be concluded that the transition between zones 5 and 6 requires further refinement. The above deviations are attributed to the fact that the above empirical charts are intended to provide information on the behavior of soils rather than reproducing soil categories defined in classification systems. Generally, the stratigraphy derived from the charts is

in good agreement with the one obtained from the direct soil classification determined on samples from the boreholes especially for the silty sands and sandy silts which are of particular attention for the purpose of this thesis because lunar and mars soils are mechanically behaving like silty sands. It is important to mention here that using the equations for the delineation of the soil zones is more practical and the procedure can be automated.

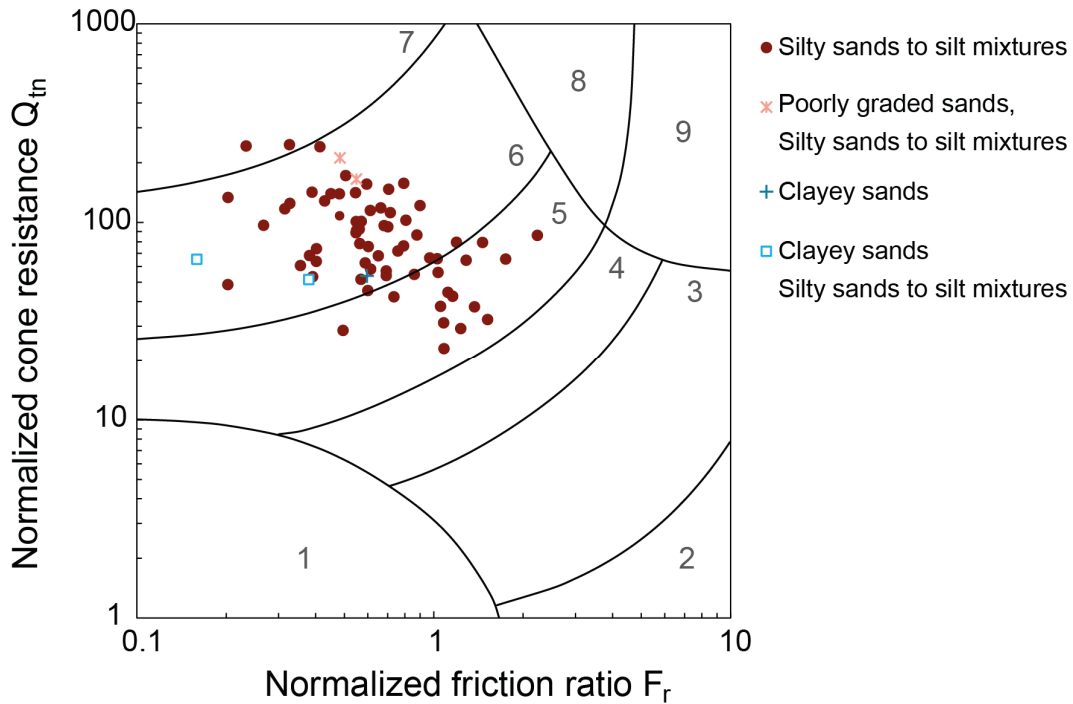


Figure 1: Soil classification for the investigated site in the SBTn chart.

### 2.1.1.2 Dynamic Probing

Dynamic Probing can be carried out in practice with different types of devices. DIN EN ISO 22476-2 distinguishes between light DPL, medium DPM, heavy DPH and super heavy DPSH dynamic probing. Annex D of this standard contains correlations for the measured number of blows per 10 cm penetration  $N_{10}$  for the two situations above and below the groundwater level (GWL). These concern i) DPL and DPH probing for poorly graded sands and ii) DPH probing for well graded gravel-sand mixtures. Values measured below groundwater are denoted by  $N_{10}'$ . The additional index L, M or H refers to DPL, DPM or DPH. In the case of the super heavy-probing DPSH the number of blows for 20 cm penetration  $N_{20}$  is measured instead.

### 2.1.1.3 Lightweight portable dynamic cone penetrometer

The Panda<sup>®</sup> is a lightweight portable dynamic cone penetrometer (DCP). It can be operated by one man to test soils down to a depth of approximately 6 meters (Langton, 1999). The test is carried out by blowing a standard hammer on the head of the piston to drive a cone with rods into the soil. In contrast to standard devices both the drop height and the applied energy can vary during testing, in order to match the strength of the material being penetrated. The driving energy is measured through strain gauges, which are installed in the anvil of the device. The speed of impact and the corresponding penetration of each blow are recorded. The dynamic cone resistance  $q_d$  is calculated by using the so-called Dutch formula (Langton, 1999).

### 2.1.1.4 Correlations between CPT and DPH

The correlations from DIN 4094, which are widely used in practice in Germany, have been partially retained, partly integrated in the corresponding DIN EN ISO standard or in DIN EN 1997-2. Data refer to three soil groups, the designation being in accordance with DIN 18196. In DIN EN 1997-2 symbols for the soil types are not used. Alternatively, the notation according to DIN EN ISO 14688-1 can be used. Specifically, these are poorly graded sands (SE) with a uniformity coefficient  $C_U \leq 3$ , well-graded sand-gravel mixtures (GW) with  $C_U > 6$ , as well as sand and gravels (SE, SW, SI, GE, GW, GI) with  $C_U \geq 2$ . The exact origin of the equations is difficult to trace. These are relationships from older studies before 1978, which were established as part of committee work (Stenzel & Melzer, 1978).

The extensive penetration experiments carried out on a natural scale in a cylindrical container filled with uniformly layered sand in Melzer (1968) provided correlations between dynamic probing tests and cone penetration tests. In addition, correlations for sand-gravel mixtures as well as for gravelly sands were derived from field trials. The equations for the CPT refer to results with the Dutch (mechanical) cone in Melzer (1968). It should be noted that in older papers on heavy / light dynamic probing the number of blows measured refers to  $N_{20}$ . A good approximation is that  $N_{20} \approx 2 N_{10}$ . The widely used, simple approximate formula  $q_c \approx N_{10}$  for the conversion of the DPH blow count to  $q_c$  in MPa is given in the withdrawn standard on bored piles DIN 4014 and was

derived from a few field tests, as outlined in Franke (1987). This relationship was adopted as a recommendation in §3.2 of the EA Piles (Deutsche Gesellschaft für Geotechnik, 2012). Similar values with  $q_c / N_{10} = 1.28$  were provided by the statistical evaluation of field investigations in BAW (1997), while relationships for the Dynamic Probing Light are subject to device related significant variations. Further CPT vs. DPH relationships obtained from field studies on sands, gravels and sand-gravel mixtures are presented in Kramer (1979). The silty to gravelly sands cover a grain size distribution range with values  $d_{50} / C_U = 0.09 \text{ mm} / 1.26$  to  $1.0 \text{ mm} / 3.0$ , while for the gravels and sandy gravels the two bounds of the grain size distribution curves are defined by  $d_{50} / C_U = 0.8 \text{ mm} / 8$  to  $20 \text{ mm} / 12$ . Relationships between  $q_c$  and the blow counts of DPH for a Medium sand ( $d_{50} = 0.3 \text{ mm}$ ,  $C_U = 2$ ) in Placzek (1985) have been derived from probings in an excavation. Relationships between CPT and DPH in Mahler & Szendefy (2009) are given as a function of the mean grain diameter and take into account the influence of the overburden pressure.

A relationship between  $N_{10H}$  from DPH and  $q_c$  from CPT taken from DIN EN 1997-2 is depicted in Figure 2 and refers to poorly graded sands (SE) as well as well-graded sands and gravels (SW and GW) above and below groundwater GWL. These curves can also be found in the old DIN 4094-3, but the underlying data could not be identified. Further results of published work are outlined in Table 1. For further information, the interested reader is referred to Vrettos & Papamichael (2018).

Table 1: Correlations between probings (a) Melzer (1968), (b) Placzek (1985), (c) BAW (1997), (d) Franke (1987) and DIN 4014, (e) Kramer (1979);  $q_c$  in MPa

Probing	Equation	Soil Type	Ref.
CPT - DPH	$q_c = 0.8 \cdot N_{20H}$	Sand	a
	$q_c = 0.9 \cdot N_{20H}$	Gravelly sand (field)	
	$q_c = 1.28 \cdot N_{10H}$	Sand	c
	$q_c = 0.43 \cdot N_{10H} + 6.3$	Sand	b
	$q_c = N_{10H}$	Sand and gravel	d
DPH - CPT	$N_{20H} = 8.534 + 1.07 \cdot q_c$	Sands and gravels	e

\* $N_{20H} = 2 N_{10H}$

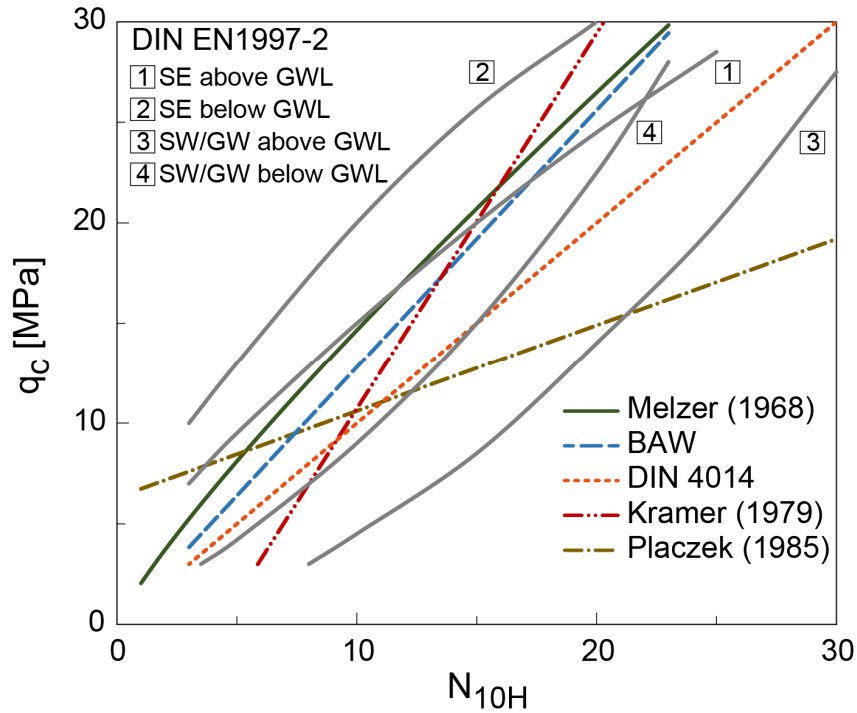


Figure 2: Comparison between different DPH to CPT correlations.

### 2.1.1.5 Pressure dependent normalization of penetration test data

If the same penetration resistance is measured in soil layers of different depth but of the same composition, the deeper layer usually exhibits a lower relative density. The main reason for this is considered to be the influence of the effective overburden pressure (Gibbs & Holz, 1957). In order to account for this effect a stress normalization factor  $C_N$  is used. Empirical equations for  $C_N$  were originally proposed on the basis of experimental results for the blow count of the SPT (Skempton, 1986; Gibbs & Holz, 1957; Liao & Whitman, 1986) and later also for the tip resistance of the CPT (Jamiokowski et al., 1988; Kulhawy & Mayne, 1990). So far, this parameter has not been considered for the dynamic probing. The atmospheric pressure  $p_a$  is usually considered the reference pressure. The normalized resistance to one atmosphere  $q_{c1N}$  is obtained by multiplying the  $C_N$  factor with the measured probing resistance and dividing by the  $p_a$ . Several suggestions for  $C_N$  exist in the literature. In practice, the following general equation is now used both for SPT and CPT:



$$C_N = (p_\alpha / \sigma'_{v0})^\alpha \quad (6)$$

where  $\sigma'_{v0}$  is the vertical effective overburden stress.

One of the easiest and practical proposals is to use  $\alpha = 0.5$  (Liao & Whitman, 1986). The application at greater depths with  $\sigma'_{v0} > 200$  kPa is subject to uncertainties according to Youd et al. (2001) and is no longer recommended for  $\sigma'_{v0} > 300$  kPa. Boulanger & Idriss (2004) recommend a maximum value of 1.7 since according to eq. (6) near the surface  $C_N$  takes very high values. Similar in DIN EN ISO 22476-3 is recommended to limit the value of  $C_N$  to 2.0 or even better to 1.5 for the normalization of the SPT. Some of the proposed equations for  $C_N$  (Boulanger & Idriss, 2004; Moss et al., 2006) - especially for the CPT - are unnecessarily complicated. Note that  $C_N$  as a function of overburden pressure depends on the in situ relative density, which is initially unknown. It should be kept in mind that both the SPT and the CPT normalization of the measured resistances by means of a function of the in-situ overburden pressure has become an integral part of all modern interpretation methods.

### 2.1.1.6 Relative density

Usually, compaction state inferred from in-situ probing is expressed in terms of relative density  $I_D$ , where

$$I_D = \frac{e_{\max} - e}{e_{\max} - e_{\min}} = \frac{\rho_{d,\max}(\rho_d - \rho_{d,\min})}{\rho_d \cdot (\rho_{d,\max} - \rho_{d,\min})} \quad (7)$$

The terms very loose / loose / medium-dense / dense / very dense correspond to values for  $I_D$  of 0 – 0.15 / 0.15 – 0.35 / 0.35 – 0.65 / 0.65 – 0.85 / 0.85 – 1.00 according to DIN EN ISO 14688-2. The two extreme void ratios  $e_{\max}$  and  $e_{\min}$ , or the associated dry densities  $\rho_{d,\min}$  and  $\rho_{d,\max}$ , are subject to non-negligible scattering despite the standardization of the respective laboratory tests. Since  $I_D$  is defined as the ratio of three quantities, small inaccuracies in the determination of  $e_{\max}$  lead to significant deviations in  $I_D$ , especially at low values of  $I_D$ . Comparisons on non-uniform soils with the same relative density have shown that the tip resistance is smaller than the one in uniform soils because of the higher compactibility  $(e_{\max} - e_{\min}) / e_{\min}$  (Melzer et al, 2017).

Another influence parameter is the mean grain diameter. Values of the void ratio range ( $e_{max} - e_{min}$ ) of cohesionless soils are determined in Cubrinovski & Ishihara (2002) and approximated by the following relationship dependent on the mean grain diameter  $d_{50}$  [mm]:

$$e_{max} - e_{min} = 0.23 + \frac{0.06}{d_{50}} \quad (8)$$

The estimation of  $e_{max}$  and  $e_{min}$  only on the basis of  $d_{50}$  is not proper because other crucial parameters are omitted. In the following some relationships are given for CPT, DPH and Panda<sup>®</sup>. For further information, the interested reader is referred to Vrettos & Papamichael (2018).

### ***-Relationships for the cone penetration test CPT***

In DIN 4020, as a supplement to DIN EN 1997-2, the relationships for the  $I_D$  previously given in DIN 4094-1 were adopted:

$$I_D = -0.33 + 0.73 \cdot \log q_c \quad \text{for Sands with } C_U \leq 3 \quad (9)$$

$$I_D = 0.25 + 0.31 \cdot \log q_c \quad \text{for Sand-gravel mixtures with } C_U \geq 6 \quad (10)$$

with  $q_c$  in MPa.

They apply from 2 m depth (below the critical depth). The previous remarks for the dynamic probing apply also here, namely that information is not up-to-date and quantification of the statistical scatter in the experimental data is usually omitted. Since no distinction is made in terms of the groundwater level, it is implied that these relationships are independent of it. Furthermore, the influence of the probing depth, and thus of the overburden pressure, is not considered.

In the international literature, the first direct correlation between  $I_D$  and the CPT tip resistance  $q_c$  has already been established in Schmertmann (1976) from experimental results on normally consolidated fine and medium sands in a calibration chamber. The research from Schmertmann (1976) and Baldi et al. (1986) constituted the basis for many of the following empirical relationships deduced from experimental results in calibration chambers.

Jamiolkowski et al. (2003) suggested the following relationship which is a synthesis of suggestions by various authors:

$$I_D = a \cdot \ln q_{c1N} - b_x \quad (11)$$

with  $C_N$  according to eq. (6),  $q_{c1N} = C_N \cdot q_c / p_a$ ,  $a=0.268$  and a mean value of  $b_x = 0.675$ . The standard deviation is  $\sigma = 0.079$ . High values of  $b_x$  correspond to low compressibility soils.

A relationship derived from experiments in calibration chambers, most of which are also included in Jamiolkowski et al. (2003), which takes into consideration compressibility, aging, and consolidation, has been proposed in Kulhawy & Mayne (1990). For normally consolidated sands, the corresponding relationship simplifies to

$$I_D = \sqrt{\frac{q_{c1N}}{300}} \quad (12)$$

with  $C_N$  according to eq. (6) and  $C_N \leq 1.7$ .

### ***-Relationships for the dynamic probing DPH***

Correlations to estimate the relative density from DPH are given in DIN EN 1997-2, Annex G. All equations for  $I_D$  have the general form

$$I_D = a_1 + a_2 \cdot \log N \quad (13)$$

$N$  corresponds to  $N_{10H}$  for DPH. Values for the constants  $a_1$  and  $a_2$  are given in DIN EN 1997-2. Values for Sands with  $C_U \leq 3$  above GW, for Sands with  $C_U \leq 3$  in GW and for Sand-Gravel-Mixtures with  $C_U \geq 3$  above GW correspond to  $a_1 = 0.10 / 0.23 / -0.14$  and  $a_2 = 0.435 / 0.38 / 0.55$  respectively. The above empirical relationships were derived already in the 1970s in the frame of the standardization work for the DIN 4094 and have not been updated since then.

### ***-Relationships for light dynamic cone penetrometer Panda®***

When using the Panda® penetrometer for compaction control, the resistance  $q_d$  is primarily used to assess the value of dry density  $\rho_d$ . The general equation reads (Chaigneau 2001):

$$\rho_d = (\alpha \ln q_d + \beta) / g \quad (14)$$

with  $q_d$  in MPa and  $\rho_d$  in Mg/m<sup>3</sup>,  $g$  is the acceleration of gravity,  $\alpha$  and  $\beta$  are material specific constants. For sandy gravel, for example,  $\alpha = 0.74$  and  $\beta = 15.44$ .

### **2.1.2 Extraterrestrial soils**

#### ***-Moon Regolith***

In the Apollo and Luna missions, samples of lunar soil were collected and in the Apollo Missions 14 and the Apollo 15 & 16, a special Apollo Simple Penetrometer ASP and a Self-Recording Penetrometer known as LSRP were used respectively. From the collected samples and the penetration tests, information regarding mechanical characteristics of the soils were carried out. Carrier et al. (1991) reports the geotechnical properties of lunar soils. To get an impression of the most important characteristics of lunar soils, a recap is stated. The lunar soil is graded from Medium sand to fine silt with 95 % finer than 1.37 mm by weight and 5 % finer than 0.0033 mm with an approximate value of  $d_{50}$  of 0.072 mm. The average coefficient of uniformity  $C_U$  and coefficient of curvature  $C_C$  are 16 and 1.2 respectively. The bulk of the lunar soil is fine silty sand/sandy silt. The particles from lunar soil are spherical to extremely angular with an average elongation of 1.35 and an average volume coefficient of 0.3. The particles have also extremely irregular surfaces. The average specific surface area is approximately 0.5 m<sup>2</sup>/g. The bulk density  $\rho$  is approximately 1.30 Mg/m<sup>3</sup> at the surface and then increases to 1.52 Mg/m<sup>3</sup> and 1.83 Mg/m<sup>3</sup> at a corresponding depth of 10 and 100 cm respectively. Thereafter the value reaches 1.92 Mg/m<sup>3</sup>. In situ relative density of lunar soil is approximately 65% in upper 15 cm and increases to values greater than 90% below depths of 30 cm. A representative value for lunar soil's specific gravity is 3.1. Porosity values ranges from 40 to 50 % decreasing with depth. Shear

strength parameters of lunar soils according to the Mohr-Coulomb failure criterion are the following: Cohesion ranges from 0.1 to 1 kPa and the friction angle from 30 to 50° according to the Apollo samples. An average value of compression Index  $C_c$  is 0.3 and a typical value for recompression index  $C_r$  is 0.003. All the above mentioned values have been taken from Carrier et al. (1991).

### ***-Mars Regolith***

During the Missions at Mars, important information regarding the Martian surface was collected. From the collected data some mechanical properties were estimated. The information given in this section is taken from various authors, specifically Moore (1989, 1999), Shaw (2009), Sullivan (2011), Pike (2011) and Arvidson (2014). Regarding the fields of the Vikings landers, four materials occur there: drift, crusty to cloddy, blocky and rock. The Drift material is characterized by grain size ranges of 0.1-10.0  $\mu\text{m}$ , bulk density of  $1.15 \pm 0.15 \text{ Mg/m}^3$ , cohesion values of  $1.6 \pm 1.2 \text{ kPa}$  and friction angle of  $18^\circ \pm 2.4^\circ$ . The Blocky material is characterized by grain size ranges of 0.1-1500  $\mu\text{m}$ , bulk density of  $1.6 \pm 0.4 \text{ Mg/m}^3$ , cohesion values of  $5.1 \pm 2.7 \text{ kPa}$  and friction angle of  $30.8^\circ \pm 2.4^\circ$ . The Crusty to cloddy material is characterized by grain size ranges of 0.1 - 10  $\mu\text{m}$ , bulk density of  $1.4 \pm 0.2 \text{ Mg/m}^3$ , cohesion values of  $1.1 \pm 0.8 \text{ kPa}$  and friction angle of  $34.5^\circ \pm 4.7^\circ$ . The rocks are characterized by grain size of  $35 \times 10^3 \mu\text{m}$ , bulk density of  $2.6 \text{ Mg/m}^3$ , cohesion values of 1000-10 000 kPa and friction angle of  $40^\circ$ - $60^\circ$ . These values were deduced from analyses of the sample trenches and surface bearing tests and from the instruments carried out by the landers e.g. X-ray fluorescence spectrometer (Moore, 1989). Most of the material at the Pathfinder landing site behave like moderately dense soils on Earth with friction angles near  $34^\circ$ - $39^\circ$  and are called cloddy deposits. Thin deposits with friction angles of  $26^\circ$ - $28^\circ$  are also present. The calculated cohesion values are relatively small and less than 1 kPa. These values were deduced from rover images, Imager for Mars Pathfinder IMP images and rotations of the rear and front wheels (Moore, 1999). The Mars Exploration Rovers landed on opposite sides of Mars where friction angles of  $30^\circ$ - $37^\circ$  and cohesions of 0-2 kPa were inferred from the wheel trenches and cohesions of 0-11 kPa where deduced from wheel scuffs in regoliths (Sullivan, 2011). Later the Mars Phoenix landed on Mars and by using the optical and atomic microscopy data acquired

by the lander, two size populations were identified: larger, mostly rounded grains and small reddish fines notably with a very low mass proportion in the clay-size range below 2  $\mu\text{m}$  which can be used to estimate that there has been exposure to liquid water over the history of the soil much less than 5,000 years (Pike, 2011). The internal friction angle of the soil in the site is  $38^\circ \pm 5^\circ$  and cohesions varied from  $0.2 \pm 0.4$  kPa to  $1.2 \pm 1.8$  kPa. Soil physical properties were inferred from analysis of force data determined from motor currents from the Robotic Arm's trenching activity and from images from the landing site (Shaw, 2009). Later on, Mars Science Laboratory Mission was launched and the Rover Curiosity was landed in Mars. The deduced landing site's values of cohesion is of 1-3 kPa and the internal friction angle is  $30^\circ$ . These data are the best match of the simulation of the imprints of the wheels of the rover into the soil surface of the landing site (Arvidson, 2014).

#### ***-Extra-terrestrial soil simulants***

Due to the difficulty of transferring soil samples of other planets to Earth, soil simulants have been invented for carrying studies and simulations for designing missions to other planets. A database with soil simulants can be found online, containing detailed information for previously used and current simulants and their purposes (CLASS, 2019). A soil simulant must exhibit the same characteristics as the actual extraterrestrial soils such as mechanical strength, grain size distribution, grain size, chemical composition or any other engineering property that is of relevance. According to their characteristics soil simulants are categorized as general purpose simulants which are designed to match multiple properties (chemical, mineralogical, geotechnical), geotechnical simulants which are designed to replicate geotechnical properties with little effort to achieve accurate mineralogy or chemistry, spectral simulants which are designed to primarily match the reflectance or emission spectra and magnetic simulants which are designed to replicate the magnetic properties of a reference material (CLASS, 2019).

The Johnson Space Center JSC-1 series is a general purpose lunar simulant made from volcanic ash and contains high glass fraction and is chemically similar to Apollo sample 14163 (McKay et al., 1994). JSC-1A is a clone of the original JSC-1. JSC Mars-1A is a spectral simulant which is the  $<1$  mm size fraction of altered volcanic ash from a Hawaiian cinder cone. The

simulant closely matches the reflectance spectrum and approximates the mineralogy, chemical composition, grain size, density, porosity and magnetic properties of Martian soil (Allen et al., 1998). Mojave Mars Simulant MMS is a crushed Miocene basalt, with local alluvial sedimentary and igneous grains (Peters et al., 2008). MMS is a geotechnical simulant which can be divided to rock, sand and dust. MSS-D is a finer Mars Soil Simulant which is a mixture of quartz and olivine sand with a bimodal grain size distribution curve with one mode smaller than sand (Golombek et al., 2018). The Jining Mars Soil Simulant JMSS-1 is a general use simulant created by mechanically crushing Jining basalt, a Miocene aged unit located in the North China craton (Jeng et al., 2015). Another Mars' simulant called WF34-Sand, which is based on quartz sand on Earth which is typically rounded by fluvial, marine, eolian activity, may be mechanically more representative (Golombek et al., 2018). Triaxial tests for shear strength are given among others for JSC-1A by Alshibli and Hasan (2009), Arslan et al. (2010) and Vrettos (2012).

## **2.2 Basic terramechanical models**

### **2.2.1 General**

Terramechanics is a relatively new research area that lack yet a standardization in methodologies, models, procedures etc which hinders quick improvement and development. In the latest years there is an initiative towards creating a single standard for the development and implementation of terramechanical models. Terramechanics are categorized in simple and complex terramechanics. The former is based on the use of pressure – sinkage and traction – slip data from experiments using bearing plates, shear rings and wheel tests. The latter includes 3D soil models that include failure and flow models and are based on laboratory soil tests e.g. cone index, bevameter, direct shear etc. These laboratory tests are utilized to calibrate the soil behavior.

The models can be further categorized as empirical models which are derived from experimental results and are validated through other experimental results, as semi-empirical which are models derived combining experimental results and theories of physics, and lastly as theoretical models which derived from

theory of physics and validated through experimental results. The model inputs consist of vehicle and soil parameters or/and experimental data and the output includes vehicle mobility parameters such as drawbar pull, rolling resistance etc (He et al., 2019). Generally, parameters that are included in the models can be known in advance, measured in real time, obtained from a terrain map or/and estimated from the current state of the vehicle/wheel (He et al., 2019).

Currently there are various parameterization methodologies for estimating the parameters of terramechanical models. Unfortunately, there are deviations among the various procedures, leading to discrepancies and difficulties when comparing results of different models or even when comparing results of a specific model that was parameterized through a different testing procedure. Standards are required to govern the methodologies for the parameterization and development of terramechanical models and as already stated above, the community is already working towards that direction.

In the following subsections relevant pressure-sinkage models and shear-displacement models are presented. There are also some vibration models which are yet insufficient and digital image correlation techniques which are rapidly evolving showing promises for real time evaluation of vehicle traversability. Nevertheless, they are not presented here as they don't fall in the scope of this thesis. For a review of these types of models the interested reader is referred to He et al. (2019).

### **2.2.2 Pressure vs sinkage models**

Pressure vs sinkage of plate-soil interaction was proposed by many researchers in the 1900s. Bekker (1956) separated the sinkage modulus to cohesion and frictional modulus, as shown in eq. (15), to account for cohesive and frictional characteristics of the soil respectively. The geometry of the contact patch is also taken into account by incorporating the parameter  $b$  which represents the smaller dimension of the contact area. Bekker's equation is the basis for subsequent efforts of various authors for development of models. Reece (1965) proposed eq. (16). Youssef and Ali (1982) proposed eq. (17) combining the aforementioned models to bearing capacity models. The above mentioned models are valid for vertically applied pressures to the



soil. For the case of tests with single wheel the soil is compressed also in the radial direction and therefore the radial stress should be accounted in the model. Wong & Reece (1967) suggested the modified model of eq. (18) assuming that the radial stress is symmetric and equal to the normal pressure acting on the same depth. Wong & Reece (1967) proposed the eq. (19) for calculating the maximum radial stress angle from the slip. Meirion-Griffith & Spenko (2011) proposed eq. (20) for the wheel-soil interaction and later modified it in 2013 as shown in eq. (21) (Meirion-Griffith & Spenko, 2013).

All these models propose an exponent  $n$  for the sinkage  $z$ . There are various other models without this exponent which can be found in He et al. (2019).

Ding et al. (2014) proposed the model of eq. (22). In cases of small normal load less than 300 N and circular plates with radii from 25 mm to 50 mm, the running gear dimension effect was characterized by the dimensionless function of eq. (23). Ding et al. (2014) proposed also the dimensionless function showing in eq. (24) and eq. (25) , for higher accuracy, specifically for the applications to the wheels. Wong et al. (1984) developed the following eq. (26) to account for unloading-reloading cycles of the pressure-sinkage relationship.

$$p = \left( \frac{\delta \cdot c}{d^n} + b \cdot \frac{\sigma \cdot \gamma}{d^n} \right) \cdot (z)^n \quad (15)$$

where  $p$  is the pressure,  $\delta$  and  $\sigma$  are dimensionless constants of proportionality,  $c$  is cohesion,  $\gamma$  is the unit weight,  $b$  is the smaller dimension of the contact patch,  $d$  is the height of the contact patch,  $z$  is the sinkage of the soil and  $n$  is the sinkage exponent.

$$p = \left( c \cdot k'_c + \gamma \cdot b \cdot k'_f \right) \cdot \left( \frac{z}{b} \right)^n \quad (16)$$

where  $k'_c$  and  $k'_f$  are the dimensionless cohesive and friction deformation modulus parameters,  $c$  is cohesion,  $\gamma$  is the unit weight,  $b$  is the smaller dimension of the contact patch,  $z$  is the sinkage of the soil and  $n$  is the sinkage exponent.

$$p = (K_1 + \alpha \cdot b \cdot K_2) \cdot (\beta)^n \cdot \left(\frac{z}{b}\right)^n \quad (17)$$

where  $K_1$  and  $K_2$  are soil shear strength values,  $\alpha$  and  $\beta$  are dimensionless geometric parameters,  $b$  is the smaller dimension of the contact patch,  $z$  is the sinkage of the soil and  $n$  is the sinkage exponent.

for  $\theta_M \leq \theta \leq \theta_1$ :

$$p(\theta) = (k_1 + b \cdot k_2) \cdot \left(\frac{r}{b}\right)^n \cdot (\cos \theta - \cos \theta_1)^n$$

for  $\theta_2 \leq \theta \leq \theta_M$ :

$$p(\theta) = (k_1 + b \cdot k_2) \cdot \left(\frac{r}{b}\right)^n \cdot \left[ \cos \left( \theta_1 - \left( \frac{\theta - \theta_2}{\theta_M - \theta_2} \right) \cdot (\theta_1 - \theta_M) \right) - \cos \theta_1 \right]^n \quad (18)$$

$$z_0 = (1 - \cos \theta_1) \cdot r$$

where  $\theta$  is an arbitrary wheel angle,  $\theta_1$  is the entry angle (the acute angle between the centerline of the wheel and the beginning of contact),  $\theta_2$  is the exit angle (the acute angle between the centerline of the wheel and the end of contact),  $\theta_M$  is the maximum radial stress point,  $p$  is the pressure,  $k_1$  and  $k_2$  are soil shear strength values,  $b$  is the smaller dimension of the contact patch,  $r$  is the radius of the wheel and  $n$  is the sinkage exponent.

$$\theta_M = (c_1 + c_2 \cdot i) \cdot \theta_1 \quad (19)$$

where  $\theta_1$  is the entry angle,  $c_1$  and  $c_2$  are model parameters and  $i$  is the slip of the wheel.

$$p = \hat{k} \cdot z^{\hat{n}} \cdot D^{\hat{m}} \quad (20)$$

where  $\hat{k}$ ,  $\hat{n}$ ,  $\hat{m}$  are the model parameters,  $z$  is the sinkage of the soil and  $D$  is the diameter of the wheel.

$$p = \hat{k} \cdot r^{\hat{n}} (\cos \theta - \cos \theta_s) \cdot (b \cdot l)^{\hat{m}} \quad (21)$$

where  $\hat{k}$ ,  $\hat{n}$ ,  $\hat{m}$  are model parameters,  $r$  is the radius of the wheel,  $\theta$  is the angle along wheel-soil contact arc in degrees,  $\theta_s$  is the static wheel-soil contact angle,

$b$  is the wheel width,  $l$  is the horizontally projected length of the wheel-soil contact patch, and  $z_0$  is the maximum wheel sinkage.

$$p = K_s \cdot z \cdot \lambda_N \quad (22)$$

where  $K_s$  is the sinkage modulus of the terrain in Pa/m,  $z$  is the sinkage and  $\lambda_N$  is a dimensionless function of plate or running gear parameters.

$$\lambda_N = \left( \frac{z}{z_0} \right)^{n_0 - 1 + n_1 (z_0/z)} \quad (23)$$

$$\lambda_N = \left( \frac{z}{z_0} \right)^{n_0 - 1 + n_1 s + n_2 s^2} \quad (24)$$

$$\lambda_N = \left( \frac{z}{z_0} \right)^{n_0 - 1 + n_1 s + n_2 s^2 + n_3 s^3} \quad (25)$$

where  $z$  is the sinkage of the soil,  $z_0 = 1$  m,  $s$  is the slip ratio of the wheel, and  $n_0$ ,  $n_1$ ,  $n_2$  and  $n_3$  are the function parameters.

$$p = p_u - k_u \cdot (z_u - z) \quad (26)$$

$$k_u = k_0 + A_u \cdot z_u$$

where  $z$  is the sinkage of the soil,  $p_u$  and  $z_u$  are the pressure and sinkage when unloading starts respectively,  $k_u$  is the average slope of the unloading-reloading line on the pressure-sinkage plot, and  $k_0$  and  $A_u$  are model parameters.

### 2.2.3 Shear stress vs displacements models

The Mohr Coulomb failure criterion is depicted in eq. (27) because it is the most widely used failure model used in terramechanical applications. Bekker (1956) proposed the shear model of eq. (28). Janosi & Hanomoto (1961) modified the Bekker model and suggested the model of eq. (29) for soils that exhibit shear stress-displacement profiles without a

hump. Senatore & Iagnemma (2011) developed the model of eq. (30) to account for the influence of the soil density on the shear stress. For some organic soils the shear stress – displacement profile has a hump without residual stress, the shear stress decrease with an increase in shear displacement.

To sum up, there are three types of shear stress - displacement for various soils: Shear stress increases until a maximum value with no hump, shear stress increases until a hump and thereafter decreases with further increase in shear displacement and shear stress increases creating a hump and thereafter decreases with an increase in displacement until it reaches a value of residual stress. Bekker's model can capture the behavior of the last two cases, Senatore & Iagnemma's model can capture only the last case whilst the Janosi & Hanomoto's model captures the first one.

$$\tau_{\max} = c + \sigma \tan \phi \quad (27)$$

where  $\tau_{\max}$  is the maximum shear strength that leads to soil failure,  $c$  is the soil cohesion,  $\sigma$  is the normal stress and  $\phi$  is the angle of soil internal shearing resistance (soil friction angle).

$$\tau = \tau_{\max} \cdot \frac{e^{(-K_2 + \sqrt{K_2^2 - 1}) \cdot K_1 j} - e^{(-K_2 - \sqrt{K_2^2 - 1}) \cdot K_1 j}}{e^{(-K_2 + \sqrt{K_2^2 - 1}) \cdot K_1 j_0} - e^{(-K_2 - \sqrt{K_2^2 - 1}) \cdot K_1 j_0}} \quad (28)$$

where  $\tau$  is the shear stress,  $j$  is the shear displacement,  $\tau_{\max}$  is the shear strength,  $j_0$  is the shear displacement at the maximum shear stress  $\tau_{\max}$ , and  $K_1$  and  $K_2$  are empirical model parameters.

$$\tau = \tau_{\max} \cdot (1 - e^{-j/k}) \quad (29)$$

where  $\tau_{\max}$  is the shear strength,  $j$  is the shear displacement and  $k$  is the slip/shear modulus.

$$\tau = \tau_{res} \left[ \frac{k_\gamma \cdot j}{k} e^{1-j/k} + (1 - e^{-j/k}) \right] \quad (30)$$

where  $\tau_{res}$  is the residual stress,  $j$  is the shear displacement,  $k_\gamma$  is the model parameter related to the influence of soil density on the shear stress, and  $k$  is a model parameter.

## 2.3 FEM models in terramechanical applications

Numerical modeling is an integral part of the development and optimization of terramechanical models. Different simulation scenarios can be carried out to develop or/and optimize a terramechanical model, a wheel design, a car design, a rover etc. Many researchers resort to numerical modeling to solve and improve problems in industry. Depending on the outer scope, different simulation techniques are utilized. For the purpose of this thesis, simulations with FEM in Abaqus were selected.

Fervers (2004) presented a two dimensional 2D FEM model of an air filled tire based on a mechanical reproduction of the basic components of a tire. The author concluded that the abilities of the model are proved by comparisons of the tire model on even and uneven road with test results.

Hambleton & Drescher (2008) conducted three- and two- dimensional numerical simulations of indentation of rigid cylindrical wheels into frictional and cohesive soils with Abaqus. The soil material was modeled with Mohr Coulomb and associated or non- associated flow. The material model was calibrated with triaxial tests results. They concluded that the simple elastoplastic model used was sufficient to capture the experimentally observed force – sinkage response. They found that the three dimensional modeling effects are minor for clays but important for sands. They also investigated the influence of Coulomb's friction values  $\mu$  of 0.1 and 10; and the effects of dilation angle values  $\psi$  of  $0^\circ/10^\circ/20^\circ$ . They concluded that  $\mu$  effects are insignificant and that  $\psi$  affect the simulation results.

Ma et al. (2009) simulated with Abaqus 2D, the performance of non-pneumatic tires on soil modeled with Drucker Prager/Cap plasticity with hardening. The so-called Lebanon Sand from literature was used for the simulations: The wheel was modeled as an elastic deformable body. The penalty contact algorithm was used. A displacement was imposed to simulate rolling. They concluded that the contact pressure is non-uniform and that further investigations are needed.

Hambleton & Drescher (2009a) conducted three dimensional numerical simulations using Abaqus, for predicting penetration of non-driving towed rigid cylindrical wheels into frictional and cohesive soils. The influence of

soil parameters and wheel's geometry on rolling force and wheel sinkage was investigated. They presented an approximate analytic model for predicting sinkage under steady-state conditions. Numerical and analytic results were compared with test results from literature. The soil material was modeled as elastic-perfectly plastic with Mohr Coulomb yield criterion with an associated or non-associated flow. The extended Drucker-Prager yield criterion was used to approximate the Mohr-Coulomb criterion. The wheel was modeled as rigid body. The contact interaction was assumed to have a coefficient of friction 0.5. Firstly a vertical force was applied on the centre of the wheel and subsequently a linear velocity was imposed. They concluded that the predicted force-sinkage using the analytical approach is similar in character to the numerical results and also match the results of small-scale experiments and data from literature.

Hambleton & Drescher (2009b) conducted two dimensional and three dimensional numerical simulations of towed wheel on a ductile material with Abaqus. The wheel was modeled as rigid and the material was modeled as an elastic perfectly plastic with von Mises yield criterion. Firstly, the wheel was indented and then when it was possible, steady rolling was imposed. They concluded that the two-dimensional analysis doesn't yield satisfactory results for the investigated narrow wheel to predict penetration. Nevertheless, the horizontal forces of both the two and three dimensional simulations follow the same trend. The steady state penetration of the two dimensional analysis was constant for different vertical forces whereas in the three dimensional simulation the penetration was increasing with increasing vertical force. Therefore, a three dimensional analysis is needed for such simulations. They also concluded that using multiple narrow wheels results in less rolling resistance than using a single wide wheel. They point out that this results in increased penetration even though force per unit width may be the same.

Ma et al. (2011) investigated the dynamic impact simulation of interaction between non-pneumatic tire and sand with obstacle placed approximately in the middle of the model, using Abaqus. The tire was simulated as an elastic deformable body with inertia effects. The so-called Lebanon sand was used for the simulations and it was realized through the modified Drucker-Prager/Cap plasticity constitutive model with hardening. The obstacle was represented as an elastic body. A vertical force of 650 N was applied to the center of the wheel. The rolling was imposed through a horizontal velocity of

1.66 m/s and 2.22 m/s at the center of the hub. It was concluded that a lower running speed deforms the wheel more when impacting with an obstacle while a higher running speed generates higher contact pressure peaks, a non-uniform contact pressure and higher stress and residual plastic strain values.

Xia (2011) used Drucker-Prager/Cap model to model the soil compaction and a user subroutine for finite strain hyperelasticity model for the tire's material. Soil compaction and tire mobility issues were studied. The parameters for the soil model were based on assumptions. The interaction between soil and tire was modeled with Coulomb's model. The author concluded that soil compaction and tire mobility related parameters can be predicted by finite element modeling.

Gasmi et al. (2012) carried out a quasi-static 2D analysis, with Abaqus, of a non-pneumatic tire on frictionless rigid ground, focusing on how the stiffness of the band and the spokes of the compliant wheel affect the contact patch, the vertical tire stiffness and the rolling resistance. Closed-form expressions of contact stress, stress-resultants and displacements at the center of the flexible band were developed and validated with computational models with Abaqus and by experimental data from Michelin tire of a golf car. The tire was modeled as a flexible curved circular beam while the spokes were modeled to act only in tension. The wheel was divided into three regions, and the analytical solutions were matched at the bounds of these regions. For the closed form solution, a numerical solution of the angles defining the three sections of the wheel, are required.

Ju et al. (2012) investigated the performance of two cases of hexagonal honeycomb spokes of a non-pneumatic wheel using Abaqus. The hexagonal honeycombs with a highly positive cell angle deemed to have better performance as they have lower local stresses and lower mass under the same vertical load carrying capability. They also concluded for higher cell angle magnitude the flexibility of the honeycomb spokes is higher, resulting in lower reaction force for a given vertical displacement.

Ma et al. (2012) investigated tread profile effects on the performance of the cellular shear band-based non pneumatic tire when interacting with sand using finite element method with Abaqus. The soil was modeled with the so-called Lebanon sand using the Drucker-Prager/Cap constitutive model with

hardening. The tire was modeled as deformable elastic body. Penalty contact algorithm was used to model the interaction between the tire and the soil. A vertical force of 625 N was applied firstly to the hub center and then a horizontal displacement was imposed. They concluded that for smaller lug height the contact pressure profile is more uniform and that the maximum von Mises stress results for higher lug height.

Ju et al. (2013) studied the rolling resistance of a non-pneumatic tire with porous elastomer composite shear band with Abaqus. A vertical load was applied to the center of the hub to evaluate the vertical stiffness of the wheel and a sinusoidal vertical load to evaluate hysteresis. A displacement was imposed to the model to simulate the roll on the ground. For the material of the wheel, hyper-elastic and viscoelastic characteristics were considered utilizing the Ogden model with  $N=3$  and the Prony series for the shear relaxation. For more information regarding the models, the reader is referred to Abaqus<sup>®</sup> documentation. The parameters for the material were taken from studies of other authors. The model considered rolling in quasi static condition with no dynamic effects. Another limitation of the considered model was that the viscoelastic material model was strain independent. The aim of this study was to investigate the effectiveness of using porous composite shear bands in non-pneumatic tires NPTs. There were no experimental data for comparisons of the stiffness of the wheel.

Li & Schindler (2013) created FEM tire-soil models and conducted single wheel tester experiments to validate the models. The influence of axle load and inflation pressure on the soil compaction and the relationship between the slip ratio, the slip angle and the tire mobility was studied. The Neo Hookean strain energy potential was utilized for the model of the tire and the modified Drucker–Prager/Cap model for the soil model. The parameters for the soil model were measured with triaxial tests. Hard contact was used for the normal behavior and Coulomb's friction for the contact in tangential direction. The authors concluded that force and soil compaction values from the simulation and the experimental results are in good quantitative agreement.

Bekakos et al. (2015) conducted transient non-linear numerical simulation of the dynamic mobility of a rigid wheel on a deformable terrain using Abaqus. The effects of the vertical load, the tread pattern, the longitudinal and lateral tread parameters and the slip ratio of the wheel on the wheel performance were



investigated and it was concluded that the tread pattern and especially the tread depth and the terrain properties are affecting the wheel response. They concluded that with increasing wheel's width and dilation angle of the soil, the sinkage is decreasing.

Aboul-Yazid et al. (2015) investigated three different configurations of the Michelin's Tweel<sup>®</sup> and Bridgestone non-pneumatic tires NPTs. The performed two-dimensional analysis was quasi-static with no mass and inertia effects to study the time dependent viscoelastic response of the wheel. The rolling was imposed as a displacement. A vertical force was also applied in the center of the tire to account for the vehicle's weight. A shear relaxation modulus was considered in terms of a Prony series for the material of the wheel. They concluded that the shape of the spokes has a great effect on the tire's behavior when the tire doesn't have a composite ring, and that the shear layer reduces the impact of the spoke's shape.

Bekakos et al. (2016a) created a numerical model of a deformable tire interacting with a deformable road with Abaqus. Two different widths of tire were considered. Various vertical loads and different inflation pressures of the tire were considered. The interaction with rigid and deformable terrain was considered. Rolling on deformable road was considered subsequently with investigations of the effects of friction coefficient, inflation pressure, rebar orientation and vertical load on the overall performance of the wheel. Implicit and Explicit method was combined. They concluded that for increasing inflation pressure, the stiffness of the tire is increasing and thus the contact area is decreasing. They also reported that the friction coefficient affects the contact area for small vertical loads and that the rebar orientation affects the deflection of the tire for large vertical loads. Further they concluded that for higher widths of wheel the sinkage is decreased.

Bekakos et al. (2016b) studied the transient rolling response of a pneumatic tire on a rigid road and on soft soil under towed and driven conditions with Abaqus. The rubber material of the wheel was modeled utilizing the Mooney-Rivlin model and the time-domain viscoelastic component was defined using one term Prony series. The models are defined in the Abaqus<sup>®</sup> documentation. A lumped mass was added at the center of the wheel and inertia effects were considered. The soil was simulated with the linear Drucker Prager failure criterion. A steady-state transport analysis was performed firstly to obtain the

free rolling conditions of the tire, which are used to simulate the impact of the tire on a rigid bump. Two different linear velocities were considered namely 5 and 10 km/h. They concluded that contrary to the on-road tires, reduction of the inflation pressure increased the traveled distance before immobilization of the wheel, the contact area increased leading to a smaller vertical displacement.

Bekakos et al. (2016c) presented an optimization procedure which couples the Abaqus and the Matlab. An initial tire model was developed and then its properties were tuned to match the eigenfrequency analysis results of a target model taken from the literature. They concluded that the proposed method can match closely modal analysis results, resulting in a realistic tire model. Therefore, the method can be used to obtain the parameters of the material model of the tire.

Du et al. (2016) investigated the dynamic interaction between a non-pneumatic tire and soil containing an obstacle with Abaqus. The hyper-elastic incompressible rubber was modeled using the Mooney-Rivlin model and the soil was modeled using the modified Drucker-Prager cap plasticity constitutive law. Different rotational speeds namely 4 and 4.5 rad/s were modeled to obtain the effects on the displacement, velocity and acceleration of the hub center. They had available force – displacement data records of the wheel. They concluded that higher rotational speeds generate more intense vibrations in the velocity and the acceleration of the wheel.

Jin et al. (2018) studied the static and dynamic behavior of non-pneumatic tires with different honeycomb spokes focusing on the stress distribution and the rolling resistance on a road with Abaqus. The tire was simulated using the Ogden model. They concluded that the angular velocity and friction coefficient have negligible effect on the rolling resistance of non-pneumatic tires based on two distinct values of each one namely 0.15 and 0.30 friction coefficient and 0.01 rad/ms and 0.0123 rad/ms. They compared the force-displacement curves with experimental data from another author.

Deng et al. (2018) simulated various steady state rolling conditions using steady state transport technology in Abaqus/Standard. The rubber material of the wheel was simulated with the Mooney Rivlin model. The vertical stiffness of the simulated wheel was compared against experimental results of force-displacement. Inertia effect was considered and the free rolling condition was

obtained. They used a pressure sensitive film to measure the predicted footprint and compared it against simulation results which yielded results with maximum 2.5% differences. Furthermore, they conducted steady state rolling experiments with various slip ratios and a constant vertical load of 8 or 14 kN. They observed that under a larger slip ratio, the longitudinal force obtained from the FEM model was deviated from the measured value. In both footprint and rolling analysis the initial friction coefficient was set to 0.6. They concluded that the developed FEM model is capable to predict the dynamic behavior of the examined tire under various rolling conditions. They observed that the high stress region lies within the central zone of the footprint.

Zhao et al. (2018) investigated the dynamic characteristics of a non-pneumatic wheel rolling over a ditch, utilizing the Abaqus/Explicit. The Mooney Rivlin model was used to model the rubber material of the wheel. The effect of the rolling speed was also analyzed and they observed that a higher rolling speed tends to result in more vibration. They applied only angular velocity of 4, 4.5 and 5 rad/s. They compared their static simulations with experimental results. They concluded that the developed FEM model can be applied to simulate the dynamic behavior of a mechanical elastic wheel.

Deng et al. (2019) simulated with Abaqus the static interaction between a non-pneumatic mechanical elastic wheel and soil considering the material and geometrical non linearity and the large contact deformation. The main material of the wheel was rubber and was simulated with the Mooney-Rivlin model. The modified Drucker Prager model with Cap Plasticity was utilized to simulate the soil. The footprint and the axle stiffness, which are the basic mechanical parameters of a tire, were simulated with results within 5.3 % relative error.

To sum up, simulating a rolling process can be carried out with imposed displacements, applied translational velocities or angular velocities and a combination of both angular and translational velocities resulting in braking, free rolling or driving conditions. Generally, the research hitherto is mainly focused on optimizing a design of non-pneumatic tires and subsequently evaluating them against real case scenarios.

# **3 In situ relative density: Reevaluation of DPH relationships and comparisons to CPT**

## **3.1 Introduction**

Part of the work presented in this chapter is published in Vrettos & Papamichael (2018). In Germany, dynamic probing is still the most commonly used method for estimating the in-situ relative density of non-cohesive soils. The respective empirical correlations from the withdrawn DIN 4094-3, which are well-established in local practice, have been published partly in DIN EN 1997-2 (Eurocode 7, Part 2) and partly in DIN 4094-2. The depth profile of the measured number of blows is converted into a corresponding profile of the relative density by utilizing these correlations, but without taking into account the influence of the current depth of the probe tip, and consequently of the overburden pressure; it is only distinguished between situations “above” and “in” groundwater. The specified relationships for the different types of probing were already established in the 1970s as part of the standardization work for the DIN 4094 and were not updated since then. Due to the format of a standard, measurements of data scatter or exact sources of literature have not been given.

Due to the inherent difficulty of obtaining undisturbed samples, correlations for the relative density of non-cohesive soils in the literature are mainly based on measurements in large sand-filled containers in the laboratory (Melzer, 1968), in calibration chambers (Jamiolkowski, 2003) or by undisturbed soil samples extracted using ground-freezing techniques (Hofmann, 2000). In practice, it is usually sufficient to identify zones of low density, which need to be improved. Densification control is performed by comparing the penetration resistance before and after the procedure. Accurate determination of relative density is only required in certain situations such as in estimating the liquefaction potential of loosely deposited sands and silty sands. For this purpose, various empirical relationships have been proposed in recent years, primarily based on the Standard Penetration Test (SPT) and the Cone Penetration Test (CPT). A transfer of these findings to the Dynamic Probing is still missing. In the context of the present comparative study of this chapter, older experiments are reevaluated, and available empirical correlations are

assessed with respect to their applicability and reliability and extended by new approaches

### 3.2 Relative density in sands

Figure 3 contains data from undisturbed samples, compiled from Mayne (2006), that lie within the prediction interval of the eq. (11) provided by Jamiolkowski (2009). This also applies to the results of recent tests on Karlsruhe sand ( $d_{10} / d_{60} = 0.14/0.31$  mm) in a calibration chamber from Meier (2009). They have been re-evaluated herein by adopting  $C_N$  according to eq. (6).

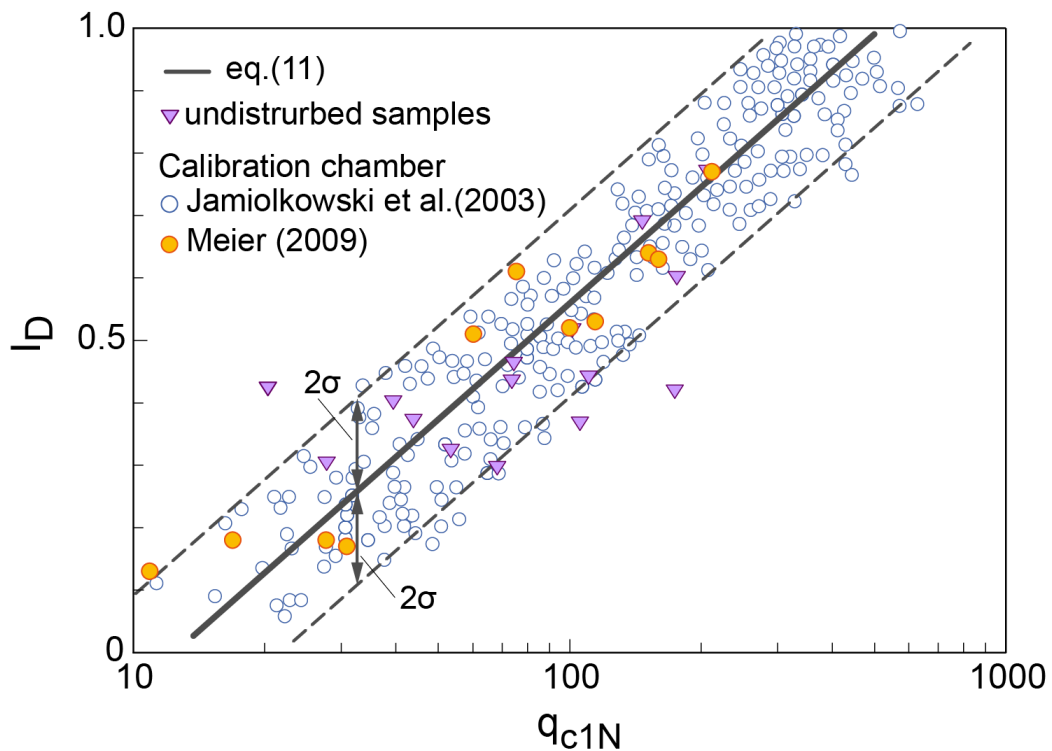


Figure 3: Results from calibration chamber tests (Jamiolkowski et al. 2003, Meier 2009) and from undisturbed samples (Mayne 2006), and approximation curve according to eq. (11) with the corresponding 95% confidence interval.

Relative densities determined in the older study (Melzer, 1968) on a natural scale under controlled laboratory conditions are subsequently used to derive a further empirical relationship as a function of the vertical effective stress.

These are penetration tests in a cylindrical shaft with a diameter of 3 m and a depth of 5.4 m. The sands investigated are characterized by  $d_{50} = 0.6$  mm and  $C_U = 2.4$ . The density was determined by means of a nuclear density gauge. In some of the experiments, the sand was dry up to a depth of -2.0m and from -3.5m and thereafter. The probes used were the mechanical Dutch cone, and the electrical Maihak cone. In the evaluation, it was assumed that the influence of each probing was in a range of about 50 cm, so that it was possible to carry out several tests within a single pit filling. Furthermore, a normalization procedure using  $C_N$  based on eq. (6) , for the  $N_{10}$  values of the DPH namely  $N_{10,1N}$  is presented. From the raw data, the following relationships were derived which has the form of eq. (11) with  $C_N$  according to eq. (6) with a limit of 1.7:

$$I_D = 0.1 \cdot \ln q_{c1N} + 0.1 \quad (31)$$

$$I_D = 0.1 \cdot \ln N_{10,1N} + 0.38 \quad (32)$$

It applies to both types of probe with slightly different standard deviations of mean value  $\sigma = 0.08 / 0.093$  for the CPT and DPH respectively. The statistical  $R^2$  value is 0.5 for all the tests. The maximum vertical effective overburden pressure  $\sigma'_v$  in the data was 80 kPa. This means that for all data  $C_N > 1.12$ , and most of the data have to be limited by the maximum value of 1.7 recommended from Youd et al. (2001) and from Boulanger & Idriss (2004) as mentioned in Chapter 2.1.1.5. The measured data and the curve determined by regression analysis are shown in Figure 4 and in Figure 5 for the two test series (shaft fillings).

A comparison of the empirical equations (11), (12) and (31) can be found in Figure 6. It can be seen that all three empirical relationships coincide at  $q_{c1N} = 100$  with a value  $I_D = 0.55$ . It should be noted that the pressure-dependent normalization in all equations utilized eq. (6) with a bound 1.7. It is also noteworthy that the standard deviation of the older experiments in the shaft and that of the newer ones in various calibration chambers, exhibit similar values.

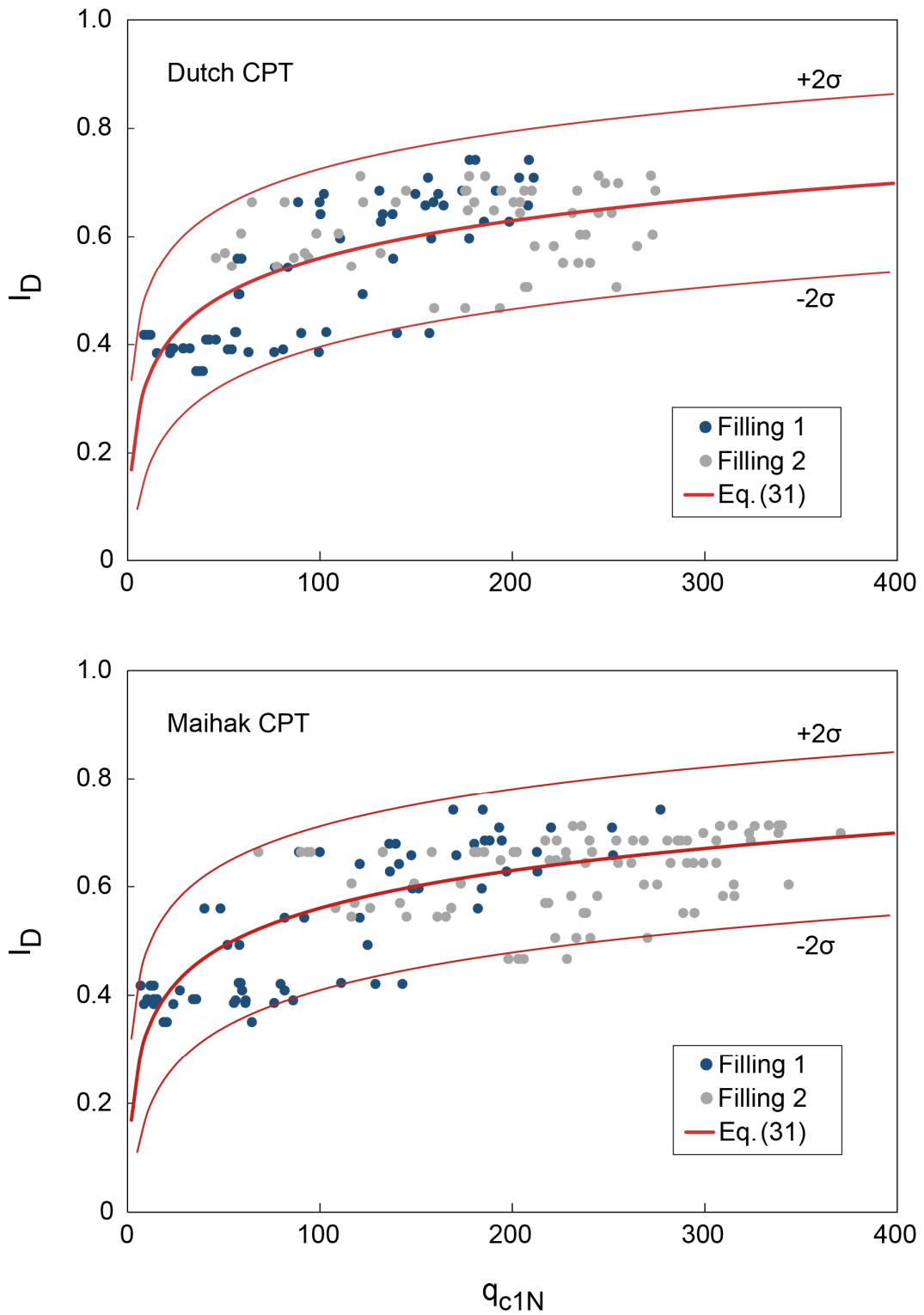


Figure 4: Evaluation of the experimental data for the two CPT types and regression curve according to eq. (31).

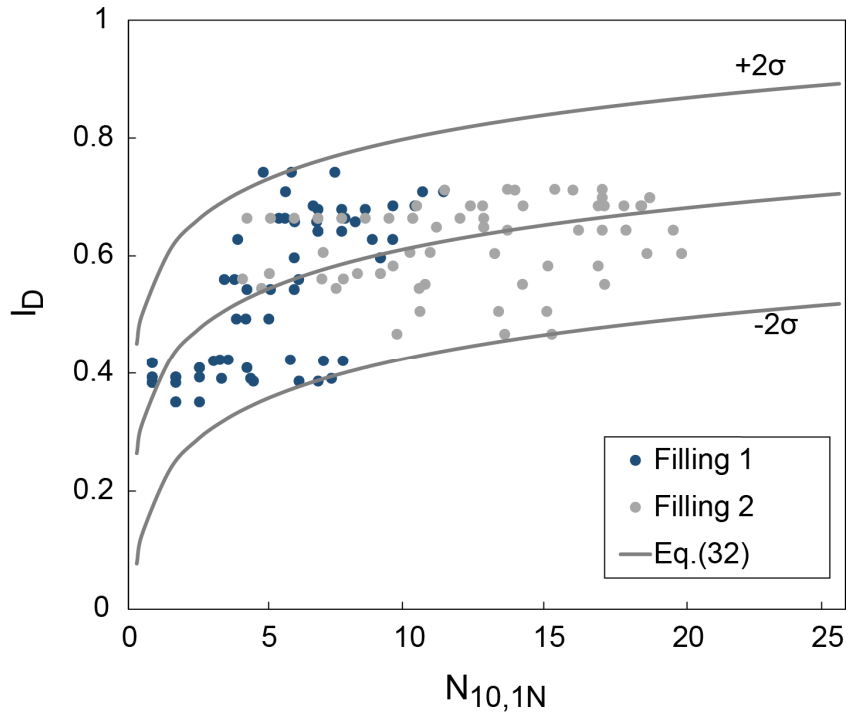


Figure 5: Evaluation of the experimental data for the DPH and regression curve according to eq. (32).

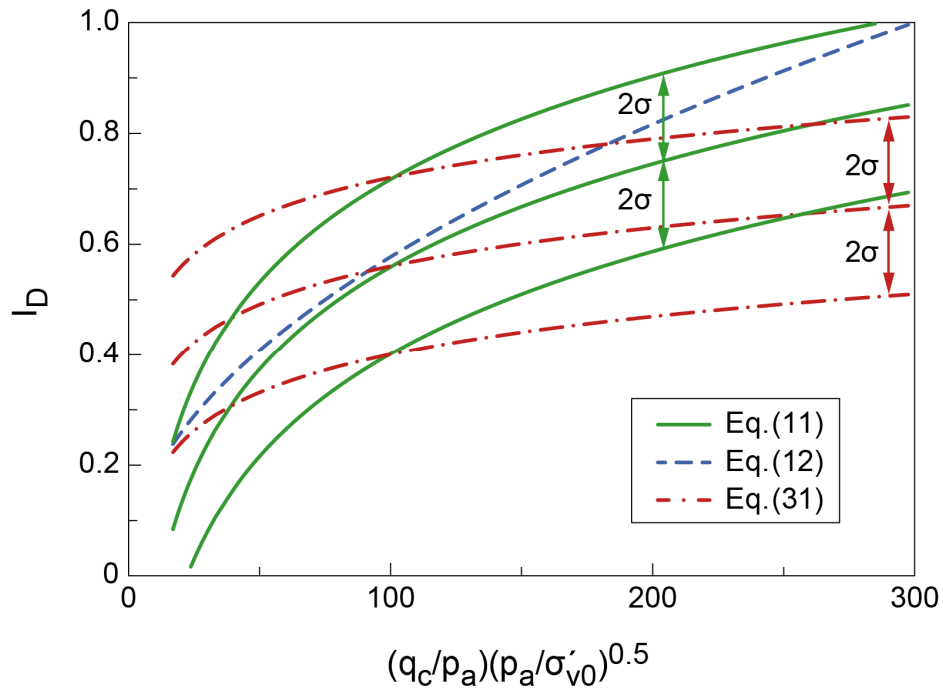


Figure 6: Comparison of empirical relations.



### 3.3 Discussion

In international practice, the interpretation of SPT and CPT is based on normalized resistance values that take into account the level of overburden pressure at the considered depth. To a good approximation, an inverse square root function of the vertical effective stress can be used for both types of probing. A differentiation between situations above and in the groundwater - as this is traditionally provided in the German standardization for the interpretation of dynamic probing - is not made. From comparative studies based on targeted field tests, a respective normalization should also be applied for dynamic probing. An attempt to demonstrate such procedure was carried out and showed promising results. This will also make more accurate the conversion of the DPH blow count to an equivalent CPT tip resistance.

The relative density as a parameter to assess the subsoil conditions is subject to considerable fluctuations because of its definition in terms of three state-parameters (void ratios). Hence, expectations for a precise, indirect determination from probings should be dampened. Thus, the estimation of geotechnical parameters (shear parameters, stiffness moduli) on the basis of the relative density is inevitably associated with considerable uncertainty. It is much more accurate to use direct correlations. A medium relative density, can reliably be recognized by the available empirical relationships.

Furthermore, algorithms can be utilized to obtain a representative smoothed curve from the irregular CPT recordings observed within homogeneous layers due to the sensing of weaker or harder soil layers above/below the investigated section.

Finally, the applicable DIN standards and the EN1997-2 should be homogenized with regard to the evaluation procedures and updated to the international state of knowledge. Furthermore, the quantification of the scatter in the data is essential especially for determining relative density from probings.

## **4 Field investigation on the planetary analogue site Mount Etna**

### **4.1 Introduction**

The work presented in this chapter is a part of the published work in Papamichael et al. (2018). Planetary analogue sites are essential for testing technologies and equipment for future exploration missions in Space. These sites exhibit extreme conditions similar to those prevailing on the Moon and on Mars, or on other planets. Mount Etna is one of the extra-terrestrial analogue sites with particular adverse conditions characterised by continuing volcanic eruptions. It has been certified as such due to its unique features similar to those of planetary bodies (Preston et al., 2012), and has already been a destination for field tests (Ciarletti et al., 2011). The lava landscape of Mount Etna has a volcanic structure, lava flows, rilles and channel systems and is composed of basalt, features of both Moon and Mars. Within the frame of the research project ROBEX which is dealing with the robotic exploration of extreme environments, dynamic penetration tests have been conducted at an altitude of over 2600 meters on Mt. Etna in order to assess parameters relevant to rover mobility. Focus is placed on the assessment of the near-surface soil properties. A light dynamic cone penetrometer with variable impact energy known as Panda<sup>®</sup> has been employed to estimate relative density and strength. In addition to the in-situ tests, samples of the volcanic soil were collected for classification and shear strength testing in the laboratory. The chapter describes the site, the experimental set up, the testing procedures and the deduced soil properties.

### **4.2 Experimental set up and site characterization**

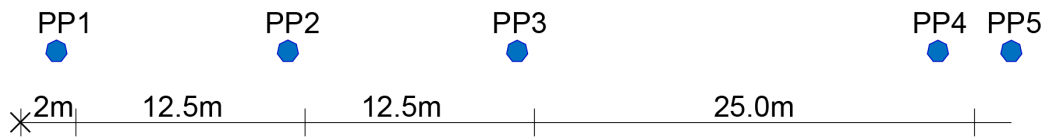
Mount Etna is an active stratovolcano for the last 500,000 years. It is located on the east coast of Sicily and lies above the convergent plate margin of the African and Eurasian Plates (James et al., 2016). As a stratovolcano, Mt. Etna has high silica content, which makes the magma more viscous. Hence, lava covers a shorter distance before it solidifies producing the typical conical

shape with steep sides. Mt. Etna has several layers of solidified lava, ash and pumice on its slopes and changes height periodically, following an eruption.

Two field campaigns to Mt. Etna took place. During the first, in September of 2016, two sites (Site No. 1 and No. 2) were investigated. During the next mission in June 2017, tests were conducted on another site nearby (Site No. 3) to supplement the collected data of the first campaign. The sites are located in the northern-east flanks near the crater Cisternazza with GPS coordinates: Site 1: 37° 43.491' N, 0.15° 00.363' E; Site 2: 37° 43.486' N, 0.15° 00.463' E; Site 3: 37° 43.584' N, 0.15° 00.413' E.

On Sites 1 and 2, a longitudinal profile of 3 points along the ground surface with a distance of 5 m between the points, was investigated. At each point, two adjacent dynamic cone penetration tests have been carried out in order to assess the repeatability of the test. Samples were collected at the points where penetration tests were conducted. The collected samples represent approximately 30 cm depth of the local soil stratigraphy. Each sample is denoted as follows: “S” stand for Site followed by “1” or “2” indicating the site number, and “P” which denotes point, followed by the number of the sample and a second number denoting the sampling sublayer of that specific point. For instance, S1-P3.2 represents the second sublayer of the point three at the first site.

On Site 3, a longitudinal profile has been defined with distinct evaluation points at distances of 2 m, 14.5 m, 27 m and 52 m from the reference point, cf. Figure 7. A photo from the site is depicted in Figure 8. Near these points, at 2 m lateral distance from the axis, dynamic cone penetration soundings were conducted at points PP1 to PP5. Next to these sounding points, in-situ density was measured at PP1 to PP4 by an appropriate simple device: A metal cylinder, 30 cm in diameter and 40 cm in height with a wall thickness of 2 mm, was carefully pushed into the soil in intervals of 10 cm. At each interval, the soil material inside the cylinder was removed and weighted. With known volume and moisture content, the in-situ bulk density  $\rho$  was determined. The values of dry density  $\rho_d$  are given in Table 2. It can be inferred that at the first two points the two top layers are denser than the third layer whereas at the other locations the density does not considerably vary with depth.



● Penetration test

Figure 7: Experimental layout at Site 3.

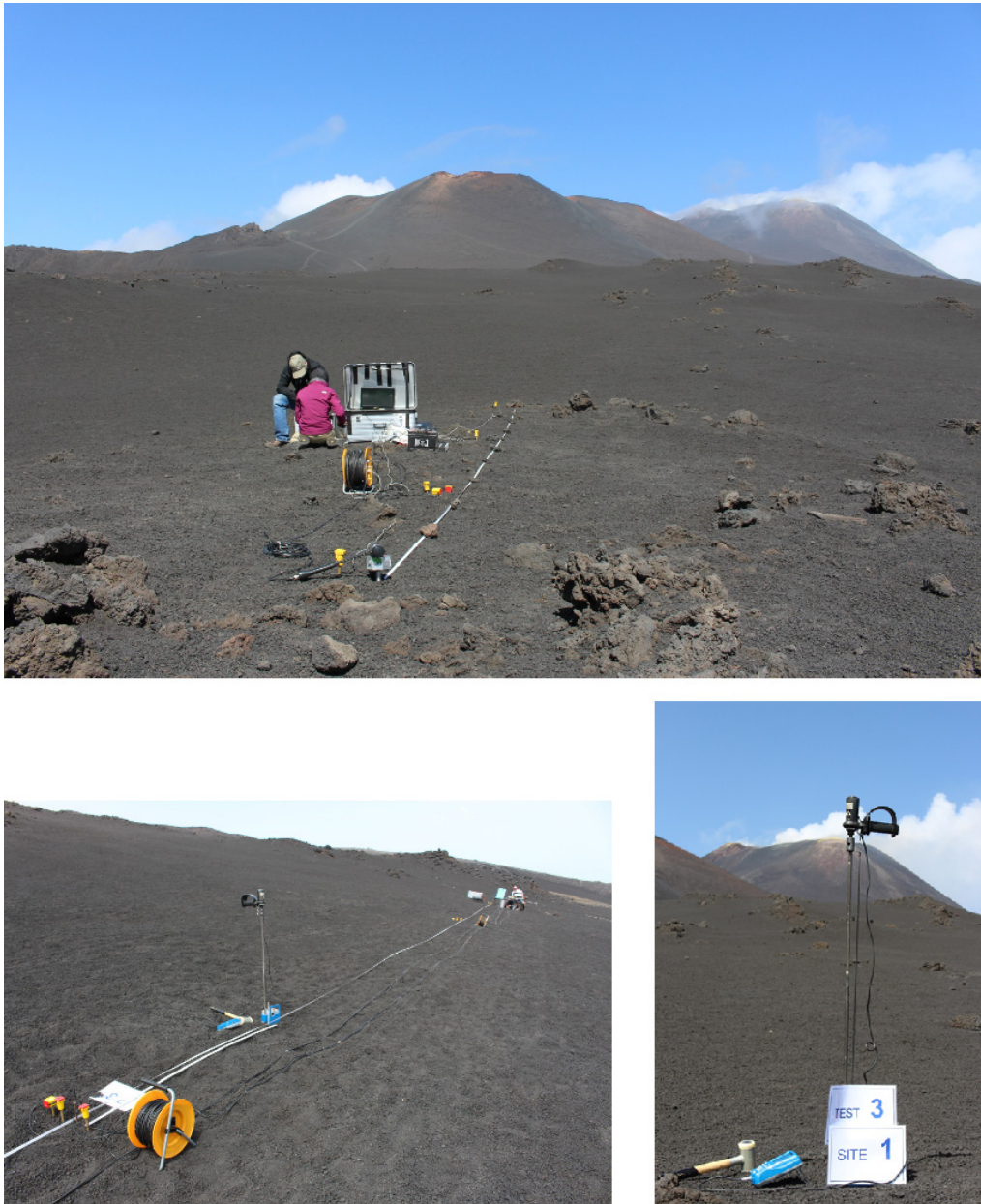


Figure 8: Photographs from the site.

Table 2: In-situ dry densities at Site 3

Depth	$\rho_d$ [Mg/m <sup>3</sup> ]			
	PP1	PP2	PP3	PP4
0 - 10 cm	1.37	1.49	1.30	1.31
10 - 20 cm	1.36	1.56	1.25	1.31
20 - 30 cm	1.08	1.12	1.29	1.30

Table 3: Grain-size distribution characteristics

Sample	$d_{50}$ [mm]	$C_U$	Sample	$d_{50}$ [mm]	$C_U$
S1-P1.1	3.68	14.8	S2-P1.1	2.51	7.0
S1-P1.2	3.42	9.7	S2-P1.2	3.10	5.5
S1-P1.3	54.3	17.8	S2-P1.3	1.86	11.9
S1-P2.1	3.25	5.1	S2-P2.1	1.23	4.3
S1-P2.2	2.92	5.0	S2-P2.2	1.25	3.9
S1-P2.3	62.59	2.0	S2-P2.3	1.16	3.5
S1-P3.1	3.18	10.4	S2-P3.1	2.29	7.0
S1-P3.2	5.60	4.9	S2-P3.2	1.84	5.2
S1-P3.3	4.56	8.7	S2-P3.3	1.95	4.9
			Site 3	2.00	5.9

The collected samples were utilized for subsequent classification and shear strength testing in the laboratory. According to the pertinent German Standard DIN 18196, the material corresponds to well graded gravel-sand mixtures, poorly graded gravel, and poorly graded sand. Site 1 comprises mainly material from the first two groups, whilst the last two groups characterize Site 2 and Site 3. For all the material, the grain size distribution was carried out according to DIN 18123. The grain diameter at 50% passing  $d_{50}$  and the uniformity coefficient  $C_U$  are given in Table 3 while the grain size distribution curves are shown in Figure 9 and Figure 10. From Figure 9 it is evident that Site 1 exhibits a lateral inhomogeneity while Figure 10 for Site 2 indicates the opposite.

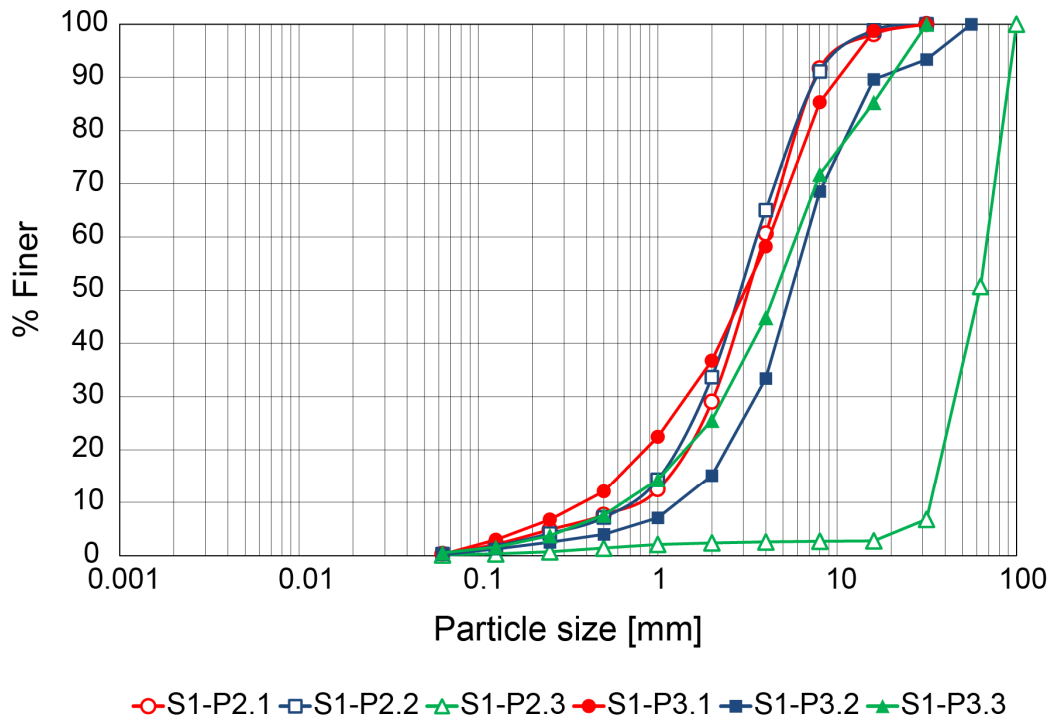


Figure 9: Grain size distribution curves for Site 1.

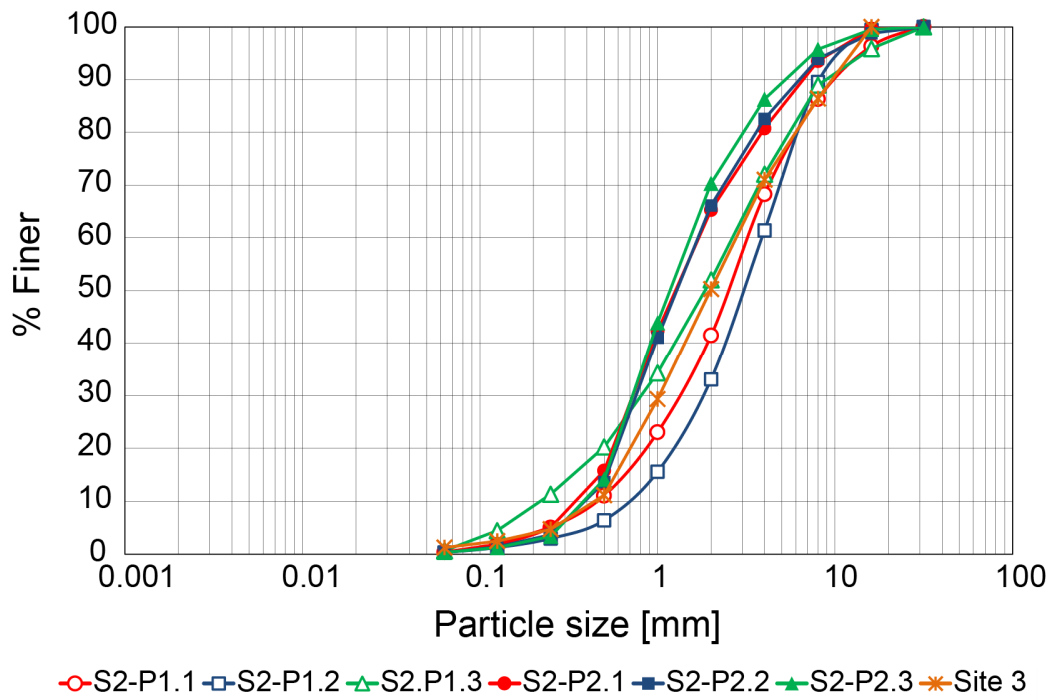


Figure 10: Grain size distribution curves for Site 2 and Site 3.

Further properties determined on soil material from Point 2 of Site 2, in accordance to DIN 18124 and DIN 18126, are the grain density  $\rho_s$  with a value 2.94 Mg/m<sup>3</sup> and the dry density at the loosest and densest conditions,  $\rho_{d,min}$  and  $\rho_{d,max}$  which equal to 0.99 and 1.30 Mg/m<sup>3</sup>, respectively. At Site 3, the respective values are  $\rho_s = 3.04$  Mg/m<sup>3</sup>, and  $\rho_{d,min} / \rho_{d,max} = 0.80 / 0.84$  Mg/m<sup>3</sup>. The laboratory device, however, is not adequate for this coarse material yielding low values. When the coarse fraction was removed the corresponding densities for the remaining fraction 0 – 2 mm increased to 1.22 / 1.39 Mg/m<sup>3</sup> respectively.

### 4.3 Shear strength testing in the laboratory

Direct shear strength tests were carried out in accordance with the specifications of DIN 18137-3:2002-09 on the material collected on Site 3, which comprised of material collected from the tested location points on the site, in a large direct shearing frame with dimensions 30 x 30 cm with a 15 mm shearing gap. The grain size distribution of the material is included in Figure 10. The Etna volcanic material EVM was tested in dry condition at dry density  $\rho_d = 1.17$  Mg/m<sup>3</sup>. Low values of the normal stress  $\sigma_v = 10$ -30 kPa were selected in order to reproduce the low in-situ near surface overburden stress. The speed of horizontal shearing was set equal to 1 mm/min. The test results in terms of shear stress vs. shear deformation and vertical displacement vs. shear deformation are plotted in Figure 11. Adopting a Mohr-Coulomb failure criterion the following “at peak” shear strength parameters are obtained: angle of internal friction equal to 41.3° and extrapolated cohesion equal to 34.5 kPa. The high value for the latter is mainly due to the interlocking of the irregularly shaped particles. The vertical deformation curves exhibit an almost pure dilatant behavior at the lower vertical stress, while at the higher stress level (30 kPa) the dilatant behavior is preceded by contraction. This complies with the findings on the shear behavior of extraterrestrial analogue soils at low stress levels (Vrettos, 2012).

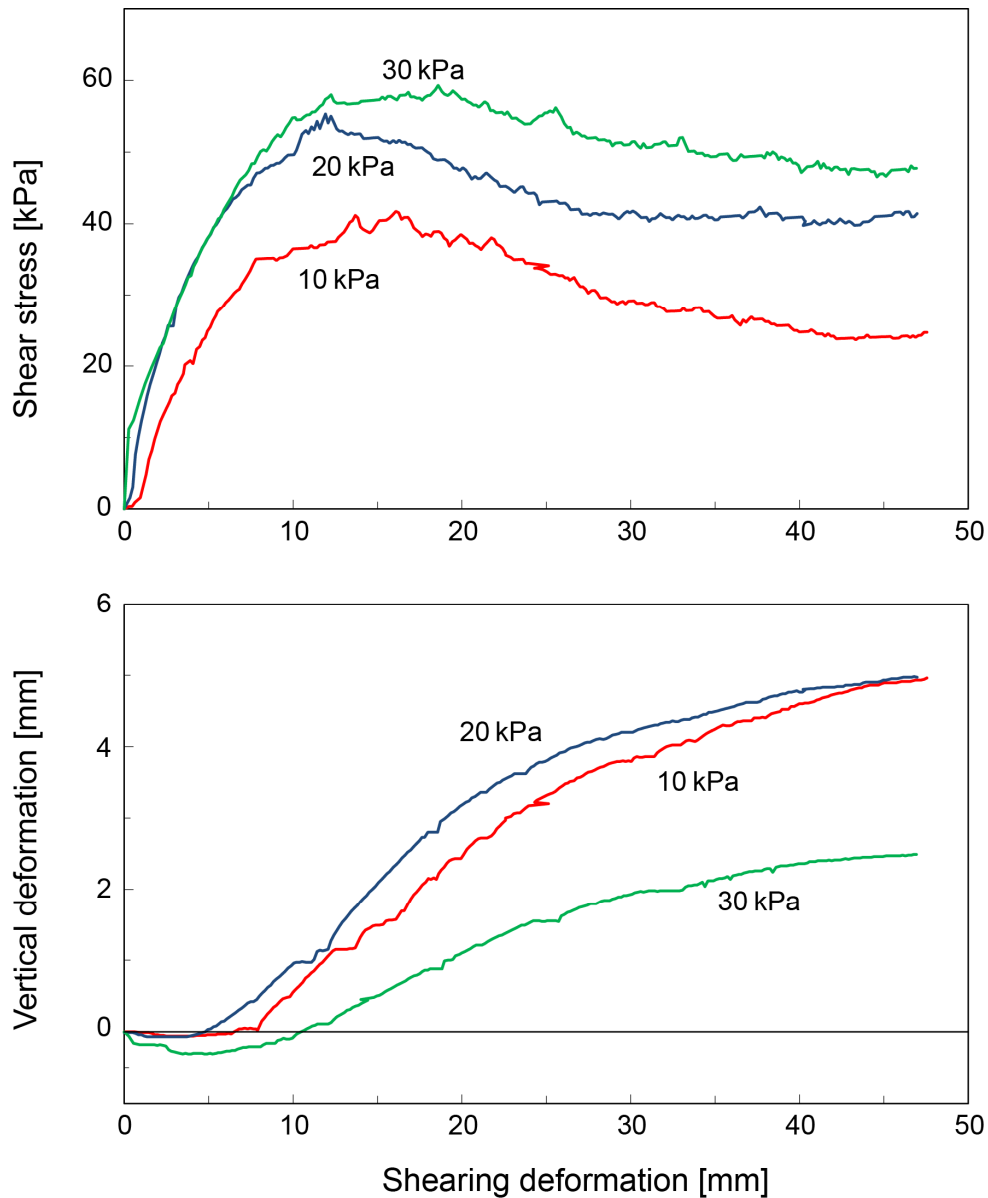


Figure 11: Results of direct shear tests on material from Site 3.

#### 4.4 In situ penetration and density tests

The Panda<sup>®</sup> lightweight portable dynamic cone penetrometer has been employed. For the purposes of this research, the cone of 2 cm<sup>2</sup> was used. When testing with the Panda<sup>®</sup> an over-sized hole is produced to avoid effects of rod friction. Of course, this becomes unavoidable in great depths. Panda<sup>®</sup>



can be used for soils with a grain size approximately up to 50 mm and tip resistance up to 50 MPa.

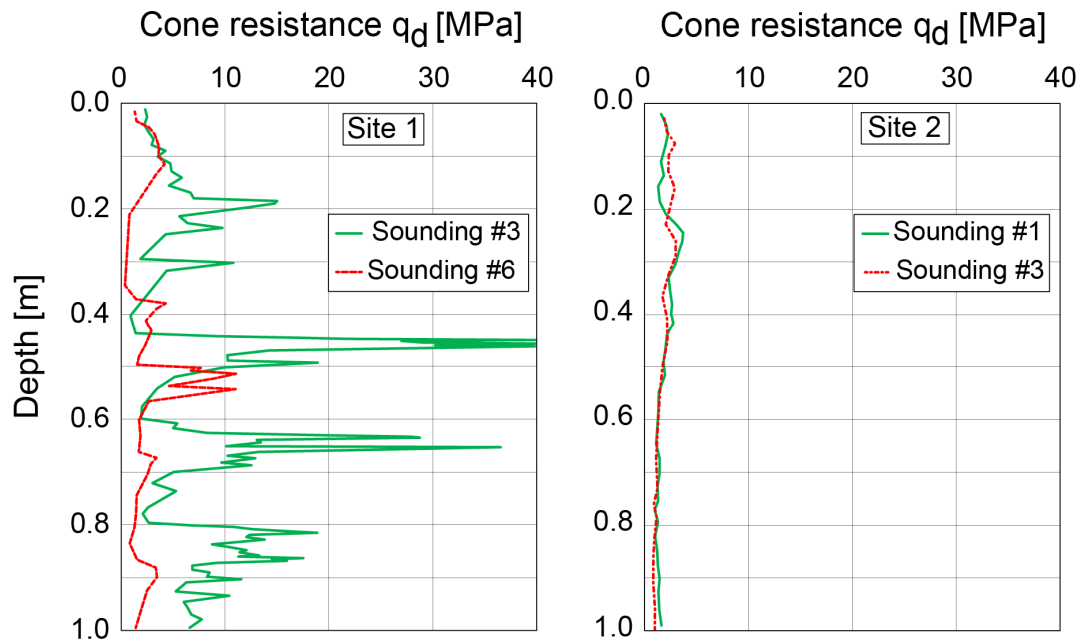


Figure 12: Penetrograms at Site 1 and Site 2.

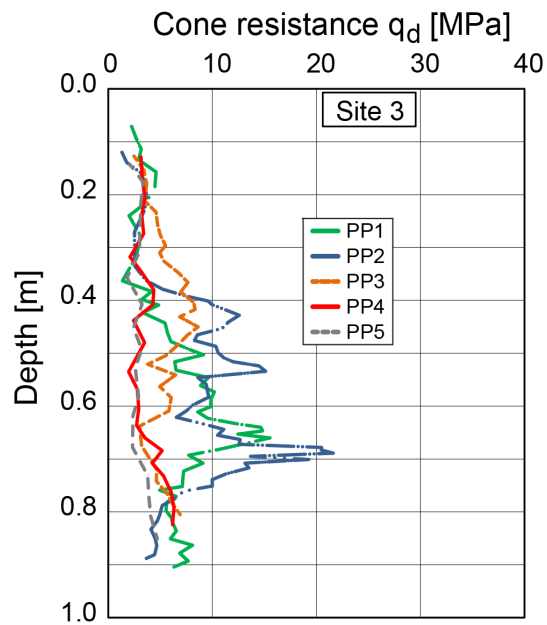


Figure 13: Penetrograms at Site 3.

Panda<sup>®</sup> penetrograms at Site 1 and Site 2 are displayed in Figure 12. The profiles at the two locations P2 and P3 on Site 1 demonstrate the natural inhomogeneity of the soil at these locations. In contrast, P1 and P2 on Site 2 are in close agreement. Penetrograms along the array at Site 3 are displayed in Figure 13. The differences in density observed in the in-situ measurements (Table 2) are captured by the test.

Previous well-documented research relevant to this thesis is that the  $q_d$  determined using Panda<sup>®</sup> corresponds approximately to the  $q_c$  value of the cone penetration test CPT for sands (Gourves and Barjot, 1995). Cross-correlating  $q_d$  with  $q_c$  of CPT enables the application of the available numerous empirical relationships derived for the  $q_c$ , in order to characterize the soils at the sites investigated herein. Mayne (2007) suggested the following equation for the CPT based procedure for silica quartz sands:

$$\rho_d = (1.89 \log q_{c1N} + 11.8) / g \quad (33)$$

It should be clarified here that the selection of this eq. (33) and not of another equation utilized for the CPT, is to comply with the one suggested originally for Panda<sup>®</sup>.

Taking the average in the top 30 cm yields  $\rho_d = 1.66 \text{ Mg/m}^3$  utilizing eq. (14). Taking an average value for the depth 0 - 30 cm and  $q_c = q_d$  we obtain  $\rho_d = 1.63 \text{ Mg/m}^3$  utilizing eq. (33). The density values compare well to each other but are much higher than the in-situ measured dry density  $\rho_d$  with an average value of  $1.31 \text{ Mg/m}^3$ . The reason for this discrepancy, which is shown in Figure 14, lies in the nature of the volcanic material prevailing at the site. Hence, assessment with other material-specific relationships is needed. The mean  $-1\sigma$  profiles of  $I_D$  at Site 3 at PP4 derived by eq. (11) and eq. (31) are shown in Figure 14. One may see that both equations are suitable in capturing the minor variation of penetration resistance at small levels of effective overburden stress.

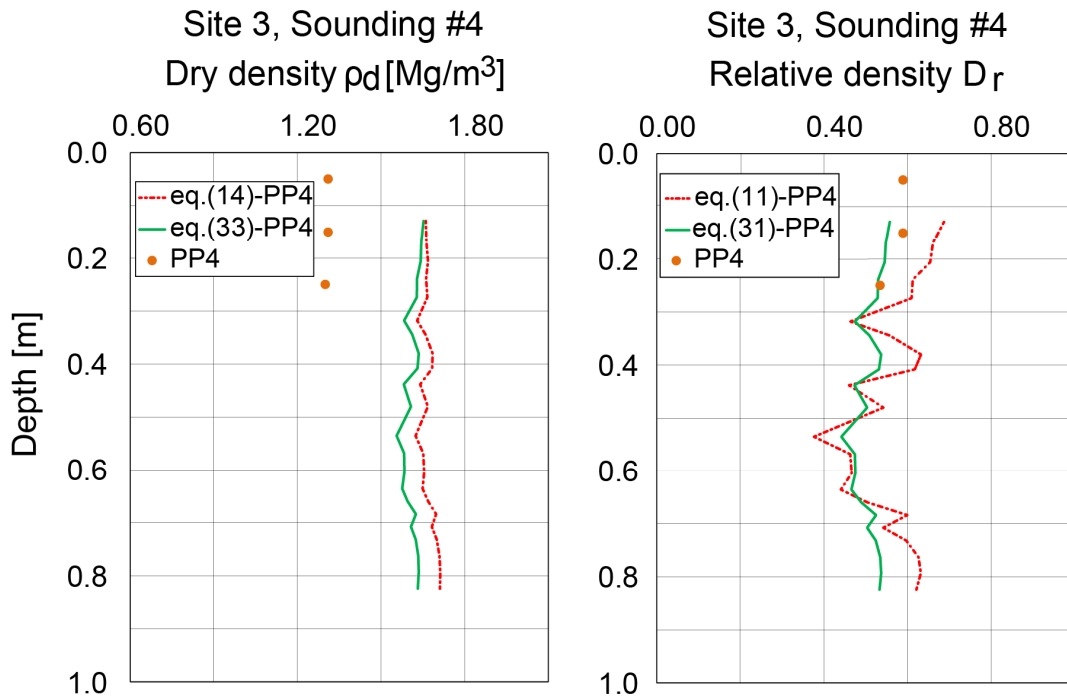


Figure 14: Derived profiles of relative density and dry density.

## 4.5 Conclusions

The transfer of correlations that are usually applied in terrestrial geotechnical soil engineering to extra-terrestrial analogue conditions of low density and overburden stress levels requires judgement and consideration of the conditions for which they were developed and calibrated. The results show the limits of available empirical relationships derived for routine geotechnical applications and the inherent need for further research. The lightweight portable penetrometer is a promising device for such field tests. After refinement and validation, the methodology employed in the context of this study may be transferred to planetary missions and off road applications.

## 5 Small scale shallow penetration tests

### 5.1 Introduction

A portable penetrometer is a possible option in order to investigate the near surface soil properties with respect to density and shear strength. A similar technique was used in Apollo missions where deeper penetrations are not possible due to lack of energy. The cone index is the basis for assessing the vehicle performance and the mobility of the NATO reference mobility model NRMM (Wong, 2001). Generally, the results of in situ penetration are correlated well with soil properties. For this purpose, a series of small scale shallow penetration tests were carried in laboratory conditions. The results can be used as a guide for a first estimation of near-surface relative density. A small part of the raw penetration data on MMS-dust, MSS-D, Quarry fines, WF34-sand, MMS-sand and medium sand (referred also as gray sand) in the small and medium container presented herein, were part of a project work in our laboratory and were published in Vrettos et al. (2014). Those data were supplemented with additional tests on other  $I_D$  values and furthermore tests were conducted in a large container.

### 5.2 Soil classification

In this chapter test results of some extraterrestrial soil simulants and two other supplementing materials namely Quarry fines and Medium sand are presented. For each material grain size distribution was carried out according to DIN 18123 and the type of the material was determined by DIN 18196. The grain density was determined in accordance with DIN 18124. The minimum and maximum densities and the corresponding porosities and void ratios were determined according to DIN 18126. The grain size distribution of each material is depicted in Figure 15; adopted from Vrettos et al. (2014) and supplemented with the grain size distribution of the material JSC-1A, JSC Mars 1A and Syar coarse. The following Table 4 and Table 5 summarize the characteristics of the tested material. The factor of compaction potential  $I_F$  is defined as  $(e_{max} - e_{min})/e_{min}$ . The properties  $\rho_s$ ,  $e_{max}$ , and  $e_{min}$  of the tested

material MMS-dust, MSS-D, Quarry fines, WF34-sand, MMS-sand and medium sand were reported in Vrettos et al. (2014).

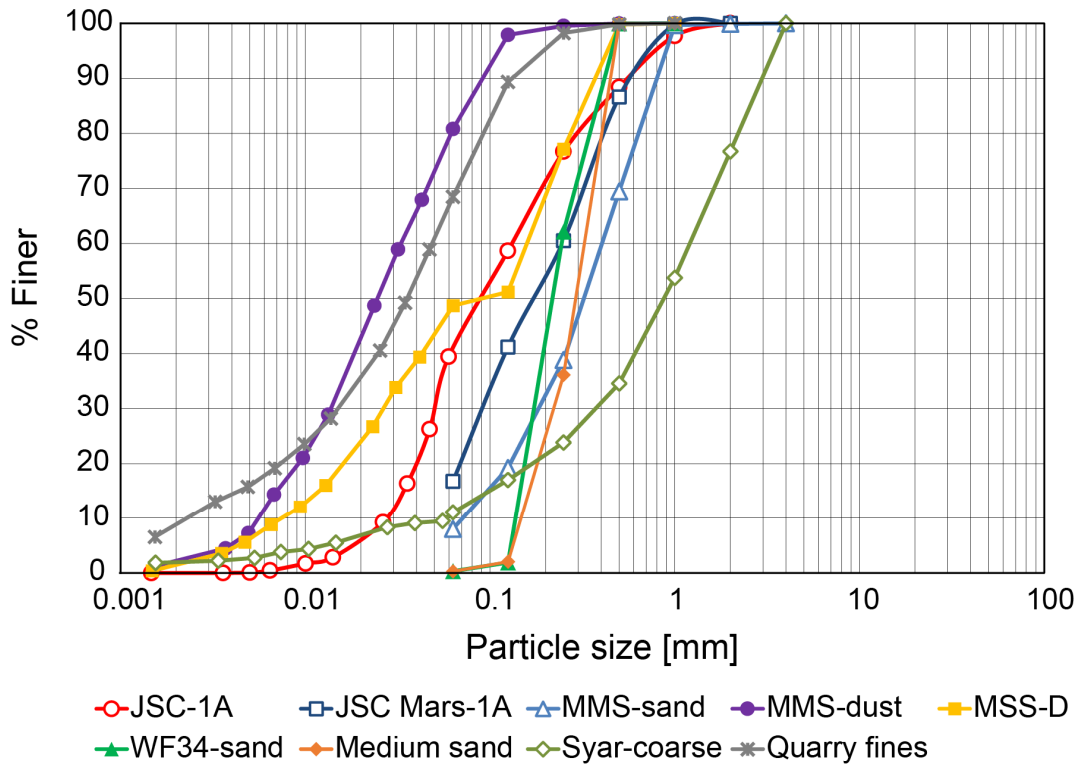


Figure 15: Grain size distributions of the tested materials.

Table 4: Characteristics of the tested material according to DIN 18123 and DIN 18196

Material	$d_{50}$ [mm]	$C_U$ [-]	$C_C$ [-]	Clay [%]	Silt [%]	Sand [%]	Gravel [%]	Soil Type
JSC-1A	0.085	4.9	0.7	0.02	41.20	58.79	0.00	SU*
JSC Mars-1A	0.200	4.1	1.1	0.91	9.45	89.63	0.00	SU
MMS-sand	0.330	5.7	1.2	0.0	8.01	91.8	0.19	SU
MMS-dust	0.025	5.9	1.0	1.99	78.75	19.26	0.00	SU*
MSS-D	0.110	22.6	0.5	1.22	47.23	51.55	0.00	SU*
WF34-sand	0.220	1.7	0.9	0.00	0.32	99.68	0.00	SE
Medium sand	0.290	1.9	1.0	0.00	0.30	99.70	0.00	SE
Syar coarse	0.899	21.2	2.2	1.97	9.08	65.45	23.50	SU
Quarry fines	0.036	29.7	2.5	11.30	57.07	31.63	0.00	SU*

Table 5: Characteristics of the tested material according to DIN 18124 and DIN 18126

Material	$\rho_s$ [Mg/m <sup>3</sup> ]	$\rho_{dmin}$ [Mg/m <sup>3</sup> ]	$\rho_{dmax}$ [Mg/m <sup>3</sup> ]	$e_{max}$ [-]	$e_{min}$ [-]	$I_F$ [%]
JSC-1A	2.89	1.472	1.819	0.964	0.590	63.4
JSC Mars-1A	2.69	0.764	0.925	2.522	1.909	32.1
MMS-sand	2.89	1.305	1.656	1.214	0.745	63.0
MMS-dust	2.83	1.039	1.490	1.719	0.896	91.8
MSS-D	2.90	1.349	2.022	1.149	0.434	164.8
WF34-sand	2.64	1.408	1.695	0.877	0.559	57.0
Medium sand	2.65	1.369	1.741	0.933	0.521	79.2
Syar coarse	2.81	1.469	1.939	0.913	0.449	103.3
Quarry fines	2.74	1.085	1.522	1.528	0.803	90.3

The soil type SU and SU\* correspond to well graded or intermediate graded sand-silt mixtures and SE corresponds to poorly graded sand. The  $d_{50}$  was used for several years as an influential parameter for establishing correlations for geotechnical purposes. Although it turned out that solely this parameter cannot accurately quantify the characteristics of soils. Other parameters such as uniformity coefficient  $C_U$  and coefficient of curvature  $C_C$  are very important for representing a specific grain size distribution. For the soils JSC-1A, JSC Mars-1A, MMS-sand, MMS-dust, WF34-sand, Medium sand with  $C_U < 6$  the soil is classified as poorly graded. Syar coarse and Quarry fines are classified as well graded with  $C_U \geq 6$  and  $1 \leq C_C \leq 3$ . Lastly, MSS-D is classified as intermediate graded with  $C_U \geq 6$  and  $C_C < 1$  or  $C_C < 3$ . The parameter  $I_F$  which equals to  $(e_{max}-e_{min})/e_{min}$  is also given in the table as is associated with the compaction potential of soils.

### 5.3 Triaxial and oedometer tests

Although there are triaxial tests results from the literature regarding specific simulants, selected material was retested in the desired state conditions. Triaxial tests were carried out in accordance with the specifications of DIN 18137-2:1990-12. Cylindrical samples of a diameter of 100 mm and 120 mm height were tested on confining pressures of 10 to 80 kPa. The deformation rate was set at 0.02 mm/min. The consolidation time was 1 hour. Tests were

carried out with different densities on dry samples. Adopting a Mohr-Coulomb failure criterion, the “at peak” shear strength parameters are obtained for each material. The initial characteristics of the tested samples and the obtained strength parameters are summarized in the following Table 6. The triaxial apparatus along with one sample is shown in Figure 16.

Table 6: Results from triaxial tests

Material	$e$ [-]	$I_D$ [-]	$\sigma_{2,3}$ [kPa]	$\varphi$ [°]	$c$ [kPa]
JSC-1A	0.763	0.549	10-80	45.1	1.3
JSC Mars-1A	2.183	0.553	10-80	43.8	2.1
WF34-Sand	0.732	0.455	10-80	37.2	2.5
Medium Sand	0.706	0.559	10-80	39.5	2.1
Quarry fines	1.104	0.585	10-80	42.5	0.5



Figure 16: Triaxial test apparatus and soil sample.

One dimensional consolidation tests known as oedometer tests, were carried out in accordance with DIN EN ISO 17892-5. Cylindrical soil specimens are

placed in a stainless steel ring. Standard oedometer containers were used that have a diameter of 100 mm and a diameter of 20 mm. Load is applied in small increments. The next load is applied after the sample reaches the maximum displacement under the current load (when the rate of deformation reaches zero). Two different densities that correspond to dense and loose conditions were tested. The results of the tests are summarized on the following Figure 17 to Figure 20 and in Table A-1 to Table A-18 in the Appendix A. The initial properties of the tested materials are summarized in Table 7. The hierarchy of the response of the material differ in loose and dense conditions. This is partially contributed to the span between minimum and maximum density that each material can exhibit. Some of the soils are really sensitive to small loading in loose conditions and therefore they consolidate immediately under slight loading as shown in Figure 17 For both loose and dense conditions, the category SU\* exhibit the highest settlements under a specific load. For the dense case the SE category has lower settlements than SU and for the loose case the SU has less settlements than SE. The slope of the material lines of Figure 19 and Figure 20 correspond to the compression index  $C_c$ .

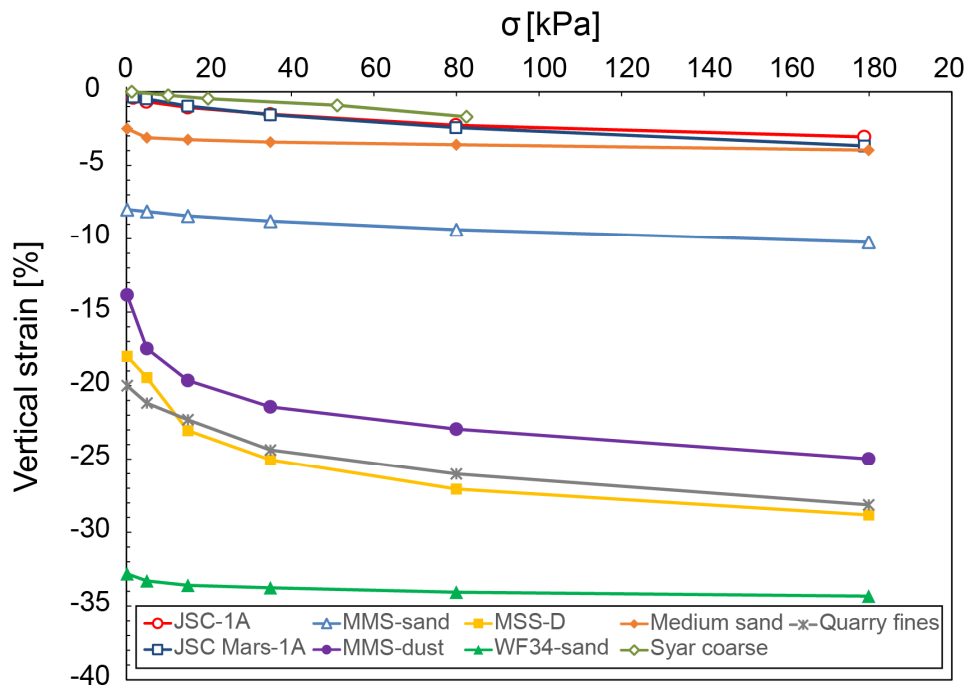


Figure 17: Results of oedometer tests for the soils in loose conditions.



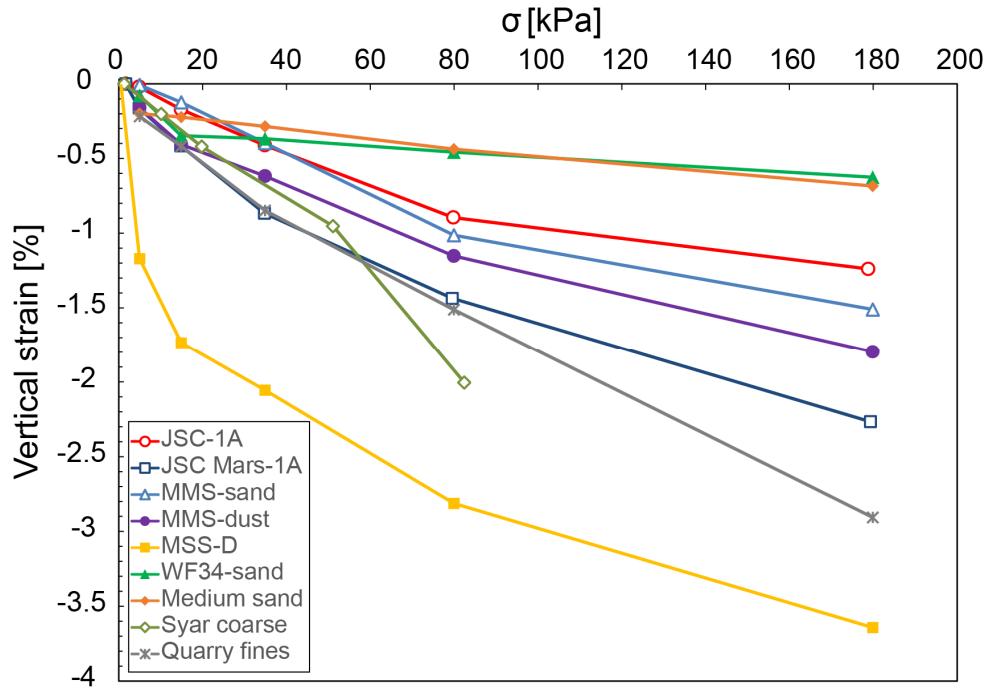


Figure 18: Results of oedometer tests for the soils in dense conditions.

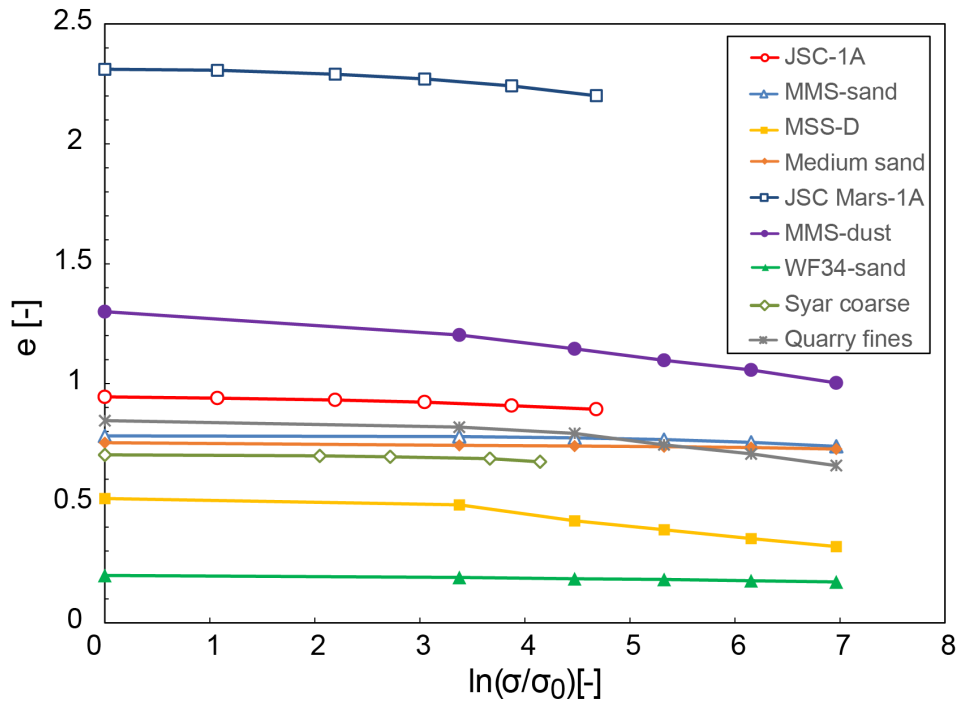


Figure 19: Void ratio vs stress for the material in loose conditions.

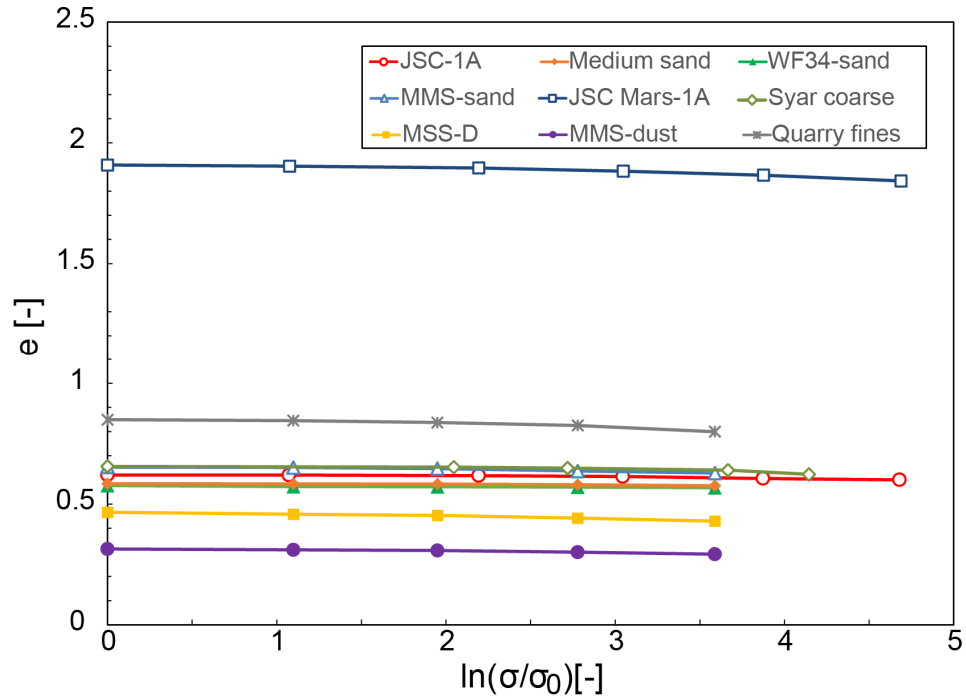


Figure 20: Void ratio vs stress for the material in dense conditions.

Table 7: Densities of the tested material loose and dense conditions

Soil	JSC-1A	JSC Mars-1A	MMS-sand	MMS-dust	-
$\rho_d$ [Mg/m <sup>3</sup> ]	1.784	0.924	1.603	1.900	-
$e$ [-]	0.620	1.908	0.653	0.316	-
	0.952	2.323	0.936	1.670	
Soil	MSS-D	WF34-sand	Medium sand	Syar coarse	Quarry fines
$\rho_d$ [Mg/m <sup>3</sup> ]	1.908	1.680	1.670	1.780	1.349
	1.349	1.486	1.474	1.651	1.084
$e$ [-]	0.483	0.577	0.587	0.579	0.853
	0.853	0.783	0.798	0.702	1.306

In some cases, the constrained modulus  $E_s$  values drop from one stage to the next one (moving towards higher stress levels) and then increases again. One possible reason is grain crushing or underestimation of the settlement rate and subsequently moving to the next step before the secondary settlements were completed. In some other cases the initial settlements were so small that the

$E_s$  couldn't be calculated. The constrained modulus  $E_s$  and compression index  $C_c$  values of each material are important for calculation of displacements under specific loading cases e.g. loading of a wheel or an entire rover in the case of the extraterrestrial missions or explorations of regions with difficult ground conditions.

## **5.4 Penetration tests in containers of different sizes**

### **5.4.1 Laboratory tests**

Shallow penetration tests were carried out on various soils in different containers and different in-situ densities to assess the influence of the sample size and density on the penetration resistance. Subsequently, correlations of the relative density with the normalized penetration resistance were produced. Boundary effects are clearly present during the penetration in the smaller containers. Initial results of the raw data of force and displacement for part of the investigated materials, specifically MMS-dust, MSS-D, Quarry fines, WF34-sand, MMS-sand and medium sand, were presented by Vrettos et al. (2014).

A steel rod penetrometer of 10 mm diameter with a flat base penetrates into the soil with a velocity of 1.2 mm/min for a total depth of 30 mm. Three different cylindrical containers' sizes were tested. The small container has 7.1 cm diameter and a height of 11.2 cm, the medium one has 15 cm diameter and a height of 12.5 cm and the large one is of an inside diameter of 29 cm with a height of 20 cm. During each test the penetration depth and the corresponding penetration resistance are measured with an appropriate load cell. The small container is depicted in Figure 21. The raw data consist of force and depth. The forces measured at the head of the penetrometer, are converted to penetration resistances by dividing with the area of the soil. The normalization is carried out utilizing the simple form of  $C_N$  of eq. (6) with  $a = 0.5$  and a reference pressure of 10 Pa which is chosen due to the low depth values and the corresponding low overburden pressure.

All the material was oven dried before the test. The material was placed on the containers with standard air pluviation techniques. To achieve a high density, the container was hit with a two-pronged fork as specified in the

German standard DIN 18126. In the reduced scale tests, the ratio of the diameter of the penetrometer to the mean grain diameter  $d_c / d_{50}$  should be above 16 in order to avoid scale effects (16 is the minimum ratio found among various researchers e.g. Lee, 1990). This means that the results of the tested soils have no scale effects, except for Syar coarse where the corresponding ratio is 11 and therefore possible scale effects exist in the data. For the tested soils of this study only Syar coarse has approximately a ratio of 11 which means that there are probably some scale effects in the data.

The maximum penetration force at the end of the penetration process is plotted vs density in Figure 22 in order to illustrate how density is linked to the penetration force. The denser the material the higher the expected penetration force. The growing rate of the penetration resistance with density is quantified by the inclination of the lines of the above mentioned figures. The slope varies from 0.06 to 0.12 for the small container, with an exception of the material JSC 1-Mars which has a slope of only 0.02. In the large container the slope varies from 0.12 to 0.16. In the medium container Quarry fines have a very high slope of 0.44 which can be attributed to considerable boundary effects. Taking as an indicative parameter the maximum force reached at the end of penetration, the soils are categorized from the stronger to the weakest as follows: Syar coarse, JSC-1A, MSS-D, MMS-sand, JSC 1A-Mars, MMS-dust, Quarry fines, Medium-sand, WF34-sand. From the other hand, taking as an indicative parameter the maximum force reached at the loosest possible state of the investigated soils the ranking is different: Syar coarse, MMS-sand, JSC-1A, WF34-sand, Medium sand, JSC 1A-Mars, MSS-D, Quarry fines, MMS-dust. Moving from the small container towards the large one, the penetration force is reduced because the boundary effect is not as pronounced as the size increases. It is obvious that the density of each material is well correlated with the penetration force. The inclination of the lines is similar, meaning that the tendency of the growth of the penetration resistance is somewhat similar for all the soils independently from other soil characteristics. JSC-1A is an exception. Including additional factors in the analysis could improve the correlations but could also make the calculations more complex and time consuming to get all the required parameters to carry down the analysis.

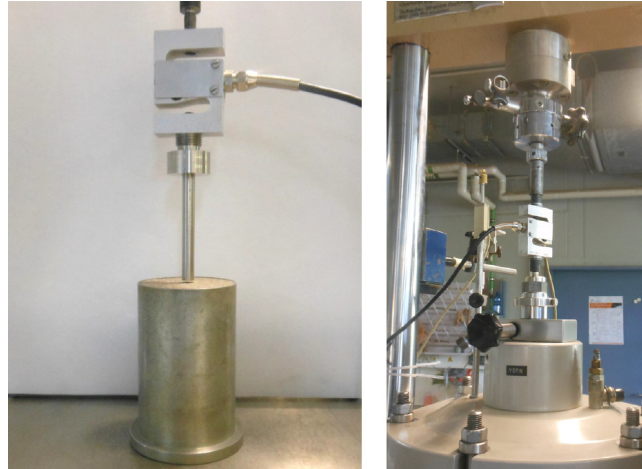


Figure 21: Small size penetration mold and measurement device.

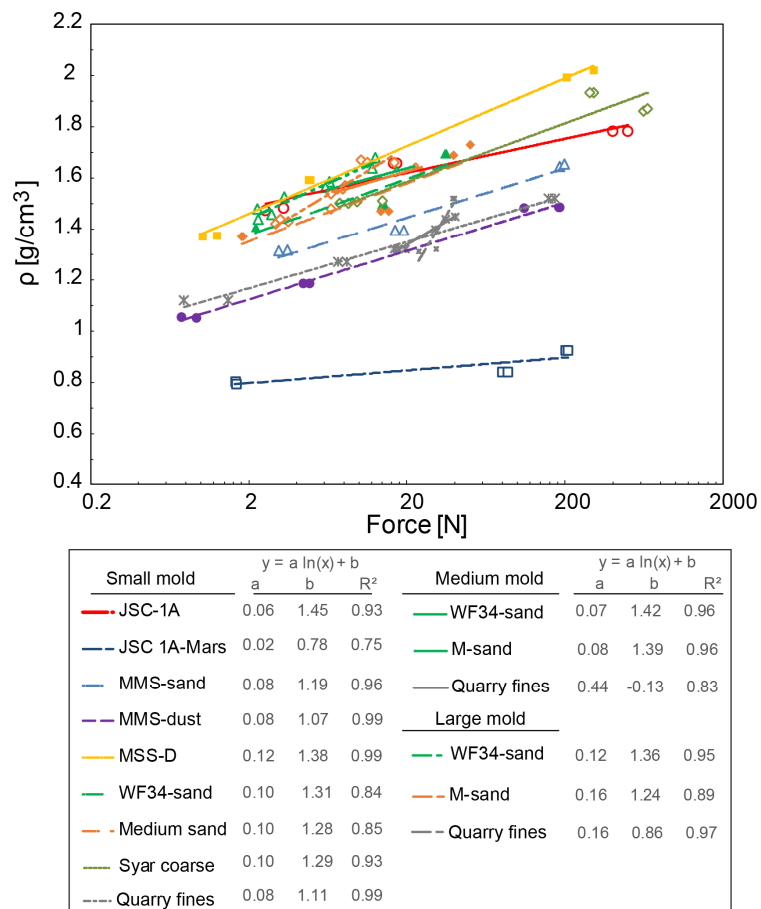


Figure 22: Maximum force reached at the end of penetration dependent on density.

### 5.4.2 Correlations for relative density

The correlations between relative density and the normalized value  $10^{-2} q_{c1N}$  are depicted in Figure 23 to Figure 27. The correlations are categorized based on the sample size or the type of soil. The container is denoted as "C." in the figures Figure 25-Figure 27. The relationship  $I_D$  vs  $10^{-2}q_{c1N}$  for all the materials for each individual material, exhibits high correlation values as shown in Figure 23 to Figure 26. The individual correlations of the soils WF34-Sand, Medium-Sand and Quarry fines for all the three utilized molds, are depicted in Figure 25 to Figure 26. It is obvious that there are size-effects in the test results. Grouping the material together for the same type of soil, and the same container leads also to high correlation values with an exception for the large container as shown in Figure 27. Correlations for the medium and large container were only possible for the group category SE. For the other categories there were not enough data available for producing grouped correlations. It is clear that more test results are needed to produce type-specific correlations.

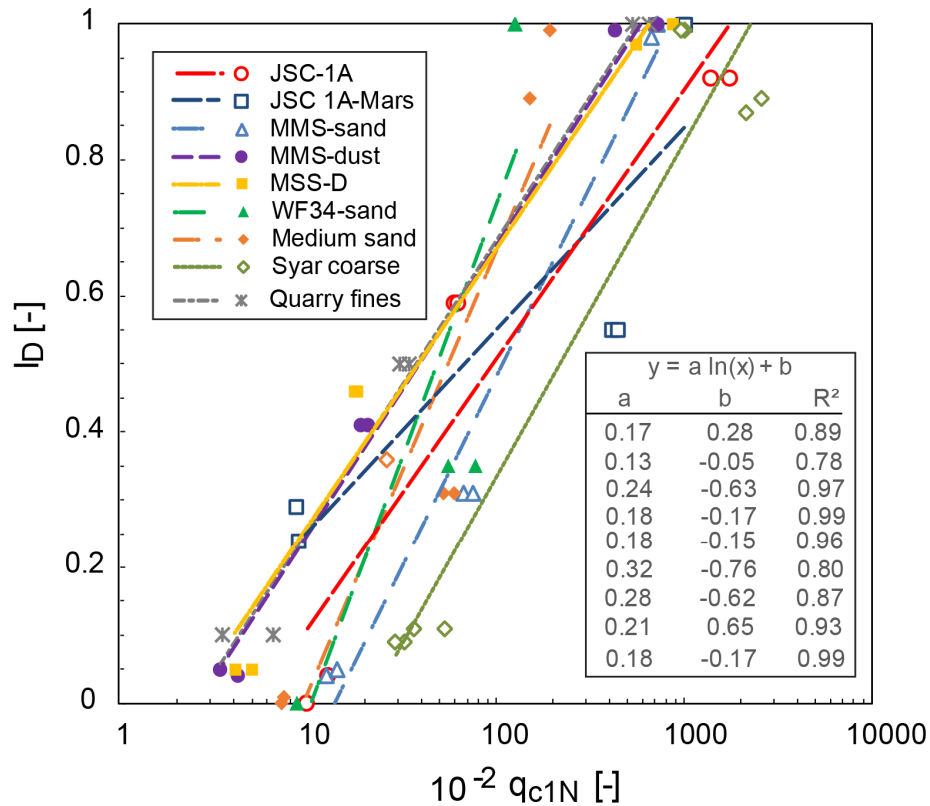


Figure 23:  $I_D$  vs  $10^{-2}q_{c1N}$  relationships for the small size container.

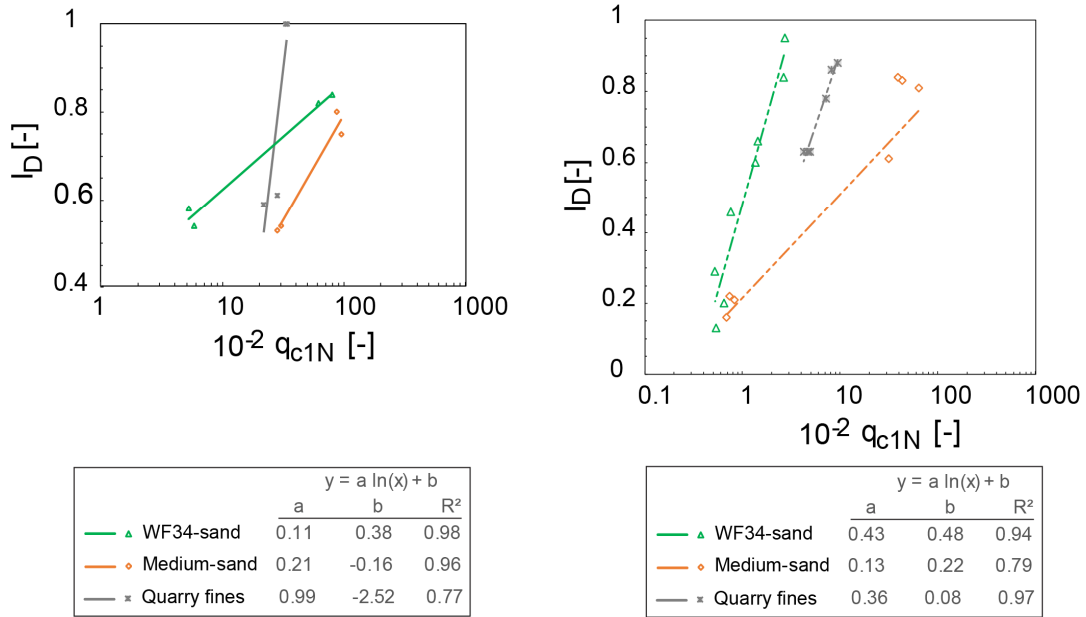


Figure 24:  $I_D$  vs  $10^{-2}q_{c1N}$  relationships for the medium (left) and large (right) container.

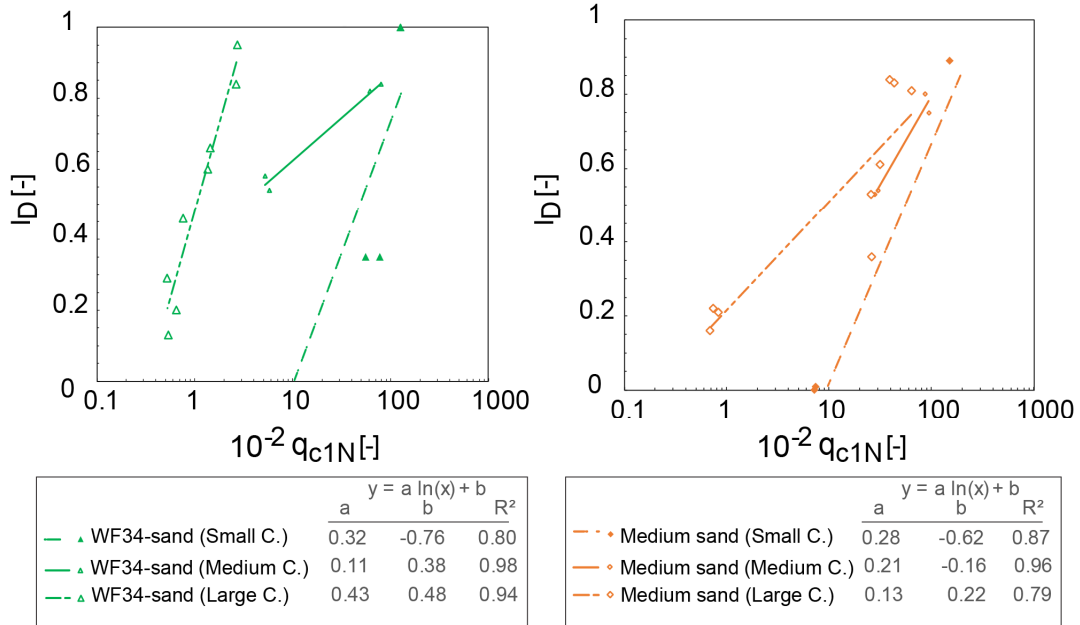
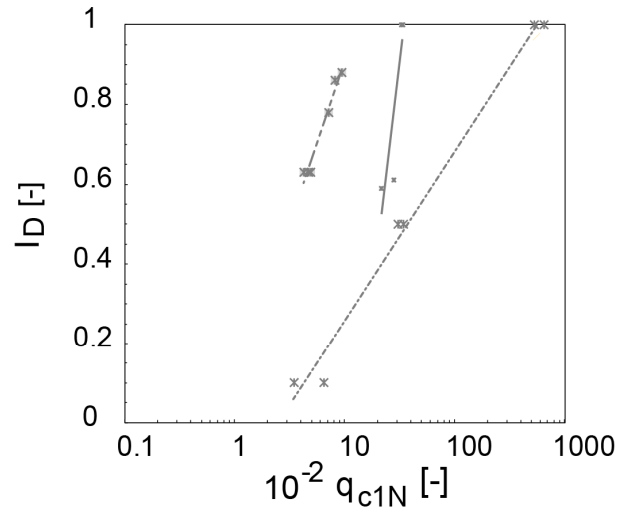
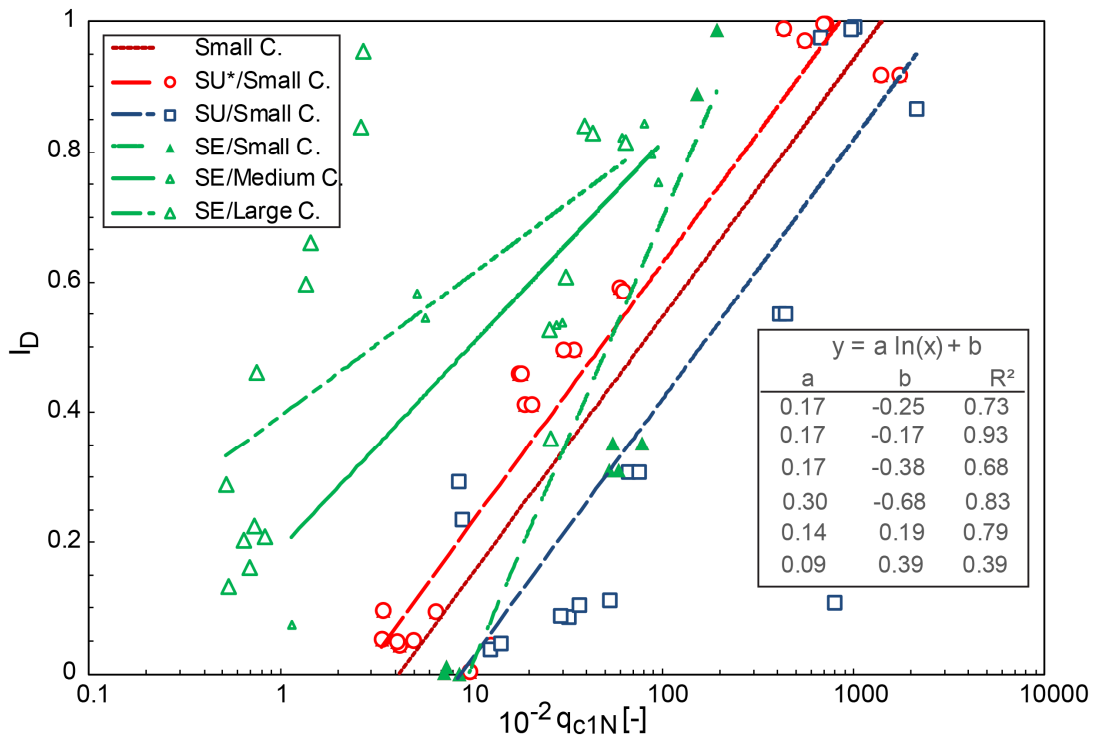


Figure 25:  $I_D$  vs  $10^{-2}q_{c1N}$  relationships for WF34 sand (left) and for medium sand (right).



	y = a ln(x) + b		
	a	b	R <sup>2</sup>
--- x Quarry fines (Small C.)	0.18	-0.17	0.99
— x Quarry fines (Medium C.)	0.99	-2.52	0.77
... x Quarry fines (Large C.)	0.36	0.08	0.97

Figure 26:  $I_D$  vs  $10^{-2}q_{c1N}$  relationships for Quarry fines.



	y = a ln(x) + b		
	a	b	R <sup>2</sup>
Small C.	0.17	-0.25	0.73
SU*/Small C.	0.17	-0.17	0.93
SU/Small C.	0.17	-0.38	0.68
SE/Small C.	0.30	-0.68	0.83
SE/Medium C.	0.14	0.19	0.79
SE/Large C.	0.09	0.39	0.39

Figure 27:  $I_D$  vs  $10^{-2}q_{c1N}$  relationships for all the soils grouped.



### 5.4.3 Correlations for the shear strength parameters

Various authors suggested correlations for estimating the effective friction angle  $\phi'$  when adopting the Mohr- Coulomb failure criterion. Kulhawy & Mayne (1990) provided the relationship in eq. (34) resulting from Calibration Chamber tests for FC% less than 30%. The relationship was later re-evaluated and validated with data from undisturbed sand samples collected by ground freezing technique from 17 sand sites. A re-evaluation of these data was carried out by Uzielli et al. (2013) and resulted in the following eq. (35).

$$\phi' = 17.6 + 11 \cdot \log(q_{c1N}) \quad (34)$$

$$\phi' = 25 + (q_{c1N})^{0.10} \quad (35)$$

Utilizing the equations from Figure 23 an attempt to produce correlation between  $10^{-2} q_{c1N}$  and  $\phi'$  was carried out which resulted in a correlation value of  $R^2=0.8$ . The correlation is shown in the following Figure 28. The results of friction angle values at specific  $I_D$  values from the triaxial tests were used to calculate the corresponding  $10^{-2} q_{c1N}$  values utilizing the individual equations of each soil. The resulted correlation has similar inclination with those suggested by eq. (34) and eq. (35). Although the available data are limited, an attempted correlation to the cohesion value  $c$  was carried out which resulted in a correlation value of  $R^2=0.49$ . The same procedure was followed as for the friction angle but this time the resulted correlation of the small container as shown in Figure 27 was utilized to calculate the corresponding  $10^{-2} q_{c1N}$  values. The resulted calibration is plotted in Figure 29.

The derived correlations were utilized with the test results from the soundings of the field investigation in Etna cf. Figure 13, at approximate depth of 0.3 m. The estimation of  $q_{c1N}$  was based on the standard normalization procedure with  $p_a$  as a reference pressure and the  $\gamma_d$  was calculated based on eq. (33). The resulted combinations of  $\phi'$  and  $c$  for the sounding 1 to 4 are  $14.26^\circ/39.85$ ,  $14.08^\circ/40.08$  kPa,  $19.23^\circ/33.56$  kPa,  $12.80^\circ/41.69$  kPa respectively. These results compare well with the experimental values of the cohesion which is 34.5 kPa but underestimate the friction angle which is  $41.3^\circ$  as obtained in Chapter 4.3. Nevertheless, it should be noted here that further research is needed since the available correlations are based on a limited number of data and cannot be considered statistically robust.

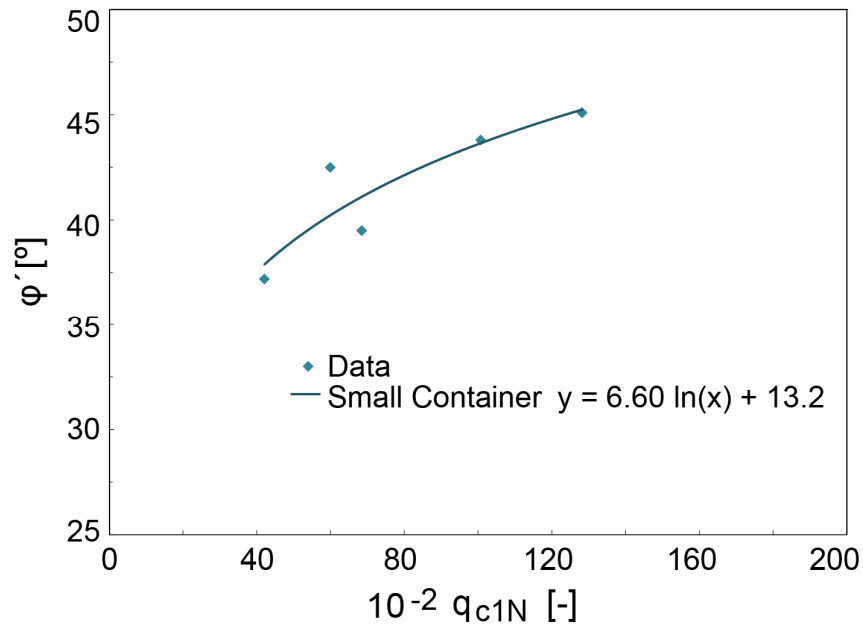


Figure 28: Correlation of  $10^{-2} q_{c1N}$  and  $\phi'$  from the tests in the small container

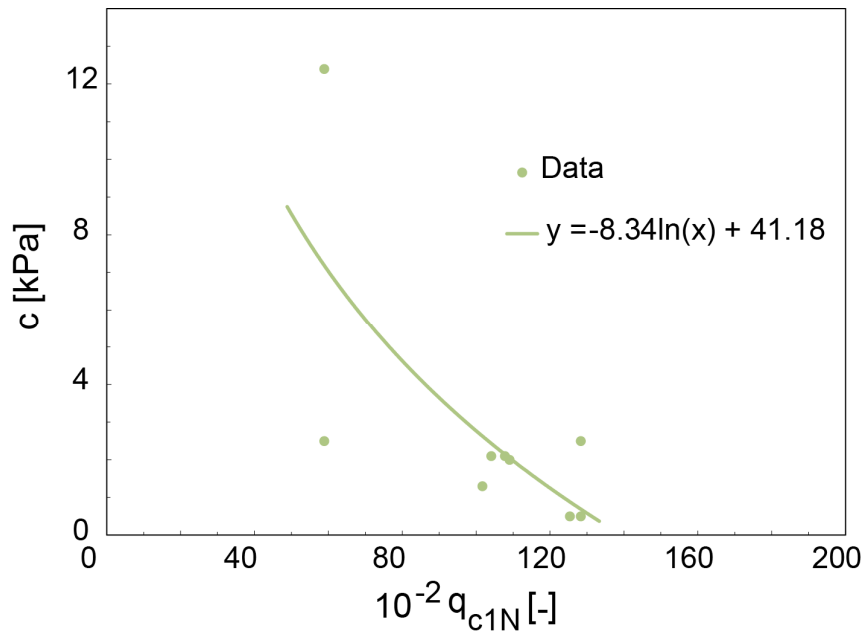


Figure 29: Correlation of  $10^{-2} q_{c1N}$  and  $c$  from the tests in the small container.

#### 5.4.4 Boundary effects

The size of the container can also affect the experimental data especially when it is not large enough. The effect depends on the ratio of the container size to that of the penetrating cone and the imposed boundary conditions. An extensive study to quantify boundary effects was carried out for the calibration chamber tests used for CPT tests by various authors. These boundary effects are also relevant for the shallow small scale penetration tests performed in the context of this study. Although, the mechanism governing the penetration and the subsequent required correction factor differs. In a usual calibration chamber there are four possible boundary conditions: BC-1: Constant stress, BC-2: zero change in strain, BC-3: Constant vertical stress and zero change in horizontal direction, BC-4: Zero change in strain in Vertical Direction and Constant Horizontal Stress. Boundary Conditions BC-1 and BC-2 corresponds to field conditions. The current shallow penetration tests were carried out in a container with fixed walls as described before, therefore they are similar to BC-2. The effect of the chamber boundary needs to be carefully considered when correlating penetration test data to relative density. The values of  $q_c$  obtained in flexible wall chambers with BC-1 and BC-4 are smaller than the corresponsive free field values. This is because the yielding at the boundaries allows a reduction in confining pressure in comparison with those prevailing in the free field conditions (Salgado et al., 1998). In the contrast, the  $q_c$  values obtained from BC-2 and BC-3 are higher than those of BC-1 and BC-4. According to Salgado et al. (1998) in rigid wall chambers, the soil samples tend to be heterogeneous and are difficult to reproduce mostly as a result of sample preparation and consolidation process.

In Bolton & Gui (2003) it is stated that a diameter ratio of at least 40 is necessary to eliminate size boundary effects on dense samples in centrifuge tests on Fontainbleau sand while the influence zone could be from 5 to 10 diameters from the base of the container Jamiolkowski et al. (2003) suggested corrections of CPT only for densities above 34% for a ratio of the diameter of the container to the one of the penetrometer  $D_c / d_c$  equally to 22, conclusion from calibration chamber CPT data on Ticino and Hokksund sands. For ratios of  $D_c / d_c$  higher than 47, a correction is necessary only for  $I_D$  values higher than 50 %. The findings of Butlanska et al. (2010) using 3D discrete element analysis are compatible with the mentioned deductions, as they didn't find any boundary effects for soils of densities lower than 45 %. Kullhawy &

Mayne (1990) proposed eq. (36) for deriving the corrected value of  $q_{c,corrected}$ . From this eq. (36) it can be concluded that for a ratio  $D_c / d_c$  of 70 or more there is no need for a correction on the value of  $q_c$ .

$$q_{c,corrected} = C_F \cdot q_{c,measured} \tag{36}$$

$$C_F = \left( \frac{D_c / d_c - 1}{70} \right)^{\frac{I_D(\%)}{200}}$$

The eq. (36) resulted from Calibration Chamber tests with boundary conditions BC-1 and BC-3. For increasing relative density, the correction factor should be decreasing for the boundary condition BC-3 and increasing for the BC-1 one. Therefore, separate correction factors should be developed for each type of boundary conditions. For this reason, new correction factors are required for the shallow penetration tests performed in the context of this study.

For the shallow penetration tests the correction factor  $C_F$  is lower than 1 meaning that the measured values are higher than the corresponding free field values. The  $C_F$  is proportional to the ratio  $D_c/d_c$ , meaning that the effect is diminishing for larger containers, and reverse proportional to the relative density, meaning that the denser the soil the more profound the boundary effect. For beginning, the  $C_F$  -trends from small to large container were calculated. The ratio  $D_c/d_c$  at which the boundary effects are no longer present was calculated based on those trends, assuming a linear relationship between  $C_F$  and  $D_c/d_c$ . The large container was taken as a reference container for the purposes of this procedure. The data that corresponded to  $D_c/d_c$  ratios lower than 29 (the ratio from the large container) were included in the analysis.

Unfortunately, after refinement there are not enough data to statistically quantify the boundary effect on all the soils. Nevertheless, an attempt was carried out for the material medium sand and WF34-Sand. From the correlations for the small and medium container it is found that only the correlations for the WF34-Sand comply with the expected relationship between  $C_F$  value and  $I_D$ . Even though that both material fall in the category SE, they exhibit different behavior during the experiments. One reason may be the  $d_{50}$  value. The medium sand has a considerable higher  $d_{50}$  value, considering the size of the small penetrometer. Probably grain crushing affects

strongly the behavior of the soil in this case. Quantification of the grain crushing is not possible with the available data. From the correlation  $C_F$  vs  $D_c/d_c$  for  $I_D$  values 0.4 and 0.5, both soils follow the expected trends for the relationship of  $C_F$  vs  $D_c/d_c$ . Only the correlation for the WF34-sand corresponding to an  $I_D$  of 0.4 has a different inclination from the rest. The reason couldn't be identified.

## 5.5 Discussion

Cross correlation of the results of the different tests to identify trends and dependencies of individual parameters was carried for each group type. The factor of compaction potential  $I_F$  is directly proportional to the required force for penetration. This is simply explained because the highest the compaction capability of the soil the highest the penetration force. The same holds for the difference  $e_{max} - e_{min}$  which essentially represents the same characteristic. Generally, it is observed that the higher the grain density the higher the penetration force. This is because the grain is stronger and a higher force is needed to break through the soil. The same holds for the minimum and maximum density. The shear strength is proportional to the force as both are related to the strength of the soil. The highest the shear angle the highest the force. The constrained modulus  $E_s$  and compression index  $C_c$  values are stress dependent and are increasing with an increase in the stress and therefore an increase in the penetration resistance.

The extraterrestrial soils exhibit in general different values than typical soil values for various geotechnical parameters. For this reason, a direct use of empirical correlations developed for terrestrial soils is not applicable. New set of correlations and testing methodologies have to be developed specifically for extraterrestrial and special soils. Developing soil-specific correlations for each type of soil is important to set a good groundwork of experience to build on in the subsequent years. Learning from the previous followed procedures for the standard terrestrial soils is important to recognize problematic areas and to find a way to overcome current drawbacks and difficulties. Procedures should be standardized in order to enable collaboration across the globe. Results should be reported on specific formats. Gathering all the knowledge to a public accessible database is important for quick improvement of current procedures and methodologies.

## 6 Stationary tests on non-pneumatic wheel

### 6.1 Introduction

Knowledge of the wheel-soil interaction is necessary to optimize the navigability in both terrestrial and extraterrestrial environments. Small autonomous and unmanned ground vehicles are becoming very important for the exploration of planets. The interaction between the wheels of the vehicle and the soil is a major challenge in modern terramechanics. A reliable design of the wheels of a vehicle should ensure that the vehicles won't stuck due to limited propulsion force or due to terrain irregularities.

Pressure vs sinkage behaviours of different soils were investigated with a custom made wheel device. A crosshead that can be moved in the vertical direction with the aid of two steel columns is used to move the wheel. Internal transducer is used to control the transverse. The testing machine has loading capabilities from 0.0005 mm/min to 2000 mm/min with a maximum load of 10 kN. Soil was placed in a container that has a rectangular shape with a length of 72.3 cm, width of 31.5 cm, height of 16 cm and 2 cm thickness. Figure 30 shows the experimental set up.

The wheel is pressed into the soil at a constant speed: A displacement sensor is mounted in the centre of the tire to record the displacement of the wheel when penetrating into the soil. The required force is also recorded. Additionally, the vertical deformation of the wheel is also recorded in order to calculate the actual penetration into the soil. The raw data are recorded as a function of time. Tests were carried out to two different materials, "Rotliegendes" and "Quarry fines", in various humidity states to quantify the influence of the water content, degree of compaction and consistency. Additionally, experiments with a steel plate as supporting medium, were carried out in order to assess the stiffness of the wheel. These tests were used to quantify the behaviour of the wheel e.g. how it deforms under specific loading conditions.

Tests were carried out in 3 different locations within the box. The second point is a control point of the first test series. The third point is chosen approximately in the middle of the first two points in order to investigate the

influence of pre-compaction to the sinking of the wheel. For assessment of multipass, the loading at each point was carried out in consecutive cycles. For the first and third point, five loading cycles were carried out. For the second control point only two loading cycles were applied. The test set up with the location points is depicted in Figure 30.



Figure 30: Test set up with distinct location points

## 6.2 Soil material tested

Basic soil properties of the two tested material are summarized in the following Table 8 and the grain size distribution is depicted in Figure 31. For each material grain size distribution was carried out according to DIN 18123 and the type of the material was determined by DIN 18196 and DIN 4022. The grain density was determined in accordance with DIN 18124. The Atterberg limits were calculated according to DIN EN ISO 17892-12. Rotliegendes is classified as middle plastic with  $35\% < w_L \leq 50\%$  and Quarry fines is classified as light plastic soil with  $w_L \leq 35\%$ . The plasticity index  $I_P$  equals  $w_L - w_P$  and is also given in Table 8 for convenience. It should be noted that most of the characteristics of Quarry fines have been already given in Chapter 5. Nevertheless, they are also provided in this chapter for reference and are complemented by further relevant information.

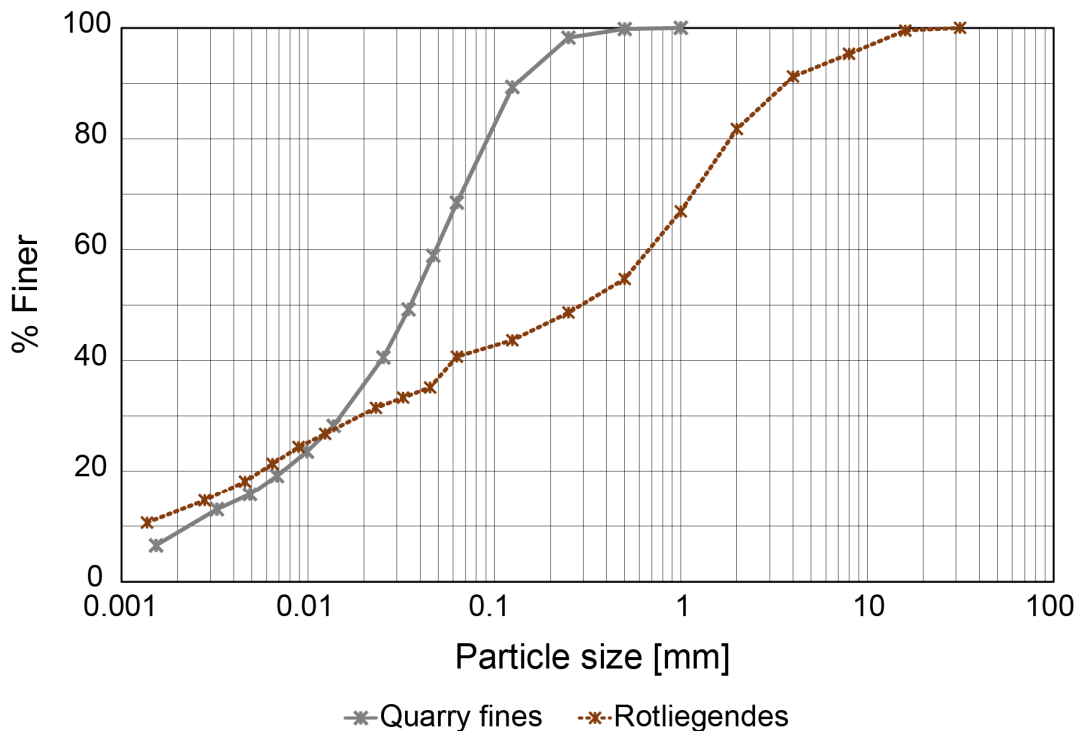


Figure 31: Grain size distributions of the tested materials for the wheel tests.



Table 8: Characteristics of the tested material

Property	Rotliegendes	Quarry fines
$d_{50}$ [mm]	0.300	0.036
$C_U / C_C$ [-]	700/0.57	29.7/2.5
Clay/ Silt/ Sand/Gravel [%]	12.7/27.5/ 41.3/18.5	11.30/57.0/31.7/0.00
Soil Type [-]	SU*	SU*
$\rho_s / \rho_{pr}$ [Mg/m <sup>3</sup> ]	2.74/1.93	2.74/1.78
$w_L / w_P$ [%]	36.8/20.6	25.3/21.6
$I_P$ [%]	16.2	3.7

### 6.3 Non pneumatic wheel

The tests were carried out with a Tweel<sup>®</sup> which is a combination of a tire and a wheel developed by Michelin for off-road applications (Michelin Tweel<sup>®</sup>, 2019). The Tweel<sup>®</sup> is made from deformable plastic spokes without any air pressure. The suspension is controlled by the deformable spokes. The wheel has a diameter of 66 cm and a width of 22.5 cm. The wheel was borrowed from Marum within the frame of the ROBEX alliance project.



Figure 32: Side view and front view of the Tweel<sup>®</sup> on the testing set up.

## 6.4 Direct shear tests

### 6.4.1 Shear tests for wheel-soil interface properties

Direct shear tests were carried out in accordance with the specifications of DIN 18137-3:2002-09 to assess the interface properties of the interaction between soil and the wheel. A flat tire section was fabricated in order to quantify the friction angle and adhesion between the wheel and soil for subsequent use in the equations governing the mechanism of soil-wheel interaction. The followed procedure is illustrated in Figure 33. Firstly, a section of the negative profile of the wheel was produced as shown in Figure 33 (a) and (b). The hardness of the material of the wheel was tested using a simple portable Shore A device as shown in (c). Then the appropriate material, which corresponded to the same hardness as the wheel material, was used to create the positive profile of the wheel as shown in (d).

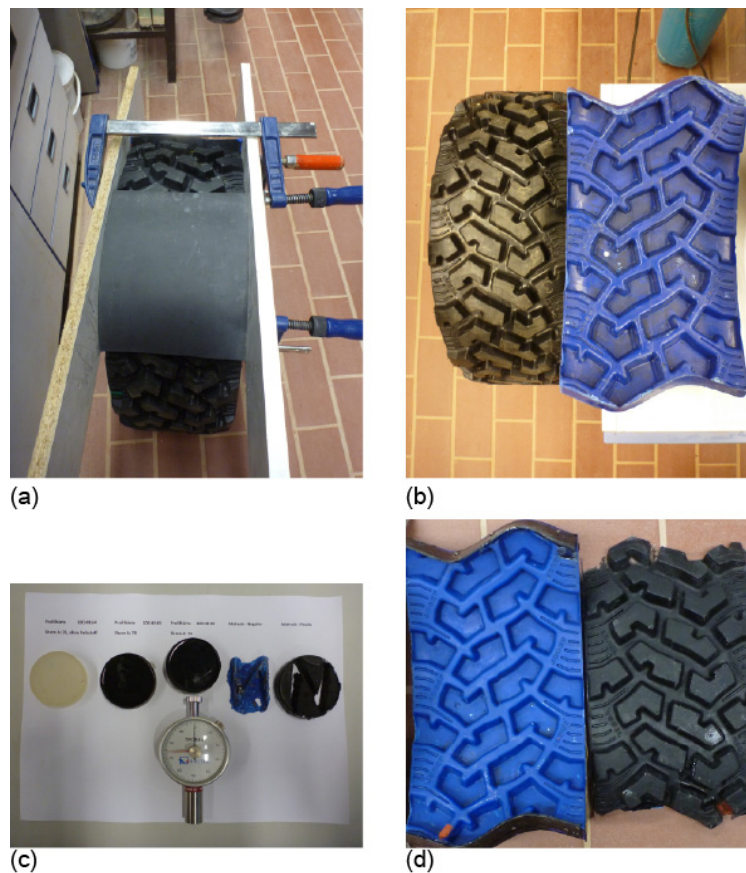


Figure 33: Illustration of the manufacturing of the flat tire section.

Shear strength tests with the flat tire section were carried out on the material used in the wheel tests namely Rotliegendes and Quarry fines, and further to the collected material from the field investigation at site 3 on the Mount Etna (see Chapter 4). The tests were carried out in a large direct shearing frame with dimensions 30 x 30 cm with a 15 mm shearing gap. The grain size distribution of the materials are depicted in the previous Figure 10 and Figure 31. Low values of the normal stress  $\sigma_v = 10-30$  kPa were selected in order to reproduce the low in-situ near surface overburden stress for the material in Etna and in general for near surface soil. Rotliegendes and Quarry fines were tested with normal stress  $\sigma_v = 20-80$  kPa. The loading rate of horizontal shearing was set equal to 1 mm/min. The test results in terms of shear stress vs. normal stress are plotted in Figure 35-Figure 37 and the test results in terms of shear stress vs. shear deformation are included in Figure B - 1 to Figure B-3 in the Appendix B. The interface friction angle and cohesion “at peak”  $\phi_{int}$  and  $c_{int}$  and “residual”  $\phi_{int,r}$  and  $c_{int,r}$  respectively, are obtained and summarized in Table 9 for the various conditions tested.

Generally, it is observed that the shear strength parameters are decreasing with increasing water content due to the decreased consistency of soils when water is present. It is important to report the consistency of the tested material and the strength levels as from the results it is obvious that the obtained parameters differ. Water content can suddenly change in real time applications due to environmental impact. The results obtained in this section are important for subsequent use in terramechanical applications, especially regarding the accurate simulation of the contact behavior between soil-tire.

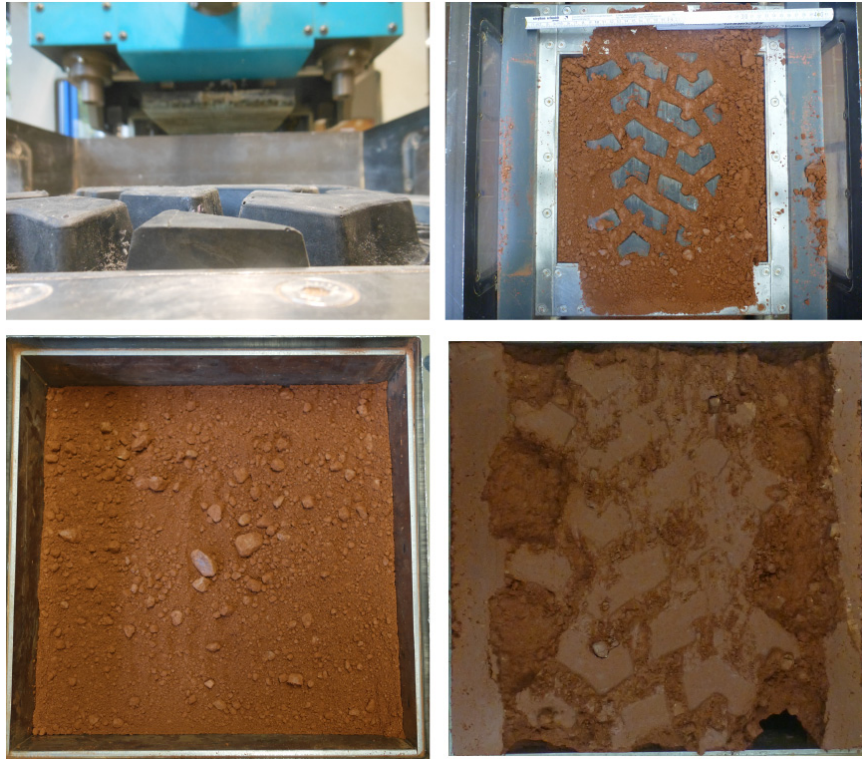


Figure 34: Direct shear tests on the custom made flat tire section of a Tweel<sup>®</sup>

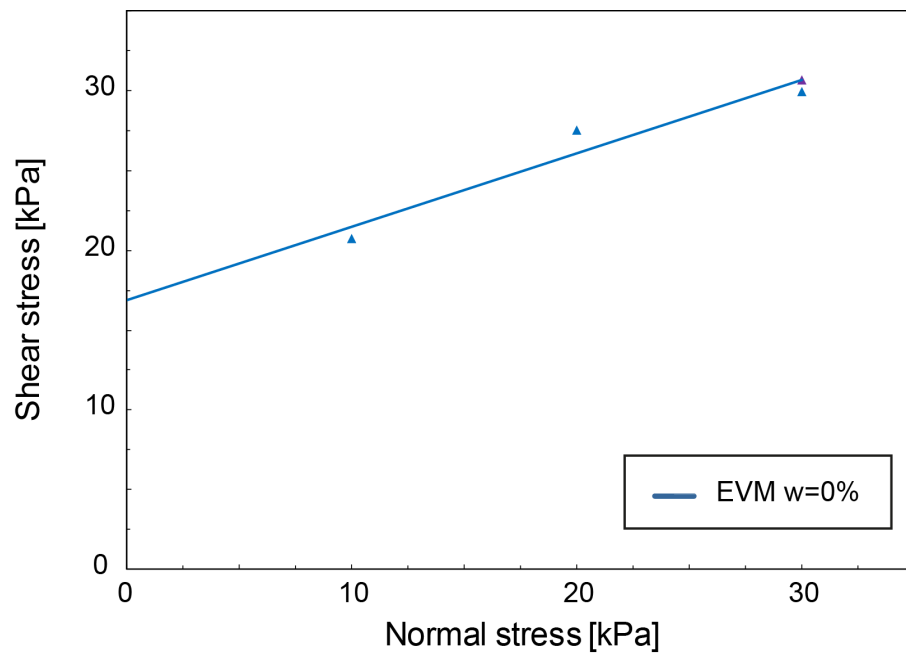


Figure 35: Results from direct shear tests on dry Etna volcanic material over an embedded flat tire section.

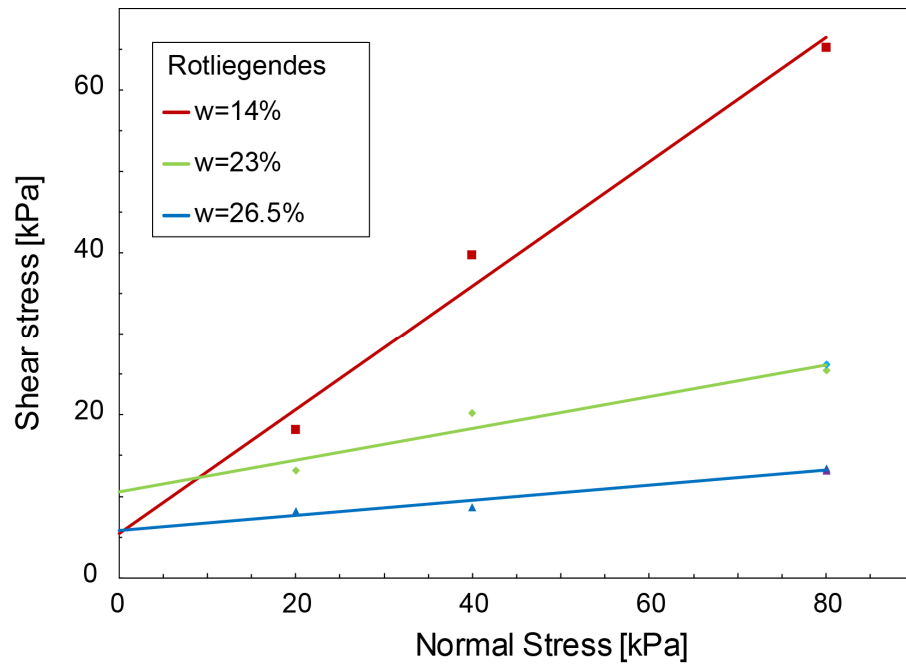


Figure 36: Results from direct shear tests on Rotliegendes over an embedded flat tire section at three values of water content.

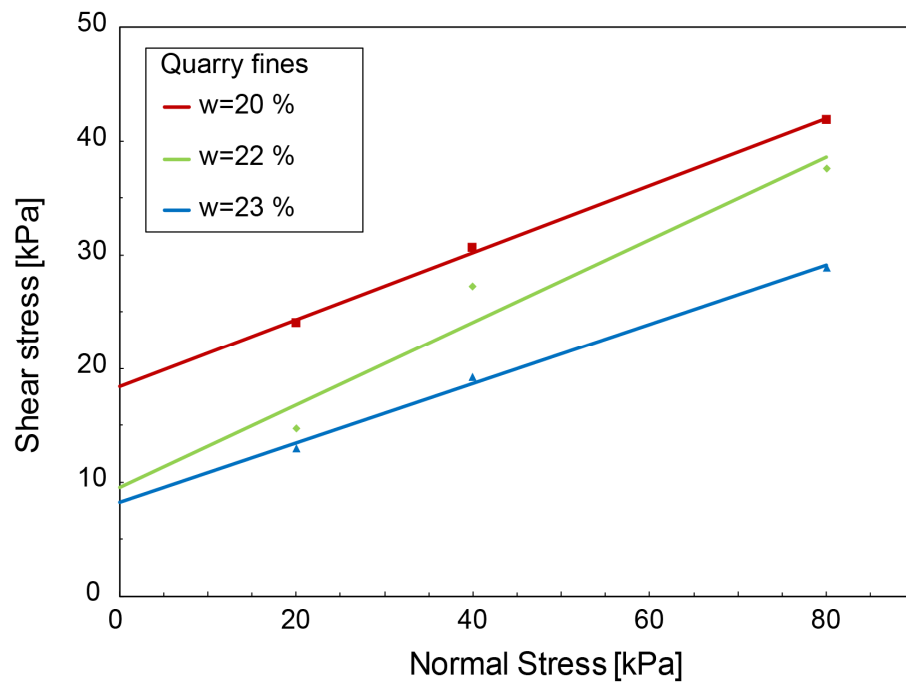


Figure 37: Results from direct shear tests on Quarry fines over an embedded flat tire section at three values of water content.

Table 9: Shear strength parameters from the direct shear tests on soils over an embedded flat tire section

Material	$w$ [%]	$\rho_d$ [Mg/m <sup>3</sup> ]	$\varphi_{int}$ [°]	$c_{int}$ [kPa]	$\varphi_{int,r}$ [°]	$c_{int,r}$ [kPa]
Etna Material 0-16 mm	0.0	1.173	24.7	16.9	18.9	6.9
Rotliegendes	14.0	1.929	37.3	5.5	23.0	0
	23.0	1.650	11.1	10.5	11.9	9.4
	26.5	1.525	5.3	5.8	4.4	6.2
Quarry fines	20.0	1.670	16.4	18.4	17.4	15.3
	22.0	1.670	20.0	9.6	22.1	5.8
	23.0	1.630	14.6	8.2	15.4	4.3

#### 6.4.2 Shear tests of soil

In this chapter, shear tests were carried out in the direct shear box, containing only the soil without the flat tire section. It should be noted here that the results from the Etna volcanic material were presented in Chapter 4.3. The purpose of these tests is to quantify the frictional angle and cohesion of the tested soils.

Rotliegendes and Quarry fines were tested with normal stress  $\sigma_v = 15-60$  kPa. The rate of horizontal shearing was set equal to 1 mm/min. The test results in terms of shear stress vs. normal stress are plotted in the following Figure 39 to Figure 40 and the results in terms of shear stress vs. shear deformation are included in the Figure B-4 and Figure B-5 in Appendix B. Adopting a Mohr-Coulomb failure criterion the friction angle and cohesion “at peak”  $\varphi$  and  $c$  and “residual”  $\varphi_r$  and  $c_r$  are obtained as summarized in Table 10. This table includes also the values from the results from Etna’s material.

The general observations gained from the tests with the flat tire section, are also valid here: the shear strength parameters are decreasing with increasing water content and therefore the consistency of the tested material should be always stated. Comparing the results of Table 10 to those of Table 9, it is inferred that the shear strength parameters in the interface of the wheel-soil are lower than the ones for soil-soil interactions. The results obtained in this section are significant for subsequent use in terramechanical applications, especially regarding the accurate simulation of the soil and its failure in shear.

Table 10: Shear strength parameters from direct shear tests

Material	$w$ [%]	$\rho_d$ [Mg/m <sup>3</sup> ]	$\varphi$ [°]	$c$ [kPa]	$\varphi_r$ [°]	$c_r$ [kPa]
Etna Material 0-16 mm	0.0	1.173	41.3	34.5	49.6	14.0
Rotliegendes	14.0	1.929	54.1	86.6	42.9	48.1
	23.0	1.650	41.6	32.1	32.4	33.6
	26.5	1.525	22.5	37.6	17.6	33.7
Quarry fines	20.0	1.670	49.9	54.6	52.5	40.2
	22.0	1.638	31.8	36.6	27.2	32.2
	23.0	1.638	24.9	26.6	29.4	15.7

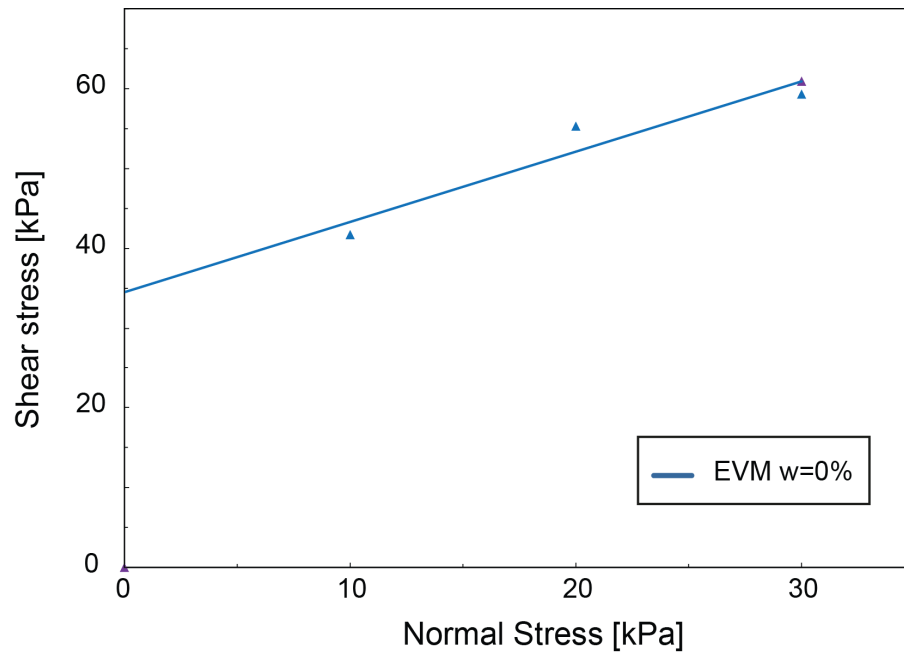


Figure 38. Results from direct shear tests on dry Etna volcanic material.

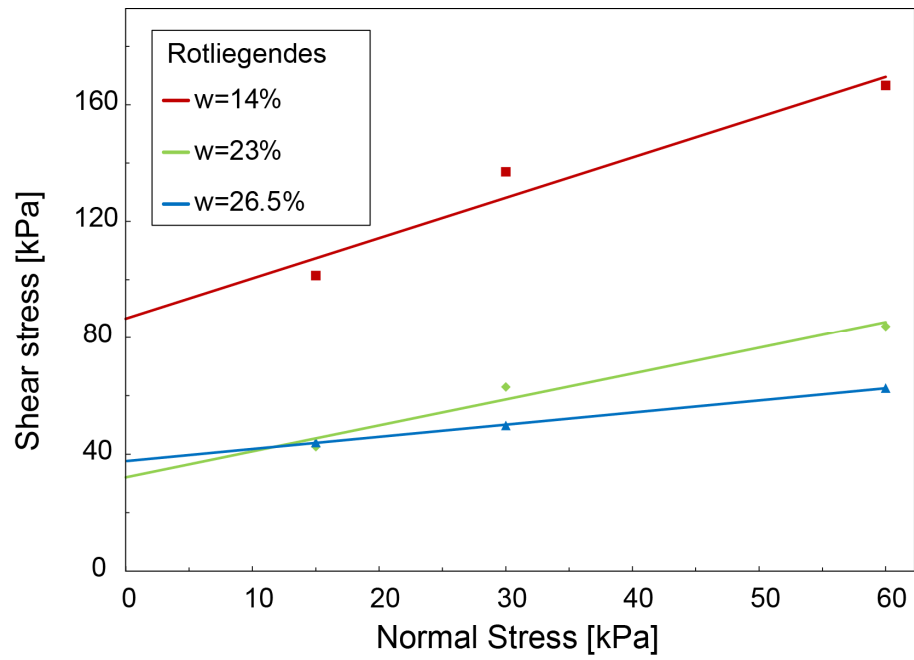


Figure 39: Results from direct shear tests on Rotliegende at three values of water content.

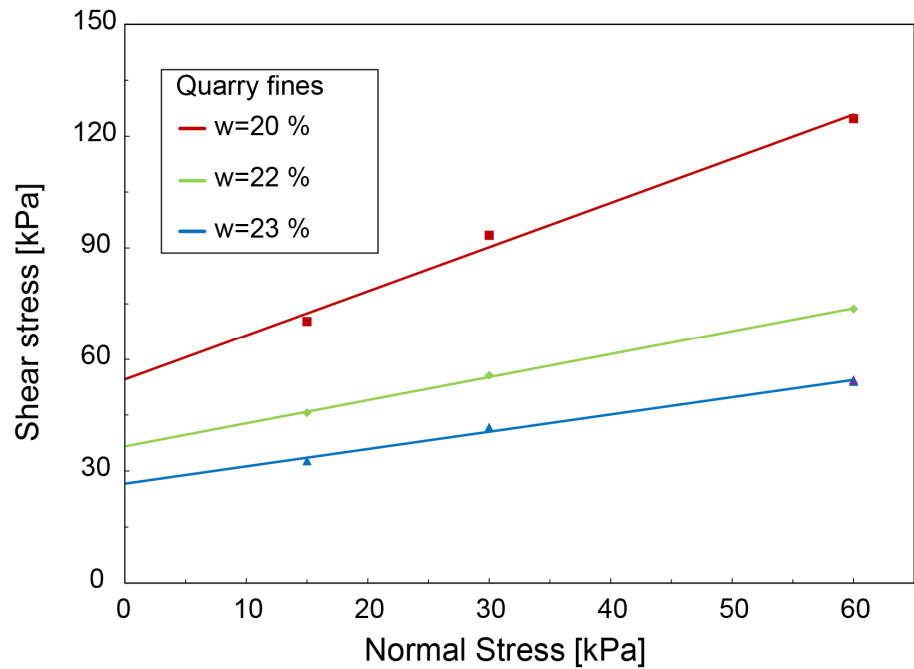


Figure 40 Results from direct shear tests on Quarry fines at three values of water content.



## 6.5 Experimental procedure for the wheel tests

The load speed was set to 1mm/min (position controlled). The Tweel® was moved vertically up to a maximum of 20 mm. The position was hold for 120 seconds. Then the wheel was retracted until the force was zero (force controlled). The distance between the first and second measurement point was 21.5 cm. The third point is positioned 10.5 cm away from the second point, 11 cm from the first one (approximately in the middle of the two measurement points). The test set up is depicted in Figure 30. For point one and three the procedure was repeated 5 times. For the second point the procedure was repeat two times. The raw data consist of time, vertical deformation of the wheel, vertical displacement and force. The timings used for the measurement of the force and the displacement differ from the measuring time for the deformation of the wheel. This leads to phase shifts problems and the subsequent analysis of the data is demanding.

The samples were built in the container in two layers with 85% proctor density. The  $\rho_{pr,85\%}$  for Rotliegendes is 1.64Mg/m<sup>3</sup>. and for Quarry fines is 1.51 Mg/m<sup>3</sup>. They were compacted to a height of 9 cm. The sample was covered over night with a foil to minimize the loss of water due to exposure to the atmosphere. The liquid index  $I_L$  and the consistency index  $I_C$  of the soils are summarized in Table 11.

Table 11: Consistency values of the soil material in the wheel tests

Rotliegendes			Quarry fines		
$w$ [%]	$I_C$ [-]	$I_L$ [-]	$w$ [%]	$I_C$ [-]	$I_L$ [-]
32.21	0.28	0.72	23.01	0.62	0.38
25.5	0.70	0.30	22.15	0.85	0.15
13.69	1.43	-0.43	20.65	1.25	-0.25

## 6.6 Results

Firstly, the wheel's performance was evaluated and quantified with an experiment against a steel plate. The raw data force vs time and force vs displacement of the machine frame are depicted in Figure 41. Results from the wheel's deformation are depicted in the following Figure 42 to Figure 43. In Figure 42 the deformation of the wheel and the displacement of the frame of the machine are plotted vs time. The observed plateau is due to creep effects or/and phase shift of the measurement device.

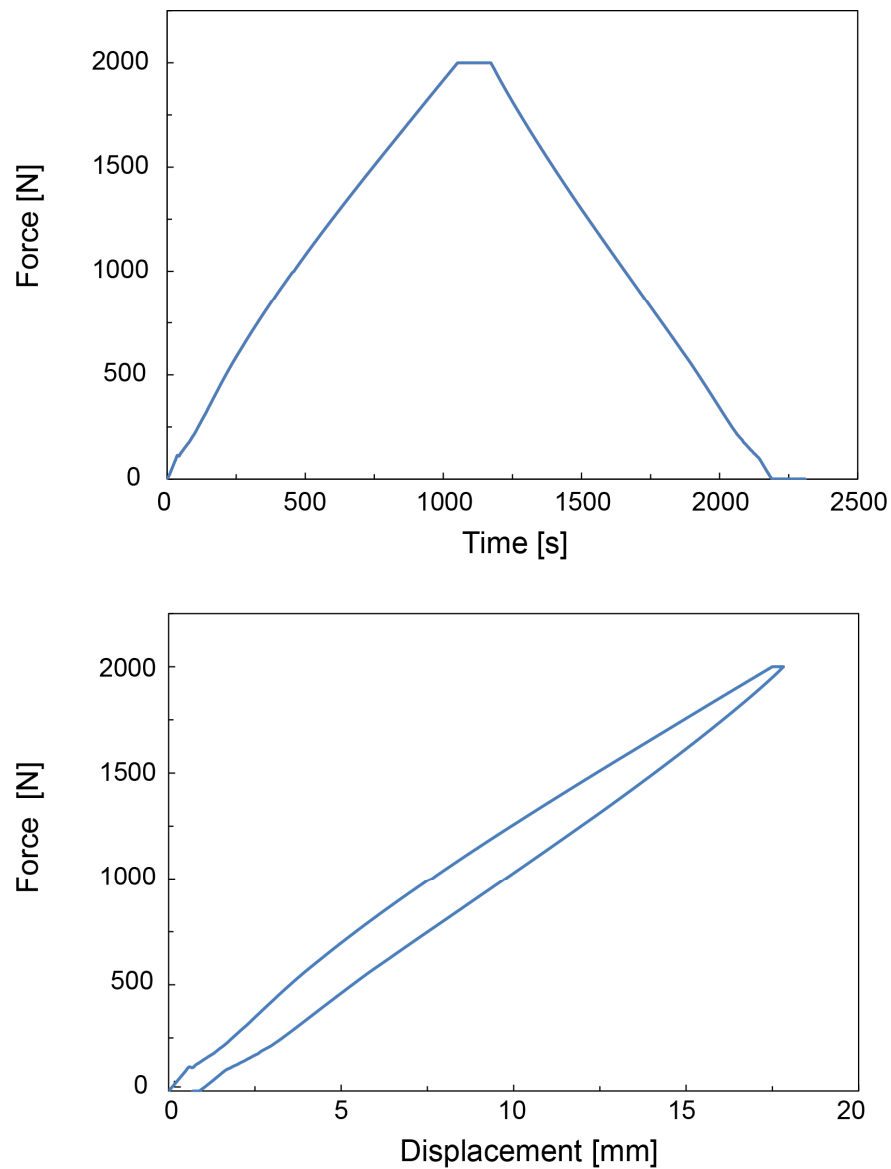


Figure 41: Force vs time and force vs displacement loading of the device.

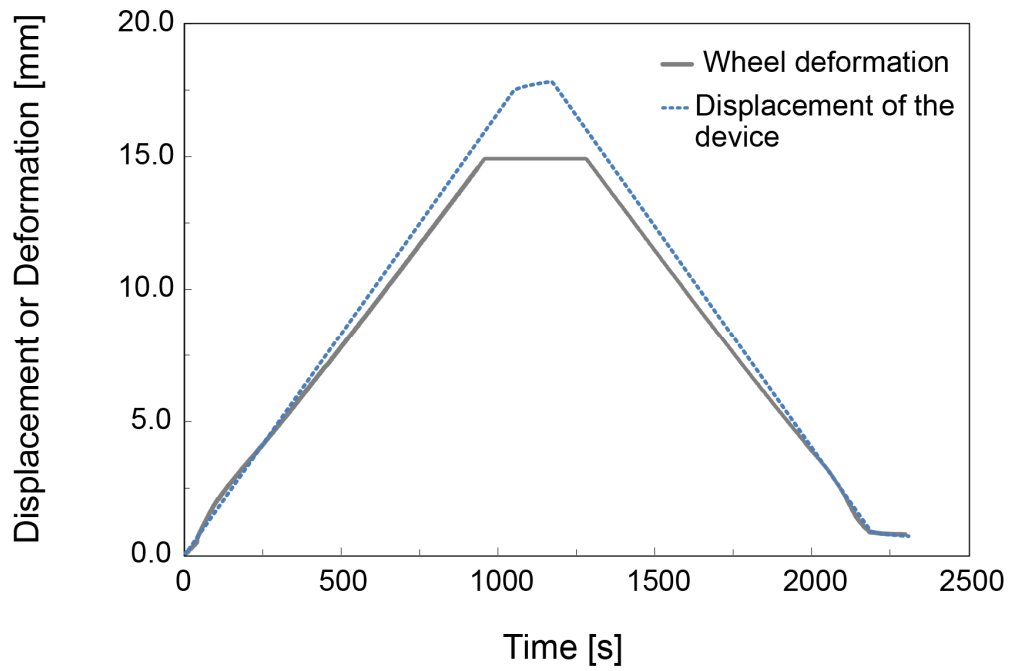


Figure 42: Deformation of the wheel and displacement of the frame vs time for the trial against steel material.

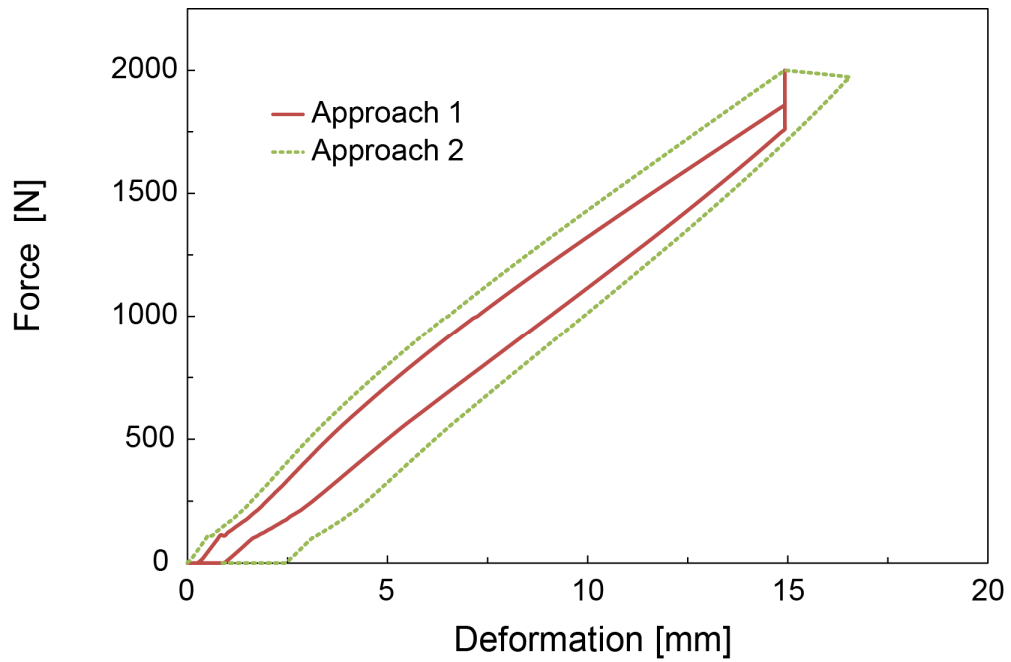


Figure 43: Force vs deformation of the wheel for the two attempts to remove bias in the timing differences of the data.

In Figure 43 the stiffness of the Tweel<sup>®</sup> is quantified from the experimental results with two different ways of data manipulation. In order to calculate the force vs wheel's displacement, the rate of deformation of the wheel vs time was calculated and it was subsequently used with the timing data of the machine in order to calculate the corresponding deformation of the wheel. This approach resulted to the deformation curve represented with solid line as shown in Figure 43. This approach contains the creep or/and time shift of the measurement devices. It was decided that another approach should be considered. Targeting the maximum deformation and the residual deformation of the wheel, the rate of deformation was adjusted and resulted to the curve represented with dotted line as shown in Figure 43. The curve number two was chosen as the representative for the wheel's stiffness for subsequent use in numerical simulations. The difference in the response during loading and unloading is a very important feature of the rubber material and it can be captured through various models.



Figure 44: Rotliegendes' footprint photographs.



Figure 45: Quarry fines' footprint photographs.

Some selected footprint results are displayed in Figure 44 and Figure 45. The results in Figure 44 left correspond to the water content  $w$  of 25.45%, the results on the right up correspond to the point #1 and #2 (see Figure 30) for water content 25.25% and to the right down to the point three for water content 32.21%. The results in Figure 45 left are from the tests with water content 20.65%, the results on the right correspond to water content 22.15%.

In Figure 46 to Figure 51 the force-displacement results for various water content at each location point for both material Rotliegendes and Quarry fines are depicted. From the figures it is inferred that even a slight water percentage change, is influencing considerably the results. Force is inversely proportional to the water percentage, meaning that the wheel will penetrate more in the soil for the same loading from a wheel/vehicle. Only some results from the data are graphically depicted here. For more information the reader is referred to the Figure C-1 to Figure C-6 in Appendix C.

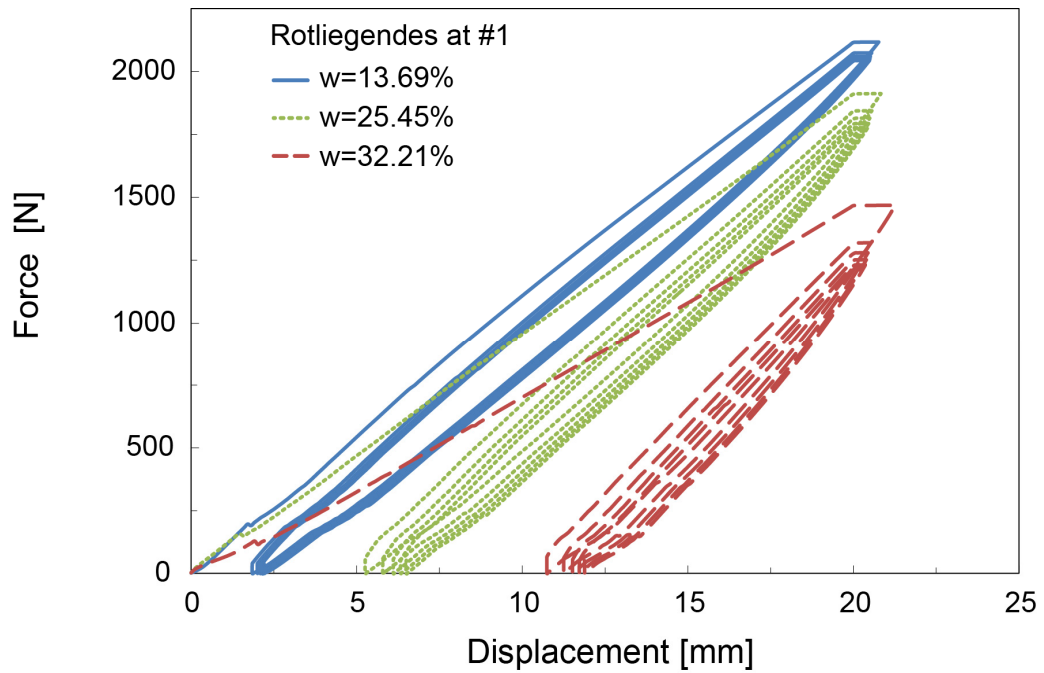


Figure 46: Results for Rotliegenden at the location point#1 at three at three values of water content.

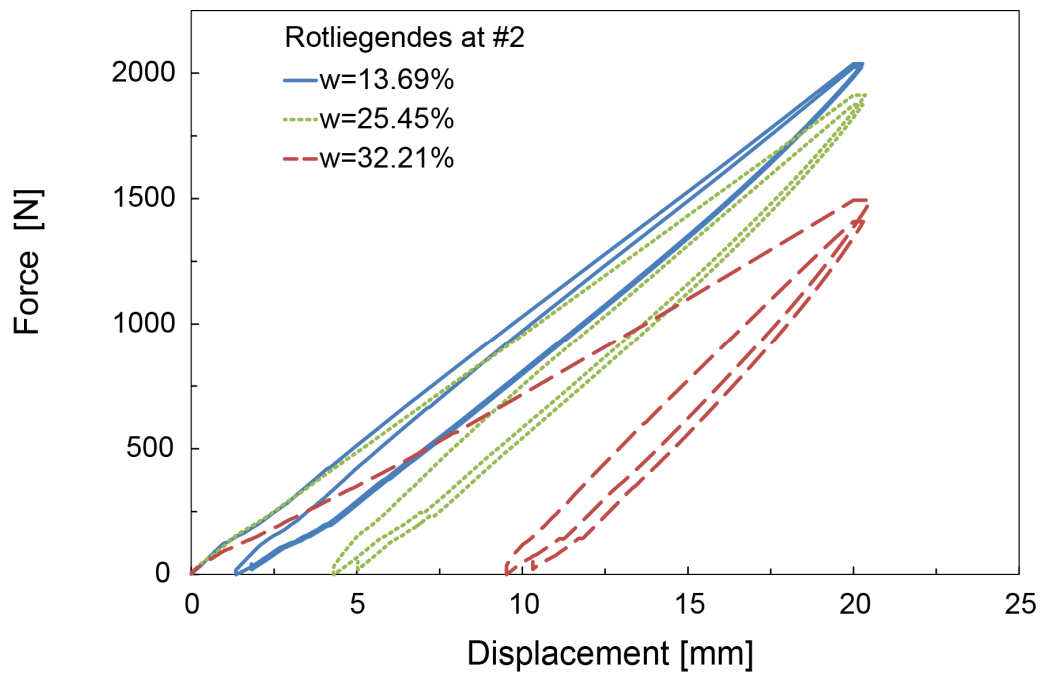


Figure 47: Results for Rotliegenden at the location point #2 at three values of water content.

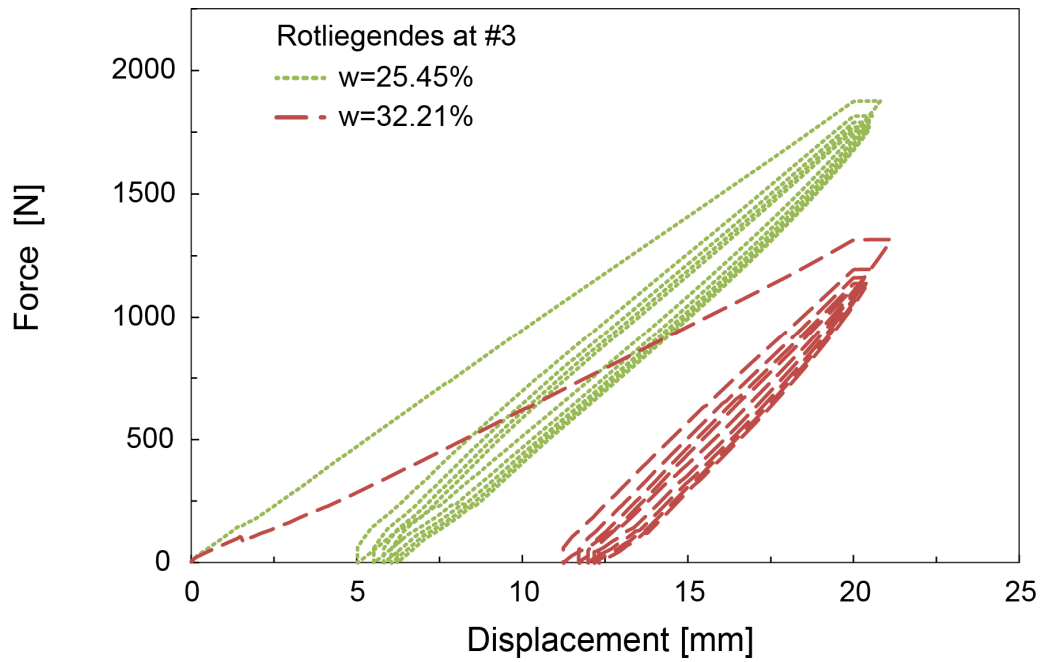


Figure 48: Results for Rotliegendes at the location point #3 at two values of water content.

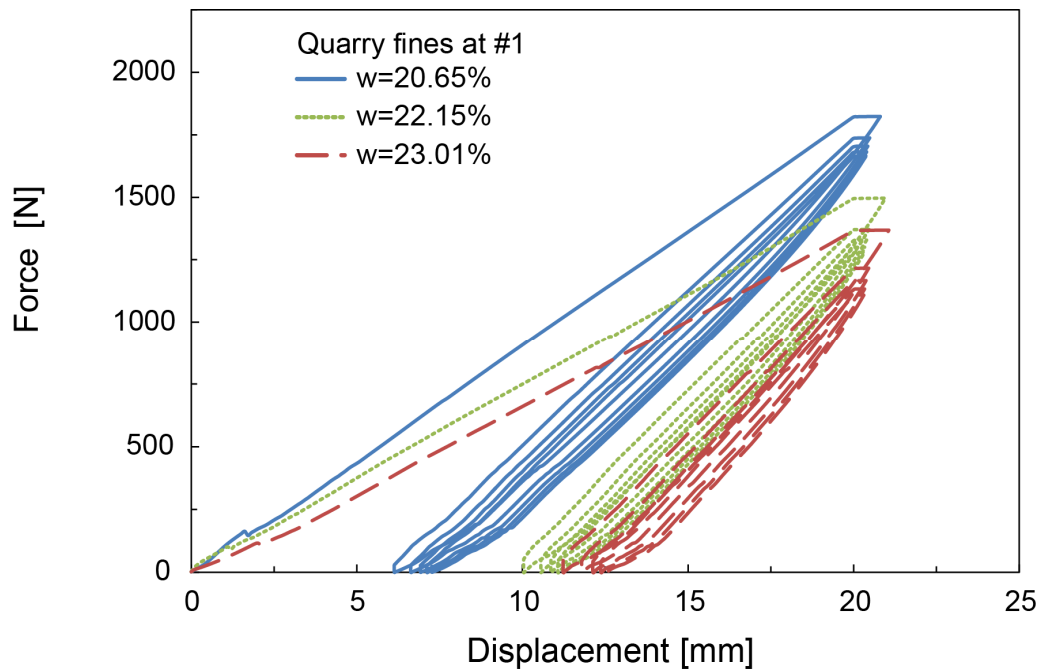


Figure 49: Results for Quarry fines a at the location point #1 at three values of water content.

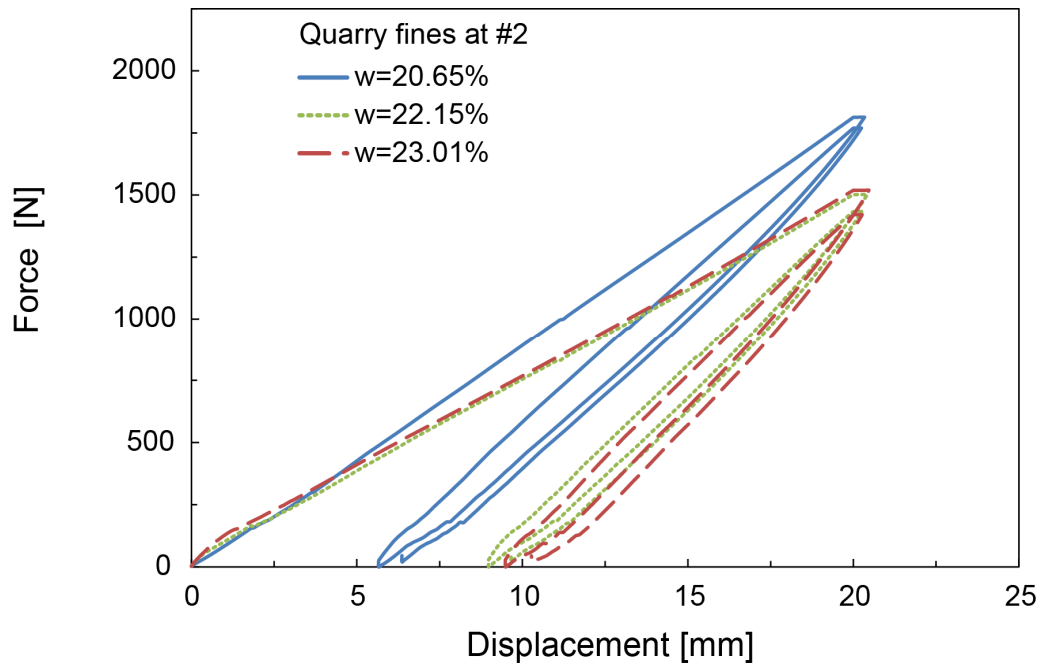


Figure 50: Results for Quarry fines at the location point #2 at three values of water content.

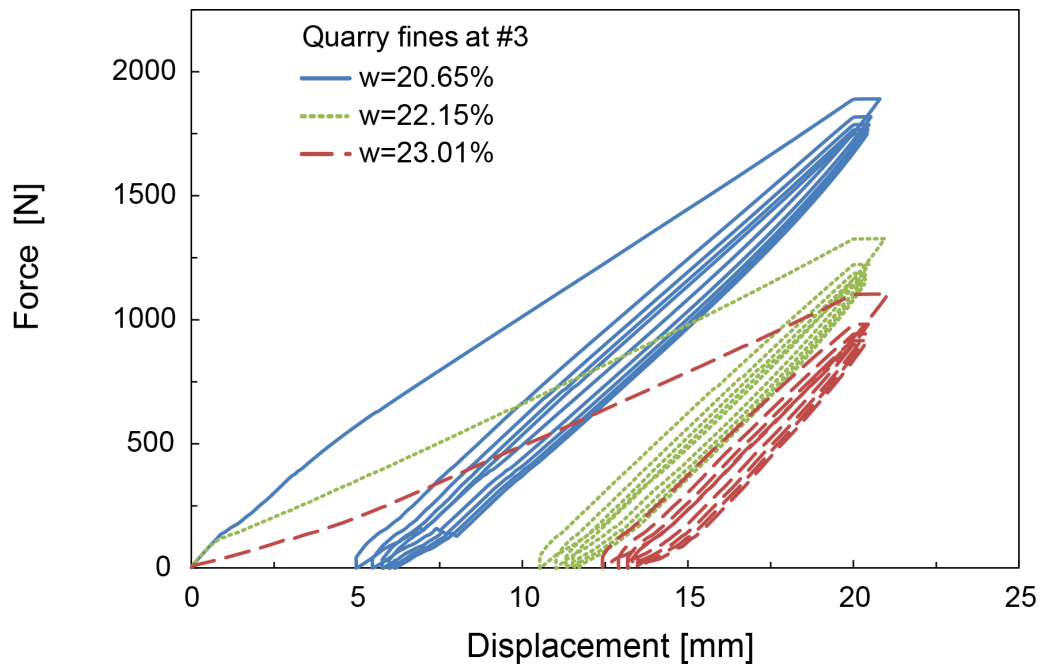


Figure 51: Results for Quarry fines at the location point #3 at three values of water content.



Table 12: Maximum force  $F_{max}$  and displacement  $d_{max}$  of each cycle for Rotliegenden

		Rotliegenden		
Location Point	Cycle number	13.69 %	25.5 %	32.21 %
#1	1	$d_{max} = 14.9 \text{ mm}$ $F_{max} = 2117 \text{ N}$	$d_{max} = 14.78 \text{ mm}$ $F_{max} = 1912 \text{ N}$	$d_{max} = 11.34 \text{ mm}$ $F_{max} = 1469 \text{ N}$
	2	$d_{max} = 14.9 \text{ mm}$ $F_{max} = 2074 \text{ N}$	$d_{max} = 14.78 \text{ mm}$ $F_{max} = 1844 \text{ N}$	$d_{max} = 10.16 \text{ mm}$ $F_{max} = 1319 \text{ N}$
	3	$d_{max} = 14.9 \text{ mm}$ $F_{max} = 2059 \text{ N}$	$d_{max} = 14.61 \text{ mm}$ $F_{max} = 1815 \text{ N}$	$d_{max} = 9.73 \text{ mm}$ $F_{max} = 1279 \text{ N}$
	4	$d_{max} = 14.9 \text{ mm}$ $F_{max} = 2051 \text{ N}$	$d_{max} = 14.44 \text{ mm}$ $F_{max} = 1793 \text{ N}$	$d_{max} = 9.61 \text{ mm}$ $F_{max} = 1252 \text{ N}$
	5	$d_{max} = 14.9 \text{ mm}$ $F_{max} = 2044 \text{ N}$	$d_{max} = 14.3 \text{ mm}$ $F_{max} = 1777 \text{ N}$	$d_{max} = 9.45 \text{ mm}$ $F_{max} = 1232 \text{ N}$
#2	1	$d_{max} = 14.46 \text{ mm}$ $F_{max} = 2038 \text{ N}$	$d_{max} = 14.31 \text{ mm}$ $F_{max} = 1913 \text{ N}$	$d_{max} = 11.3 \text{ mm}$ $F_{max} = 1409 \text{ N}$
	2	$d_{max} = 14.46 \text{ mm}$ $F_{max} = 2024 \text{ N}$	$d_{max} = 14.31 \text{ mm}$ $F_{max} = 1875 \text{ N}$	$d_{max} = 10.58 \text{ mm}$ $F_{max} = 1494 \text{ N}$
#3	1		$d_{max} = 14.24 \text{ mm}$ $F_{max} = 1877 \text{ N}$	$d_{max} = 10.48 \text{ mm}$ $F_{max} = 1315 \text{ N}$
	2		$d_{max} = 14.24 \text{ mm}$ $F_{max} = 1816 \text{ N}$	$d_{max} = 9.49 \text{ mm}$ $F_{max} = 1195 \text{ N}$
	3		$d_{max} = 14.24 \text{ mm}$ $F_{max} = 1790 \text{ N}$	$d_{max} = 9.22 \text{ mm}$ $F_{max} = 1161 \text{ N}$
	4		$d_{max} = 14.24 \text{ mm}$ $F_{max} = 1772 \text{ N}$	$d_{max} = 9.04 \text{ mm}$ $F_{max} = 1137 \text{ N}$
	5		$d_{max} = 14.18 \text{ mm}$ $F_{max} = 1757 \text{ N}$	$d_{max} = 8.9 \text{ mm}$ $F_{max} = 1119 \text{ N}$

Table 13: Maximum force  $F_{max}$  and displacement  $d_{max}$  of each cycle for Quarry fines

Location Point	Cycle number	Quarry fines		
		20.65 %	22.15 %	23.01 %
#1	1	$d_{max} = 14.88$ mm $F_{max} = 1823$ N	$d_{max} = 11.33$ mm $F_{max} = 1469$ N	$d_{max} = 10.56$ mm $F_{max} = 1368$ N
	2	$d_{max} = 14.2$ mm $F = 1737$ N	$d_{max} = 10.38$ mm $F_{max} = 1371$ N	$d_{max} = 9.42$ mm $F_{max} = 1216$ N
	3	$d_{max} = 13.88$ mm $F_{max} = 1704$ N	$d_{max} = 10.05$ mm $F_{max} = 1328.7$ N	$d_{max} = 9.04$ mm $F_{max} = 1166$ N
	4	$d_{max} = 13.67$ mm $F_{max} = 1681$ N	$d_{max} = 9.84$ mm $F_{max} = 1300$ N	$d_{max} = 8.78$ mm $F_{max} = 1133$ N
	5	$d_{max} = 13.52$ mm $F_{max} = 1664$ N	$d_{max} = 9.69$ mm $F_{max} = 1280$ N	$d_{max} = 8.6$ mm $F_{max} = 1108$ N
#2	1	$d_{max} = 14.26$ mm $F_{max} = 1813$ N	$d_{max} = 11.4$ mm $F_{max} = 1502$ N	$d_{max} = 11.17$ mm $F_{max} = 1519$ N
	2	$d_{max} = 13.79$ mm $F_{max} = 1770$ N	$d_{max} = 10.85$ mm $F_{max} = 1433$ N	$d_{max} = 10.38$ mm $F_{max} = 1421$ N
#3	1	$d_{max} = 14.2$ mm $F_{max} = 1890$ N	$d_{max} = 10.5$ mm $F_{max} = 1327$ N	$d_{max} = 8.82$ mm $F_{max} = 1104$ N
	2	$d_{max} = 14.2$ mm $F_{max} = 1818$ N	$d_{max} = 9.64$ mm $F_{max} = 1222$ N	$d_{max} = 7.86$ mm $F_{max} = 982$ N
	3	$d_{max} = 14.2$ mm $F_{max} = 1787$ N	$d_{max} = 9.35$ mm $F_{max} = 1187$ N	$d_{max} = 7.56$ mm $F_{max} = 943$ N
	4	$d_{max} = 14.2$ mm $F_{max} = 1765$ N	$d = 9.14$ mm $F_{max} = 1163$ N	$d_{max} = 7.34$ mm $F_{max} = 916$ N
	5	$d_{max} = 14.2$ mm $F_{max} = 1750$ N	$d_{max} = 8.99$ mm $F_{max} = 1144$ N	$d_{max} = 7.24$ mm $F_{max} = 902$ N

The maximum values of each cycle and each location are summarized in Table 12 for Rotliegendes and in Table 13 for Quarry fines. Generally, with increasing cycles, the material becomes softer and therefore less force is required to penetrate the soil at a specific depth. The same reasoning holds for the results of the location point #3 which lies between the first two points. The #2 point was carried out for validation purposes and to quantify the natural

inhomogeneity of the soil and to check the accuracy of the experiments. For the soil Rotliegendes the highest deviation for the last two water percentages are 3% and 4% respectively. For the soil Quarry fines the corresponding values for the three different water percentages lie at approximately 4%, 5% and 10% respectively. Generally, the natural variability lies within the expected range. The tests of the #3 location point quantify consolidation characteristics of the soils through the increased soil displacement. Comparing the maximum deformations of the Tweel<sup>®</sup> for each cycle of each measurement point, the difference is up to approximately 10.5% for Rotliegendes and 16.5% for Quarry fines.

## **6.7 Discussion**

Wheel tests are an integral part for the optimization of terramechanical applications providing valuable information about the localized physical problem. By optimizing the wheel design, the vehicle design is indirectly enhanced. The single tire tests enable the separation of the soil's response from the full vehicle dynamics and thus, the tests provide an invaluable opportunity to minimize the stress applied in the soil during passage of a vehicle. The tests reported out in this chapter were utilized in the following chapter for calibration of a model simulation in a FEM code. Model simulations are enabling the use of complex terramechanical models for further improvement of the predictions of real applications scenarios. It is noteworthy to repeat that the effect of the water is considerable in all the investigated scenarios.

## 7 FEM simulations

### 7.1 Introduction and model set up

FEM is an integral tool for development and optimization procedures in many engineering areas. The robust and widely used for research purposes FEM program Abaqus was selected to carry out the numerical modelling in this thesis. Abaqus/Standard is used for problems in which the response period is long compared with the vibration frequency of the model and for problems that are slightly nonlinear with smooth nonlinearities. Abaqus/Explicit is used for high speed dynamic simulations and for problems with discontinuous nonlinearities (Abaqus®). Abaqus/Standard and Abaqus/Explicit were considered as options for carrying out FEM simulations. Initial attempts with Abaqus/Standard didn't yield satisfactory results regarding the simulation time of the model. From the other hand, initial modelling scenarios with Abaqus/Explicit deemed quick and suitable. Comparing the modeling capabilities of both and taking into consideration the application objective of this thesis, the Abaqus/Explicit was chosen to carry out all the simulations.

Abaqus Explicit uses explicit time integration scheme to calculate the transient dynamic or quasi static response of a system. The minimum stable time increment  $\Delta t_{min}$  should be less than a critical value given by eq. (37).

$$\Delta t_{min} \leq \frac{2}{\omega_{max}} \left( \sqrt{1 + \xi^2} - \xi \right) \quad (37)$$

where  $\omega_{max}$  is the highest eigenvalue and  $\xi$  is the critical damping in the highest mode (Abaqus®).

The loading in Abaqus/Explicit should be applied by defining amplitudes over the time step, which can be defined in the time scale of a single step, or over the total time which corresponds to the time accumulated over all the general steps (Abaqus®). Data output requests of the model should be carried out with caution in order to avoid excess unnecessary data. Output field data should be requested for the whole model to visualize the deformed model and for creating x-y plots. Output history data should be requested for specific part of

the model to create x-y plots. A restart output should be requested to enable the continuation of an analysis that stopped for a specific reason.

In the first part of the numerical investigation, calibration of the wheel tests was carried out. In the subsequent second part, rolling simulations were considered. Different models dealing with force-displacement interactions were created. Firstly, the Tweel<sup>®</sup> interacting with a rigid base was modeled. This model served to quantify the stiffness of the wheel from the experimental data of the previous Chapter 6. It was decided to model the body of the steel plate as rigid because it is much stiffer than the Tweel<sup>®</sup> with which it will come in contact. The motion of the rigid body, which is a collection of nodes and elements, is governed by the motion of a reference node (Abaqus<sup>®</sup>). A vertical displacement was imposed in the centre of the Tweel<sup>®</sup> and the corresponding vertical force was measured. The material model parameters of the Tweel<sup>®</sup> were adjusted to match the experimental values of force vs deformation shown in Figure 43. Secondly, the interaction of Tweel<sup>®</sup> vs soil was modeled. The results of the first cycle of the wheel tests at the location point #1 depicted in Figure 46 and Figure 49 and in the Table 12 and Table 13 were used as target values. The effect of water percentage in the soils was investigated by adjusting the soil material parameters corresponding to the specific humidity states under investigation.

In the second part of the numerical investigation, different scenarios of rolling of a non-pneumatic wheel on soil were analysed. Namely, the influence of material, angular velocity and vertical force were investigated. Inertia and mass effects were considered in the model. The calibrated models of wheel and soils from the first part of the investigation corresponding to the experiments described in Chapter 6 were used. Additionally, the volcanic material collected from Etna EVM, was modeled and further a case of two different layers was considered. The varied parameters were as follows: angular velocities of 5 and 10 rad/s, vertical force of 2 and 4 kN, Quarry fines and Rotliegendes material with three different water percentages, Etna volcanic material EVM and a two layered soil consisting of a top layer of Rotliegendes and a bottom layer of Quarry fines. Lastly, the geometrical effects of the size of the soil model were investigated. The model was gradually increased until the difference in the modelling results were negligible. The models created with imposed angular velocity and vertical force correspond to free rolling. A free rolling condition is the state between

braking and driving and it results when the rolling resistance force and torque applied on the axle are zero. The resultant torque on the tire acts in the opposite or in the same direction of the angular velocity for the case of braking and driving respectively. The material Rotliegendes was chosen to investigate the differences between driving, free rolling and braking.

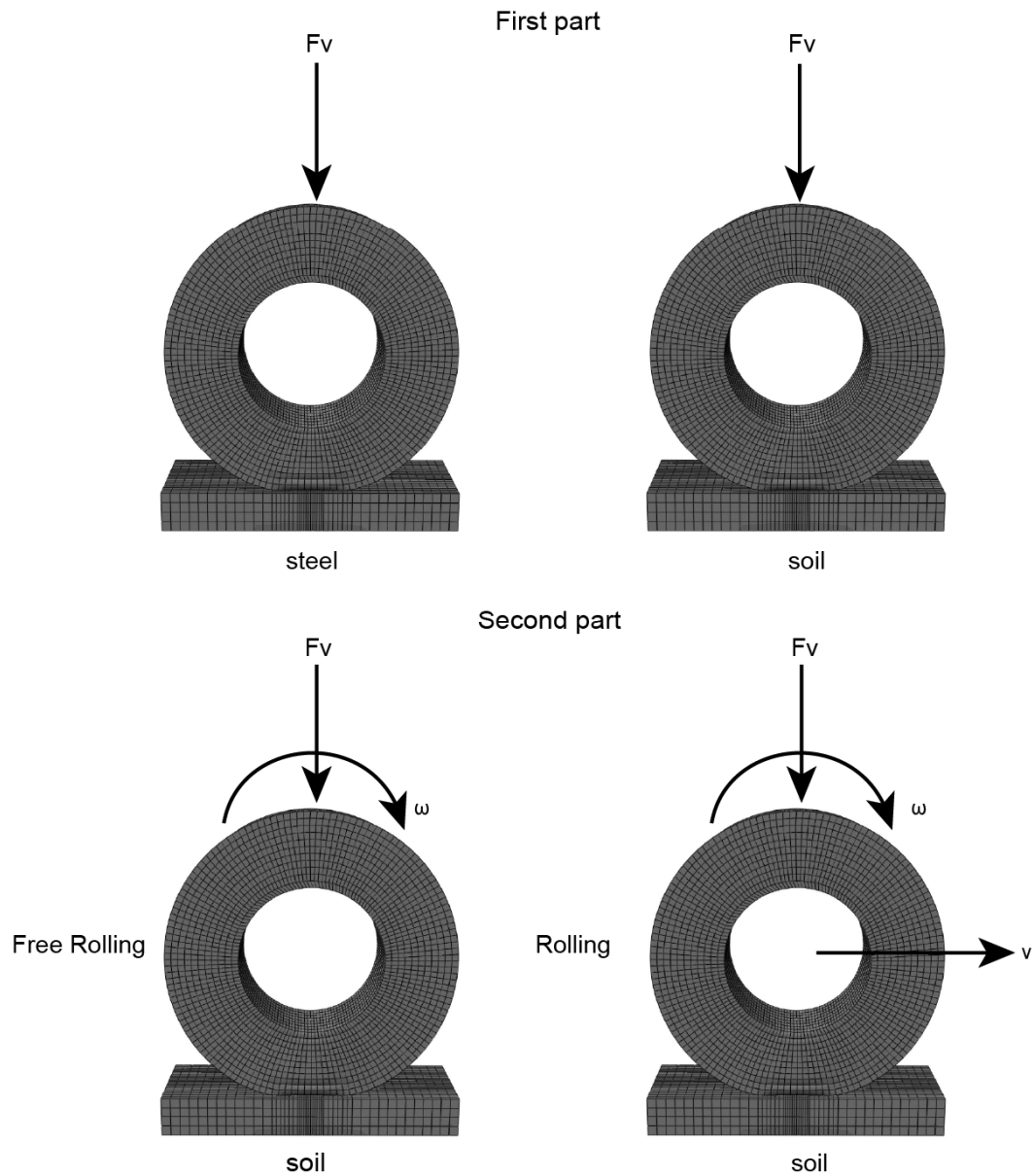


Figure 52: Investigated model scenarios.

A general contact domain was used in Abaqus/Explicit as it is required for the hyperelastic model that was used for the modelling of the Tweel<sup>®</sup> as it will be explained in subsequent subchapter. The normal behaviour of the contact property is defined as "Hard" Contact with the default enforcement method and allowing separation after contact. The tangential behaviour was modelled with a penalty friction formulation with a friction coefficient of  $\tan\phi$  accordingly to the soil type. Friction is a highly nonlinear effect which causes the equation system to be unsymmetric (Abaqus<sup>®</sup>). An exemption was the model of the tire against the steel plate where the interaction was modelled as frictionless. All the nodes on the inner surface of the Tweel<sup>®</sup> are attached to the reference node located at the centre of the tire using kinematic coupling constraints.

A finer mesh is created in the middle part of the soil and in the bottom part of the wheel by creating partitions to the model which enables definition of local seeds and thus finer mesh on the specific regions. Hexahedral/tetrahedral meshing is utilized as they provide more accurate results. Parametric studies were carried out in the mesh density of the regions of higher interest: the middle part of the soil and the wheel bottom which come in contact during the test. The mesh elements were gradually decreased in size until the differences in the results were meaningless. For both parts the same C3D8R elements -8 node linear hexahedron brick, reduced integration, enhanced hourglass control, hybrid elements- are used. The first order elements which are used in the models of this research, are less sensitive to distortion. Usually the second order elements can capture better the geometry, but for the simple geometries used in this section the first order elements deemed adequate and more effective for the purposes of analysis. Final size of typical mesh used for the Tweel<sup>®</sup> was 122232 elements and 15012 nodes. The Tweel<sup>®</sup> in the model has diameter of 0.66 m and width 0.225 m. The soil's mesh for the footprint analysis constitutes of 41184 elements and 46102 nodes for the soil with dimensions of height of 0.09 m, length of 0.68 m and width of 0.275 m and for the rolling simulation the mesh constitutes of 15120 elements and 18634 nodes for a soil with dimension of height of 0.28 m, length 3.0 m and width of 0.8 m. The dimensions of the simulated soil and wheel can be easily modified to correspond to any desired size. For finer mesh or/and size of the model, the simulation cost increases.

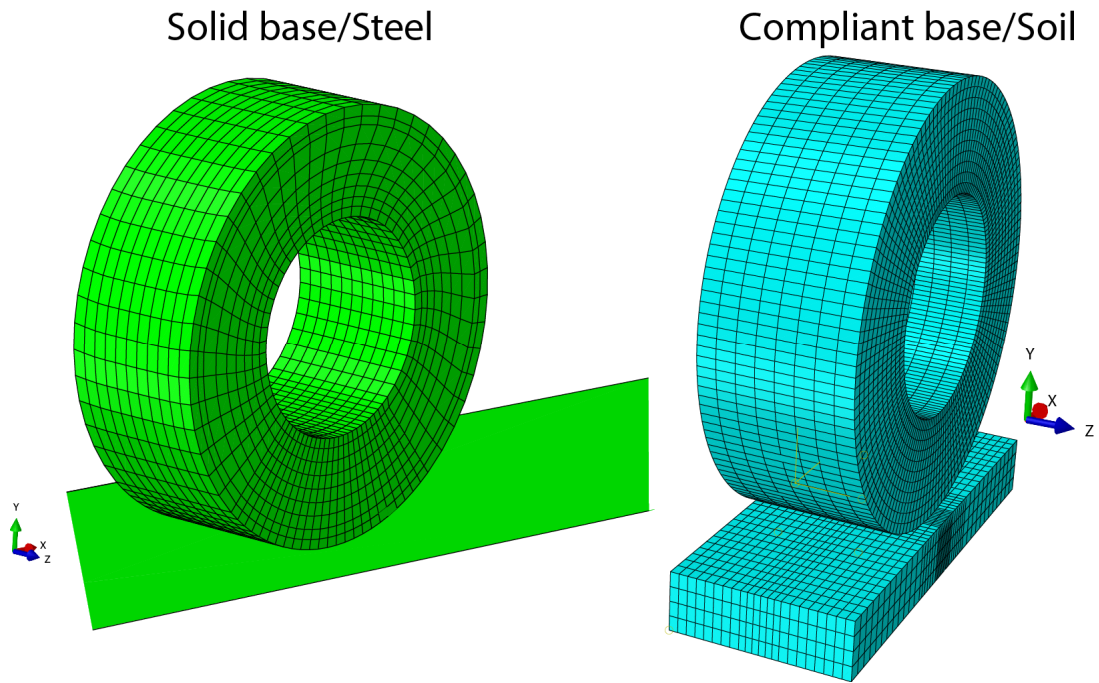


Figure 53: Mesh of the step one of the simulation.

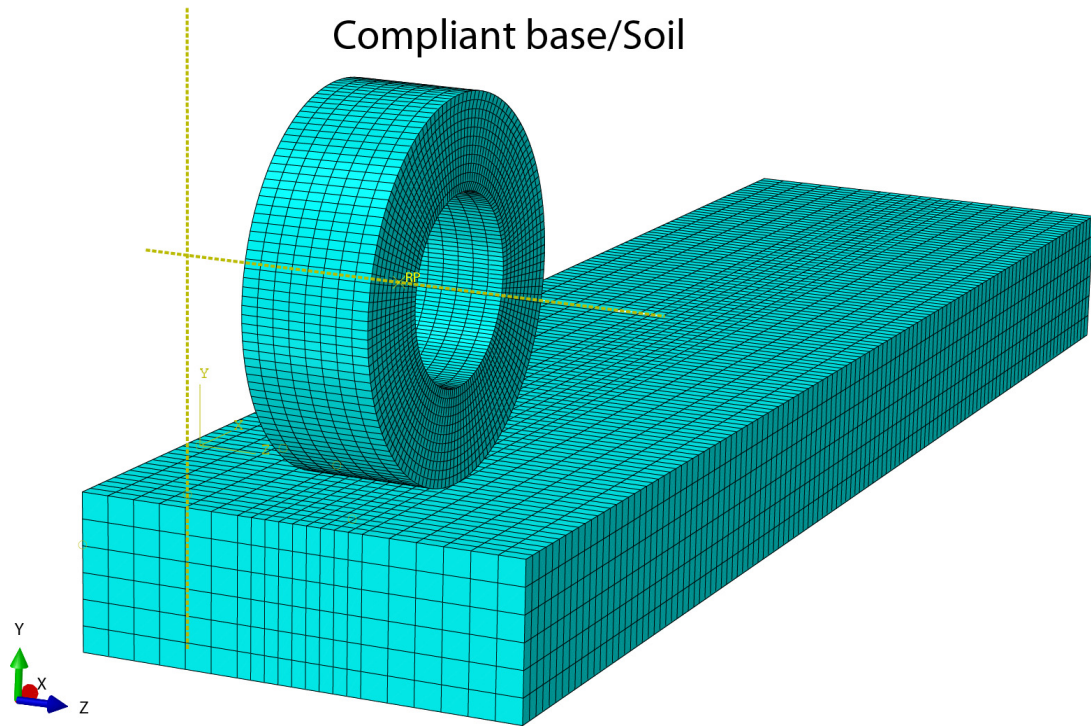


Figure 54: Mesh used in the second part of the simulations.



## 7.2 Wheel material model

The Michelin Tweel<sup>®</sup> consists of a tread; belts, a steel rim, polyresin spokes and cables forming a semi rigid shear beam (Michelin Tweel<sup>®</sup>, 2019). For the purpose of the current modelling scenarios it was chosen to model the Tweel<sup>®</sup> as one uniform wheel made from rubber without tread pattern. This simplification doesn't reduce the integrity of the results of the current modelling scenarios. Exact modelling of the Tweel<sup>®</sup> including tread pattern, thickness and orientation of the spokes, material of the rim etc. serves mainly for optimization design procedures. The purpose of the models of this thesis is to investigate the performance of the specific design of the wheel.

The rubber material can be modelled with hyperelastic material models in Abaqus. There are many so called strain energy potential models available in the Abaqus environment such as Arruda-Boyce, Marlow, Mooney-Rivlin, Neo Hooke, Ogden, generally Polynomial and Reduced Polynomial models, Van der Waals and Yeoh etc. The Yeoh model is a reduced polynomial model that provide better fit when limited test data are available, as the case here. The interested reader is referred to Yeoh (1993) for more information regarding the model. The Yeoh strain energy potential is defined by eq. (38).

$$U = C_{10}(\bar{I}_1 - 3) + C_{20}(\bar{I}_1 - 3)^2 + C_{30}(\bar{I}_1 - 3)^3 + \frac{1}{D_1}(J^{el} - 1)^2 + \frac{1}{D_2}(J^{el} - 1)^4 + \frac{1}{D_3}(J^{el} - 1)^6 \quad (38)$$

$$\bar{I}_1 = \bar{\lambda}_1^2 + \bar{\lambda}_2^2 + \bar{\lambda}_3^2 \quad (39)$$

$$\bar{\lambda}_i = J^{-1/3} \lambda_i \quad (40)$$

$$J^{el} = \frac{J}{J^{th}} = \frac{J}{(1 + \varepsilon^{th})^3} \quad (41)$$

$$\mu_0 = 2C_{10} \quad (42)$$

$$K_0 = \frac{2}{D_1} \quad (43)$$

where  $U$  is the strain energy per unit of reference volume,  $C_{i0}$  and  $D_i$  are temperature dependent material parameters,  $\bar{I}_1$  is the first deviatoric strain invariant,  $J^{el}$  is the elastic volume ratio,  $\bar{\lambda}_i$  are the deviatoric stretches,  $J$  is the total volume ratio,  $\lambda_i$  are the principal stretches,  $J^{th}$  is the thermal volume ratio,  $\varepsilon^{th}$  is the linear thermal expansion strain;  $\mu_0$  is the initial shear modulus and  $K_0$  is the initial bulk modulus.

Viscoelasticity is also considered for the Tweel<sup>®</sup> by a Prony series expansion of the dimensionless relaxation modulus given by eq.(44).

$$g_R(t) = 1 - \sum_{i=1}^N \bar{g}_i^P (1 - e^{-t/\tau_i^G}) \quad (44)$$

where  $i=1,2,..N$  and  $\tau_i^G$  are material constants,  $\bar{g}_i^P$  is the shear relaxation or shear traction relaxation modulus ratio and  $t$  is time.

### 7.3 Soil model

For a deformable interaction surface, soil was chosen. The available experimental data of the shear tests of the soils, presented in Chapter 4.3 and Chapter 6.4.2 were utilized to calibrate the model parameters. The aim was to investigate the interaction of the interface between deformable soil and compliant wheel, and therefore it was decided to carry out the shearing tests in a large direct shearing frame. Experiments utilizing a section of the compliant wheel, are not possible in a standard triaxial apparatus. The soil material is modeled with the Drucker Prager DP constitutive model. The initial evaluation of the shear test data was carried out by assuming a Mohr-Coulomb MC failure criterion. There are two ways to proceed: either reevaluating the raw data considering a Drucker Prager model or by calculating the equivalent parameters of the DP from the MC parameters. Assuming that the shear strength parameters resulting by direct shear and in triaxial test are equivalent, the corresponding DP model parameters can be calculated from the given matching equations from Abaqus<sup>®</sup> documentation.

This option is demonstrated in this thesis because the procedure is desired to be experimentally independent as usually for many well-documented soil, the shear parameters  $\varphi$  and  $c$  are known.

The linear Drucker-Prager model is utilized for calibrating all the soil material in this thesis. Therefore, the material angle of friction  $\beta$  and the dilation angle  $\psi$  correspond to those obtained from the linear yield surface in the p-t meridional plane. The cohesion parameter  $d$  is defined as the intersection of the yield surface with the y-axis. The linear yield surface is defined by eq. (45). The linear model can capture a noncircular yield surface in the deviatoric plane to match different values in triaxial tension and compression, associated inelastic flow in the deviatoric plane and separate dilation and friction angles (Abaqus®).

$$F = t - p \cdot \tan \beta - d = 0 \quad (45)$$

$$t = \frac{1}{2}q \left[ 1 + \frac{1}{K} - \left( 1 - \frac{1}{K} \right) \left( \frac{r}{q} \right)^3 \right] \quad (46)$$

$$p = -\frac{1}{3} \text{trace}(\sigma) \quad (47)$$

$$q = \sqrt{\frac{3}{2} (S : S)} \quad (48)$$

$$S = \sigma + p \cdot I \quad (49)$$

$$r = \left( \frac{9}{2} S \cdot S : S \right)^{1/3} \quad (50)$$

where  $t$  is stress,  $p$  is the equivalent pressure stress,  $\beta$  is the friction angle of the material,  $d$  is the cohesion parameter,  $q$  is the Mises equivalent stress,  $K$  is the flow stress ratio,  $S$  is the stress deviator and  $r$  the third invariant of the deviatoric stress.

The evolution of the yield surface with plastic deformation is described in terms of the equivalent stress  $\bar{\sigma}$  which can be chosen as either the uniaxial compression yield stress, the uniaxial tension yield stress or the shear

(cohesion) yield stress. The equivalent plastic strain rate for the linear DP is defined by eq. (51), when hardening is defined in pure shear as in the case under investigation. To ensure that the yield surface remains convex,  $K$  values in eq. (46) are ranging from 0.778 to 1.0. The cohesion parameter  $d$  of the material is defined by eq. (52). The flow potential is defined by eq. (53). Non associated flow is defined when the dilation angle  $\psi$  is different than the friction angle  $\beta$ , and usually smaller. For the case when  $\psi = \beta$  the flow is associated. It is worthy to note here that the original DP model can be obtained by setting  $K = 1$  and  $\psi = \beta$ . For all the investigated scenarios, non-associated flow was assumed, meaning that the material stiffness matrix is not symmetric. To match the triaxial test response of MC eq. (54) to eq. (56) are utilized to define the equivalent DP parameters. For the two extreme cases of plane strain response  $\psi = \beta$  and  $\psi = 0$  the eq. (57) is valid. To match the plane strain response of MC the eq. (58) and (59) can be utilized. The plane strain case was utilized to calculate another value of yield stress for defining the hardening of the DP model, mainly for comparison purposes of the model sets.

$$\bar{\varepsilon}^{pl} = \dot{\gamma}^{pl} \sqrt{3} = \gamma^{pl} \sqrt{3} \quad (51)$$

$$d = \frac{\sqrt{3}}{2} \tau \left( 1 + \frac{1}{K} \right) \quad (52)$$

$$G = t - p \tan \psi \quad (53)$$

$$\tan \beta = \frac{6 \sin \phi}{3 - \sin \phi} \quad (54)$$

$$K = \frac{3 - \sin \phi}{3 + \sin \phi} \quad (55)$$

$$\sigma_c^0 = 2c \frac{\cos \phi}{1 - \sin \phi} \quad (56)$$

$$\sigma_c^0 = \frac{1}{1 - \frac{1}{3} \tan \beta} d \quad (57)$$

$$\sin \phi = \frac{\tan \beta \sqrt{3(9 - \tan^2 \psi)}}{9 - \tan \beta \tan \psi} \quad (58)$$

$$\cos \phi = \frac{\sqrt{3(9 - \tan^2 \psi)} d}{9 - \tan \beta \tan \psi c} \quad (59)$$

where  $\bar{\epsilon}^{pl}$  is the equivalent plastic strain,  $\dot{\gamma}^{pl}$  is the strain rate,  $\gamma^{pl}$  is the engineering shear plastic strain,  $d$  is the cohesion parameter,  $\tau$  the yield stress,  $K$  is the flow stress ratio,  $G$  is the flow potential,  $p$  is the equivalent pressure stress,  $\beta$  is the friction angle of the material for the DP model,  $\sigma_c^0$  is the uniaxial compression stress,  $\phi$  is the friction angle of the material for the MC model,  $\psi$  is the dilation angle and  $c$  is the cohesion of the MC model.

Table 14: Model parameters for the Drucker-Prager model for the Etna volcanic material EVM inferred from direct shear tests

Parameter	EVM
$\nu$ [-]	0.35
$\rho$ [Mg/m <sup>3</sup> ]	1.17
$\tan \phi$ [-]	0.46
$\beta$ [°]	59.42
$K$ [-]	0.78
$\psi$ [°]	3
$d_2$ [kPa]	58.66
Peak stress [kPa]	59.30
$\bar{\epsilon}^{pl}$	10.35
$E$ [MPa]	5.4

Table 15: Model parameters for Rotliegendes for the Drucker-Prager model inferred from direct shear tests

Rotliegendes						
Parameter	13.69%		25.5%		32.21%	
case	1i	1ii	2i	2ii	3i	3ii
$\nu$ [-]	0.35	0.35	0.35	0.35	0.35	0.35
$\rho$ [Mg/m <sup>3</sup> ]	1.64	1.64	1.64	1.64	1.64	1.64
$\tan\phi$ [-]	0.76	1.38	0.20	0.89	0.10	0.41
$\beta$ [°]	56.64	65.74	22.36	59.61	11.81	41.26
$K$ [-]	0.78	0.78	0.88	0.78	0.93	0.78
$\psi$ [°]	3.0	3.0	3.0	3.0	3.0	3.0
$d_1$ [kPa]	10.97	139.13	22.02	61.65	10.30	79.64
$d_2$ [kPa]	53.58	101.67	20.10	62.86	7.19	27.97
Peak stress [kPa]	65.16	166.62	25.52	83.90	13.47	62.60
$\bar{\epsilon}^{pl}$ [%]	3.21	4.96	28.15	16.82	28.19	8.92
$E$ [MPa]	18.1	47.8	6.9	28.3	3.6	32.7

Table 16: Model parameters for Quarry fines for the Drucker-Prager model inferred from direct shear tests

Quarry fines						
Parameter	20.65%		22.15%		23.01%	
	1i	1ii	2i	2ii	3i	3ii
$\nu$ [-]	0.35	0.35	0.35	0.35	0.35	0.35
$\rho$ [Mg/m <sup>3</sup> ]	1.51	1.51	1.51	1.51	1.51	1.51
$\tan\phi$ [-]	0.29	1.19	0.36	0.62	0.26	0.46
$\beta$ [°]	31.94	64.03	37.67	51.97	28.83	44.41
$K$ [-]	0.83	0.78	0.80	0.78	0.84	0.78
$\psi$ [°]	3.0	3.0	3.0	3.0	3.0	3.0
$d_1$ [kPa]	38.97	94.41	20.36	75.47	17.33	56.13
$d_2$ [kPa]	24.74	122.71	23.60	65.63	19.19	33.07
Peak stress [kPa]	41.81	124.75	37.57	73.65	28.88	54.02
$\bar{\epsilon}^{pl}$ [%]	28.08	20.48	28.08	17.20	27.89	3.81
$E$ [MPa]	8.1	62.8	6.0	59.7	3.6	16.1

The calculated parameters for the DP model for Rotliegendes, Quarry fines, and Etna volcanic material EVM are summarized in Table 14 to Table 16. The parameters were calculated from the equations for matching the Mohr Coulomb parameters. The value  $d_1$  was calculated using the plane strain conditions matching equations and the  $d_2$  corresponds to matching the triaxial test. The values of  $\nu$  and  $\psi$  were assumed as constant. The Young's modulus  $E$  was calculated from the initial part of the shear tests of each material. In each case, the highest confining stress case was chosen.

## 7.4 Calibration procedure for wheel-soil interaction

For ease in the readability of the results the three different water contents are referred with the number 1,2 and 3, while each case scenario is referred to a, b and c as presented in the subsequent sections. For instance, Rotliegendes 3c refers to the calibrated material model set of Rotliegendes with the first water content value meaning 13.69% and calibrated in the *c* case.

### 7.4.1 Steel rigid base

The measured force-displacement curve is given in Figure 43. This curve was used as a reference for the calibration of the material model of the Tweel<sup>®</sup>. It exhibits a hysteric behavior with load/unload following a different path. The chosen model described in Chapter 7.2 is capable to reproduce this type of response. A simple one term Prony series was selected for the model meaning that  $k_i$  is zero, with a value of the shear relaxation modulus ratio  $g_i$ , of 0.3 and the associated relaxation time  $\tau_i$  of 0.1. The values adopted for the Prony series were taken from the literature (Johnson & Chen, 2005) since there were no data available to calibrate them for the specific compliant wheel used. A typical value of density of 1.1 Mg/m<sup>3</sup> was used for the density parameter of the model for the rubber material.

For the strain energy potential various models were evaluated with the build in 'evaluate' procedure of Abaqus. The Yeoh, Ogden and the Neo-Hooke models, were considered as suitable for the investigated Tweel<sup>®</sup>. The Yeoh model yielded the most satisfactory results in the followed calibration

procedure and was used for all the subsequent analyses. For the calculation of the model parameters of the Yeoh model, firstly, the set of the maximum force-displacement was used as a target value. The model parameters were adjusted to match primarily the specific highest response and secondary the followed path as close as possible. The calibrated behavior of the Yeoh model is depicted in Figure 55. The resulted calibrated coefficients of the Yeoh model are:  $C_{10} = 1.16 \cdot 10^5$ ;  $C_{20} = -7.34 \cdot 10^5$ ;  $C_{30} = 4.17 \cdot 10^6$ ;  $D_1 = 1.73 \cdot 10^{-8}$ ;  $D_2 = D_3 = 0$ .

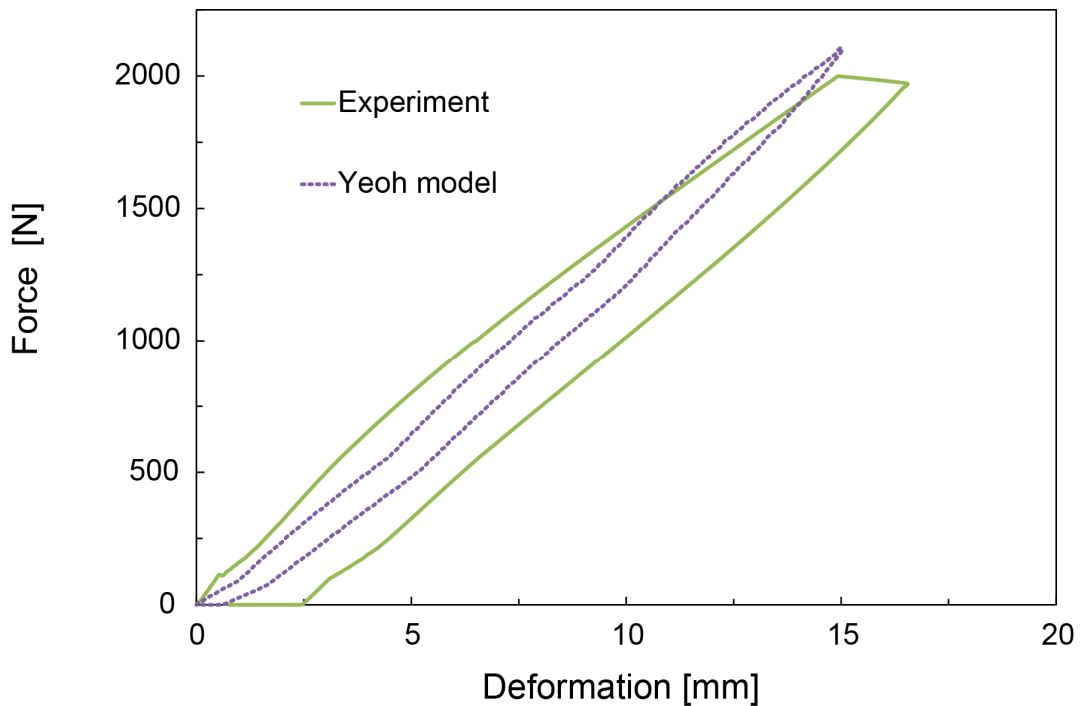


Figure 55: Force vs displacement curve for the Tweel® in the test and the numerical simulation.

#### 7.4.2 Compliant base

Initial runs with the model parameters as defined in Table 15 and Table 16 yielded results that differ from the experimental values. Specifically, for the Rotliegendes model set 1, 2 and 3 the experimental soil displacement was inferred to be 0.1 mm, 0.22 mm and 3.64 mm while the simulations resulted to values of 0.31 mm, 2.14 mm and 10.98 mm respectively. For Quarry fines model set 1, 2 and 3 the soil displacement from the experiments were calculated to be 0.12 mm, 3.67 mm and 4.44 mm while the simulations



yielded 1.21 mm, 1.43 mm and 3.08 mm respectively. Therefore, it was decided to carry down a calibration procedure to match closely the experimental values.

The main parameters that affect highly the simulation results of the footprint analyses are the Young's modulus and the yield stress. Three different calibrations were attempted for each material. Firstly, with fixed value of yield stress  $d_1$  and subsequently, with fixed value of  $d_2$ , the  $E$  was varied. Lastly, the value of  $E$  was held constant and the yield stress  $d$  was varied. For the last case, a converged simulation result wasn't always successful and therefore  $E$  was gradually increased until the desired simulation result was obtained. As a reminder, these efforts are denoted with a, b, c respectively. In Table 17 and Table 18 the calibrated  $E$  and  $d$  sets are presented. The  $d$  values are denoted as  $\sigma_{yield}$  for consistency. For the material Rotliegendes, for the higher studied water content, a solution with the selected  $d$  values wasn't successful with investigated values for  $E$  up to 300MPa. Thus, only one calibration is available. It should be noted that generally other combinations could yield the desired results. The scope was to use as closely as possible the calculated parameters of each soil model to develop a calibration procedure for soils. A graphical representation of the results of the analysis of the Rotliegendes model set 3c and the associated footprint are depicted in Figure 56 and Figure 57.

Table 17: Calibrated results for Rotliegendes

Rotliegendes					
Model set	13.69%	Model set	25.5%	Model set	32.21%
1a	E = 75 MPa $\sigma_{yield} = 11$ kPa	2a	E = 80 MPa $\sigma_{yield} = 22$ kPa	3a	-
1b	E = 56 MPa $\sigma_{yield} = 54$ kPa	2b	E = 90 MPa $\sigma_{yield} = 20$ kPa	3b	-
1c	E = 50 MPa $\sigma_{yield} = 20$ kPa	2c	E = 25 MPa $\sigma_{yield} = 45$ kPa	3c	E = 3.6 MPa $\sigma_{yield} = 22$ kPa

Table 18: Calibrated results for Quarry fines

Quarry fines					
Model set	20.65%	Model set	22.15%	Model set	23.01%
1a	E = 47 MPa $\sigma_{\text{yield}} = 39 \text{ kPa}$	2a	E = 1.9 MPa $\sigma_{\text{yield}} = 20 \text{ kPa}$	3a	E = 2.3 MPa $\sigma_{\text{yield}} = 17 \text{ kPa}$
1b	E = 87 MPa $\sigma_{\text{yield}} = 25 \text{ kPa}$	2b	E = 1.6 MPa $\sigma_{\text{yield}} = 24 \text{ kPa}$	3b	E = 2.1 MPa $\sigma_{\text{yield}} = 19 \text{ kPa}$
1c	E = 47 MPa $\sigma_{\text{yield}} = 40 \text{ kPa}$	2c	E = 6 MPa $\sigma_{\text{yield}} = 11 \text{ kPa}$	3c	E = 3.6 MPa $\sigma_{\text{yield}} = 13 \text{ kPa}$

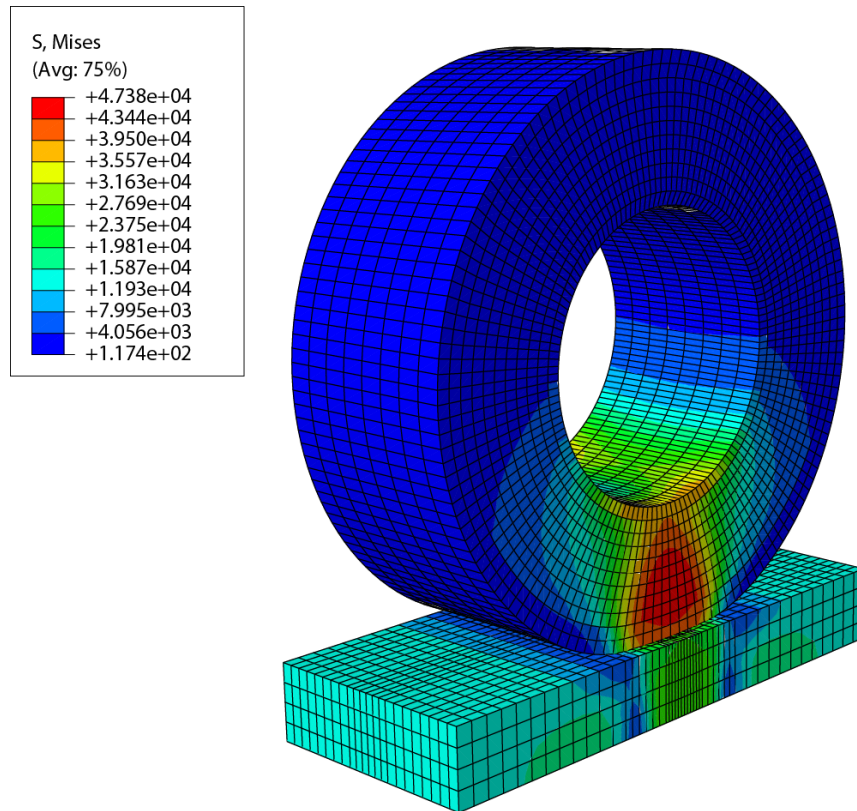


Figure 56: Von Mises stress results from Rotliegendes' model set 3c.

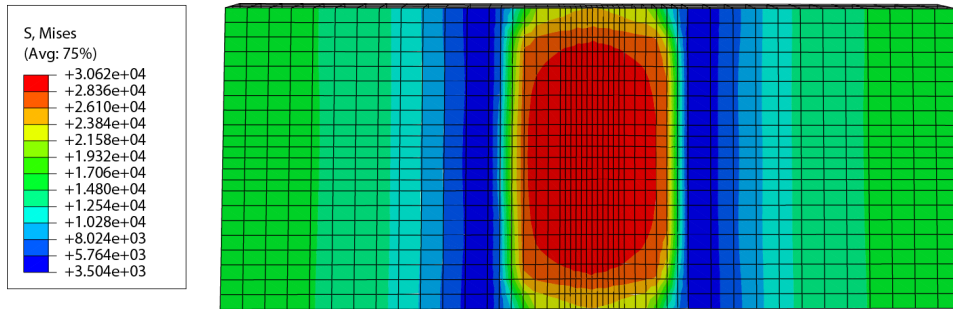


Figure 57: Footprint on the soil from Rotliegendes' model set 3c.

The calibrations are graphically presented in the following Figure 58 to Figure 63. The results curves show that the difference among the calibrations lie mainly along the path that leads to the desired force-displacement combination. The cases with the lowest  $E$  follows a lower path meaning that initially the required force for a specific deformation is less (concave upward), and subsequently the rate of increase is increased leading to the desired value.

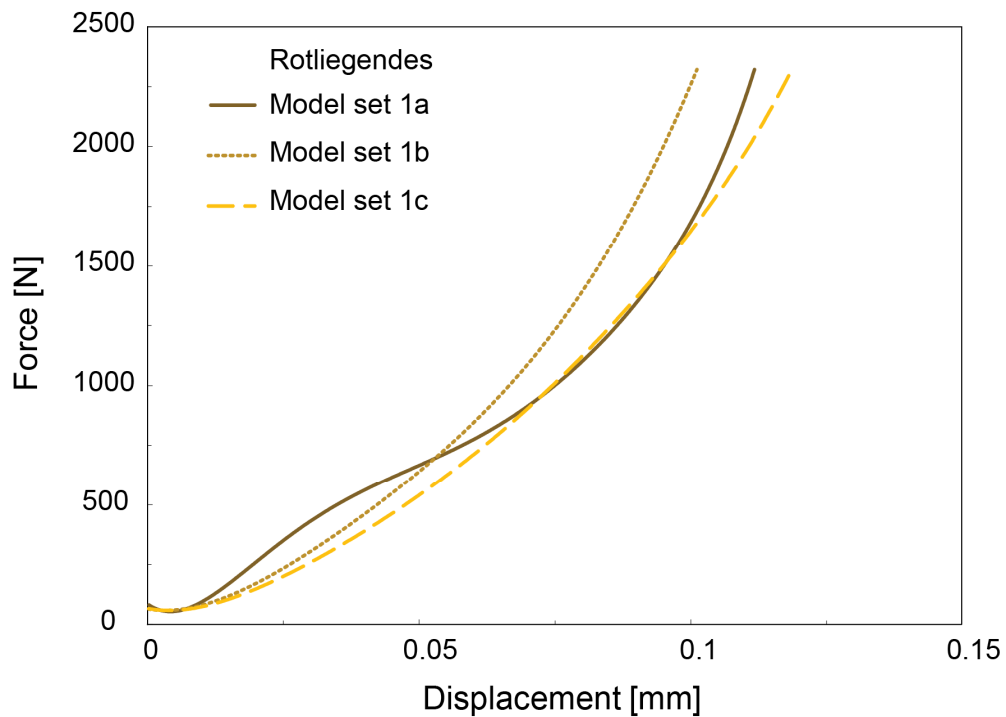


Figure 58: Simulation results for calibrated model sets for Rotliegendes with  $w=13.69\%$ .

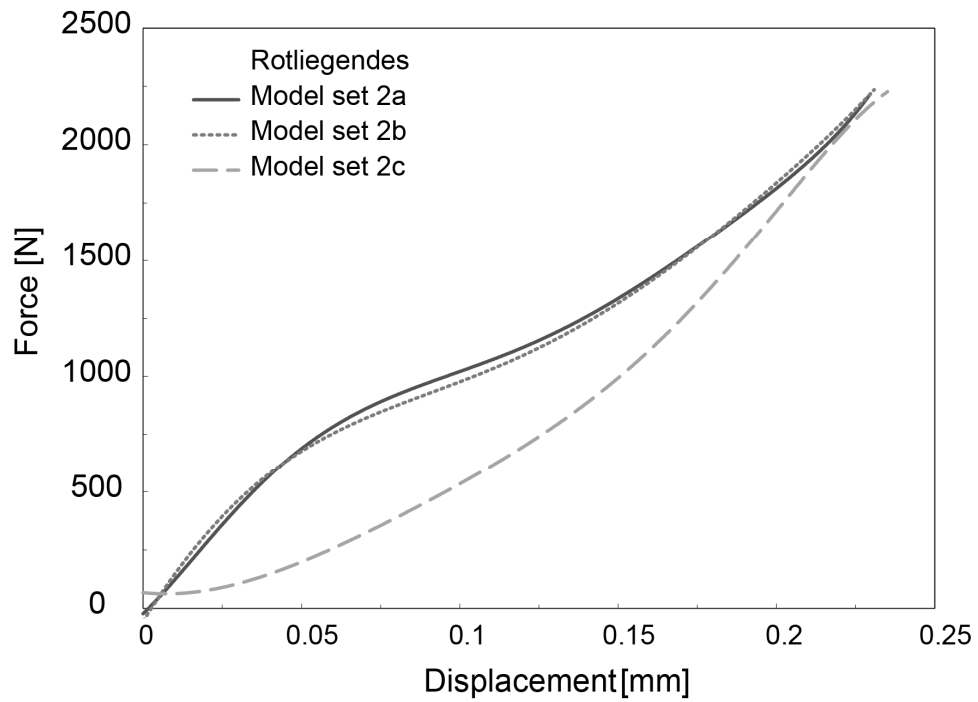


Figure 59: Simulation results for calibrated model sets for Rotliegendes with  $w=25.45\%$ .

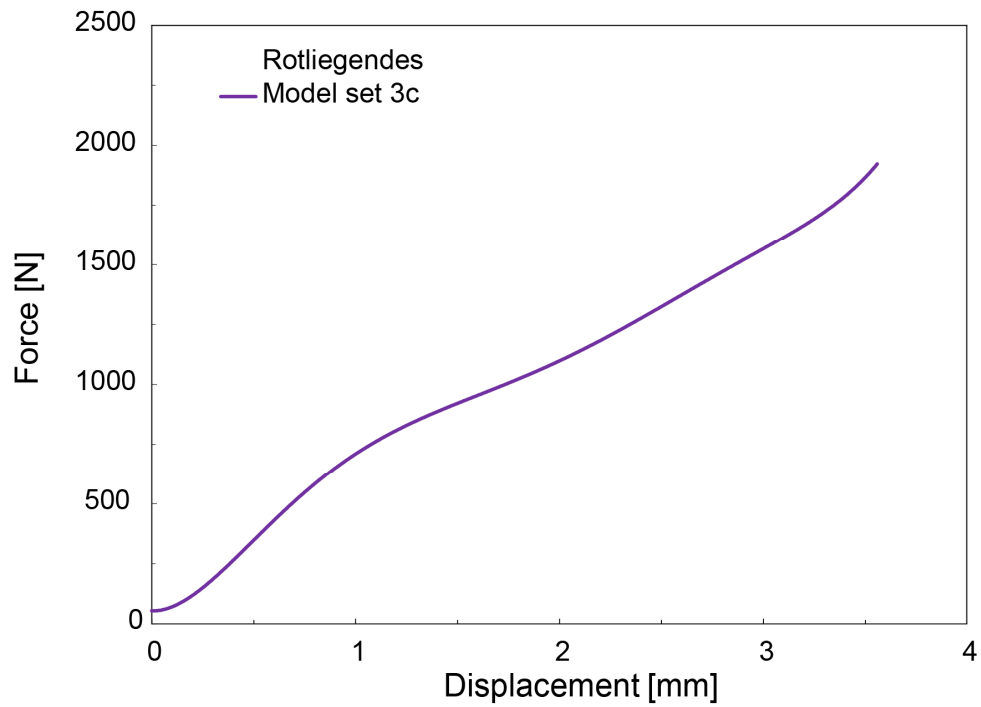


Figure 60: Simulation results for calibrated model sets for Rotliegendes with  $w=32.21\%$ .

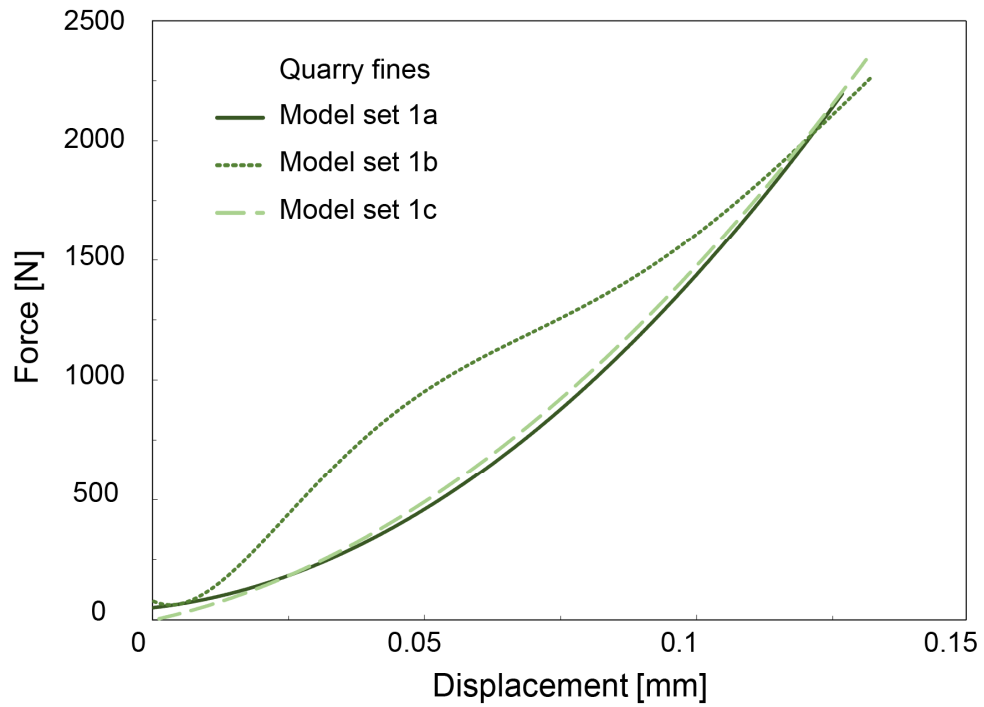


Figure 61: Simulation results for calibrated model sets for Quarry fines with  $w=20.65\%$ .

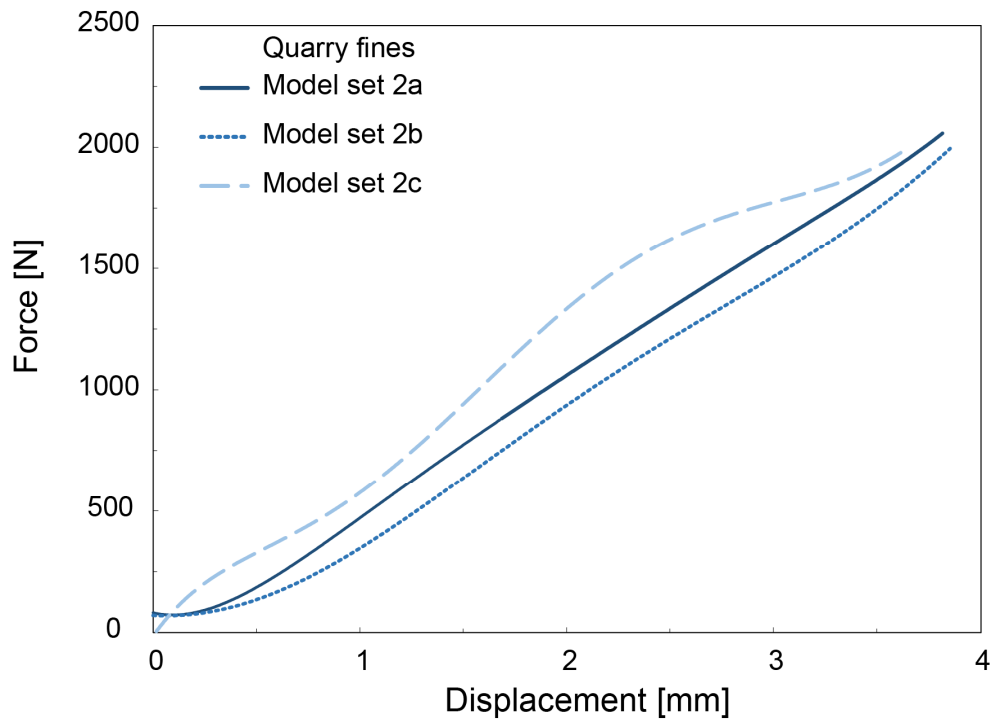


Figure 62: Simulation results for calibrated model sets for Quarry fines with  $w=22.15\%$ .

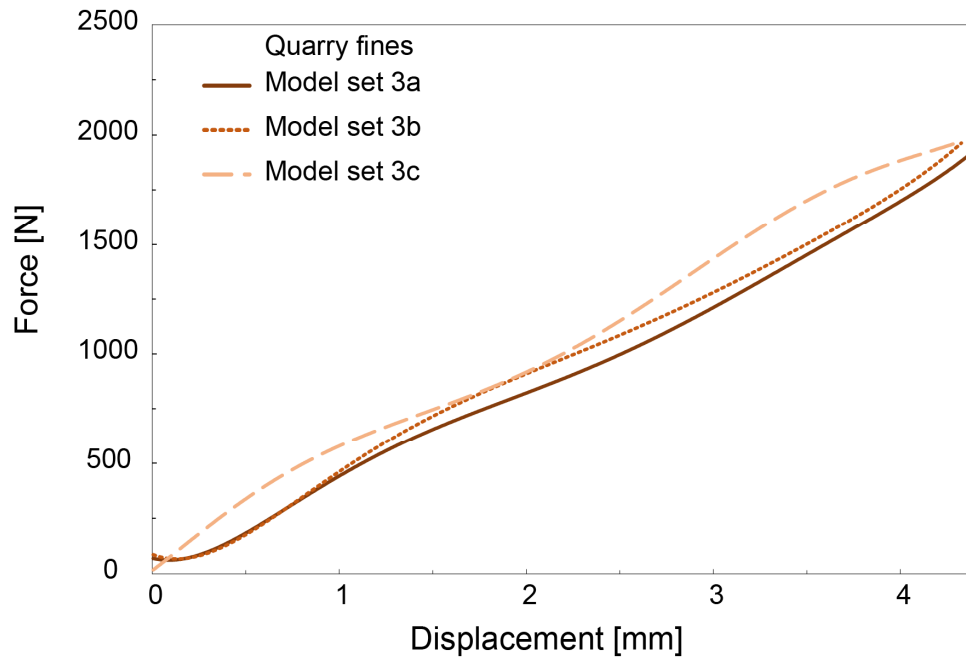


Figure 63: Simulation results for calibrated model sets for Quarry fines with  $w=23.01\%$ .

## 7.5 Results from the rolling simulation

### 7.5.1 Free rolling of various materials

For the free rolling simulations homogeneous material models of Rotliegendes, Quarry fines, Etna volcanic material EVM and a model of a two layered soil, were considered. For the case of the two layers, the half top part of soil was modeled with the model set of Rotliegendes 3c while the bottom part was modeled with the model set of Quarry fines 1b. The contact area and the true distance in the models are defined as shown in Figure 64 and Figure 65. In Figure 66 a comparison in terms of normal stress, between the layered soil and the cases of having a uniform layer of either Rotliegendes 3c or Quarry fines 1b for a velocity of 5 rad/s and a vertical loading force of 2 kN is plotted. It is obvious that the response of the layered soil, corresponds to the response of the top layer. The stress is slightly increased from a value of 73.42 kPa to 75.14 kPa, which is attributed to the influence of the bottom layer.

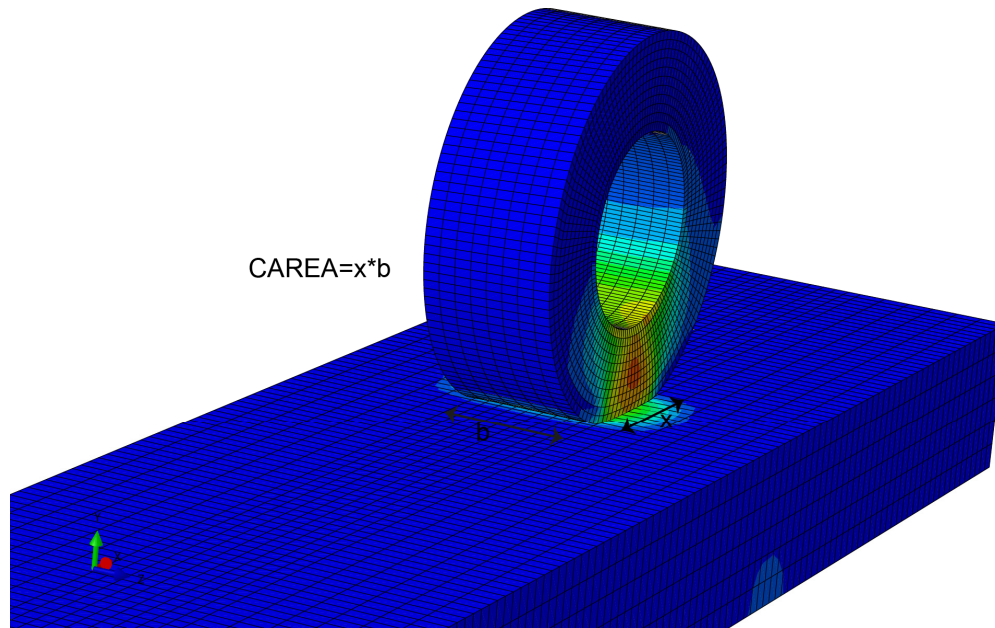


Figure 64: Contact area.

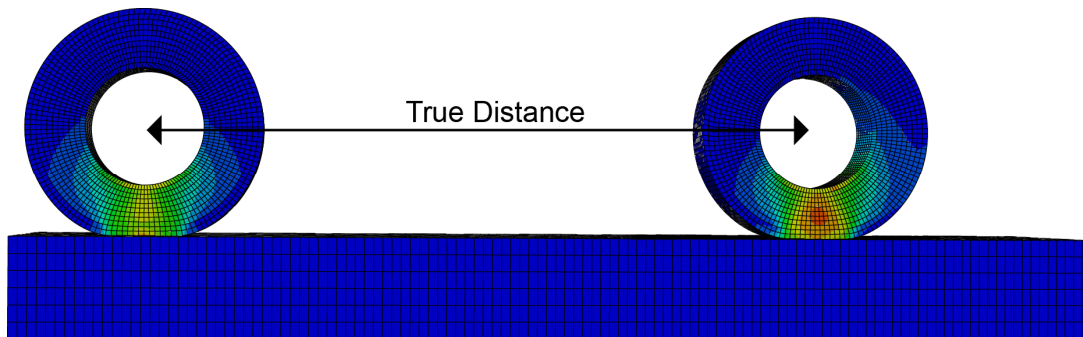


Figure 65: True distance definition.

Further results of other model sets corresponding to the same velocity of 5 rad/s and the same vertical loading force of 2 kN are displayed in the following in Figure 67 to Figure 72. The viscous dissipated energy ALLVD, calculated by Abaqus, is plotted in Figure 67. The material EVM has the highest ALLVD, followed by Rotliegendes 3c, Quarry fines 2b and Quarry fines 3b. The rest of the material exhibit similar smaller values. As shown in Figure 68 there is only a minor difference to the corresponding horizontal displacement of the wheel for the specific materials displayed in the graph.

The highest contact area CAREA calculated by Abaqus, as displayed in Figure 69, results from the material Quarry fines 2b&3b and for Rotliegendes 3c. The rest of the material exhibit similar lower values.

The vertical stresses, the horizontal displacement and the vertical displacement of the soil along the true distance are displayed in the Figure 70, Figure 71 and Figure 72 respectively. The highest stresses are resulting from Rotliegendes 1b, 2b and Quarry fines 1b, followed by EVM and Rotliegendes 3c. The lowest stresses are resulted by Quarry fines model set 2b &3b. In Figure 71 is shown that Rotliegendes 3c exhibit the highest horizontal displacements of the soil along the specific path, followed by Quarry fines 3b & 2b and EVM. Smaller values are resulting from Quarry fines 1b, Rotliegendes 2b and the lowest one from Rotliegendes 1b. The vertical displacement in the soil across the path is displayed in Figure 72, where the model sets exhibit highest to lowest value with the following order: Quarry fines 2b, Quarry fines 3b, Rot 3c, EVM, Rotliegendes 1b, Rotliegendes 2b.

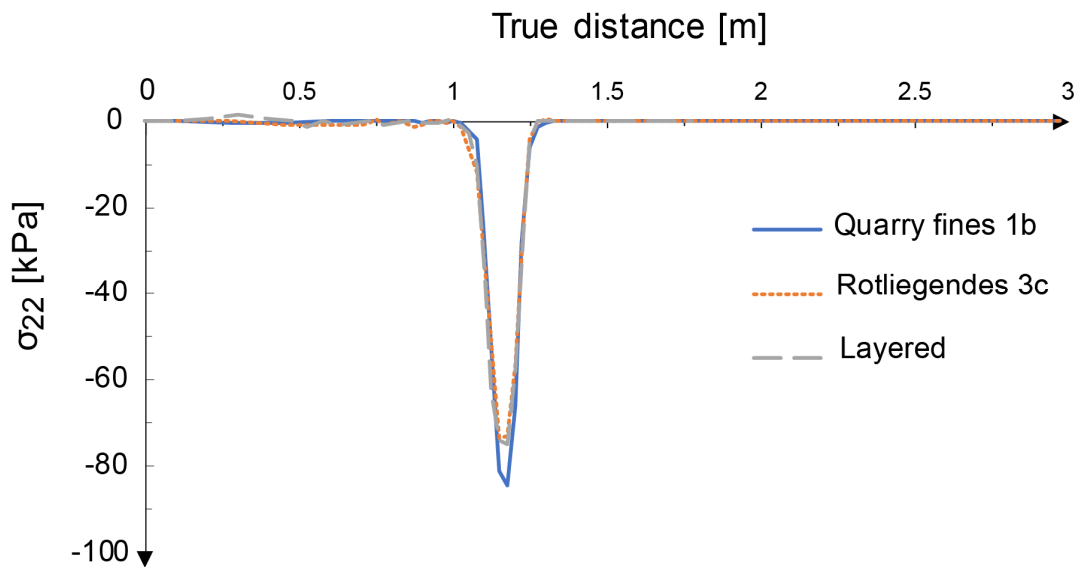


Figure 66: Vertical stress in the soil versus true distance for velocity of 5 rad/s and vertical force of 2 kN.



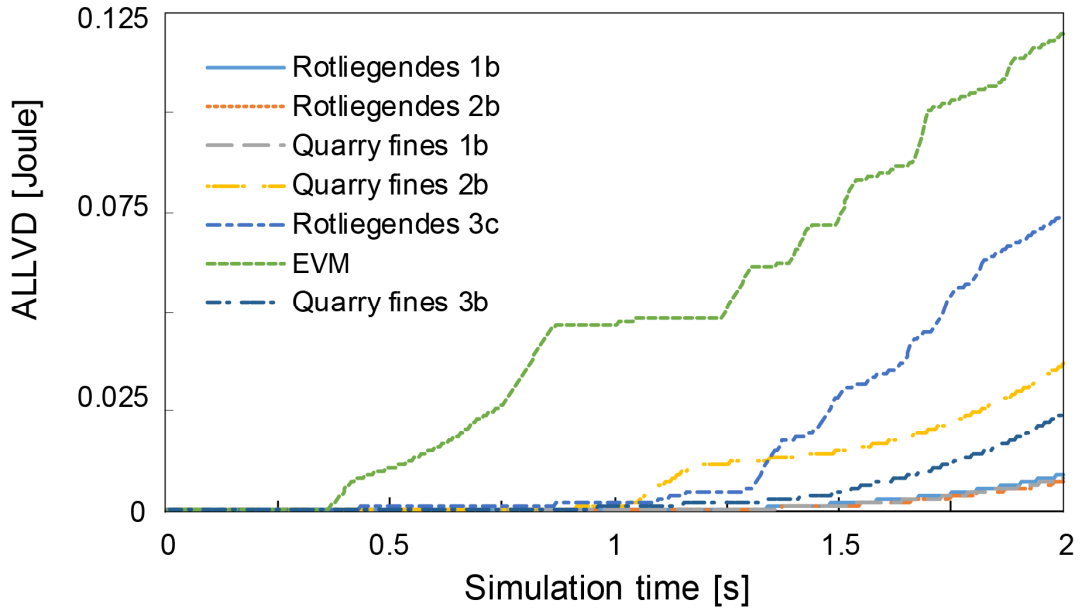


Figure 67: Viscous dissipated energy for velocity of 5 rad/s and vertical force of 2 kN for various soils.

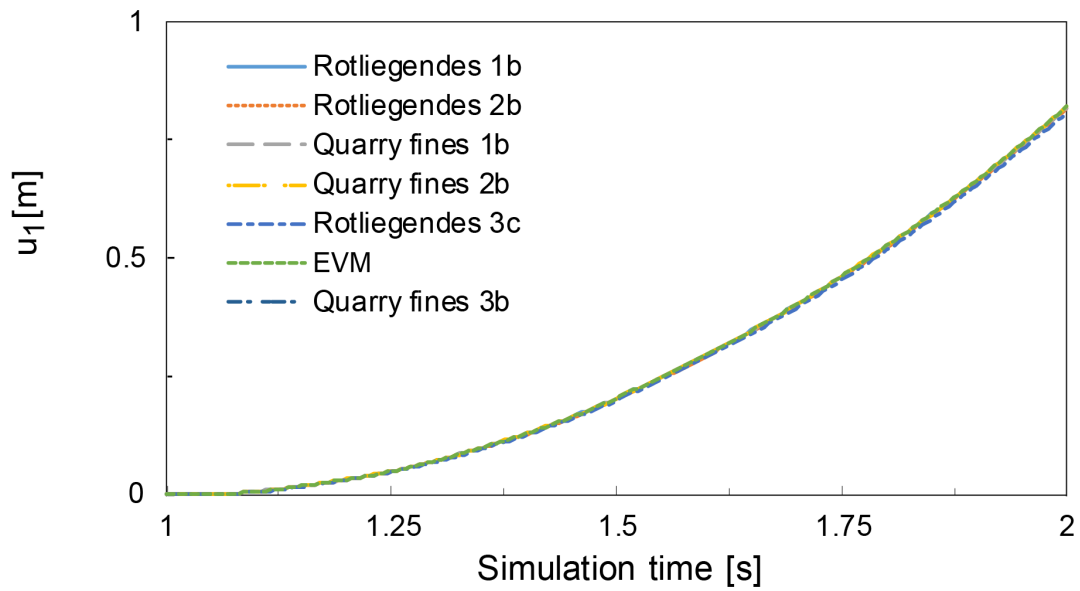


Figure 68: Horizontal displacement  $u_1$  for velocity of 5 rad/s and vertical force of 2 kN for various soils.

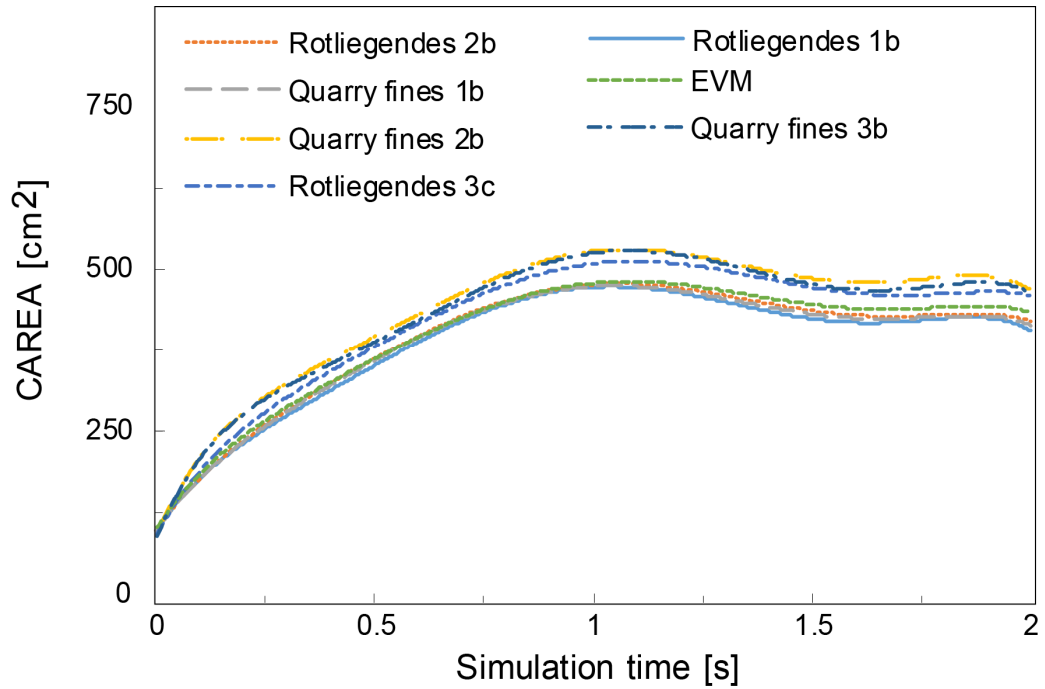


Figure 69: Contact area of the wheel and the soil versus time for velocity of 5 rad/s and vertical force of 2 kN for various soils.

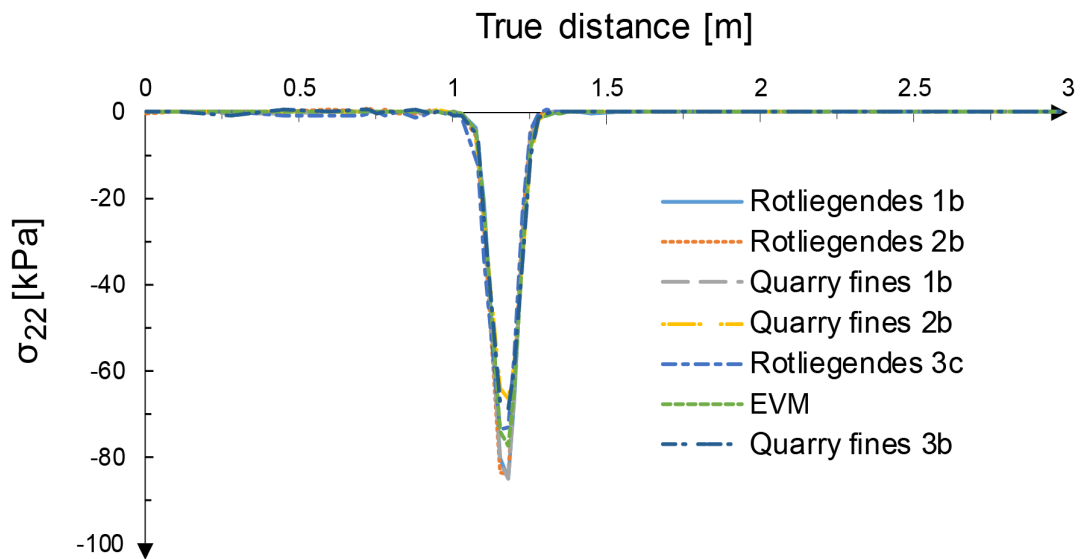


Figure 70: Vertical stress in the soil versus true distance for velocity of 5 rad/s and vertical force of 2 kN for various soils.

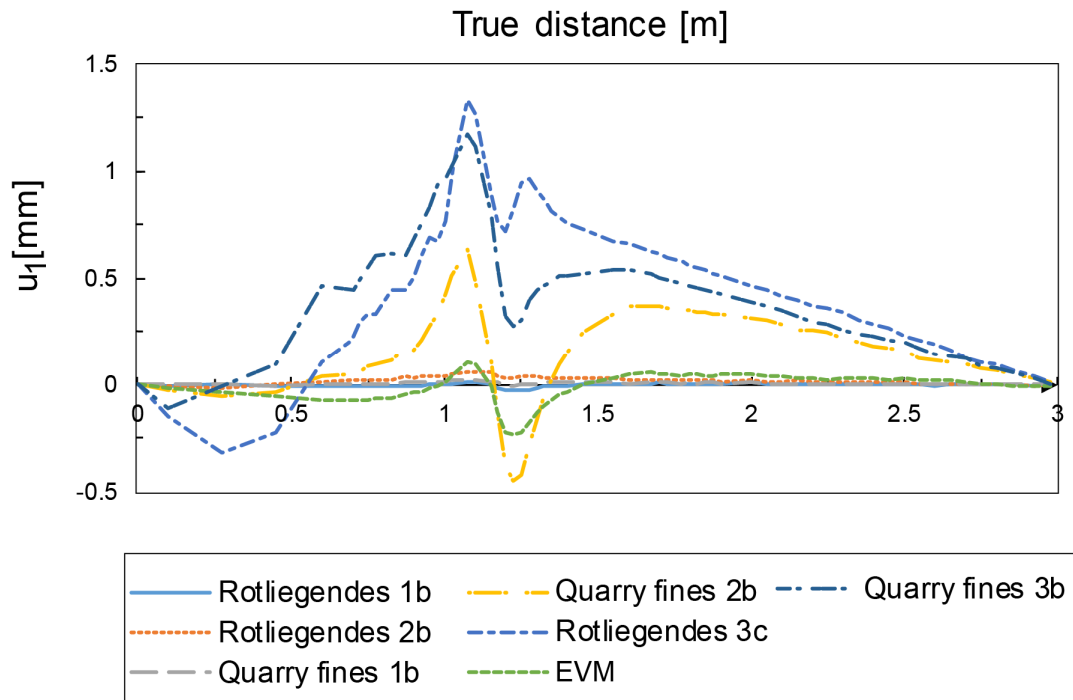


Figure 71: Horizontal displacement  $u_1$  in the soil versus true distance for velocity of 5 rad/s and vertical force of 2 kN for various soils.

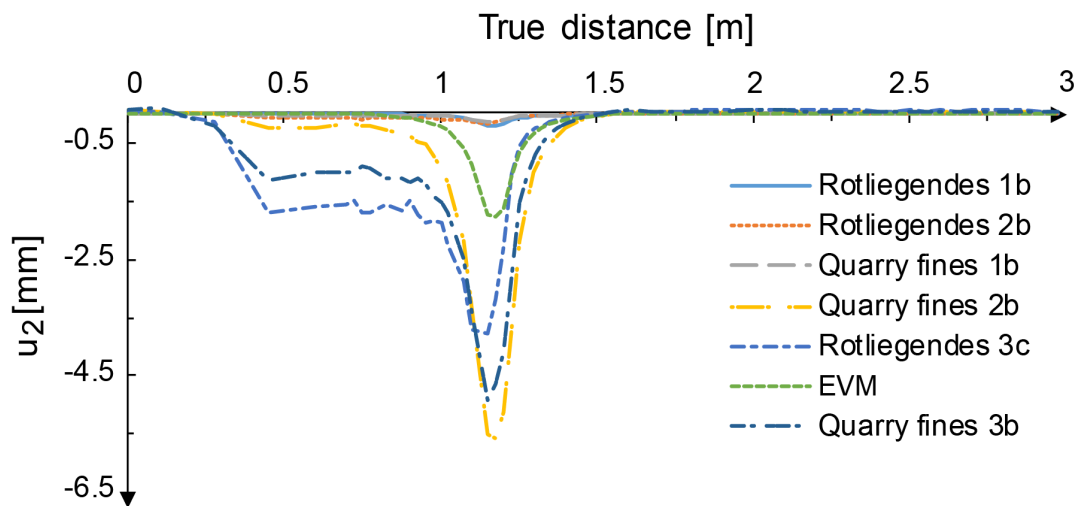


Figure 72: Vertical displacement  $u_2$  in the soil versus true distance for velocity of 5 rad/s and vertical force of 2 kN for various soils.

Furthermore, it was decided to compare the different calibrated model sets to assess the influence of the different combinations of Young's modulus and yield stress. Comparisons were carried out for a vertical force of 2 kN and an angular velocity of 5 rad/s only for the model sets that had noteworthy differences in the calibrated values of  $E$  and  $d$ . In Figure 73 and Figure 74 the model sets of Rotliegendes 1b&1c and the model sets of Rotliegendes 2b&2c are compared respectively. The results of the model sets Quarry fines 1a&1b and Quarry fines 2b&2c are compared in Figure 75 and Figure 76 respectively. Generally, the calibrated model sets exhibit similar values of stresses with an exception of the model sets of Quarry fines 2b and 2c where the difference is approximately 10kPa.

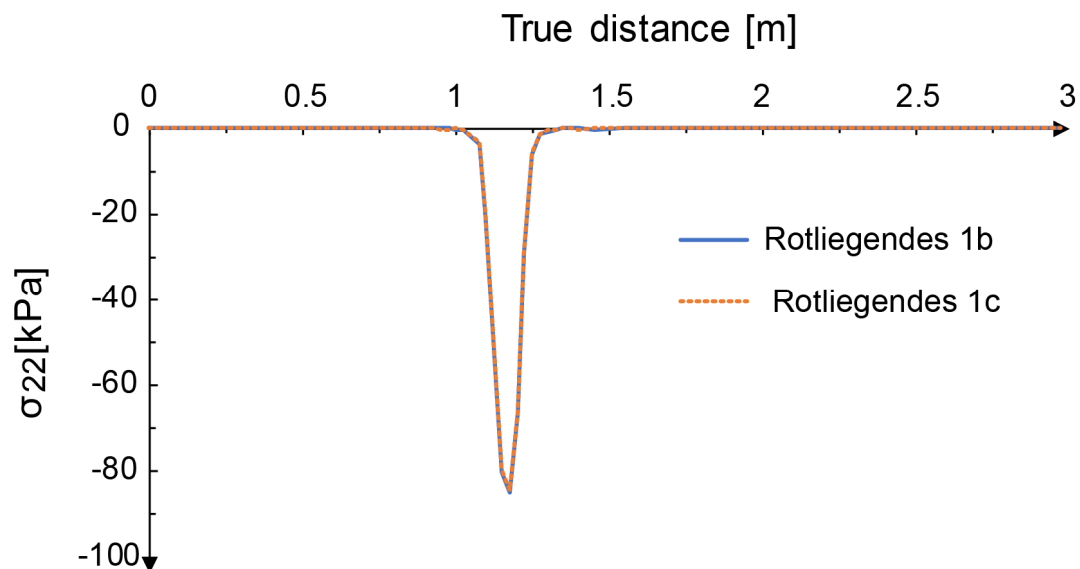


Figure 73: Comparison of the response in terms of normal stress for two model sets of Rotliegendes.

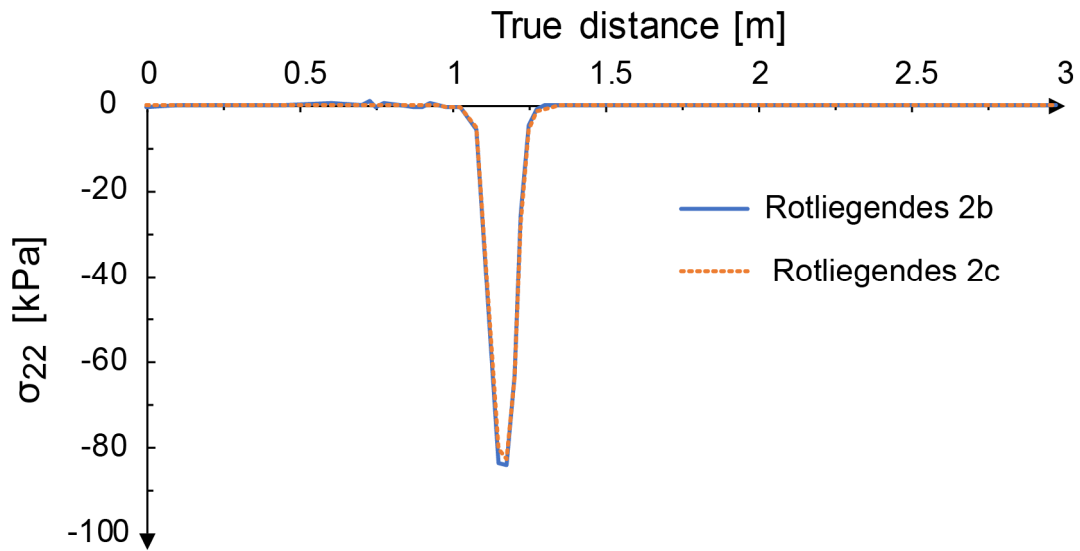


Figure 74: Comparison of the response in terms of normal stress for two model sets of Rotliegendes.

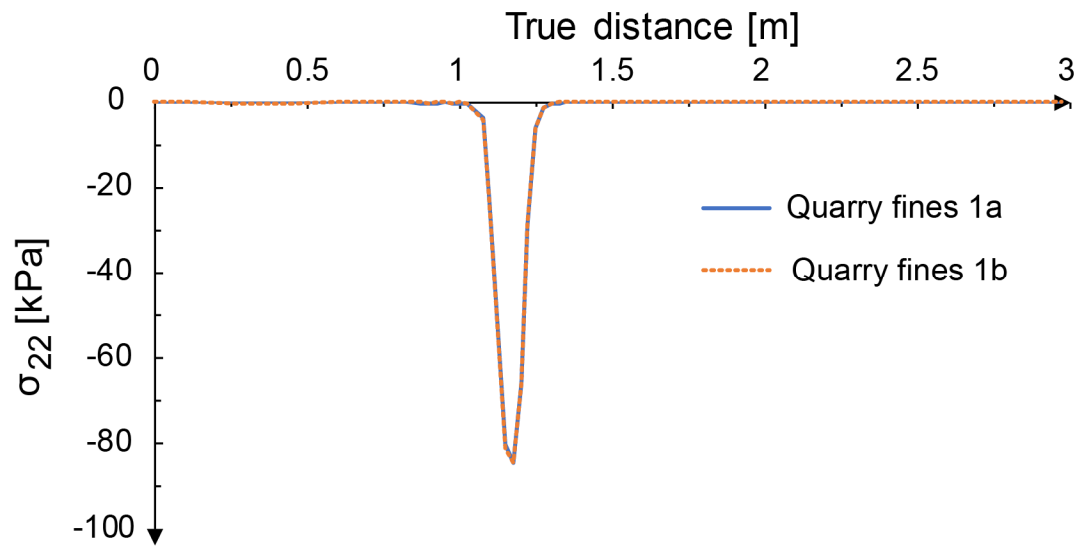


Figure 75: Comparison of the response in terms of normal stress for two model sets of Quarry fines.

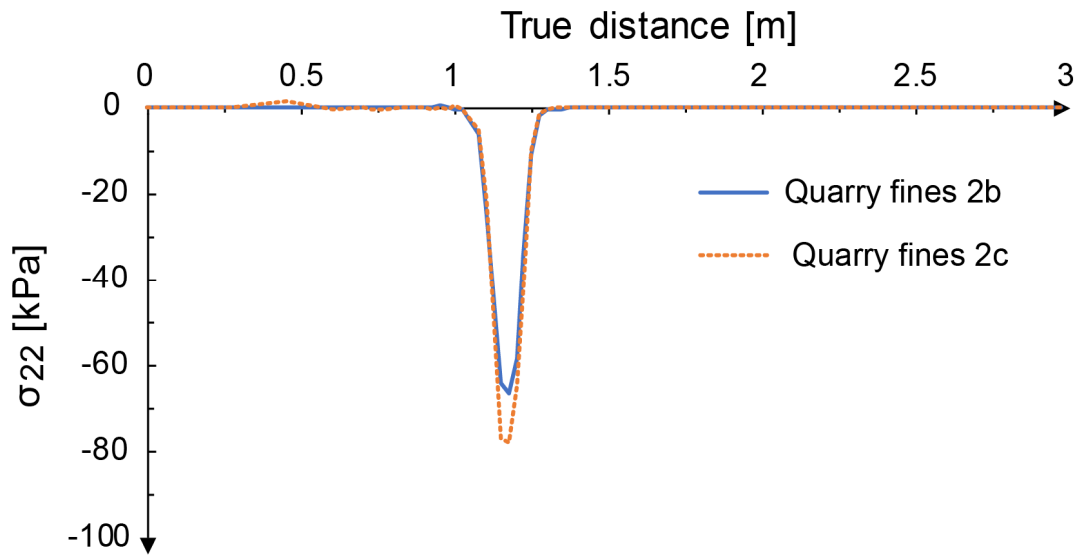


Figure 76: Comparison of the response in terms of normal stress for two model sets of Quarry fines.

Analyses with the (ii) model parameters displayed in Table 15 and Table 16, which corresponds to the direct shear test results of the soils carried out without the flat tire section, were also conducted. Comparisons are made with the corresponding models resulted from the (i) case which corresponds to the shear test results from the soils with the flat tire section, for a vertical force of 2 kN and an angular velocity of 5 rad/s. The comparisons are plotted in the following Figure 77 to Figure 82. The differences between the resulted normal stress between the model parameters (i) and (ii) for Rotliegendes 1, 2 and 3 and Quarry fines 1, 2 and 3 are 1.86 kPa, 3.96 kPa, 50.32 kPa, 5.97 kPa, 7.97 kPa, 8.60 kPa respectively. The differences are generally within acceptable limits, except for the case of the Rotliegendes 3 where the difference is very high. The latter can be attributed to the high water content of Rotliegendes 3 which may lead an unstable response.

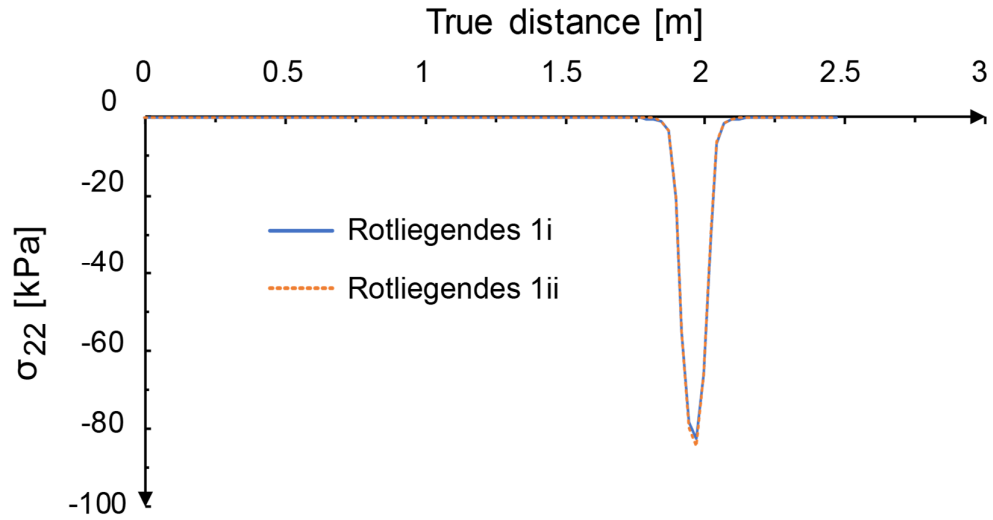


Figure 77: Comparison of the response in terms of normal stress for two model sets of Rotliegendes.

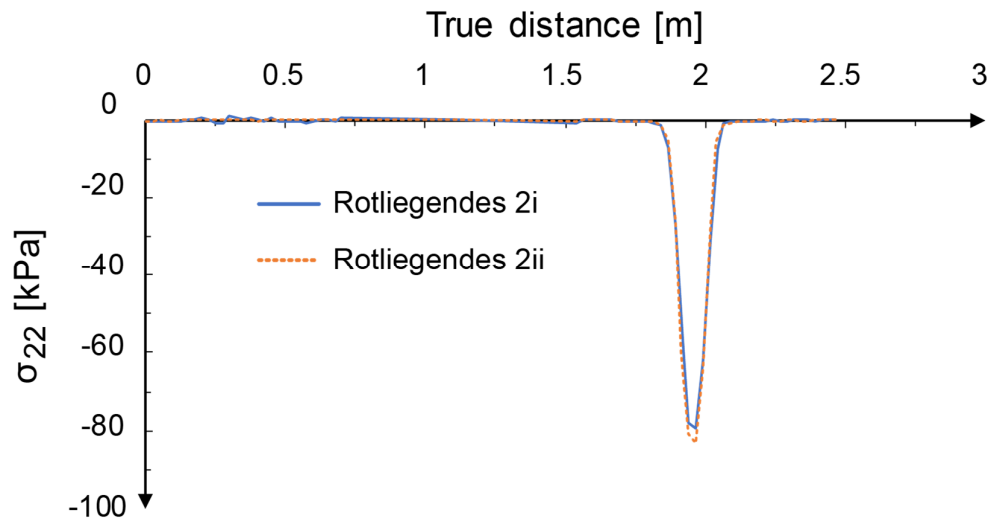


Figure 78: Comparison of the response in terms of normal stress for two model sets of Rotliegendes.

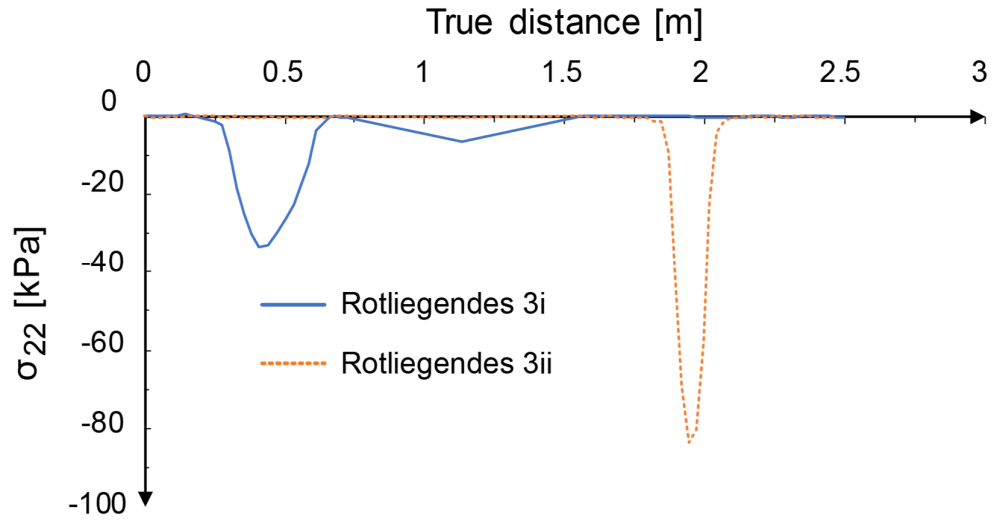


Figure 79: Comparison of the response in terms of normal stress for two model sets of Rotliegende.

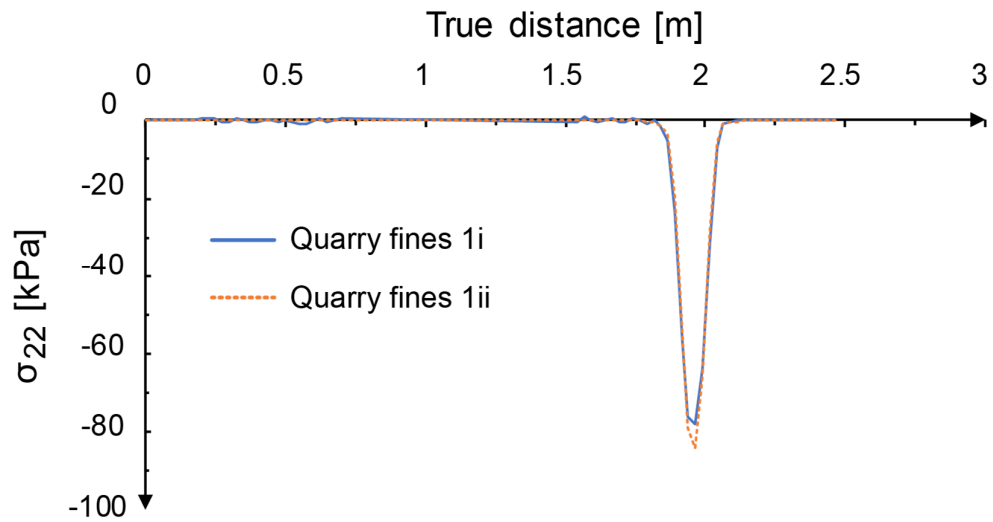


Figure 80: Comparison of the response in terms of normal stress for two model sets of Quarry fines.



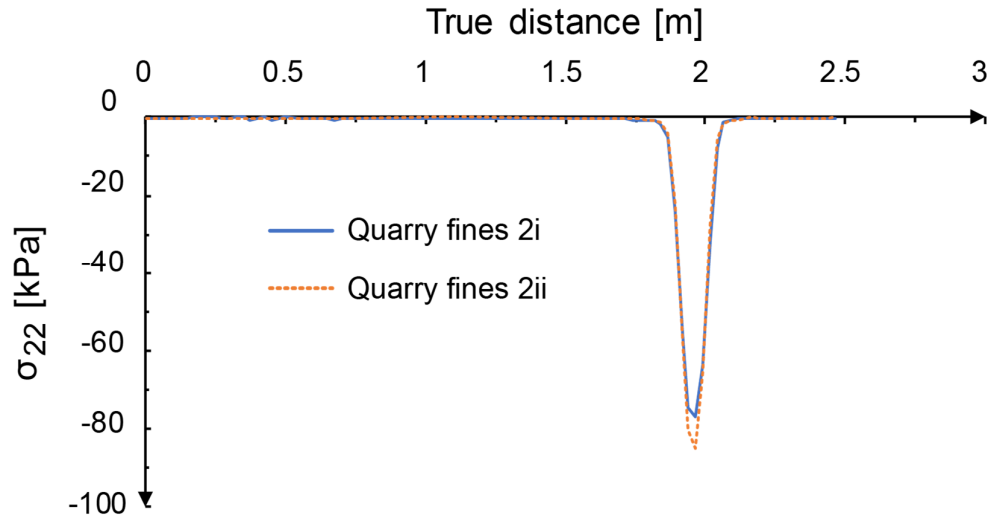


Figure 81: Comparison of the response in terms of normal stress for two model sets of Quarry fines.

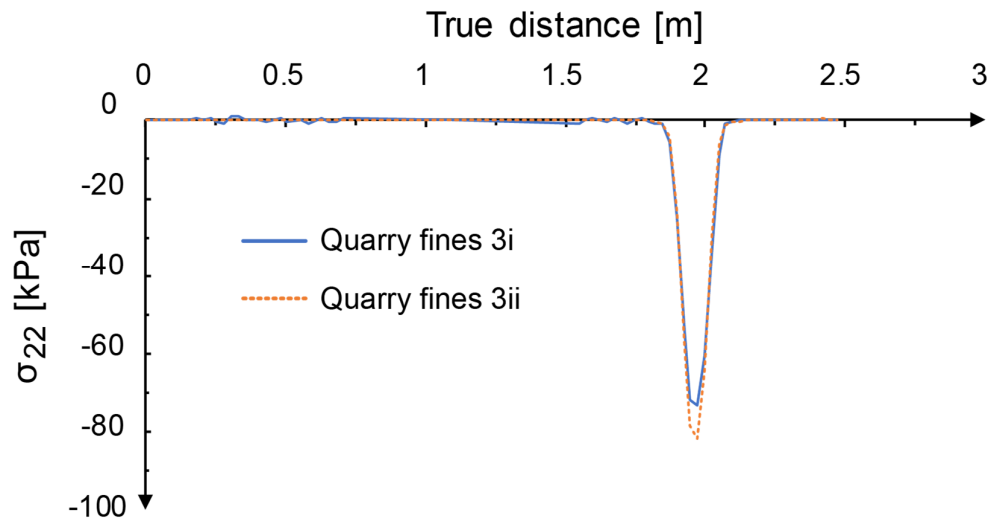


Figure 82: Comparison of the response in terms of normal stress for two model sets of Quarry fines.

### 7.5.2 Sensitivity to vertical force and to angular velocity

Results investigating different combinations of angular velocities and vertical forces are displayed in Figure 83 to Figure 88. From Figure 83 it is inferred that for higher vertical force and for higher rolling speed, the dissipated energy

increases. Overall the case of Rotliegendes 3c with 4kN vertical force and an angular velocity of 10 rad/s exhibits higher dissipated energies. From Figure 84 it is inferred that the change of vertical force doesn't affect significantly the results for Rotliegendes 3c. An increase in the translational velocity results in highest travelled distance. As shown in Figure 85 the highest the vertical force, the highest the contact area while the imposed angular velocity affects only mildly the values of contact area. Figure 86 displays the stresses in the soil along the followed path, at the end of the analysis. An increase of the vertical force causes an increase in the stress, while the increased velocity just shifts the maximum stress further away as the wheel travels for more distance. From Figure 87 it is inferred that higher angular velocity and vertical force causes higher negative values of horizontal displacement of the soil, meaning that some soil is pushed backwards to sustain movement. An increase in vertical force, causes an overall increase in the values of horizontal displacement of the soil  $u_1$ . On the other hand, an increase in the angular velocity leads to both lower and higher  $u_1$  values. As shown in Figure 88, an increase in force causes an increase in the vertical displacement while an increase in the velocity, shifts the location of the highest settlement values as the wheel travels for further distance.

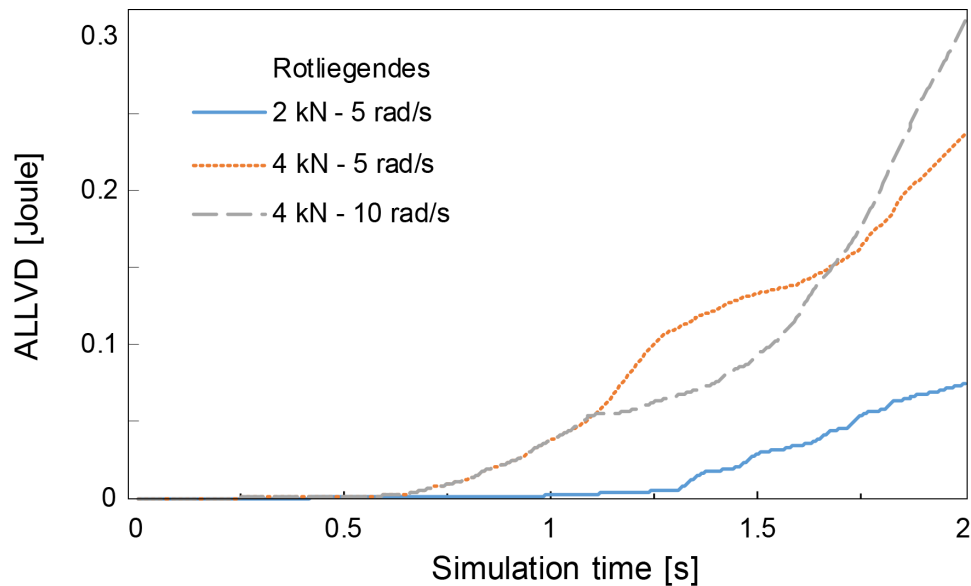


Figure 83: Viscous dissipated energy vs simulation time for selected combinations of velocities (5 and 10 rad/s) and vertical forces (2 and 4 kN) for Rotliegendes 3c.

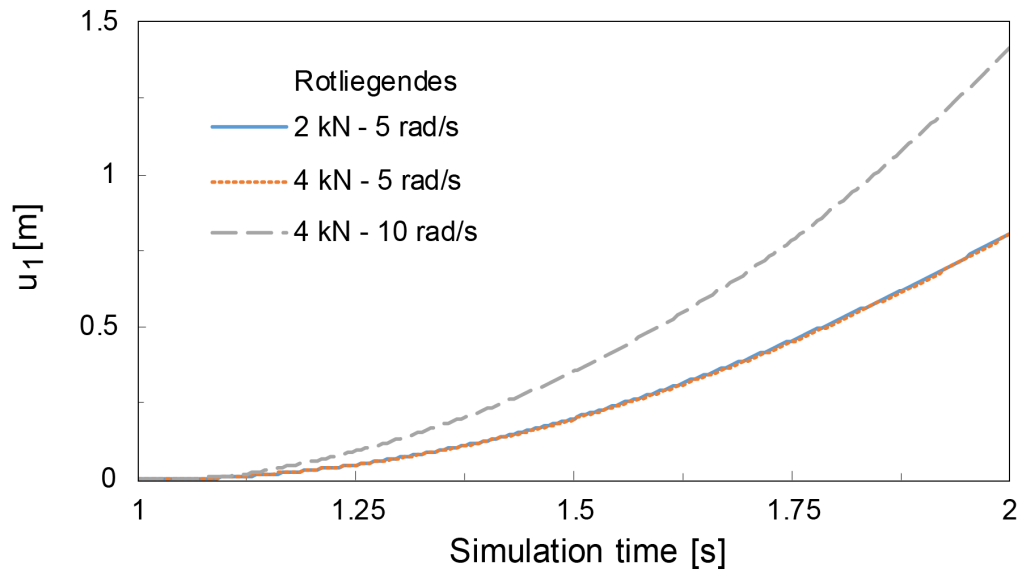


Figure 84: Horizontal displacement  $u_1$  vs simulation time for combinations of velocities (5 and 10 rad/s) and vertical forces (2 and 4 kN) for Rotliegendes 3c.

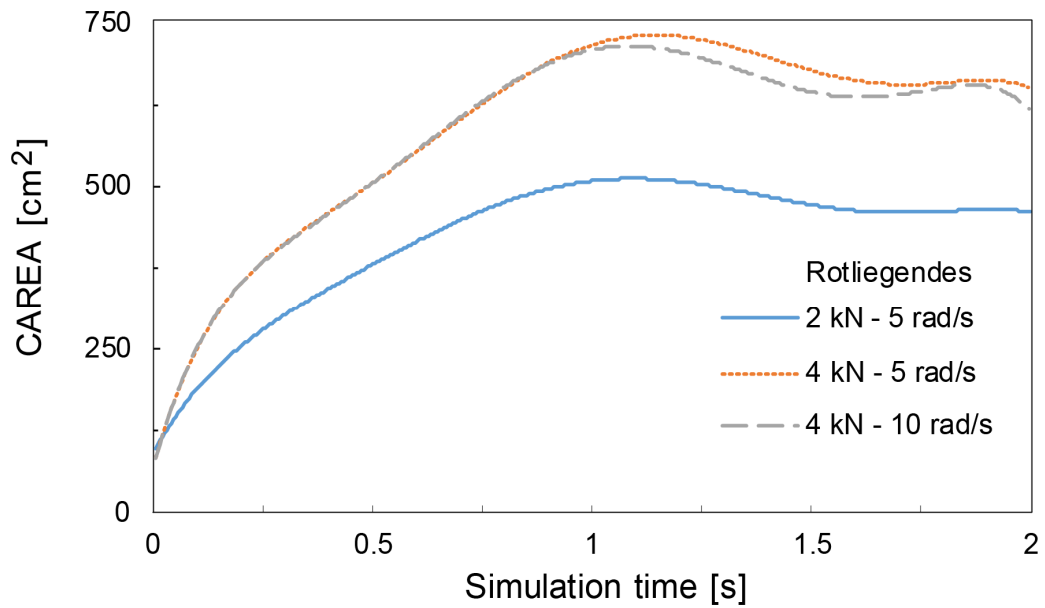


Figure 85: Contact Area of the wheel-soil vs simulation time for selected combinations of velocities (5 and 10 rad/s) and vertical forces (2 and 4 kN) for Rotliegendes 3c.

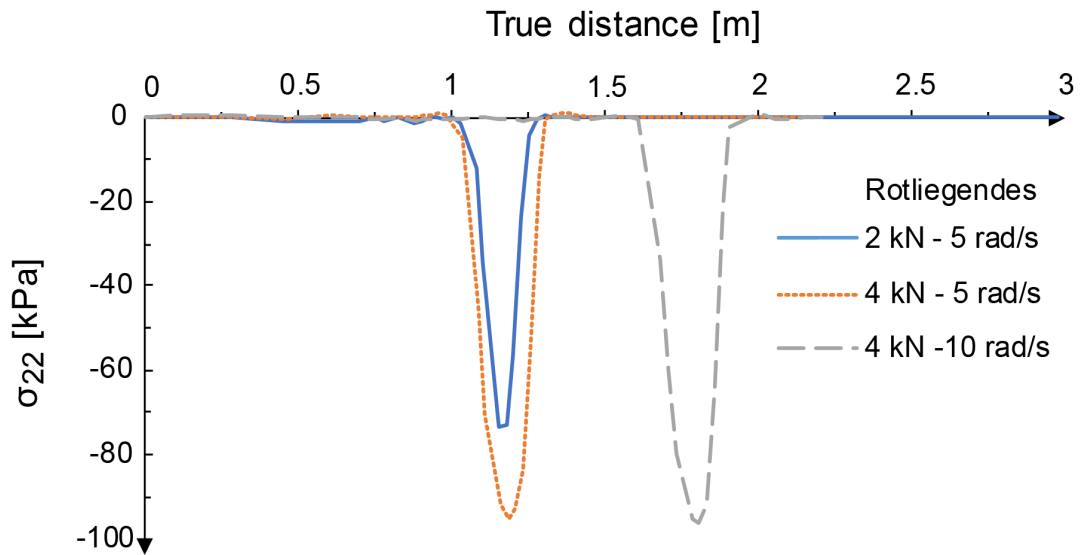


Figure 86: Vertical stress in the soil vs true distance for selected combinations of velocities (5 and 10 rad/s) and vertical forces (2 and 4 kN) for Rotliegende 3c.

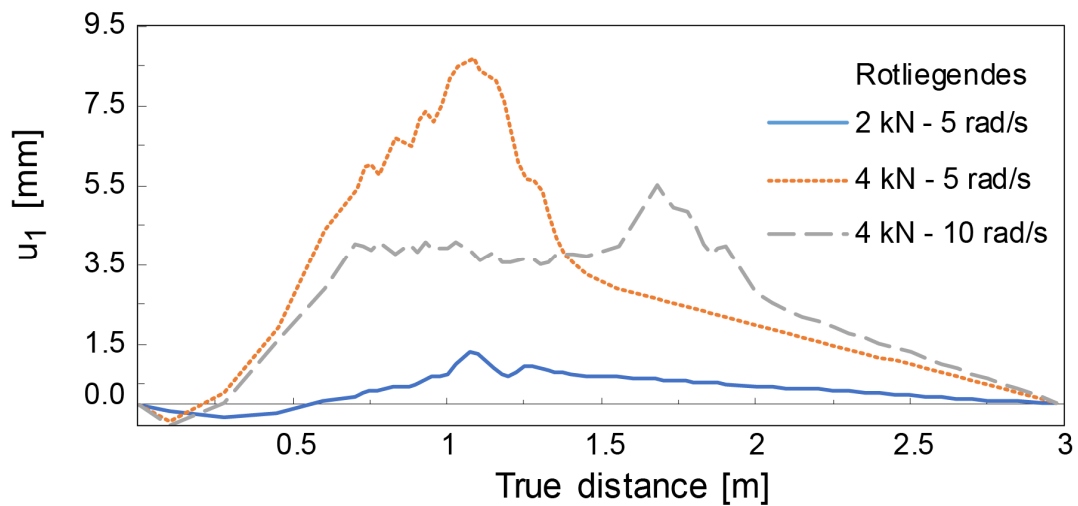


Figure 87: Horizontal displacement  $u_1$  in the soil vs true distance for selected combinations of velocities (5 and 10 rad/s) and vertical forces (2 and 4 kN) for Rotliegende 3c.

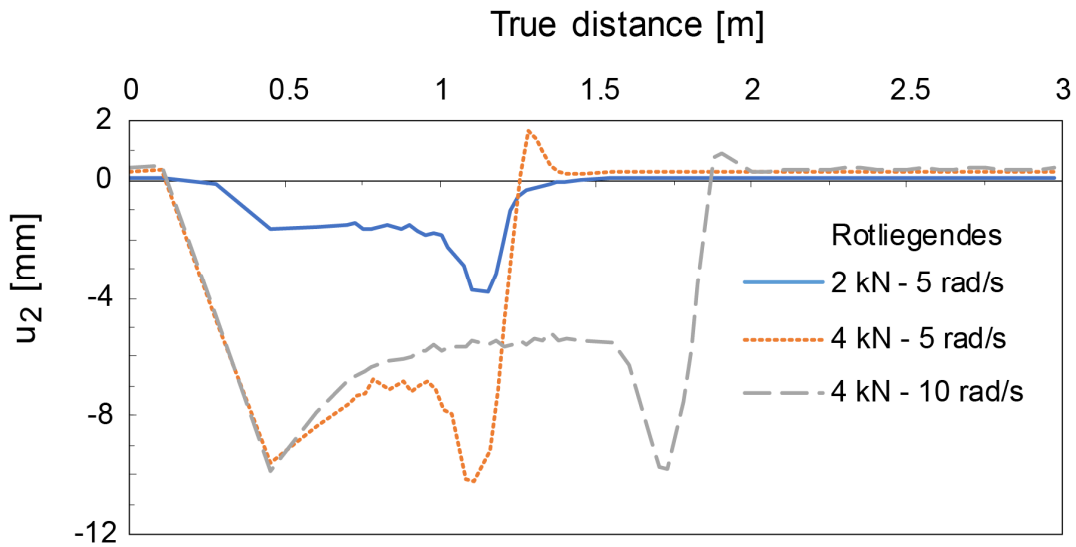


Figure 88: Vertical displacement  $u_2$  in the soil vs true distance for selected combinations of velocities (5 and 10 rad/s) and vertical forces (2 and 4 kN) for Rotliegende 3c.

### 7.5.3 Braking, free rolling, driving

Applying an angular velocity to the model results in the corresponding free rolling translational velocity. By using the results of the first part of the simulation, where only an angular velocity of 5 rad/s was imposed on the wheel along with a vertical force of 2 kN, the approximated corresponding free rolling velocity for the model set Rotliegende 3c is 1.63 m/s. For the braking and driving case, typical velocity values of 1 and 3 m/s were chosen respectively. As shown in Figure 89 the driving case has the highest energy loss, which is approximately 5 times higher than the free rolling case, followed by the braking case. Contrary, in the following figures the response has generally the following order: driving, free roll, braking. From Figure 90 is shown that for higher initial translational velocities the wheel travels further which is attributed to the higher initial kinetic energy. Regarding the resulting contact area plotted in Figure 91, there is only a slight difference for the investigated cases between braking, free rolling and driving. The maximum vertical stress along the traveled path is shown in Figure 92 where all the cases exhibit similar stress values, specifically 72.9 kPa, 74.97 kPa and 75.29 kPa for braking, free rolling and driving respectively. As shown in Figure 93, the highest horizontal soil's displacement results are from the driving case while

for the case of braking more part of the soil has negative horizontal displacement, meaning that the soil is pushed backwards. The maximum vertical displacement of soil as shown in Figure 94, exhibit similar values for all the 3 cases with values 4.17 mm, 4.04 mm and 3.61 mm for braking, free rolling and driving respectively.

The total horizontal reaction force  $RF_1$  acting on the axle of the wheel, is plotted in Figure 95 where it is shown how the  $RF_1$  turns from negative to positive for moving from braking to driving conditions. For the free rolling condition, the resultant resistance is zero. The corresponding moment in the axle of the wheel  $RM_3$  is plotted in Figure 96. The transition from negative to positive value of moment is caused from the transition of braking to driving conditions. The fluctuations are due to the dynamic effects of the simulation. To reduce the noise in the results of the simulation, a smoothly increasing amplitude for the loading of the wheel was utilized.

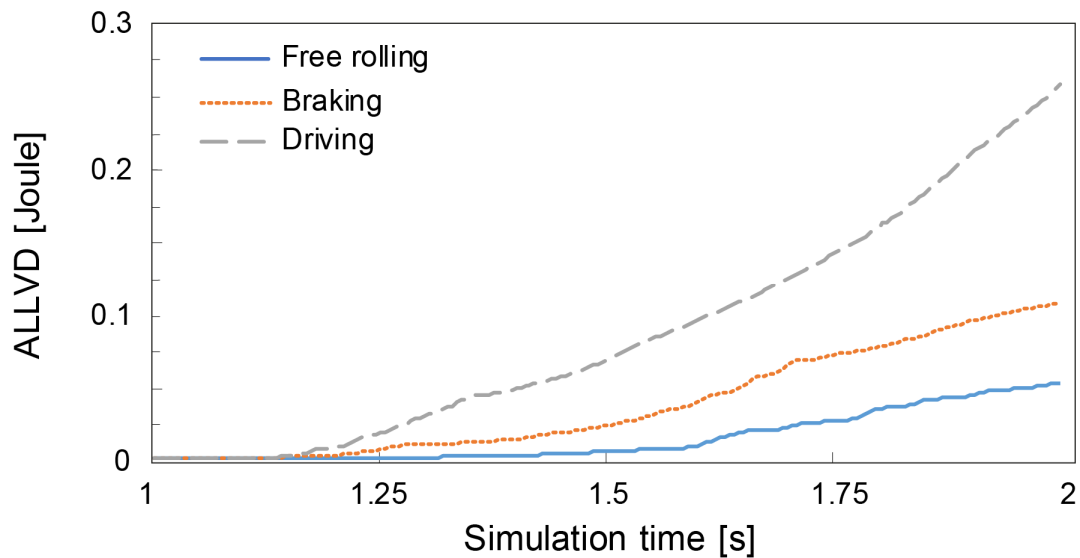


Figure 89: Viscous dissipated energy vs simulation time for the model set Rotliegendes 3c for braking, free rolling and driving conditions with a vertical force of 2 kN.

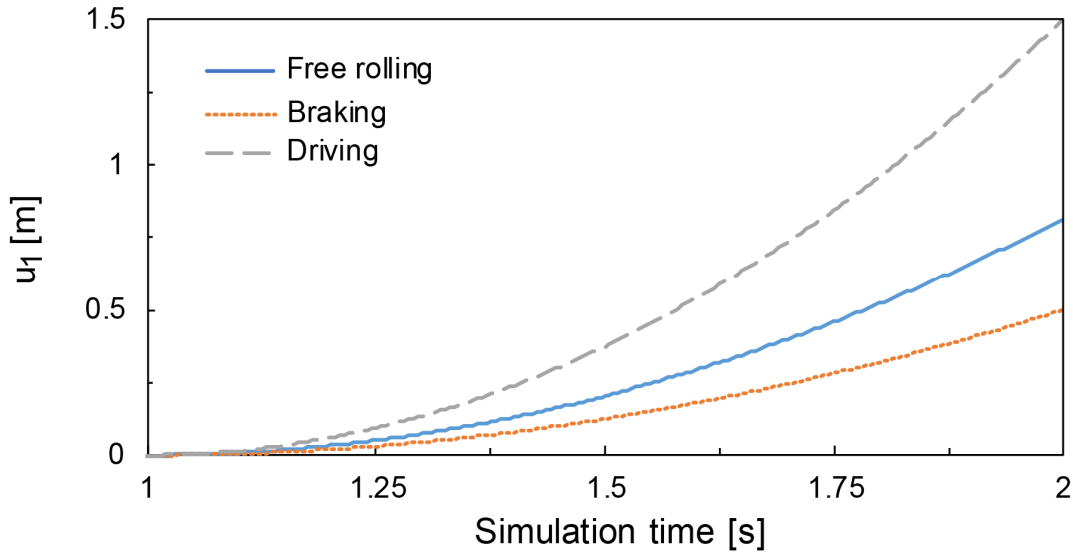


Figure 90: Horizontal displacement of the wheel vs simulation time for the model set Rotliegendes 3c for braking, free rolling and driving conditions with a vertical force of 2 kN.

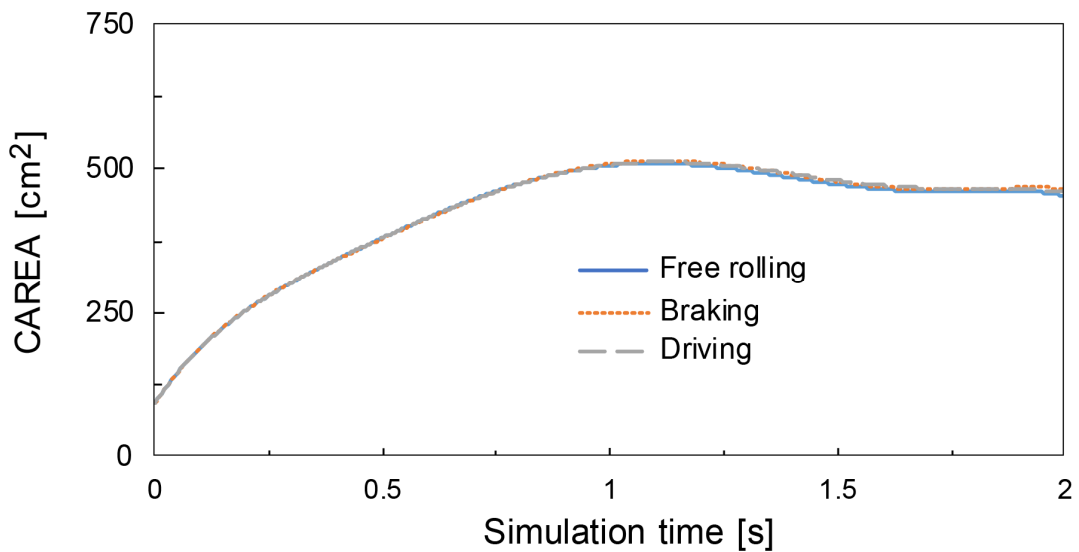


Figure 91: Contact area vs simulation time for the model set Rotliegendes 3c for braking, free rolling and driving conditions with a vertical force of 2 kN.

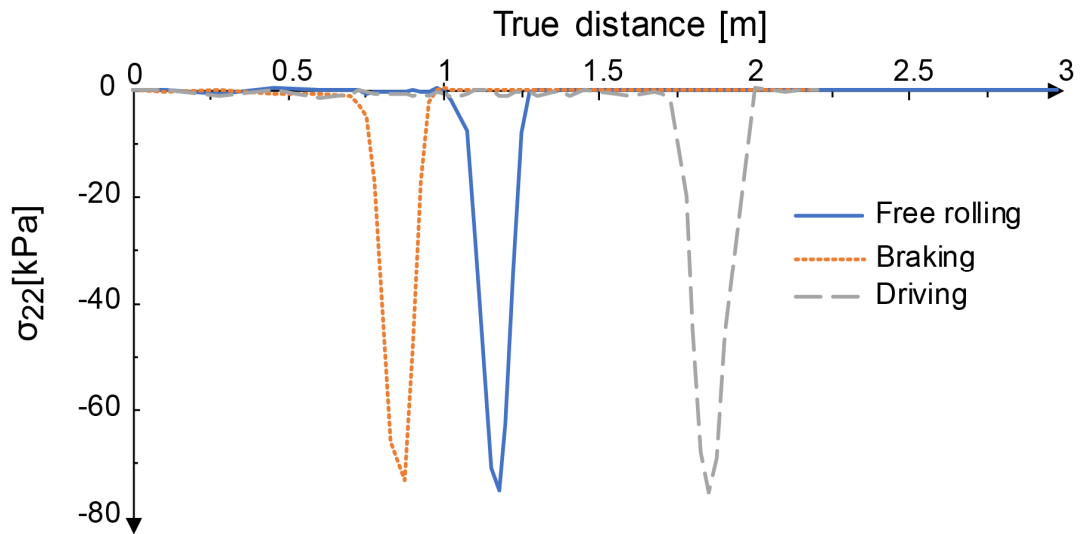


Figure 92: Vertical stress in the soil vs true distance for the model set Rotliegendes 3c for braking, free rolling and driving conditions with a vertical force of 2 kN.

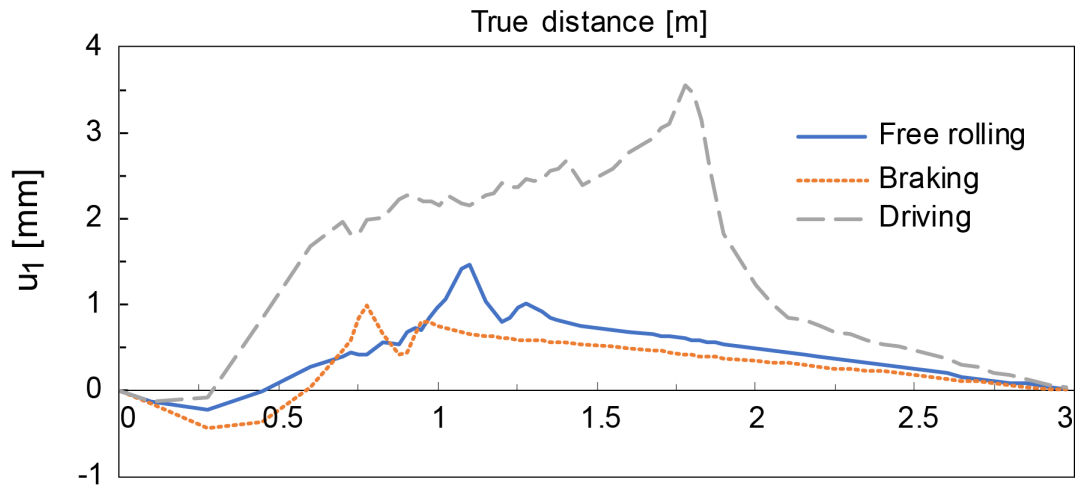


Figure 93: Horizontal displacement  $u_1$  in the soil vs true distance for the model set Rotliegendes 3c for braking, free rolling and driving conditions with a vertical force of 2 kN.



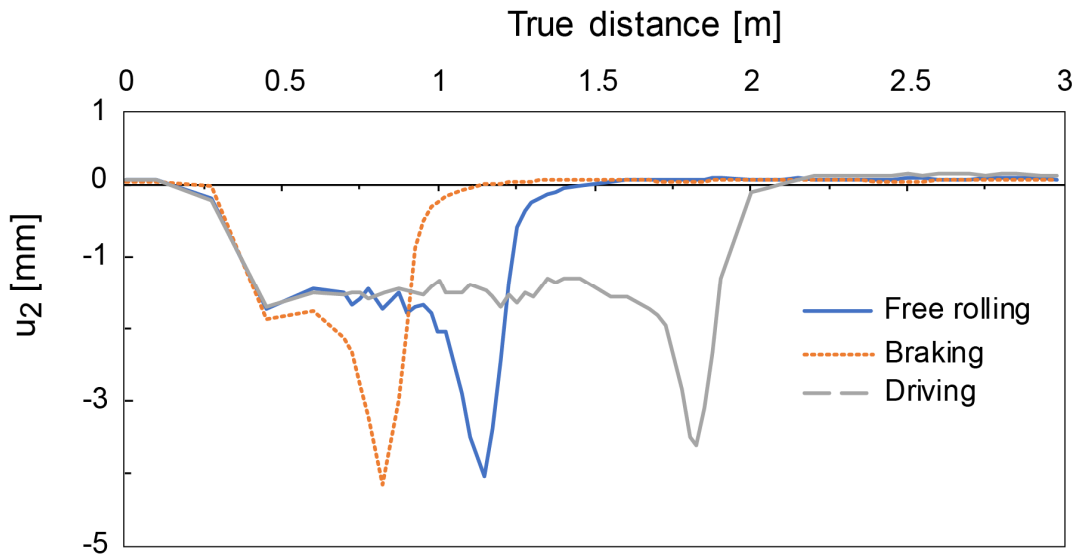


Figure 94: Vertical displacement  $u_2$  in the soil vs true distance for the model set Rotliegendes 3c for braking, free rolling and driving conditions with a vertical force of 2 kN.

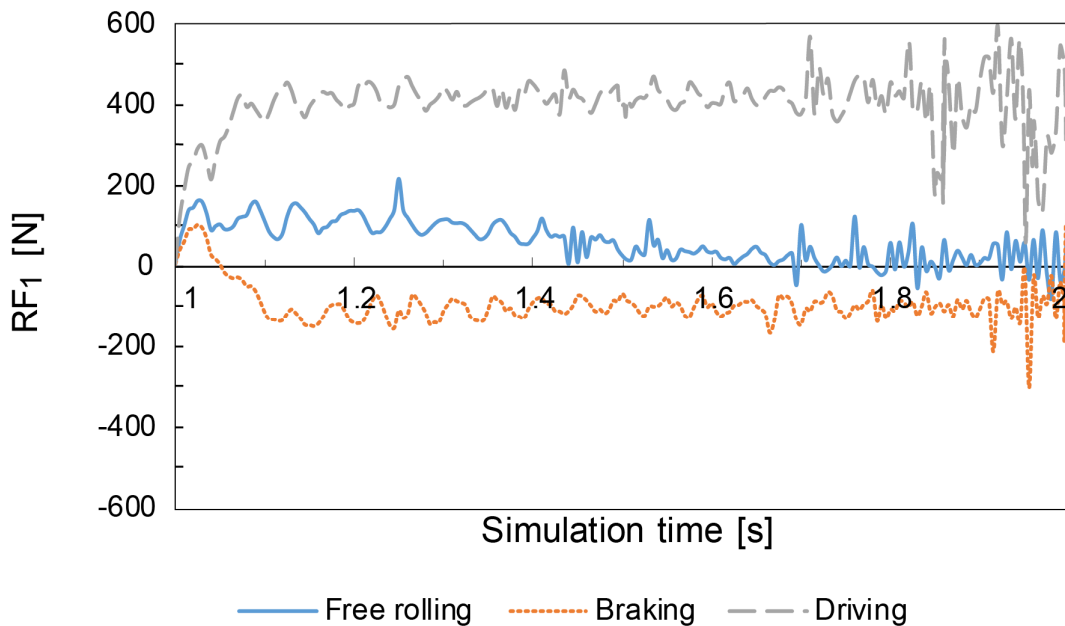


Figure 95: Horizontal reaction force vs simulation time for the model set Rotliegendes 3c for braking, free rolling and driving conditions with a vertical force of 2 kN.

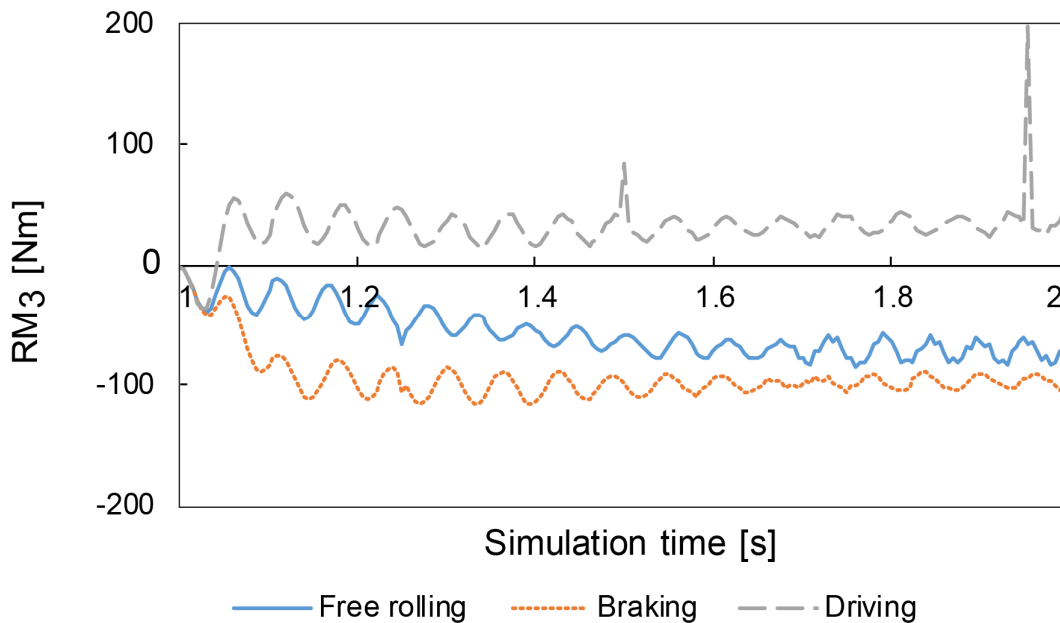


Figure 96: Rotational Moment vs simulation time for the model set Rotliegendes 3c for braking, free rolling and driving conditions with a vertical force of 2 kN.

## 7.6 Discussion

In this chapter, numerical simulations were utilized for calibration of a specific wheel design and specific soil types. The calibration was based on the experimental results of the stationary tests on non-pneumatic wheel described in the Chapter 6. Firstly, the wheel model was calibrated by utilizing experiments against a steel plate. Secondly, the interaction of the wheel with soil was calibrated by creating soil models corresponding to the soils used in the experiments. It was shown that the main influential parameters are the Young's modulus and the yield stress of soil for the footprint analyses. It was shown that different combinations of Young's modulus  $E$  and yield stress  $\sigma_{yield}$  can lead to the same final results, but the followed path of force - displacement differs in each case.

Subsequently, the calibrated soil parameters were used to simulate rolling scenarios. Comparing the results of the various model sets it was inferred that

for the sets with lower Young's modulus values the contact area increase and subsequently the stresses in the soil decrease. The rolling response in terms of normal stress of the different model sets for each soil was similar, meaning that the calibration of the soil by means of single tire-soil tests is adequate. The results from the calibrations based on the direct shear tests with the flat tire section and the tests with only soil, exhibit similar normal stress values with an exception of the model sets of Rotliegendes 3 where there is a significant change in the response which can be attributed to the high water content of the material.

For higher vertical force and higher rolling velocity the dissipated energy increases. An increase in the angular velocity results in an increased travelled distance due to the higher initial kinetic energy. A higher contact area and higher peak stresses are resulted from an increase in the vertical force. An increase in angular velocity affects slightly the results of contact area and stress - it just shifts the location of the maximum peak stress as the wheel travels further. On the other hand, the higher angular velocities cause higher negative values of horizontal displacements in the soil, meaning that the soil is pushed backwards. For an increase in vertical force the horizontal displacement in the soil generally increases. On the contrary, an increase in the angular velocity leads to partly decreased and partly increased  $u_1$  displacements which is attributed to the mobility of the wheel under the specific loading conditions. The vertical settlement of the soil increases with increasing vertical force while an increased angular velocity shifts the maximum settlement but not its value.

Moving on to the comparisons between braking, free rolling and driving, five times more energy is dissipated for the case of driving compared to the free rolling case. The maximum peak vertical stress in the soil is similar to all the three cases, where the highest stress peak results from driving as it is associated with higher velocity. The maximum vertical subsidence results from the case of braking while the lowest one is the one from the driving conditions. For the case of driving the resulted travelled distance of the wheel and the associated horizontal displacement of the soil was higher compared to the cases of braking and free rolling. For the case of braking, the more soil was pushed backwards resulting in more negative  $u_1$  values of the soil. The high frequency noise in the reaction force and in the moment of the wheel's center is attributed to the repeated dynamic impact of the nodes of the wheel

as they come in contact with the soil. The main damping mechanism in the wheel is due to the viscoelastic characteristics defined in the model. A negative force and a negative moment, indicate braking while positive values indicate driving conditions. In Figure 97 and Figure 98 a typical time lapse of the footprint on the soil and the movement of the wheel are plotted.

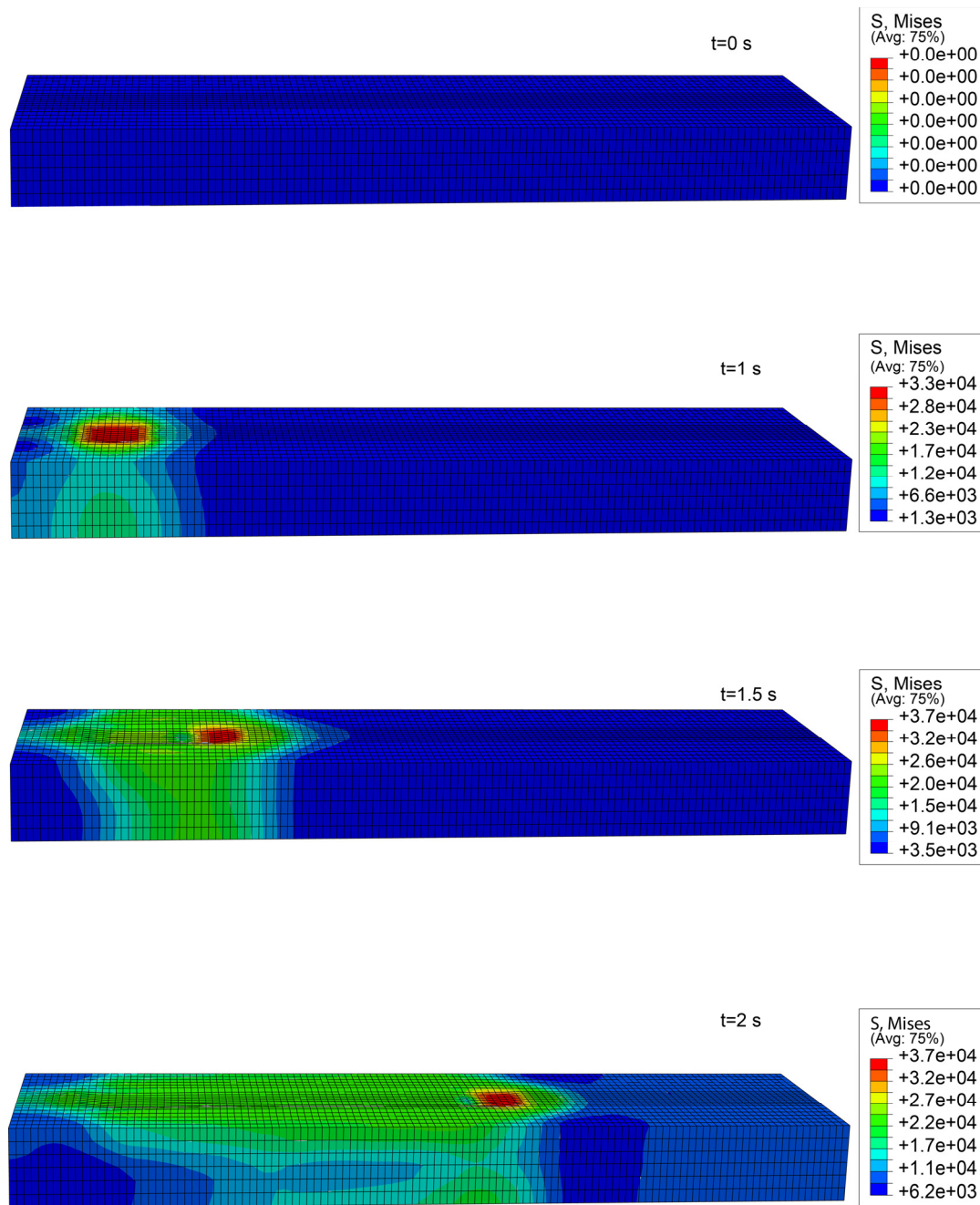


Figure 97: Evolution of the footprint with time on the soil of Rotliegendes 3c at 4kN vertical force and angular velocity of 10 rad/s.

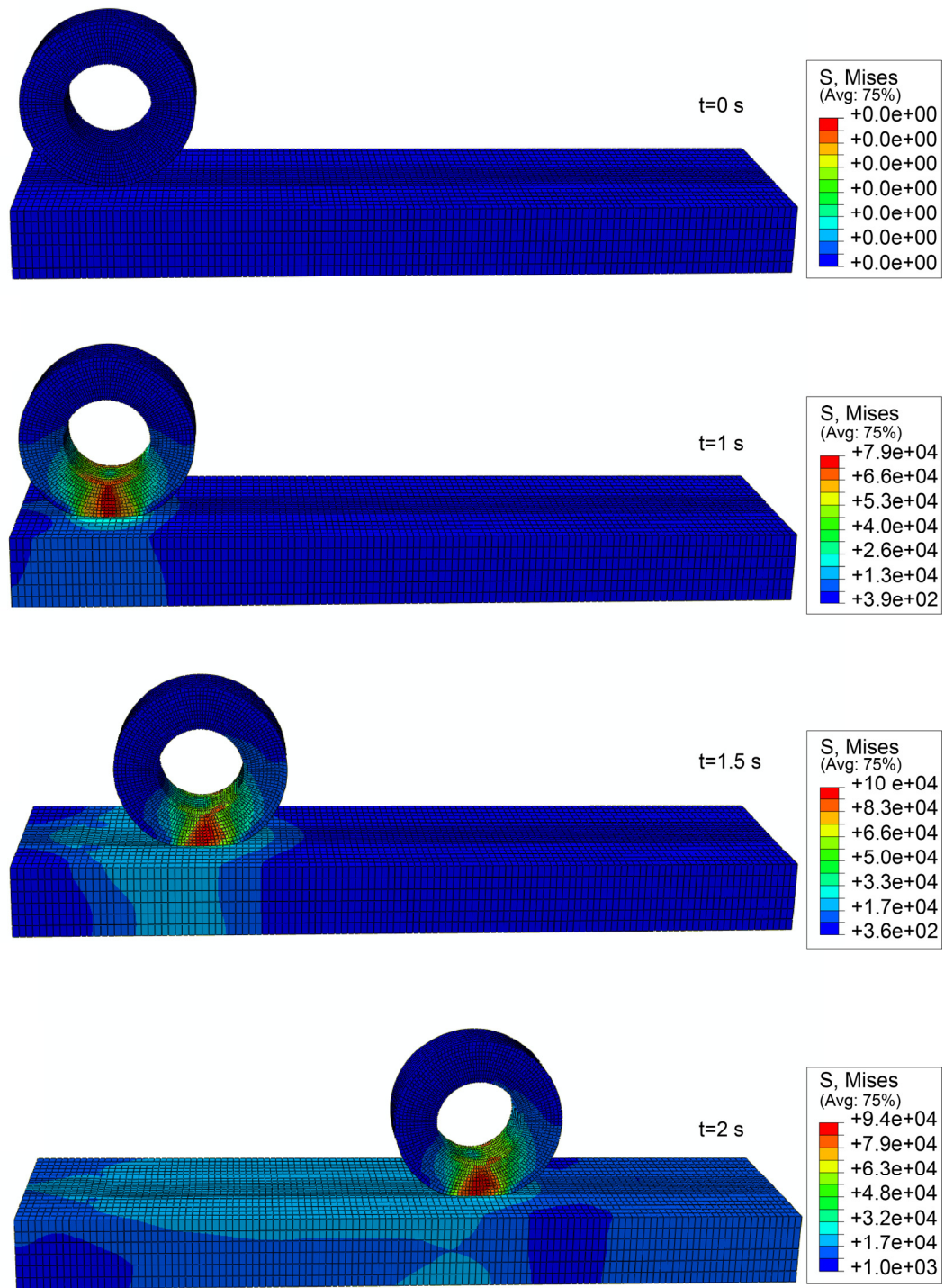


Figure 98: Evolution of moving wheel with time of Rotliegendes 3c with 4kN vertical force and angular velocity of 10 rad/s.

## 8 Summary and Outlook

For estimating soil properties, in-situ testing is used worldwide as a quick and reliable mean. Both static and dynamic penetration tests were considered in this thesis. Specifically, focus was placed on the cone penetration test CPT, the dynamic penetration test DPH and subsequently to a lightweight dynamic penetrometer Panda®. From the conducted research it is identified that some advances and techniques currently used in CPT procedures, haven't been transferred to the corresponding evaluating procedures of dynamic probing DPH. Specifically, a normalization of the value of DPH is not carried out and therefore the currently used relationships for calculating the relative density, don't include any effect of overburden pressure. This also constraints the attempts for cross correlating the values of static cone penetration test CPT and dynamic probing heavy DPH. A demonstration of a normalization of the values of DPH was carried out by utilizing data from an older study. The data were also used to develop new equations for estimating relative density from the CPT and the DPH where the effect of overburden pressure is included in the corresponding normalized values.

A demonstration of testing methodologies and procedures was achieved with a field investigation to the planetary analogue site Mount Etna. Particular attention was placed on a portable lightweight dynamic penetrometer which can be conveniently used in planetary missions and at difficult to reach areas. The new proposed correlation for evaluating the relative density showed promising results for capturing the variation of relative density along the depth of the soil. Nevertheless, the limitations of the current methodologies were pointed out and the inherent need for further research was confirmed. Transferring of correlations that are usually used for deeper soil layers to near-surface soil, requires judgement and consideration of the conditions for which they were developed and calibrated. After refinement and validation, the methodology employed in the context of the field investigation study may be utilized for assessment of soil properties of near-surface soil.

Subsequently, focus was placed on laboratory tests on primarily soil simulants. Triaxial tests, oedometer tests and small scale shallow penetration tests were considered. Additionally, grain size distribution, maximum and minimum densities and the corresponding void ratios were determined. The shallow

penetration tests were utilized to develop material specific correlations for determining relative density. Further, correlations for the shear strength parameters  $c$  and  $\phi$  were produced. These correlations were used with the data from the field site investigation on Etna, showing promising results. The boundary effects of the used containers couldn't be accurately quantified due to the limited number of tests and it should be kept in mind that the proposed correlations are influenced by the boundary effects.

Successively, focus was placed on wheel-soil tests, which are integral part of the optimization of terramechanical applications providing valuable information about the localized physics. The stiffness of the wheel was firstly assessed. The wheel was moved towards a steel plate and the required force and displacement were measured. Further single tire tests were carried out on two different soils with three different water contents to investigate how the water content alters the strength of a soil and the associated global response of the tire-soil system. This is of particular importance when the trafficability of specific terrain is assessed. Shear strength tests of the investigated soils with the flat tire section were carried down to determine the parameters of the interaction between them.

The Finite Element Method in Abaqus was used to conduct various simulation analysis scenarios to demonstrate how to use numerical simulations for assessment, development and optimization procedures in terramechanical applications. The experimental data of the previous chapters were utilized for the calibration of the material of wheel and soil in the models. The Yeoh model and the Drucker Prager model were used for the wheel and soil respectively. Furthermore, rolling on the calibrated soils, on the volcanic Etna material and a two layered soil was investigated. The effect of angular velocity, vertical force, soil material and water content in the soil were examined. The differences among the cases of braking, free rolling and driving was demonstrated. The size of the model was also considered: the model's size was gradually increased until the difference in the modelling results were negligible for the purpose of this research.

It was shown that the main influential parameters for the footprint analyses are the Young's modulus and the yield stress of soil. It was found that different combinations of  $E$  and  $\sigma_{yield}$  can lead to the same final results, but the followed path of force displacement differs in each case. A higher vertical force led to

an increased dissipated energy, higher contact area, higher peak stresses, higher horizontal displacement of soil and increased vertical settlement. On the other hand, an increase in the angular velocity resulted to higher dissipated energy, increased horizontal velocity, slightly decreased contact area, higher negative values of horizontal displacement in the soil and decreased and subsequently increased values of horizontal displacements in the soil along the travelled path.

Moving on to the comparisons between braking, free rolling and driving, five times more energy was dissipated for the case of driving compared to the one of free rolling. The maximum peak vertical stress in the soil is similar to all the three cases. In the case of braking the soil was pushed backwards and therefore has higher negative horizontal displacement  $u_1$  values. The maximum vertical settlement results from the case of braking while the lowest one is the one from the driving conditions. A negative force and a negative moment, indicate braking while positive values indicate driving conditions.

Summing up, current relationships for estimating relative density were reevaluated for near surface soil and compared for static and dynamic penetration tests. Correlations for estimation of shear strength parameters were carried out by utilizing laboratory experiments on extraterrestrial soil simulants and other terrestrial soils. Single tire-soil experiments were conducted in the laboratory and complemented by shear strength tests of the investigated soils. The experimental results were used for calibration with finite element analysis in Abaqus. The calibrated model was used for subsequent rolling simulations in order to evaluate the soil response and the mobility of the tire for different rolling scenarios of the investigated non-pneumatic wheel.

Further research and tests should be conducted to set a good groundwork of experience to build on in the subsequent years. An investment for developing a comprehensive database with soil characteristics of soils worldwide should be of a first priority. The stochastics should be included in the data and in any subsequent correlations for evaluation of parameters. A transfer of the knowledge between soil mechanics and vehicle engineering should be enhanced, as clearly there is still room for improvement. Single tire tests are cost effective and aid in the isolation of the soil response from the complicated full vehicle dynamics to enable the assessment of the soil-tool interaction and



therefore should be considered as a standard mean in terramechanics. Standards are required to govern the development and implementation of terramechanics in order to ensure that the knowledge and experience is spread and incorporate worldwide and therefore a quick advance could be possible.

Starting from the root of the terramechanical models, firstly an improvement should be focus on a better understanding of the soil behavior and the corresponding parameters that could be used in vehicle models. A comprehensive database with single tire-soil models is needed. This is a cost effective solution for calibration of the wheel-soil interaction. Field rolling tests should be carried out to complement the tests and to validate the FEM models that are based on the model set calibrations of the single tire-soil experiments. FEM is a powerful tool that is expected to be utilized comprehensively for investigations of real rolling scenarios of different types of wheels meaning different sizes or/and various tread patterns, spokes systems etc, to advance the understanding of vehicle's mobility and traversability over various types of soil.

## Literature

Aboul Yazid, A.M., Emam, M.A.A., Shaaban, S., El-Nashar, M.A. (2015): Effect of spokes structures on characteristics performance of non-pneumatic tires, *International Journal of Automotive and Mechanical Engineering (IJAME)* 11, 2212-2223.

Alshibli, K.A., Hasan, A. (2009): Strength properties of JSC-1A lunar regolith stimulant, *J. Geotech. Geoenviron. Eng.* 135(5), 673-679.

Arslan, H., Batiste, S., Sture, S. (2010): Engineering properties of lunar soil simulant JSC-1A, *J. Aerospace Eng.* 23(1), 70-83.

Arvidson, R.E., Bellutta, P., Calef, F. et al. (2014): Terrain physical properties derived from orbital data and the first 360 sols of Mars Laboratory Curiosity rover observations in Gale Crater, *Journal of Geophysical Research: Planets*, 119, 1322–1344. doi:10.1002/2013JE004605.

Baldi, G., Bellotti, R., Ghionna, V., Jamiolkowski, M., Pasqualini, E. (1986): Interpretation of CPT's and CPTU's – 2nd Part: Drained penetration of sands, *Proceedings of the 4th International Geotechnical Seminar Field Instrumentation and In-Situ Measurements*, Nanyang Technological Institute, Singapore, 143–156.

Bekakos, C.A., Papazafeiropoulos, G., O'Boy, D.J., Prins, J. (2015): Dynamic response of rigid wheels on deformable terrains, *Proceedings of the 13<sup>th</sup> ISTVS European Conference*, Italy.

Bekakos, C.A., Papazafeiropoulos, G., O'Boy, D.J., Prins, J. (2016a): Pneumatic tyres interacting with deformable terrains, *13th International Conference on Motion and Vibration Control*, UK.

Bekakos, C.A., Papazafeiropoulos, G., O'Boy, D.J., Prins, J. (2016b): Finite element modelling of a pneumatic tyre interacting with rigid road and deformable terrain, *International Journal of Vehicle Performance* 3(2), 142-166.

Bekakos, C.A., Papazafeiropoulos, G., O'Boy, D.J., Prins, J. (2016c): Development of accurate pneumatic tyre finite element models based on an optimization procedure, *ECOMAS Congress 2016, VII European Congress on Computational Methods in Applied Sciences and Engineering*, Greece.

Bekker, M.G. (1956): *Theory of Land Locomotion: The Mechanics of Vehicle Mobility*, The University of Michigan Press, Ann Arbor, Michigan.

Bundesanstalt für Wasserbau BAW (1997): Bewertung von Ergebnissen unterschiedlicher Sondierverfahren zur Ermittlung der Festigkeit nichtbindiger Böden, Schlußbericht.

Boulangier, R.W., Idriss, I.M. (2004): State normalization of penetration resistance and the effect of overburden stress on liquefaction resistance, *Proceedings of 11th International Conference on Soil Dynamics and 3rd International Conference on Earthquake Geotechnical Engineering*, Stallion Press, 2, 484-491.

Carrier III, W.D., Olhoeft, G.R., Mendell, W. (1991): Physical properties of the lunar surface in Heiken, G.H., Vaniman, D.T., French, M., *Lunar Sourcebook, a user's guide to the moon*, Cambridge, University Press, USA, 475-594.

Center for Lunar and Asteroid Surface Science CLASS: Planetary Simulant Database, <https://sciences.ucf.edu/class/planetary-simulant-database>. Accessed on 25 July 2019.

Chaigneau, L. (2001): *Caractérisation des milieux granulaires de surface à l'aide d'un pénétromètre*, Thèse de l'Université Blaise Pascal, Clermont-Ferrand.

Ciarletti, V., Clifford, S., Vieau, A.-J., Lustrement, B., Hassen-Kodja, R., Cais, P., Plettemeier, D. (2011): The 2018 ExoMars WISDOM GPR on Mt. Etna: First field test results in a Mars analogue volcanic environment, *Geophysical Research Abstracts* 13:EGU2011-12723-1.

Cubrinovski, M., Ishihara, K. (2002): Maximum and minimum void ratios characteristics of sands, *Soils and Foundations* 42(6), 65-78.

Dassault Simulia (2018): Abaqus® documentation 2018.

Deng, Y., Zhao, Y., Lin, F., Xiao, Z., Zhu, M., Li, H. (2018): Simulation of steady-state rolling non-pneumatic mechanical elastic wheel using finite element method, *Simulation Modeling Practice and Theory* 85, 60-79.

Deng, Y. J., Zhao, Y. Q., Xu, H., Zhu, M. M., Xiao, Z. (2019): Finite element modeling of interaction between non-pneumatic mechanical elastic wheel and soil, *Journal of Automobile Engineering*. doi: 10.1177/0954407018821555

Deutsche Gesellschaft für Geotechnik e.V. (2012): *Empfehlungen des Arbeitskreises „Pfähle“: EA-Pfähle*, 2. Auflage, Ernst & Sohn, Berlin.

DIN 4014:1990-03: Bohrpfähle - Herstellung, Bemessung und Tragverhalten

DIN 4094-1:2002-06 Baugrund – Felduntersuchungen Teil 1: Drucksondierungen.

DIN 4094-3:2002-01 Baugrund – Felduntersuchungen, Teil 3: Rammsondierungen.

DIN EN 1997-2:2010-10. Eurocode 7: Entwurf, Berechnung und Bemessung in der Geotechnik – Teil 2: Erkundung und Untersuchung des Baugrunds.

DIN EN ISO 14688-1:2013-12: Geotechnische Erkundung und Untersuchung - Benennung, Beschreibung und Klassifizierung von Boden - Teil 1: Benennung und Beschreibung.

DIN EN ISO 17892-12: Geotechnische Erkundung und Untersuchung-Laborversuche an Bodenproben Teil 12: Bestimmung der Fließ- und Ausrollgrenzen.

DIN EN ISO 22476-1:2013-10. Geotechnische Erkundung und Untersuchung –Felduntersuchungen Teil 1: Drucksondierungen mit elektrischen Messwertaufnehmern und Messeinrichtungen für den Porenwasserdruck. Deutsche Fassung.

DIN EN ISO 22476-2:2012-03 Geotechnische Erkundung und Untersuchung - Felduntersuchungen – Teil 2: Rammsondierungen.

DIN EN ISO 22476-12:2009-10. Geotechnische Erkundung und Untersuchung – Felduntersuchungen – Teil 12: Drucksondierungen mit mechanischen Messwertaufnehmern.

Ding, L., Gao, H., Deng, Z., Li, Y., Liu, G. (2014): New perspective on characterizing pressure-sinkage relationship of terrains for estimating interaction mechanics, *Journal of Terramechanics* 52, 57–76.

- Du, X., Zhao, Y., Wang, Q., Fu, H. (2016): Numerical analysis of the dynamic interaction between a non-pneumatic mechanical elastic wheel and soil containing an obstacle, *Journal of Automobile Engineering*. doi: 10.1177/0954407016660946.
- Eslami, A., Fellenius, B. H. (2004): CPT and CPTu data for soil profile interpretation: Review of methods and proposed new approach, *Iranian Journal of Science and Technology* 28,69-86.
- Fervers, C. (2004): Improved FEM simulation model for tire–soil interaction, *Journal of Terramechanics* 41, 87–100. doi: 10.1016/j.jterra.2004.02.012.
- Franke, E. (1987): Einige Fragen zur DIN 4094, Teil 2, *geotechnik* 10(1), 41-46.
- Gasmi, A., Joseph, P.F., Rhyne, T.B., Cron, S.M. (2012): Development of a two-dimensional model of a compliant non-pneumatic tire, *International Journal of Solids and Structures* 49, 1723-1740. doi: 10.1016/j.ijsolstr.2012.03.007.
- Gibbs, H.J., Holtz, W.G. (1957): Research on determining the density of sands by Spoon Penetration Testing, *Proceedings of 4th International Conference on Soil Mechanics and Foundation Engineering ICSMFE*, London, 1, 35-39.
- Gourves, R., Barjot, R. (1995): The Panda ultralight dynamic penetrometer, *Proceedings of 11th European Conference on Soil Mechanics and Foundation Engineering*, Copenhagen, 3, 83–88.
- Hambleton, J.P., Drescher, A. (2008): Modeling wheel-induced rutting in soils: Indentation, *Journal of Terramechanics* 45(6), 201–211.
- Hambleton, J.P., Drescher, A. (2009a): Modeling wheel-induced rutting in soils: Rolling, *Journal of Terramechanics* 46(2), 35-47.
- Hambleton, J.P., Drescher, A. (2009b): On modeling a rolling wheel in the presence of plastic deformation as a tree- or two- dimensional process, *International Journal of Mechanical Sciences* 51(11), 846-855. doi: 10.1016/j.ijmecsci.2009.09.024.
- He, R., Sandu, C., Khan, A.K., Guthrie, A.G., Els, P.S., Hamersma, H.A. (2019): Review of terramechanics models and their applicability to real – time

applications, *Journal of Terramechanics* 81, 3-22. doi: 10.1016/j.jterra.2018.04.003.

Hofmann, B.A., Sego, D.C, Robertson, P.K. (2000): In situ ground freezing to obtain undisturbed samples of loose sand, *Journal of Geotechnical and Geoenvironmental Engineering* 126(11), 979-989.

James, P., Chester, D.K., Duncan, A.M. (2016): Development and spatial distribution of soils on an active volcano: Mt. Etna, Sicily, *CATENA* 137,277–297.

Jamiolkowski, M., Ghionna, V.N., Lancellotta, R. and Pasqualini, E. (1988): New correlations of penetration tests for design practice, *Proceedings of the First International Symposium on Penetration Testing, ISOPT-1*, A.A. Balkema, Rotterdam, 263-296.

Jamiolkowski, M., Lo Presti, D.C.F., Manassero, M. (2003): Evaluation of relative density and shear strength of sands from CPT and DMT, *Soil Behavior and Soft Ground Construction (GSP 119)*, ASCE, Reston, VA, 201-238.

Janosi, Z., Hanamoto, B. (1961): The analytical determination of drawbar-pull as a function of slip for tracked vehicles in deformation soils, *Proceedings of the 1st Int. Conf. of Terrain-Vehicle Systems*, Torino, 707-726.

Jin, X., Hou, C., Fan, X., Sun, Y., Lv, J., Lu, C. (2018): Investigation on the static and dynamic behaviors of non-pneumatic tires with honeycomb spokes, *Composite Structures* 187, 27-35.

Johnson, A.R., Chen, T.K. (2005): Approximating thermo-viscoelastic heating of largely strained solid rubber components, *Computer methods in applied mechanics and engineering* 194, 313-325.

Ju, J., Kim, D.M., Kim, K. (2012): Flexible cellular solid spokes of a non-pneumatic tire, *Composite Structures* 94, 2285-2295. doi: 10.1016/j.compstruct.2011.12.022.

Ju, J., Veeramurthy, M., Summers, J. D., Thompson, L. (2013): Rolling resistance of a non-pneumatic tire having a porous elastomer composite shear band, *Tire Science and Technology TSTCA* 41(3), 154-173.

- Senatore, C., Iagnemma, K. (2011): Direct shear behaviour of dry, granular soils for low normal stress with application to lightweight robotic vehicle modelling, *Proceedings of the 17th ISTVS International Conference*, Blacksburg, Virginia.
- Kramer, H. (1979): Vergleichsuntersuchungen für den Einsatz der Drucksonde und der schweren Rammsonde, *Tiefbau* 11, 899-903.
- Kulhawy, F.H., Mayne, P.W. (1990): *Manual on Estimating Soil Properties for Foundation Design*. Electric Power Research Institute, Palo Alto, California.
- Langton, D.D. (1999): The PANDA light-weight penetrometer for soil investigation and monitoring material compaction, *Ground Engineering*, September, 33-37.
- Lee, S.Y. (1990): *Centrifuge modeling of cone penetration testing in cohesionless soils* (Ph.D. thesis), Cambridge University, Cambridge, UK.
- Li, H., Schindler, C. (2013): Analysis of soil compaction and tire mobility with finite element method, *Journal of Multi-body Dynamics* 227(3), 275-291.
- Liao, S.C., Whitman, R.V. (1986): Overburden correction factors for SPT in sand, *Journal of Geotechnical Engineering* 112(3), 373-377.
- Ma, J., Kolla, A., Summers, J.D., Joseph P.F., Blouin, V.Y., Biggers, S. (2009): Numerical simulation of new generation non-pneumatic tire (Tweel) and sand, *Proceedings of the ASME International Design Engineering Technical Conferences & Computers and Information in Engineering Conference IDETC/CIE*, San Diego, California, USA.
- Ma, J., Summers, J.D., Joseph, P. (2011): Dynamic impact simulation of interaction between non-pneumatic tire and sand with obstacle, *SAE Technical Papers*. doi: 10.4271/2011-01-0184.
- Ma, J., Summers, J.D., Joseph, P. (2012): FE-Simulation of tread profile effects on the performance of the cellular shear band based non-pneumatic tire, *SAE International*. doi: 10.4271/2012-01-0768.
- Mahler, A., Szendefy, J. (2009): Estimation of CPT resistance based on DPH results, *Periodica Polytechnica Civil Engineering* 53(2), 101-106.

- Mayne, P.W. (2006): Undisturbed sand strength from seismic cone tests. The 2nd James K. Mitchell Lecture, *Journal of Geomechanics and Geoengineering* 1(4), 239-258.
- Mayne, P.W. (2007): *Cone Penetration Testing: State of Practice*, NCHRP Report, No. 20-05, Washington, D.C.: Transportation Research Board.
- Meirion-Griffith, G., Spenko, M. (2011): A modified pressure-sinkage model for small, rigid wheels on deformable terrains, *Journal of Terramechanics* 48, 149–155.
- Meirion-Griffith, G., Spenko, M. (2013): A pressure-sinkage model for small-diameter wheels on compactive, deformable terrain, *Journal of Terramechanics* 50, 37-44. doi: 10.1016/j.jterra.2012.05.003.
- Meier, T. (2009): *Application of hypoplastic and viscohypoplastic constitutive models for geotechnical problems*. Veröffentlichungen des Instituts für Bodenmechanik und Felsmechanik der Universität Karlsruhe, Heft 171.
- Melzer, K.-J. (1968): *Sondenuntersuchungen in Sand*. Mitteilungen des Instituts für Verkehrswasserbau, Grundbau und Bodenmechanik an der TH Aachen, Heft 43.
- Melzer, K.-J., Fecker, E., Westhaus, T. (2017): *Baugrunduntersuchungen im Feld*, Grundbautaschenbuch, 8. Auflage, Teil 1, 45-137.
- Moore, J.H., Jakoshy, B.M. (1989): Viking Landing Sites, Remote-Sensing Observations, and Physical Properties of Martian Surface Materials, *ICARUS* 81,164-184.
- Moore, J.H., Bickler, D.B., Crisp, A.J., Eisen, H.J., Gensler, J.A, Haldemann, A.F.C., Matijevic, J.R., Reid, L.K., Pavlics, F. (1999): Soil-like deposits observed by Sojourner, the pathfinder rover, *Journal of Geophysical Research*, 104(4), 8729-8746.
- Moss, R.E.S., Seed, R.B., Olsen, R.S. (2006): Normalizing the CPT for overburden stress, *Journal of Geotechnical and Geoenvironmental Engineering* 132(3), 378-387.
- Michelin Tweel<sup>®</sup>, <https://www.michelintweel.com/tweel-UTV.html>. Accessed on 25 July 2019.



- Papamichael, S., Becker, A., Vrettos, C. (2018): Combined seismic and penetration tests on the planetary analogue site Mount Etna, *Earth & Space 2018, Proceedings of the 16th ASCE International Conference on Engineering, Science, Construction and Operations in Challenging Environments*, Cleveland, Ohio, 68-78.
- Papamichael, S., Vrettos, C. (2018): CPT interpretation and correlations to SPT for near-shore marine Mediterranean soils, *Proceedings of the 4th International Symposium on Cone Penetration Testing (CPT'18)*, CRC Press, 499-504.
- Pike, W.T., Staufer, U., Hecht, M.H., Goetz, W., Parrat, D., Sykulski-Lawrence, H., Vijendran, S., Madsen, M.B. (2011): Quantification of the dry history of the Martian soil inferred from in situ microscopy, *Geophysical Research Letters* 38. doi:10.1029/2011GL049896.
- Placzek, D. (1985): Vergleichende Untersuchungen beim Einsatz statischer und dynamischer Sonden, *geotechnik* 8(2), 68-75.
- Preston, L., Grady, M., Barber, S. (2012): *CAFE - Concepts for Activities in the Field for Exploration - TN2: The Catalogue of Planetary Analogues*. The Planetary and Space Sciences Research Institute, The Open University, UK, under ESA contract: 40000104716/11/NL/AF.
- Reece, A.R., (1965): Principles of soil-vehicle mechanics, *Proc. Inst. Mech. Eng.* 180(2A), 45–46.
- Robertson, P.K. (1990): Soil Classification using the cone penetration test, *Canadian Geotechnical Journal* 27(1), 442-459.
- Robertson, P.K. and Wride, C.E. (1998): Evaluating cyclic liquefaction potential using the cone penetration test, *Canadian Geotechnical Journal* 35(1), 151-158.
- Robertson P.K. (2010): Soil behavior type from the CPT: an update, 2nd Int. Symp. on Cone Penetration Testing, Huntington Beach, USA.
- Robertson, P.K., Cabal, K.L. (2015): *Guide to Cone Penetration Testing for Geotechnical Engineering*. Signal Hill, California: Gregg Drilling & Testing, Inc.

Salgado, R., Mitchell, J.K., Jamiolkowski, M. (1998): Chamber size effects on penetration resistance measured in calibration chambers, *Journal of Geotechnical Engineering*, ASCE 124(9), 878-888.

Schmertmann, J.H. (1976): An updated correlation between relative density  $D_r$  and Fugro-type electric cone bearing  $q_c$ . Contract Report DACW 38-76-M 6646, Waterways Experiment Station Vicksburg, MS, Vol. 145.

Shaw, A., Arvidson, R.E., Bonitz, R., Carsten, J., Keller, H.U., Lemmon, T.M., Mellon, M.T., Robinson, M., Trebi-Ollenu, A. (2009): Phoenix soil physical properties investigation, *Journal of Geophysical Research*, 114. doi:10.1029/2009JE003455.

Skempton, A.W. (1986): Standard Penetration Test procedures and the effects in sands of overburden pressure, relative density, particle size and overconsolidation, *Géotechnique* 36(3), 425-447.

Stenzel, G., Melzer, K.-J. (1978): Bodenuntersuchungen durch Sondierungen nach DIN 4094, *Tiefbau* 3, 155-160 & 240-244.

Sullivan, R., Anderson, R., Biesiadecki, J., Bond, T., Stewart, H. (2011): Cohesions, friction angles, and other physical properties of Martian regolith from Mars Exploration Rover wheel trenches and wheel scuffs, *Journal of Geophysical Research* 116. doi:10.1029/2010JE003625.

Uzielli, M., Mayne, P.W., Cassidy, M.J. (2013): Probabilistic assessment of design strengths for sands from in-situ testing data, *Modern Geotechnical Design Codes of Practice, Advances in Soil Mechanics & Geotechnical Engineering (series)*, IOS-Millpress, Amsterdam, 1, 214-227.

Vrettos, C., Papamichael, S. (2018): Lagerungsdichte von nichtbindigen Böden aus Ramm- und Drucksondierungen: Eine aktualisierte Bewertung empirischer Beziehungen, *geotechnik* 41, 186-196.

Vrettos, C., Becker, A., Merz, K., Witte, L. (2014): Penetration tests in a mold on regolith quasi-analogues at different relative densities, *Earth & Space 2014, 14th ASCE International Conference on Engineering, Science, Construction and Operations in Challenging Environments*.

Vrettos, C. (2012): Shear strength investigations for a class of extra-terrestrial analogue soils, *Journal of Geotechnical and Geoenvironmental Engineering*, ASCE 138, 508-515.

Wong, J.-Y., Reece, A.R. (1967): Prediction of rigid wheel performance based on the analysis of soil-wheel stresses. Part I. Performance of driven rigid wheels, *Journal of Terramechanics* 4, 81-98.

Wong, J.Y., Garber, M., Preston-Thomas, J. (1984): Theoretical prediction and experimental substantiation of the ground pressure distribution and tractive performance of tracked vehicles, *Proc. Inst. Mech. Eng. Part D Transp. Eng.* 198, 265–285.

Wong, J.Y.(2001): *Theory of Ground Vehicles*, Third Edition, John Wiley & Sons.

Xia, K. (2011): Finite element modelling of tire/terrain interaction: Application to predicting soil compaction and tire mobility, *Journal of Terramechanics* 48, 113-123. doi:10.1016/j.jterra.2010.05.001.

Yeoh, O.H. (1993): Some forms of the strain energy function for rubber, *Rubber Chemistry and Technology* 66(5), 754-771.

Youd, T.L., Idriss, I.M., Andrus, R.D. (2001): Liquefaction resistance of soils: Summary report from the 1996 NCEER and 1998 NCEER/NSF workshops on evaluation of liquefaction resistance of soils, *Journal of Geotechnical and Geoenvironmental Engineering* 127(10), 817-833.

Youssef, A.-F. A., Ali, G. A. (1982): Determination of soil parameters using plate test, *Journal of Terramechanics* 19(2), 129–147.

Zhao, Y. Q., Deng, Y. J., Lin, F., Zhu, M. M., Xiao, Z. (2018): Transient dynamic characteristics of a non-pneumatic mechanical elastic wheel rolling over a ditch, *International Journal of Automotive Technology* 19(3), 499-508.

# Appendices

## A Results of oedometer tests

Table A-1: JSC-1A with  $\rho_d=1.784\text{Mg/m}^3$  and  $e=0.620$ .

Stress level [kPa]	$e$ [-]	$E_s$ [MPa]	$C_c$ [-]
0.00-1.66	0.6204	-	0.0E+00
1.66-4.85	0.6200	15.96	3.0E-04
4.85-14.88	0.6176	6.61	2.2E-03
14.88-34.87	0.6137	8.34	4.6E-03
34.87-79.83	0.6059	9.30	9.5E-03
79.83-178-81	0.6003	28.80	6.9E-03

Table A-2: JSC-1A with  $\rho_d=1.481\text{Mg/m}^3$  and  $e=0.952$ .

Stress level [kPa]	$e$ [-]	$E_s$ [MPa]	$C_c$ [-]
0.00-1.66	0.9444	0.41	0.0E+00
1.66-4.85	0.9392	1.21	4.8E-03
4.85-14.88	0.9316	2.56	6.8E-03
14.88-34.87	0.9225	4.31	1.1E-02
34.87-79.83	0.9081	6.08	1.7E-02
79.83-178.81	0.8926	12.45	1.9E-02

Table A-3: JSC Mars-1A with  $\rho_d=0.924\text{Mg/m}^3$  and  $e=1.908$ .

Stress level [kPa]	$e$ [-]	$E_s$ [MPa]	$C_c$ [-]
0.00-1.65	1.9079	-	0.0E+00
1.65-4.84	1.9032	1.97	4.4E-03
4.84-14.80	1.8958	3.93	6.6E-03
14.80-34.75	1.8827	4.42	1.5E-02
34.75-79.56	1.8661	7.87	2.0E-02
79.56-179.35	1.8420	12.01	3.0E-02

Table A-4: JSC Mars-1A with  $\rho_d=0.809\text{Mg/m}^3$  and  $e=2.323$ .

Stress level [kPa]	$e$ [-]	$E_s$ [MPa]	$C_c$ [-]
0.00-1.66	2.3109	0.46	0.0E+00
1.66-4.85	2.3068	2.58	3.8E-03
4.85-14.88	2.2904	2.04	1.5E-02
14.88-34.87	2.2708	3.38	2.3E-02
34.87-79.83	2.2420	5.18	3.5E-02
79.83-178-81	2.2007	7.96	5.1E-02

Table A-5: MMS-sand with  $\rho_d=1.603\text{Mg/m}^3$  and  $e=0.653$ .

Stress level [kPa]	$e$ [-]	$E_s$ [MPa]	$C_c$ [-]
0.00-4.97	0.6351	62.04	0.0E+00
4.97-14.90	0.6512	8.55	1.7E-03
14.90-34.90	0.6467	7.34	5.3E-03
34.90-79.96	0.6365	7.30	1.2E-02
79.96-179.88	0.6283	20.11	1.0E-03

Table A-6: MMS-sand with  $\rho_d=1.369\text{Mg/m}^3$  and  $e=0.936$ .

Stress level [kPa]	$e$ [-]	$E_s$ [MPa]	$C_c$ [-]
0.00-0.17	0.7810	0.00	0.0E+00
0.17-4.97	0.7786	3.72	7.4E-04
4.97-14.90	0.7727	3.26	5.4E-03
14.90-34.90	0.7658	5.63	8.1E-03
34.90-79.96	0.7544	7.64	1.4E-02
79.96-179.88	0.7376	11.57	2.1E-02

Table A-7: MMS-dust with  $\rho_d=1.900\text{Mg/m}^3$  and  $e=0.316$ .

Stress level [kPa]	$e$ [-]	$E_s$ [MPa]	$C_c$ [-]
0.00-4.97	0.3137	3.10	0.0E+00
4.97-14.90	0.3104	4.04	2.9E-03
14.90-34.90	0.3077	9.48	3.3E-03
34.90-79.96	0.3006	8.42	8.5E-03
79.96-179.88	0.2921	15.50	1.0E-02

Table A-8: MMS-dust with  $\rho_d=1.060\text{Mg/m}^3$  and  $e=1.670$ .

Stress level [kPa]	$e$ [-]	$E_s$ [MPa]	$C_c$ [-]
0.00-0.17	1.3001	0.00	0.0E+00
0.17-4.97	1.2030	0.13	2.9E-02
4.97-14.90	1.1453	0.46	5.3E-02
14.90-34.90	1.0975	1.12	5.6E-02
34.90-79.96	1.0571	2.98	4.9E-02
79.96-179.88	1.0027	4.90	6.7E-02

Table A-9: MSS-D with  $\rho_d=1.908\text{Mg/m}^3$  and  $e=0.483$ .

Stress level [kPa]	$e$ [-]	$E_s$ [MPa]	$C_c$ [-]
0.00-4.97	0.4657	0.42	0.0E+00
4.97-14.90	0.4573	1.76	7.6E-03
14.90-34.90	0.4525	6.24	5.6E-03
34.90-79.96	0.4413	5.95	1.4E-02
79.96-179.88	0.4290	12.05	1.5E-02

Table A-10: MSS-D with  $\rho_d=1.349\text{Mg/m}^3$  and  $e=0.853$ .

Stress level [kPa]	$e$ [-]	$E_s$ [MPa]	$C_c$ [-]
0.00-0.17	0.5197	0.00	0.0E+00
0.17-4.97	0.4928	0.33	8.0E-03
4.97-14.90	0.4261	0.28	6.1E-02
14.90-34.90	0.3891	1.00	4.4E-02
34.90-79.96	0.3517	2.24	4.5E-02
79.96-179.88	0.3189	5.65	4.0E-02

Table A-11: WF34-sand with  $\rho_d=1.680\text{Mg/m}^3$  and  $e=0.577$ .

Stress level [kPa]	$e$ [-]	$E_s$ [MPa]	$C_c$ [-]
0.00-4.97	0.5769	6.36	0.0E+00
4.97-14.90	0.5770	3.68	3.9E-03
14.90-34.90	0.5752	102.39	3.6E-04
34.90-79.96	0.5727	50.15	1.7E-03
79.96-179.88	0.5706	59.49	3.3E-03

Table A-12: WF34-sand with  $\rho_d=1.486\text{Mg/m}^3$  and  $e=0.783$ .

Stress level [kPa]	$e$ [-]	$E_s$ [MPa]	$C_c$ [-]
0.00-0.17	0.1979	0.00	0.0E+00
0.17-4.97	0.1894	1.00	2.5E-03
4.97-14.90	0.1840	3.30	4.9E-03
14.90-34.90	0.1812	12.80	3.3E-03
34.90-79.96	0.1757	14.61	6.6E-03
79.96-179.88	0.1710	37.79	5.8E-03

Table A-13: Medium sand with  $\rho_d=1.670\text{Mg/m}^3$  and  $e=0.587$ .

Stress level [kPa]	$e$ [-]	$E_s$ [MPa]	$C_c$ [-]
0.00-4.97	0.5837	2.49	0.0E+00
4.97-14.90	0.5833	42.37	3.4E-04
14.90-34.90	0.5823	32.00	1.2E-03
34.90-79.96	0.5799	29.58	2.9E-03
79.96-179.88	0.5760	40.60	4.8E-03

Table A-14: Medium sand with  $\rho_d=1.474\text{Mg/m}^3$  and  $e=0.798$ .

Stress level [kPa]	$e$ [-]	$E_s$ [MPa]	$C_c$ [-]
0.00-0.17	0.7526	0.01	0.0E+00
0.17-4.97	0.7415	0.78	3.3E-03
4.97-14.90	0.7391	7.26	2.2E-03
14.90-34.90	0.7362	12.49	3.4E-03
34.90-79.96	0.7329	24.54	4.0E-03
79.96-179.88	0.7263	27.21	8.1E-03

Table A-15: Syar coarse with  $\rho_d=1.697\text{Mg/m}^3$  and  $e=0.656$ .

Stress level [kPa]	$e$ [-]	$E_s$ [MPa]	$C_c$ [-]
0.00-1.31	0.6559	-	0.0E+00
1.31-10.11	0.6525	4.35	1.6E-03
10.11-19.80	0.6489	4.45	5.4E-03
19.80-51.11	0.6401	5.89	9.3E-03
51.11-82.42	0.6227	2.97	3.6E-02

Table A-16: Syar coarse with  $\rho_d=1.651 \text{ Mg/m}^3$  and  $e=0.702$ .

Stress level [kPa]	$e$ [-]	$E_s$ [MPa]	$C_c$ [-]
0.00-1.31	0.7020	-	0.0E+00
1.31-10.11	0.6979	3.68	2.0E-03
10.11-19.80	0.6940	4.19	5.9E-03
19.80-51.11	0.6863	6.96	8.1E-03
51.11-82.42	0.6731	4.03	2.8E-02

Table A-17: Quarry fines with  $\rho_d=1.349 \text{ Mg/m}^3$  and  $e=0.853$ .

Stress level [kPa]	$e$ [-]	$E_s$ [MPa]	$C_c$ [-]
0.00-4.97	0.8492	2.27	0.0E+00
4.97-14.90	0.8455	4.98	3.4E-03
14.90-34.90	0.8375	4.65	9.4E-03
34.90-79.96	0.8252	6.79	1.5E-02
79.96-179.88	0.7994	7.17	3.2E-02

Table A-18: Quarry fines with  $\rho_d=1.084 \text{ Mg/m}^3$  and  $e=1.306$ .

Stress level [kPa]	$e$ [-]	$E_s$ [MPa]	$C_c$ [-]
0.00-0.17	0.8450	0.00	0.0E+00
0.17-4.97	0.8178	0.41	8.1E-03
4.97-14.90	0.7918	0.88	2.4E-02
14.90-34.90	0.7441	0.97	5.6E-02
34.90-79.96	0.7060	2.73	4.6E-02
79.96-179.88	0.6573	4.73	6.0E-02



## B Results from direct shear tests

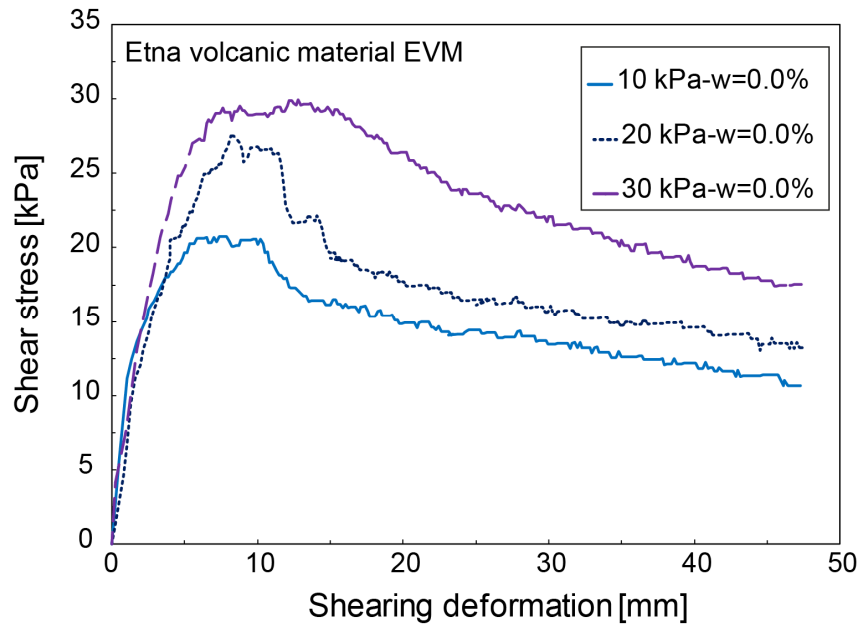


Figure B -1: Shear test results for the material from Etna vs flat tire section.

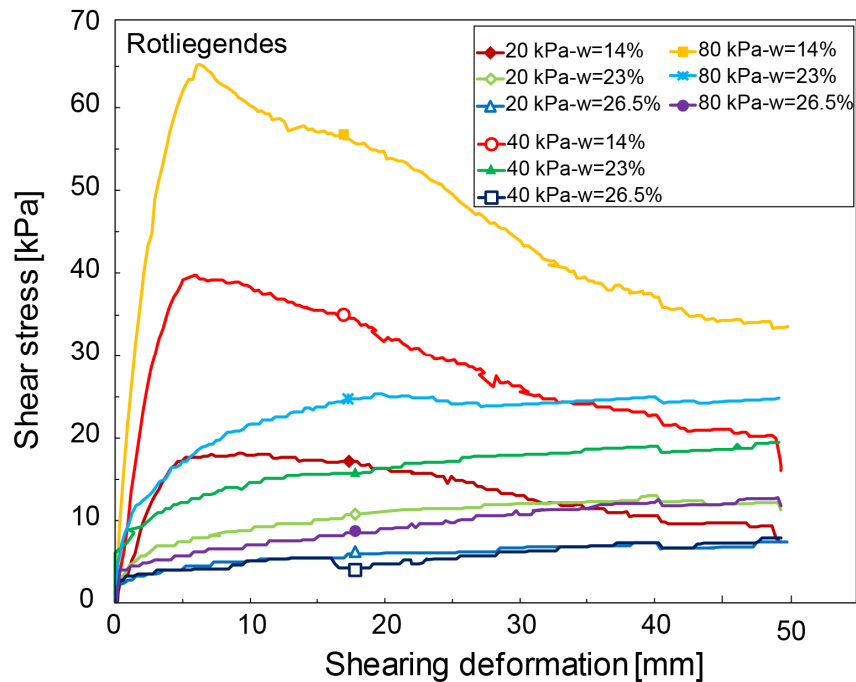


Figure B-2 Shear test results for the material Rotliegendes vs flat tire section

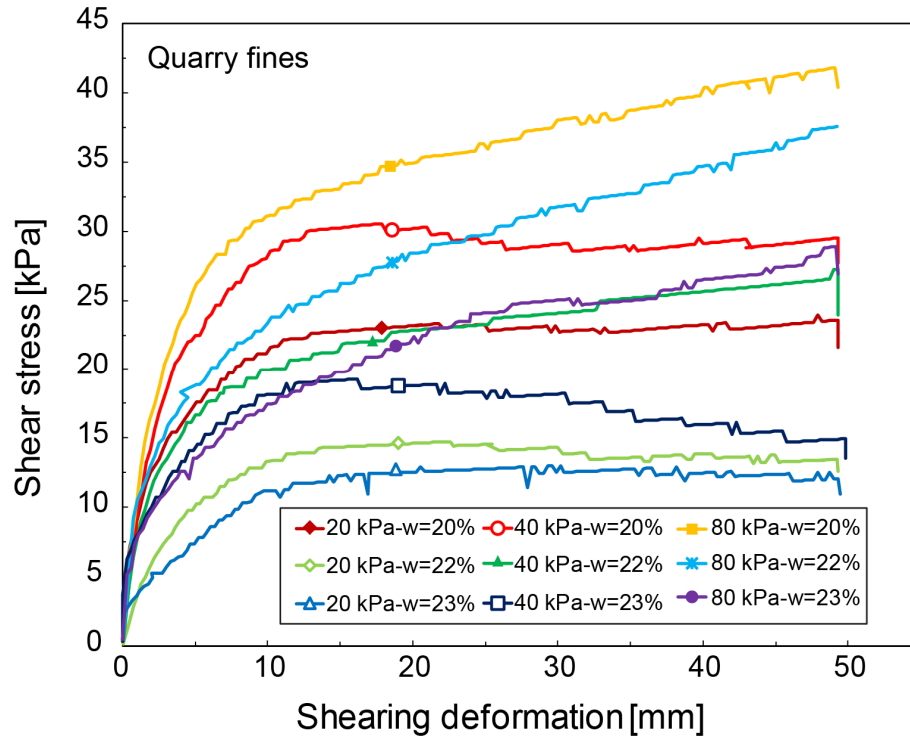


Figure B-3: Shear test results for the material Quarry fines vs flat tire section

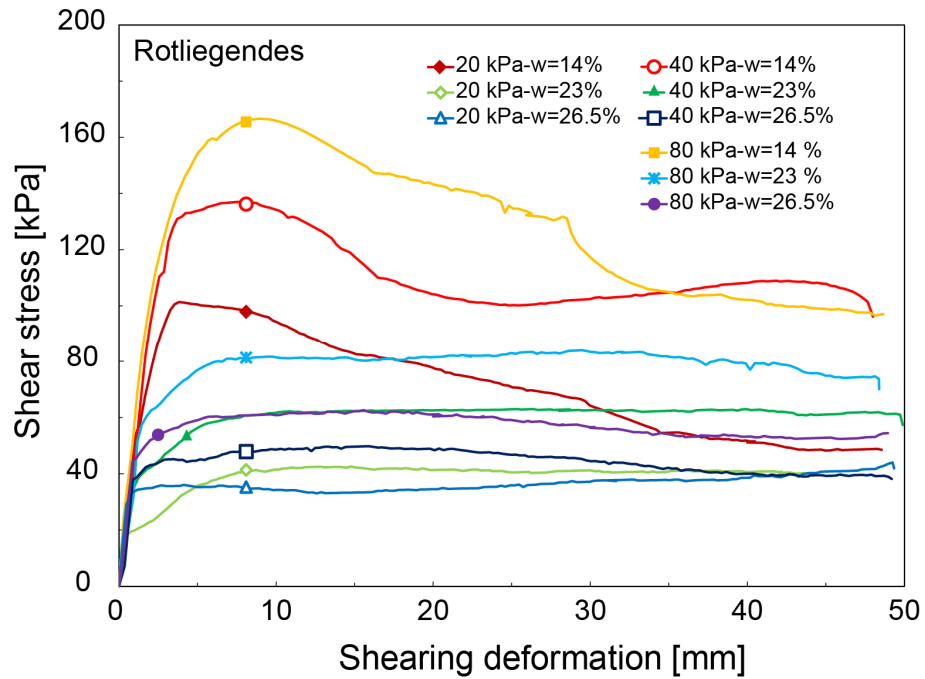


Figure B-4: Shear test results for the material Rotliegendes.

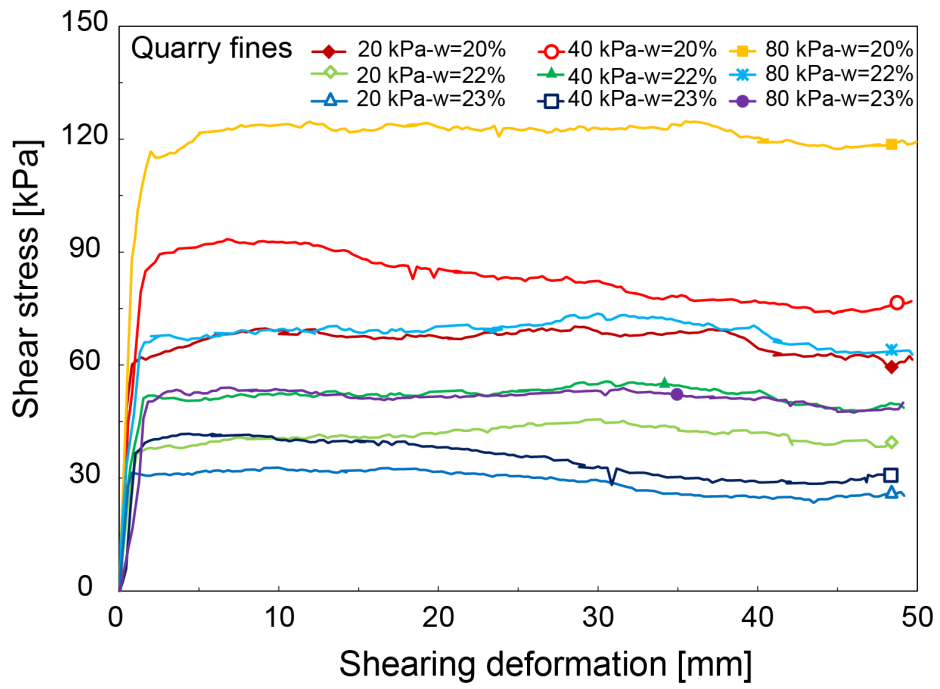


Figure B-5: Shear test results for the material Quarry fines.

### C Further results from the wheel's tests

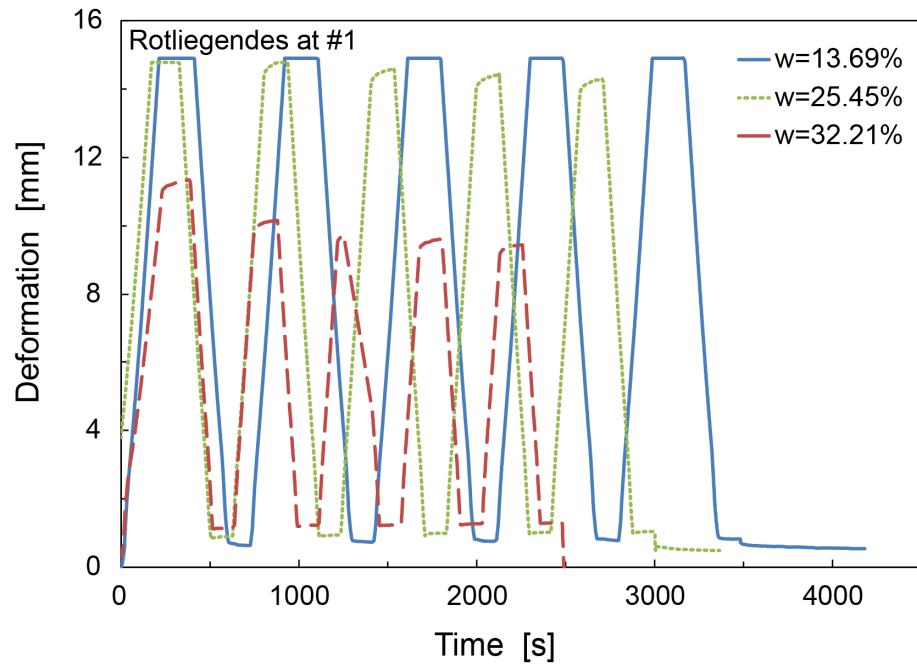


Figure C-1: Results of wheel tests for Rotliegende at the location point #1.

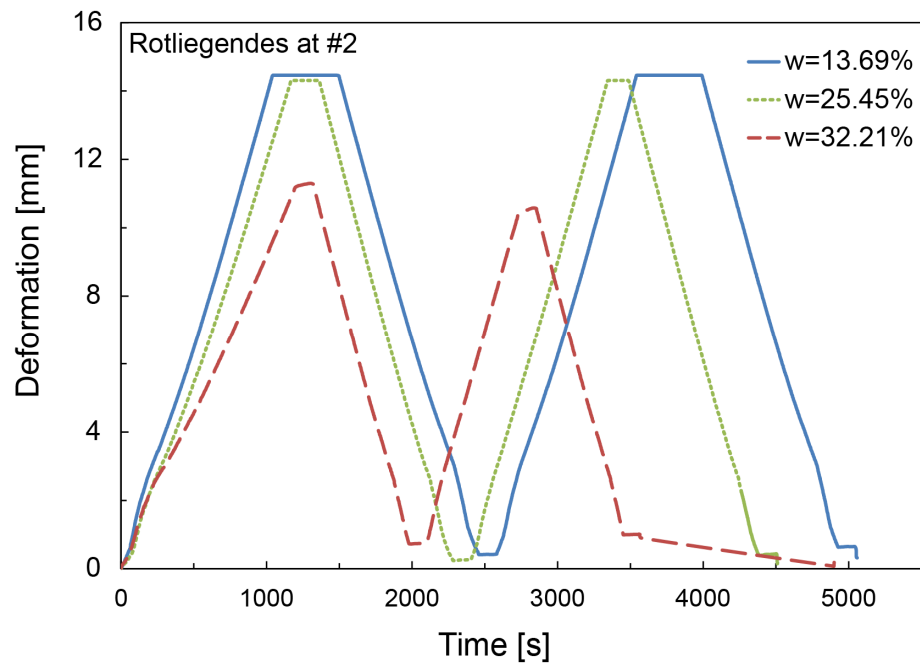


Figure C-2: Results of wheel tests for Rotliegende at the location point #2.

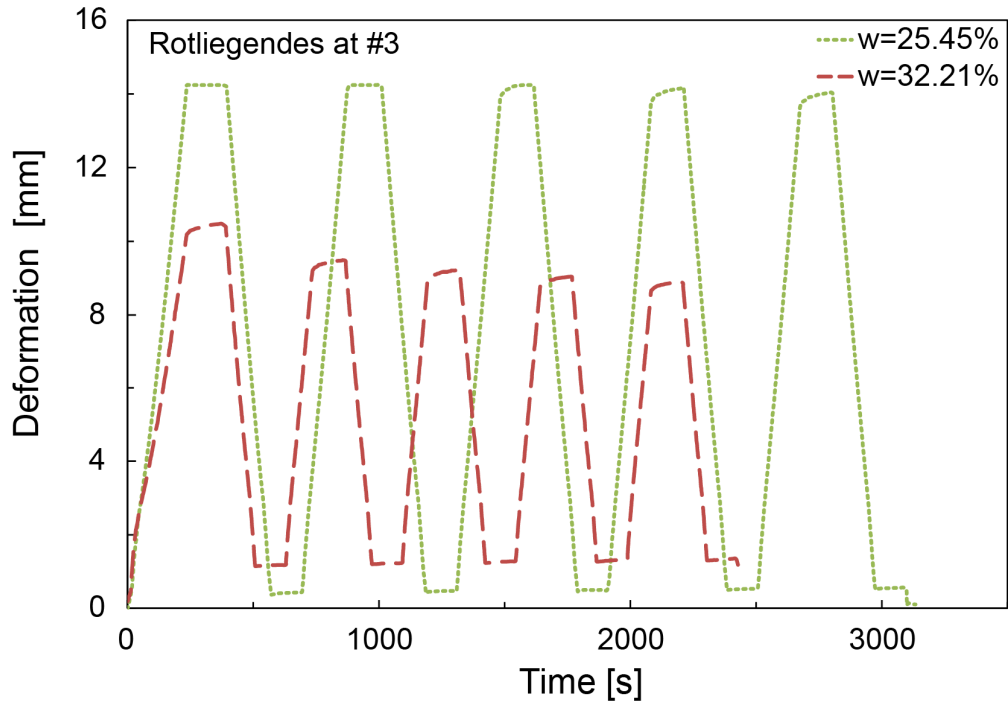


Figure C-3: Results of wheel tests for Rotliegendes at the location point #3

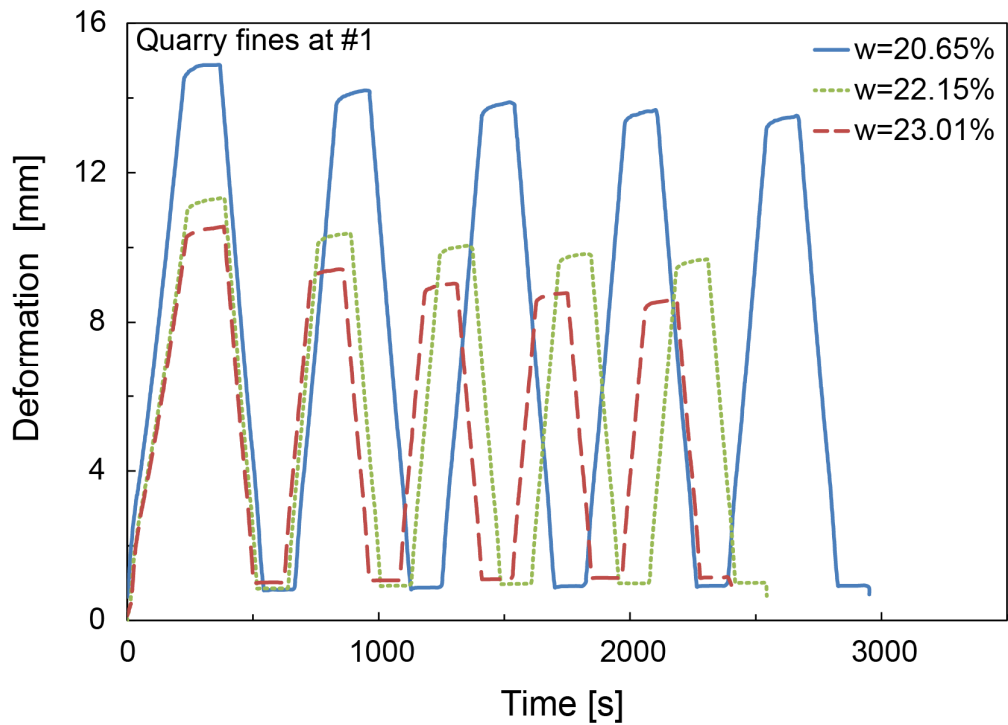


Figure C-4: Results of wheel tests for Quarry fines at the location point #1.

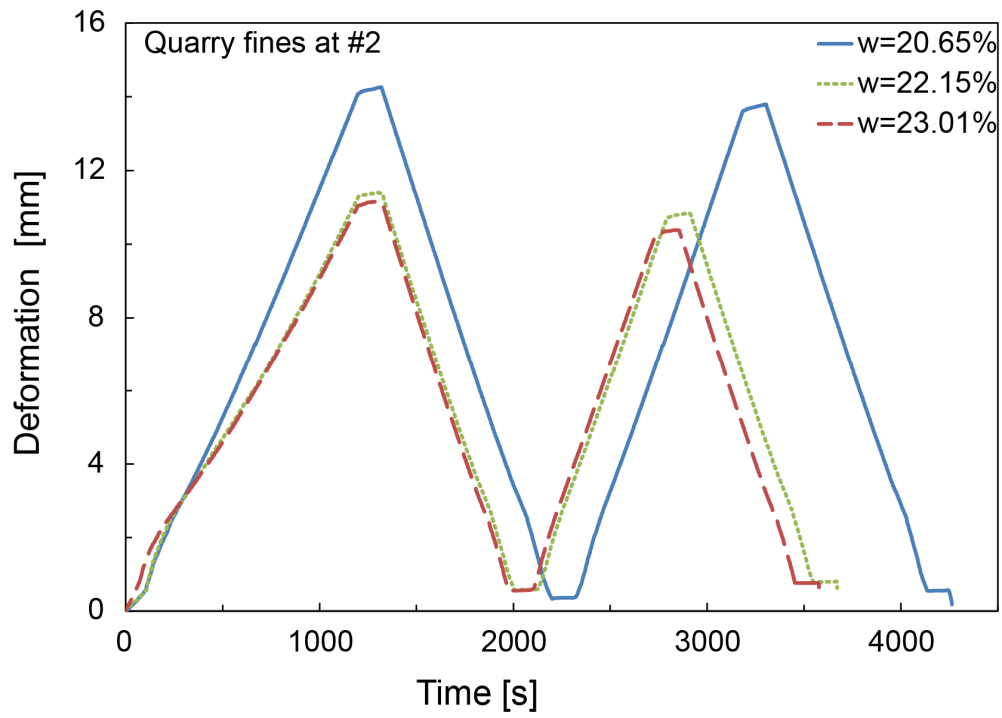


Figure C-5: Results of wheel tests for Quarry fines at the location point #2.

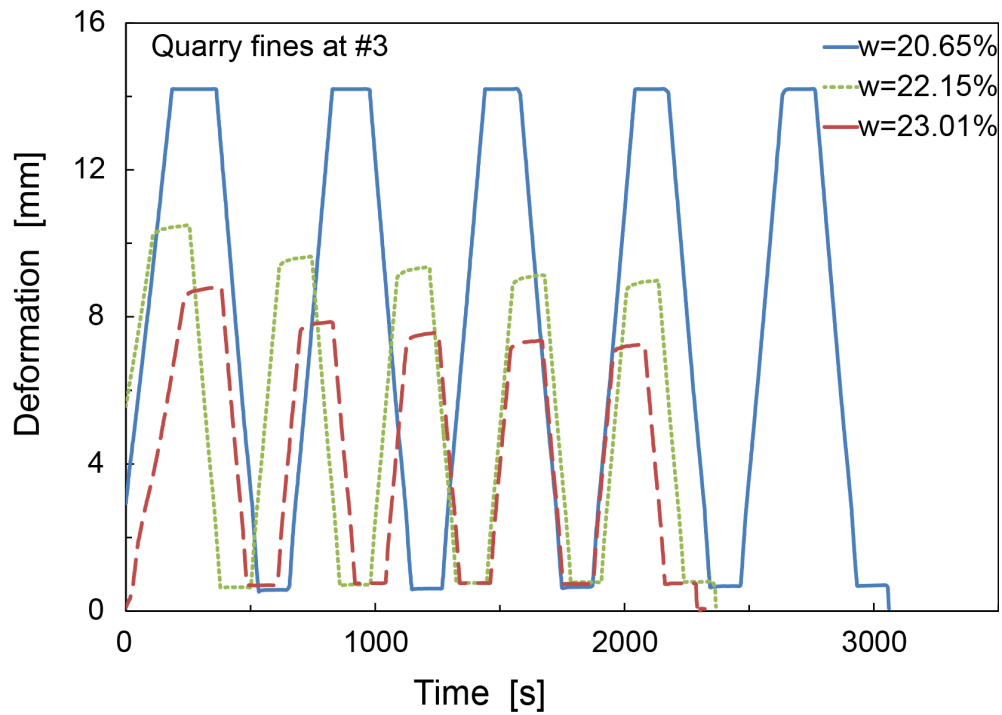


Figure C-6: Results of wheel tests for Quarry fines at the location point #3.

# Lebenslauf

## Beruflicher Werdegang

- 05/2015 - 11/2019 Wissenschaftliche Mitarbeiterin, Fachgebiet Bodenmechanik und Grundbau der TU Kaiserslautern
- 09/2014 - 04/2015 Bauingenieurin, Stadtverwaltung Paphos, Zypern

## Studium

- 05/2015 - 11/2019 Doktorandin am Fachgebiet Bodenmechanik und Grundbau der TU Kaiserslautern
- 09/2013 - 09/2014 Master Abschluss, Studiengang Erdölingenieurwesen, Universität Zypern, Zypern
- 09/2009 - 07/2013 Bachelor Abschluss, Studiengang Bauingenieurwesen und Umwelttechnik, Universität Zypern, Zypern

## Auszeichnungen

- 10/2015-09/2017 Promotionstipendium der Stiftung zur Förderung begabter Studierender und des wissenschaftlichen Nachwuchses, Rheinland-Pfalz, Deutschland
- 2011 2. Preis der Abteilung für Bau- und Umweltingenieurwesen zum Erreichen des zweitbesten Ergebnisses im 2. Jahr des Bachelor-Studiums
- 2010 1. Preis der Abteilung für Bau- und Umweltingenieurwesen zum Erreichen der besten Note im ersten Jahr des Bachelor-Studiums





# **Veröffentlichungen des Fachgebietes Bodenmechanik und Grundbau der Technischen Universität Kaiserslautern**

**Herausgegeben von Prof. Dr.-Ing. habil. Helmut Meißner**

- Nr. 1 Johannes Vogt (1992)  
Tragverhalten von Schlitzwandelementen
  
- Nr. 2 Frank Rogmann (1992)  
Untersuchungen zum Stoffverhalten von Kohle im Hinblick auf  
Hohlraumstandsicherheiten
  
- Nr. 3 Wolfgang Weckbecker (1993)  
Beitrag zur Berechnung oberflächennaher Tunnel
  
- Nr. 4 Egbert Adam (2001)  
Untersuchungen zum temperaturabhängigen Materialverhalten kristalliner und  
sedimentärer Gesteine
  
- Nr. 5 Andreas Becker (2002)  
Stoffmodell und numerisches Modell für zyklisch beanspruchte, teilgesättigte  
Sande
  
- Nr. 6 Katja Abel (2002)  
Zugspannungen in Kunststoffdichtungsbahnen geneigter  
Deponiebasisabdichtungen
  
- Nr. 7 Tao Li (2002)  
Zweiflächen-Stoffmodell für wassergesättigte bindige Böden unter zyklischer  
Beanspruchung
  
- Nr. 8 Solomon Taye Abebe (2002)  
Foundation pits in saturated highly expansive soils
  
- Nr. 9 Festschrift anlässlich des 65. Geburtstages von Prof. Dr.-Ing. habil. Helmut  
Meißner und dem 20-jährigen Bestehen des Fachgebietes Bodenmechanik und  
Grundbau an der Technischen Universität Kaiserslautern (2003)

**Herausgegeben von Prof. Dr.-Ing. habil. Christos Vrettos**

Nr. 10 Sanaa Wendling (2004)

Untersuchungen zur Entstehung von Austrocknungsrisen in mineralischen Deponieabdichtungen

Nr. 11 Yi Lei Shen (2005)

Unterfangung belasteter Fundamente durch Bohrpfähle

Nr. 12 Stefan Jung (2007)

Nichtlinearer horizontaler Bettungsmodulansatz für Trägerbohlwände in mitteldicht gelagertem Sand

Nr. 13 Markus Dobrowolsky (2008)

Quellverhalten teilgesättigter bindiger Böden mit mittlerem Quellpotential

Nr. 14 Viktoria Schwarz (2011)

Mechanisches Verhalten eines teilgesättigten Tons: Experimentelle Untersuchungen, Stoffmodell und Implementierung

Nr. 15 Thomas Becker (2012)

Materialverhalten eines teilgesättigten bindigen Bodens unter zyklischer Belastung

Nr. 16 Dong Chen (2014)

Flachgründungen auf Böden mit tiefenabhängiger Steifigkeit unter vertikaler dynamischer Belastung: Ergebnisse von numerischen Berechnungen im Frequenz- und Zeitbereich

Nr. 17 Andreas Becker (2017)

Untersuchungen zu neuartigen und gängigen Methoden der Baugrundertüchtigung

Nr. 18 Salomi Papamichael (2019)

Experimental and numerical investigations on wheel-soil interactions in calibrated near-surface soil model

ISBN 978-3-95974-121-7